

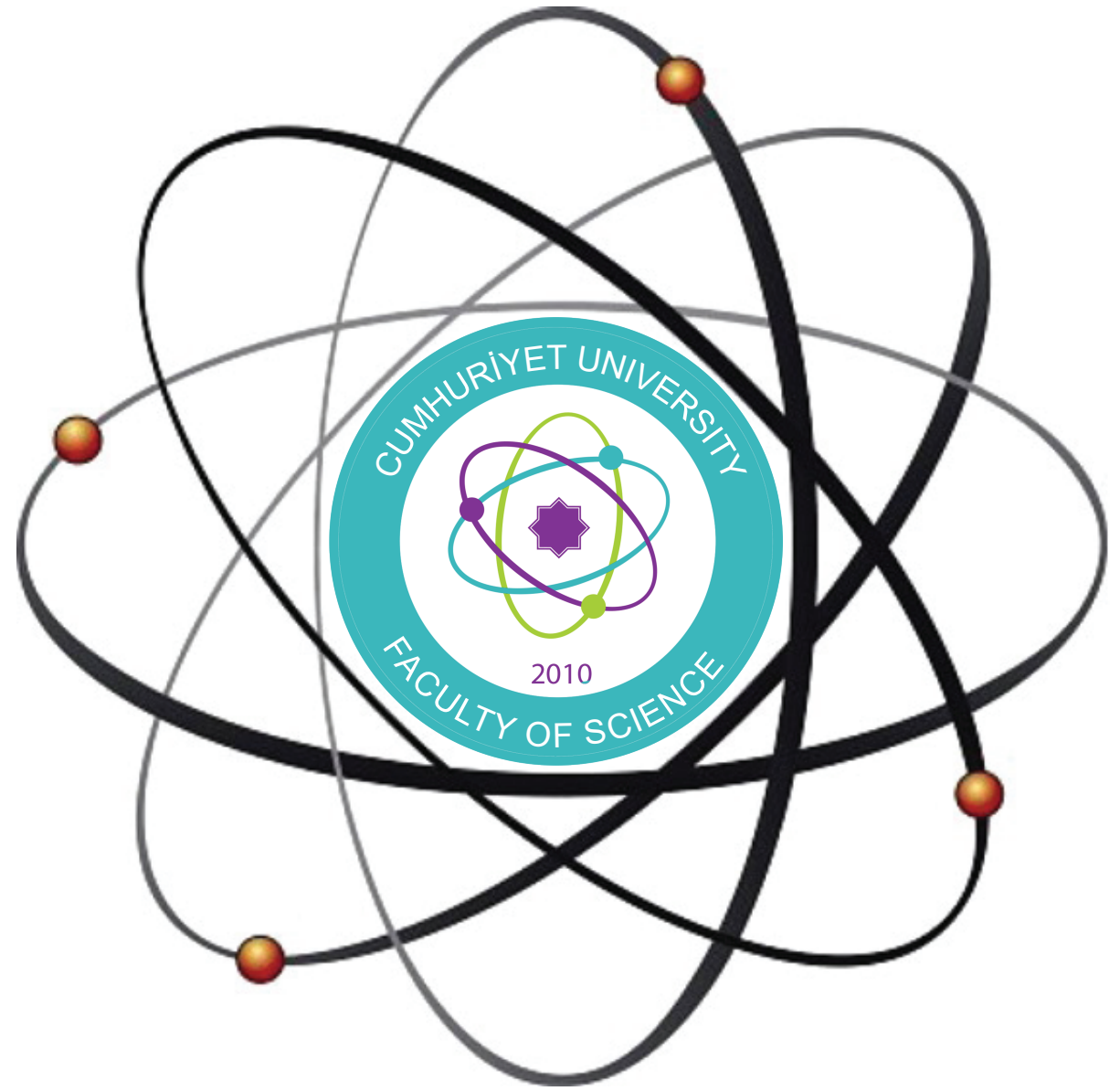


Cumhuriyet University

ISSN : 2587-2680

e-ISSN : 2587-246X

Cumhuriyet Science Journal



Volume : 41

Number : 3

Year : 2020



ISSN: 2587-2680
e-ISSN: 2587-246X
Period: Quarterly
Founded: 2002
Publisher: Cumhuriyet
University

Cumhuriyet Science Journal (CSJ)

Journal Previous Name: Cumhuriyet Üniversitesi Fen-Edebiyat Fakültesi Fen Bilimleri Dergisi

Old ISSN: 1300-1949

Owner on behalf of the Cumhuriyet University, Faculty of Science

Prof. Dr. İdris Zorlutuna (Sivas Cumhuriyet University)

Editor in Chief

Prof. Dr. İdris ZORLUTUNA (Sivas Cumhuriyet University)

Managing Editor

Assoc. Prof. Dr. Adil ELİK (Sivas Cumhuriyet University)

Editors

Prof. Dr. Baki KESKİN

bkeskin@cumhuriyet.edu.tr

Subjects: Mathematics and Statistics

Institution: Sivas Cumhuriyet University

Assoc. Prof. Dr. Adil ELİK

elik@cumhuriyet.edu.tr

Subjects: Chemistry and Chemical Engineering, Environmental Sciences, Basic Sciences (General)

Institution: Sivas Cumhuriyet University

Prof. Dr. Nilüfer TOPSAKAL

ntopsakal@cumhuriyet.edu.tr

Subjects: Applied Mathematics

Institution: Sivas Cumhuriyet University

Prof. Dr. Serkan AKKOYUN

sakkoyun@cumhuriyet.edu.tr

Subjects: Physics and Physical Engineering

Institution: Sivas Cumhuriyet University

Prof. Dr. Hülya KURŞUN

hkursun@cumhuriyet.edu.tr

Subjects: Earth Sciences

Institution: Sivas Cumhuriyet University

Subjects: Molecular Biology and Genetics, Biochemistry

Institution: Sivas Cumhuriyet University

Prof. Dr. Halil İbrahim ULUSOY

hiulusoy@cumhuriyet.edu.tr

Subjects: Chemistry, Analytical Chemistry, Drug Analysis, Pharmacy

Institution: Sivas Cumhuriyet University

Abstracted&Indexing

ULAKBİM TR-Dizin

Index Copernicus (ICI Journals Master List)

Clarivate Analytics Zoological Record

Crossref

Directory of Open Access Journals (DOAJ)

WorldCat

Akademik Dizin

Arastirmax Bilimsel Yayın İndeksi

Bielefeld Academic Search Engine (BASE)

Directory of Research Journal Indexing (DRJI)

Google Scholar

Research Gate

Idealonline

Field Editors

Prof.Dr. Sezai ELAGÖZ (Aselsan)

Prof.Dr. Muhammet BEKÇİ (Sivas Cumhuriyet University)

Assoc.Prof.Dr. Duran KARAKAŞ (Sivas Cumhuriyet University)

Assoc. Prof. Dr. Yaşar ÇAKMAK (Sivas Cumhuriyet University)

Assoc.Prof.Dr. Sevgi DURNA DAŞTAN (Sivas Cumhuriyet University)

Assist. Prof. Dr. Didem ALTUN (Sivas Cumhuriyet University)

Editorial Board

Prof. Dr. Mustafa SOYLAK (Erciyes University)

Prof.Dr. Münevver SÖKMEN (KGTU)

Prof.Dr. Hüseyin MERDAN (TOBB ETU)

Prof.Dr. Chuan Fu Yang (Nanjing University of Science and Technology)

Prof.Dr. Mehmet AKKURT (Erciyes University)

Prof.Dr. Mustafa KAVUTÇU (Gazi University)

Prof.Dr. Abuzar KABIR (International Forensic Research Institute)

Prof. Dr. Mustafa TÜZEN (GOP University)

Prof.Dr. Ali Fazıl YENİDÜNYA (Sivas Cumhuriyet University)

Prof.Dr. Songül KAYA MERDAN (METU)

Prof.Dr. Yeşim SAĞ AÇIKEL (Hacettepe University)

Prof.Dr. Mehmet ŞİMŞİR (Sivas Cumhuriyet University)

Prof.Dr. Atalay SÖKMEN (KGTU)

Prof. Dr. Marcello LOCATELLI (University "G. d'Annunzio" of Chieti-Pescara).

Dr. Ricardo I. JELDRES (Universidad de Antofagasta)

Dr. Jose Javier Valiente-Dobon (INFN-LNL, Padova University)

Prof.Dr. Mustafa YILDIRIM (Sivas Cumhuriyet University)

Assoc.Prof.Dr. Ali DELİCEOĞLU (Erciyes University)

Assoc.Prof.Dr. Tuncay BAYRAM (Karadeniz Technical University)

Assoc.Prof.Dr. Gökhan KOÇAK (Erciyes University)

Dr. Francois VOS (The University of Queensland)

Dr. Nadjat Laouet (Freres Mentouri Constantine-1 University)

Layout Editors:

Research Assistant Esra Merve YILDIRIM

Copyeditors:

Research Assistant Özgür İNCE

Research Assistant Doğa Can SERTBAŞ

Research Assistant Dr. Hacı Ahmet KARADAŞ

Proofreader:

Assist. Prof. Dr. Yener ÜNAL

Assist. Prof. Dr. Tuğba MERT

Publication Type. Peer Reviewed Journal

Cite Type: Cumhuriyet Sci. J.

Contact Information

Faculty of Science Cumhuriyet University 58140

Sivas- TURKEY

Phone: +90(346)2191010-1522

Fax: +90(346)2191186

e-mail: csj@cumhuriyet.edu.tr

<http://dergipark.gov.tr/csj>

CONTENTS	PAGES
Ozan ÖZTÜRK, Emine ÖZTÜRK, Sezai ELAGÖZ <i>Electronic characteristics of asymmetric triple GaAlAs/GaAs and GaInAs/GaAs quantum wells depending on Al and In concentration</i>	565-570
Özge KURAN, Seçil YALAZ <i>Henderson's method approach to Kernel prediction in partially linear mixed models</i>	571-579
Ayşe GÜNDOĞDU, Uğur ÇARLI <i>Microbiological pollution and some physicochemical properties of sıkarağaçlar creek in sinop (Black Sea-Turkey)</i>	580-593
Bahar MERYEMOĞLU, Burçak KAYA ÖZSEL, Berna NİŞ <i>A research on antioxidant activity evaluation of waste lignocellulosic biomass: optimization using response surface methodology</i>	594-601
Gülcan GENCER, Kerem GENCER <i>Comparison of estimators under different loss functions for two-parameter bathtub - shaped lifetime distribution</i>	602-611
Yılmaz ÇEVEN, Doğan OZAN <i>Neutrosophic triplets in some neutrosophic rings</i>	612-616
Uğur ULUSU, Fatih NURAY <i>Lacunary I-invariant convergence</i>	617-624
Evrin TOKLU, Neslihan KARAGÖZ <i>On some geometric properties of normalized Wright functions</i>	625-634
Ahmet Şevki TAŞKIRAN, Yaşar TAŞTEMUR <i>The comparison of inflammatory markers in pentylene-tetrazole-induced acute epileptic seizure model and chronic epilepsy model in rats</i>	635-641
Ümit TOKEŞER, Ömer ALSAN <i>Equality of internal angles and vertex points in conformal hyperbolic triangles</i>	642-650
Adnan ALDEMİR, Ali Rıza KUL <i>Isotherm, kinetic and thermodynamic studies for the adsorption of methylene blue on almond leaf powder</i>	651-658
Duran KARAKAŞ <i>Computational study on molecular structure, vibrational spectrum analysis and acidity strength of P4On (n = 6-10) phosphorus oxides with cage structure</i>	659-664
Fatoş Ayça ÖZDEMİR OLGUN, Birsan DEMİRATA ÖZTÜRK <i>Evaluation of tetracycline, oxytetracycline and penicillin G residues in chicken meat samples by high performance liquid chromatography with pda detection</i>	665-670
Cemalettin UYAN, Ersin YULMAZ <i>UV-VIS spectrophotometric determination of magnesium after complexing with 8-hydroxy quinoline in sodium dodecyl sulphate micellar medium</i>	671-679
Burçak ZEREYKAYA, Dilek ESKİKÖY BAYRAKTEPE, Zehra YAZAN <i>An adsorptive stripping voltammetric study based on disposable pencil graphite sensor for the determination of caffeine in local brand ice tea</i>	680-689
Ahmet ERDEM <i>pH and thermoresponsive comb-type grafted hydrogels based on polyethylene glycol diglycidyl ether and monoamino/diamino terminated jeffamines: synthesis, characterization and physicochemical properties</i>	690-698

Pınar BAŞER

Pressure and temperature effects on magnetoelectric band energies in GaAs / InxGa1-xAs cylindrical quantum wires..... 699-705

İdil ÇETİN

Antiproliferative effects of cetuximab on triple negative breast cancer cell line MDA-MB-231..... 706-711

Arzu KARATEPE, Ahmet ÇETİN

Antioxidant and prooxidant activity of new 1,2-diols and thiadiazoles derivatives in Saccharomyces cerevisiae yeast cells..... 712-719

Abdulkadir ŞEKER, Banu DİRİ, Halil ARSLAN, Fatih AMASYALI

Summarising big data: public GitHub dataset for software engineering challenges..... 720-724

Lale CİVAN, Macid NURBAŞ

Investigation of 58S bioactive glass tablets..... 725-731

Ayla DOĞAN, Mecit SİVRİOĞLU, Şenol BAŞKAYA

Numerical investigation of heat transfer from heat sources placed in a horizontal rectangular channel..... 732-740

Ozhan PAZARCI, Yunus TORUN, Serkan AKKOYUN

Estimation of the future fracture epidemiology in the patients applying to the emergency department with long short time memory method 741-746



Electronic characteristics of asymmetric triple GaAlAs/GaAs and GaInAs/GaAs quantum wells depending on Al and In concentration

Ozan Öztürk^{1*}, Emine Öztürk², Sezai Elagöz³

¹ Sivas Cumhuriyet University, Department of Nanotechnology Engineering, 58140, Sivas-TURKEY

² Sivas Cumhuriyet University, Department of Physics, 58140, Sivas-TURKEY

³ ASELSAN - Microelectronics, Guidance & Electro-Optics, Ankara-TURKEY

Abstract

Herein, the electronic characteristics of asymmetric triple Ga_{1-x}Al_xAs/GaAs quantum wells (A model) and Ga_{1-x}In_xAs/GaAs quantum wells (B model) have been examined as dependent on Al and In concentration. The energy levels, the wave functions and the finding probability of electron in quantum well (QW) of these systems under effective mass approach were concluded by Schrödinger equation solution. According to our results, the main differences between models A and B are effective mass and energy gap. For A model, GaAlAs is the barrier and GaAs is the well. Whereas for B model, GaAs is the barrier and GaInAs is the well. Also, the energy levels and the potential height of B model are unceasingly higher than of B model. The concentration ratio has a great impact on the electronic features of the asymmetric triple quantum well (ATQW). These features have a convenient attention for the purpose of adjustable semiconductor devices.

Article info

History:

Received:28.11.2019

Accepted:19.02.2020

Keywords:

Asymmetric triple GaAlAs/GaAs quantum well,
Asymmetric triple GaInAs/GaAs quantum well,
Concentration ratio,
Electronic characteristics.

1. Introduction

The electronic characteristics of the low-dimensional structures (LDSs) are extremely reliant on the pressure of the asymmetry of the potential profile of a semiconductor quantum well (QW). Such asymmetry of the potential shape could be provided by an electric field or the potential profile may be altered by an alloy ratio. We are concerned in observing the structure of an asymmetric triple quantum wells (ATQW) formed by two different semiconductors (e.g, GaAs/GaAlAs and InGaAs/GaAs). These structures contain three QWs coupled by two barriers. They are very suitable structure for observing quantum electronic transport. Because GaAlAs / GaAs QW systems are applied in modern photo-electronics and high-speed electronic devices, the electrical and optical properties of the related systems have been widely investigated under both the pressure and external fields [1-6]. The segregation of indium atoms in the GaInAs

layer has been extensively researched in current times, as the considerate of high-performance devices desires sudden hetero-interfaces [7-11]. These indium atoms are powerfully related to the growth temperature and the GaInAs/GaAs structure is allocated from the growing surface throughout MBE growth.

ATQW structures are the ultimate structures for examining the mechanisms of carrier transfer [12-14], related to single and double QWs. These systems are very motivating for the device industry because by the interlayer distance between QWs and the barrier alters, a development in the transport features is realized. The focus benefit of asymmetric multiple quantum well (AMQW) semiconductors over single QW is the advanced exciton electro-optic reply. The opto-electronic features of the excitons in AMQWs ensure a range of potential practices in high-speed spatial light modulators and switches. This study focused on the theoretical research of the electronic qualities of Ga_{1-x}Al_xAs/GaAs ATQWs and Ga_{1-x}In_xAs/GaAs

*Corresponding author. Email address: ozanozturk@cumhuriyet.edu.tr

<http://dergipark.gov.tr/csj> ©2020 Faculty of Science, Sivas Cumhuriyet University

ATQWs depending on the x-concentration (where x represents the contribution rate of Al and In in ATQW, individually). A model and B model will be named for $\text{Ga}_{1-x}\text{Al}_x\text{As}/\text{GaAs}$ ATQWs and $\text{Ga}_{1-x}\text{In}_x\text{As}/\text{GaAs}$ ATQWs, correspondingly. There are

on the left hand side “semi parabolic QW”, the middle hand side “semi half inverse parabolic-half parabolic QW” and on the right hand side “semi inverse parabolic QW”. The motivation for using many ATQWs with different images is to create multi wavelength optical devices.

2. Materials and Methods

Under the effective-mass approach, the wave functions and the energy levels for electrons in ATQW could be realized by dissolving the one-dimensional Schrödinger equation.

$$\left(-\frac{\hbar^2}{2m^*} \frac{d^2}{dz^2} + V(z)\right) \Psi(z) = E \Psi(z) \quad (1)$$

where $V(z)$ is the confined potential, and E and $\Psi(z)$ are the eigen-energy and eigen-function of the Eq. (1) solution.

The confinement potential of ATQW for the particle z -direction, b_L and b_R being the left and right barrier widths, L_L , L_M and L_R being the left, middle and the right quantum widths, respectively, are given by

$$V(z) = V_0 \begin{cases} \frac{2}{L_L^2} \left(z + b_L + \frac{(L_M + L_L)}{2} \right)^2 - \left(L_L + b_L + \frac{L_M}{2} \right) & - \left(L_L + b_L + \frac{L_M}{2} \right) \leq z \leq - \left(b_L + \frac{L_M}{2} \right) \\ -\frac{2}{L_M^2} z^2 + \frac{1}{2} & -\frac{L_M}{2} \leq z \leq 0 \\ \frac{2}{L_M^2} z^2 & 0 \leq z \leq \frac{L_M}{2} \\ -\frac{2}{L_R^2} \left(z - b_R - \frac{(L_M + L_R)}{2} \right)^2 + \frac{1}{2} & \frac{L_M}{2} + b_R \leq z \leq \frac{L_M}{2} + b_R + L_R \\ 1 & \text{elsewhere} \end{cases} \quad (2)$$

The discontinuity in the conduction band edge and the effective mass of electron of $\text{Ga}_{1-x}\text{Al}_x\text{As}/\text{GaAs}$ [15-17] and $\text{Ga}_{1-x}\text{In}_x\text{As}/\text{GaAs}$ [15-16, 18] are analyzed using the next equations.

$$m_{\text{GaAlAs}}^* = (0.067 + 0.083 x) m_0 \quad (3a)$$

$$m_{\text{GaInAs}}^* = (0.067 - 0.04 x) m_0 \quad (3b)$$

$$V_0^{\text{GaAlAs}} = 0.6 (E_g^{\text{GaAlAs}} - E_g^{\text{GaAs}}) \quad (4a)$$

$$V_0^{\text{GaInAs}} = 0.6 (E_g^{\text{GaAs}} - E_g^{\text{GaInAs}}) \quad (4b)$$

Where $E_g^{\text{GaAlAs}} = (E_g^{\text{GaAs}} + 1247 x) \text{ meV}$, $E_g^{\text{GaInAs}} = (E_g^{\text{GaAs}} - 1619 x + 555 x^2) \text{ meV}$, $E_g^{\text{GaAs}} = 1424 \text{ meV}$, and m^* is the effective mass depending on the material composition.

The QW confined potential is essential for the limitation of the electrons. Therefore, the finding probability of the electron in different QWs is provided by,

$$P_i^W = \int |\Psi_i^W(z)|^2 dz \quad (i = 1, 2, 3; \quad W = L, M, R) \quad (5)$$

where L, M and R indicate the left QW (LQW), the middle QW (MQW) and the right QW (RQW), correspondingly.

3. Results and Discussion

It has been notionally examined the electronic features of A and B models depending on the x-concentration for ATQW. In this study, all well widths are $L_L = L_M = L_R = 8$ nm, $b_L = b_R = 2$ nm and $T = 300$ K.

For different x-values, Fig. 1 (A model) and Fig. 2 (B model) demonstrate the confinement potential, the bound energy levels and squared wave functions referred to these energy levels. As understood from Eq. (3) and Eq. (4), the major differences of A and B type are the effective mass and the energy gap. While for A model the well is GaAs and the barrier is GaAlAs, for B model the well is GaInAs and the barrier is GaAs. As estimated, the energy levels of A model with lower potential height are continuously lower than the energy levels of B model. As can be seen from these figures, there are three, four and five energy states in A structure for $x = 0.10$, $x = 0.15$ and $x = 0.20$ respectively, whereas B structure with the same ratios has three, three and four confined energy levels, respectively. For both models, the electron in the ground state is commonly located in LQW, while the electrons at the second and third energy levels are encircled in MQW and RQW, respectively. As the height of the potential profile changes depending on the concentration ratio, both the bound state energy levels and the probability

densities of electrons at these energy levels change. The sensitivity of A model to the x-concentration ratio appears to be higher than B model.

For structure A and B, the resulting bounded state energy levels corresponding to the change in the concentration ratio between $x = (0.10 - 0.25)$ are given in Fig. 3a and Fig. 3b, serially. As expected, as the concentration ratio increases, the height of the limited potential and consequently the values of the energy levels increase, and more confined state energy levels exist in QWs. The fourth bound state energy is seen at $x \geq 0.15$ in A structure and $x \geq 0.16$ in B structure. In A model, the fifth energy level was found within the enclosed potential at $x \geq 0.20$, whereas this energy level appeared in the B model at $x \geq 0.24$. The differences are due to the fact that the effective mass of the electron in B structure is smaller than A structure and thus the energy levels rise to higher values. Therefore, if it

is desired to obtain more bound state energy levels depending on the x-concentration value, then A model should be preferred.

In Fig. 4a and Fig. 4b, the finding probability of the electrons in LQW, MQW and RQW for first three bounded energy states as a function of the x-concentration is shown for both A and B model, respectively.

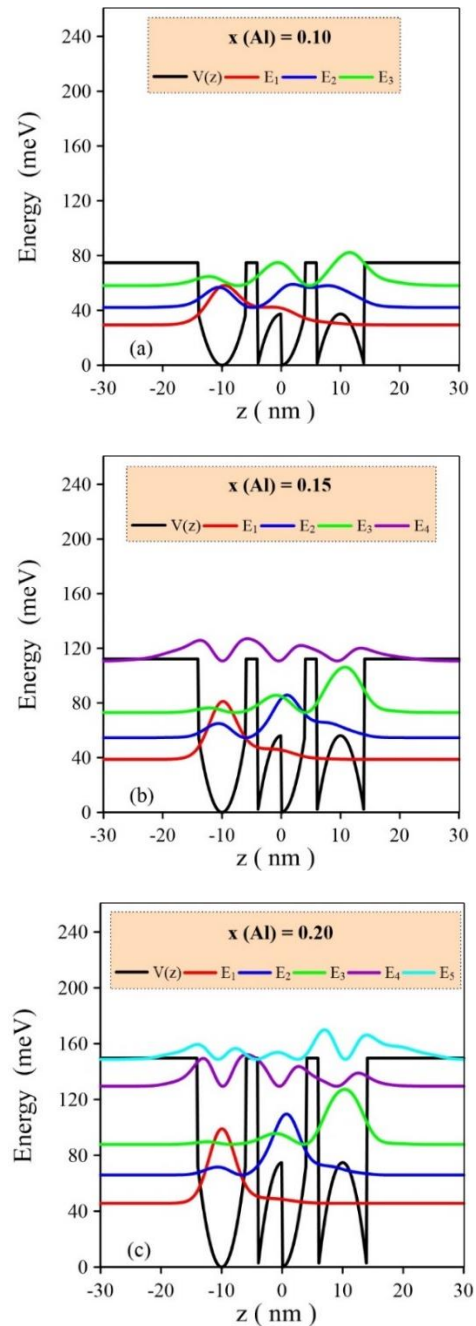


Figure 1. For ATQW (A model), the confined potential and the bound energy levels with their squared wave functions for a) $x = 0.10$, b) $x = 0.15$, c) $x = 0.20$.

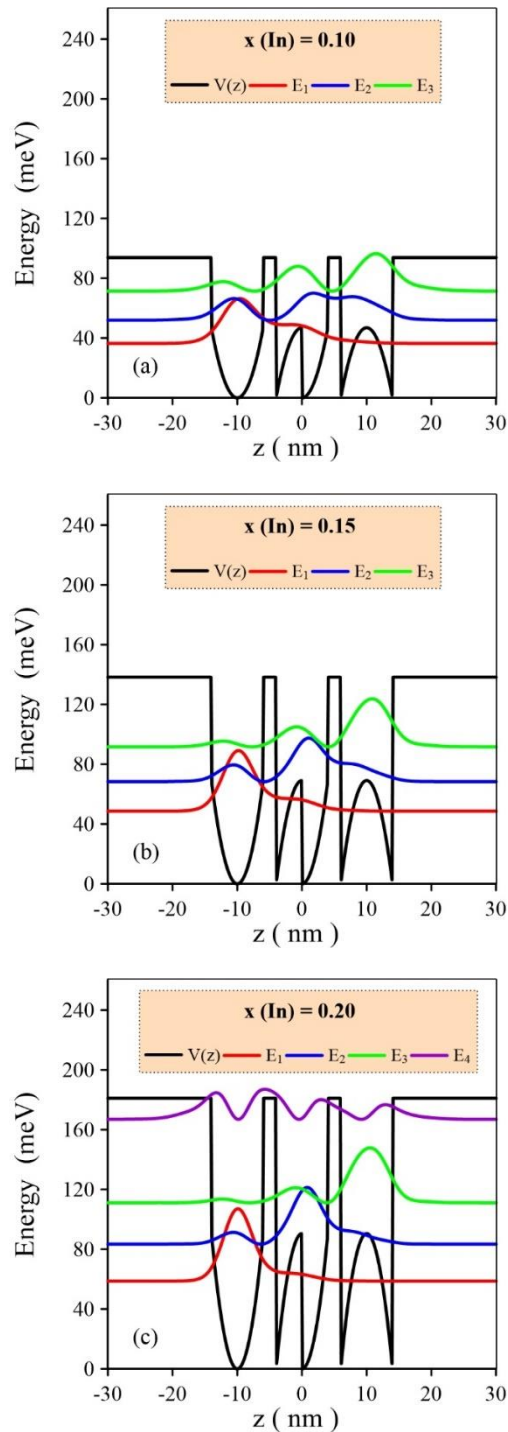


Figure 2. For ATQW (B model), the confined potential and the bound energy levels with their squared wave functions for a) $x = 0.10$, b) $x = 0.15$, c) $x = 0.20$.

In both models, for the first value $x = 0.10$, the ground, second and third state energy levels are located in LQW, MQW and RQW, respectively, and these probability densities in the same QWs rise as the concentration ratio increases. The probability densities in B model is slightly lower than A model.

4. Conclusions

In present work, the electronic qualities of asymmetric triple $\text{Ga}_{1-x}\text{Al}_x\text{As}/\text{GaAs}$ and $\text{Ga}_{1-x}\text{In}_x\text{As}/\text{GaAs}/\text{GaAs}$ QWs are observed related to the x -concentration value. The greatest essential difference between these models is the size of energy levels. We analyzed the potential height, the bound energy levels and the finding probabilities of the electrons in ATQW. In particular, we have

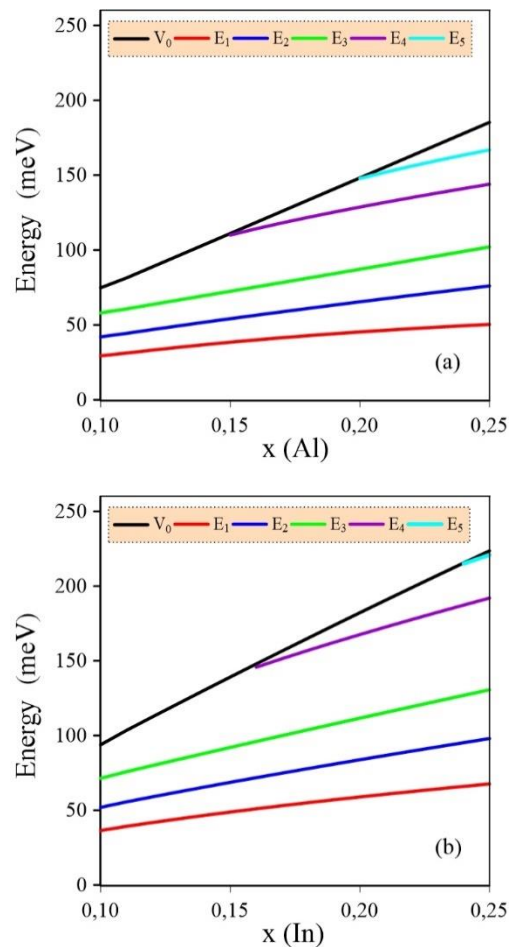


Figure 3. For ATQW the variation of the confined potential height and the bound energy levels versus the x -concentration ratio values for a) A model, b) B model.

calculated the eigen-energies and the eigen-functions of these models. It is found that depending on the x-concentration value of the electronic features of ATQW varies for A and B model. These features could be crucial in the improvement of continual wave operation of ATQW semiconductor devices. So, we think that these consequences will supply a development in multiple electro-optical semiconductor devices applications, for proper selection of the structural parameters.

Acknowledgment

This work is supported by the Scientific Research Project Fund of Sivas Cumhuriyet University under the project number M-679.

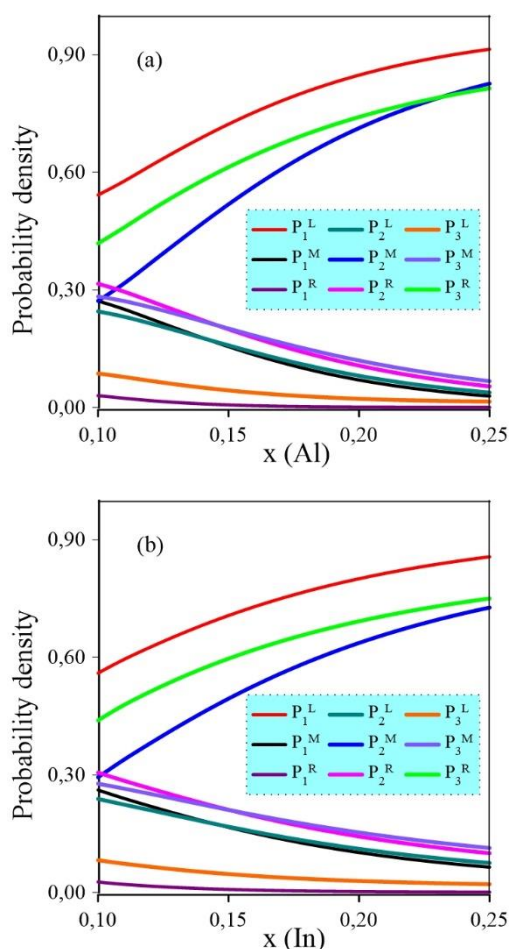


Figure 4. The probability density of the electrons in LQW, MQW and RQW for first three bound energy state as a function of the x-concentration ratios for a) A model, b) B model.

REFERENCES

- [1] Zhao G. J., Liang X. X., Ban S. L., Binding energies of donors in quantum wells under hydrostatic pressure, *Phys. Lett. A*, 319 (2003) 191-197.
- [2] Ozturk E., Simultaneous effects of the intense laser field and the electric field on the nonlinear optical properties in GaAs/GaAlAs quantum well, *Opt. Commun.*, 332 (2014) 136-143.
- [3] Raigoza N., Morales A. L., Duque C. A., Effects of hydrostatic pressure on donor states in symmetrical GaAs-Ga_{0.7}Al_{0.3}As double quantum wells, *Physica B*, 363 (2005) 262-270.
- [4] Peter A. J., Navaneethakrishnan K., Simultaneous effects of pressure and temperature on donors in a GaAlAs/GaAs quantum well, *Superlattice Microst.*, 43 (2008) 63-71.
- [5] Ozturk E., Sokmen I., Nonlinear intersubband absorption and refractive index changes in square and graded quantum well modulated by temperature and hydrostatic pressure, *J. Lumin.*, 134 (2013) 42-48.
- [6] Kasapoglu E., Duque C. A., Mora-Ramos M. E., Restrepo R. L., Urgan F., Yesilgul U., Sari H., Sokmen I., Combined effects of intense laser field, electric and magnetic fields on the nonlinear optical properties of the step-like quantum well, *Materials Chemistry and Physics*, 154 (2015) 170-175.
- [7] de la Cruz G. G., The influence of surface segregation on the optical properties of quantum wells, *J. Appl. Phys.*, 96 (2004) 3752-3755.
- [8] Martini S., Quivy A. A., Lamas T. E., da Silva E. C. F., Real-time RHEED investigation of indium segregation in InGaAs layers grown on vicinal GaAs(001) substrates, *Phys. Rev. B*, 72 (2005) 153304-153307.
- [9] Wu S., Huang Z., Liu Y., Huang Q., Guo W., Cao Y., The effects of indium segregation on the valence band structure and optical gain of GaInAs/GaAs quantum wells, *Physica E*, 41 (2009) 1656-1660.

- [10] Ozturk E., Electric and intense laser field effect on the electronic properties of Ga_{1-x}Al_xAs/GaAs and Ga_{1-x}In_xAs/GaAs semi-parabolic quantum wells, *Laser Physics*, 26 (2016) 096102-096110.
- [11] Baser P., Altuntas I., Elagoz S., The hydrostatic pressure and temperature effects on hydrogenic impurity binding energies in GaAs/In_xGa_{1-x}As/ GaAs square quantum well, Superlattice, *Microst.*, 92 (2016) 210-216.
- [12] Fukuta, S., Goto, H., Sawaki, N., Suzuki, T., Ito, H., & Hara, K., Modulation of optical spectra in an asymmetric triple quantum well structure. Semiconductor Science and Technology, 8(10) (1993) 1881–1884.
- [13] Hernández-Cabrera A., Valance-band mixing effect on exciton dipole terahertz emission from asymmetric triple quantum wells, *J. Appl. Phys.*, 80 (3) (1996) 1547-1552.
- [14] Alaydin B. O., Ozturk E., Elagoz S., Interband transitions dependent on indium concentration in Ga_{1-x}In_xAs/GaAs asymmetric triple quantum wells, *International Journal of Modern Physics B*, 32 (5) (2018) 18550052-1855067.
- [15] Ozturk O., Ozturk E., Elagoz S., Linear and nonlinear optical absorption coefficient and electronic features of triple GaAlAs/GaAs and GaInAs/GaAs quantum wells depending on barrier widths, *Optik*, 180 (2019) 394-405.
- [16] Zorrry P. S. Jr., Quantum well lasers, Academic Press, Boston: 1993; p.79.
- [17] Niculescu E.C., Eseanu N., Spandonide A., Laser field effects on the interband transitions in differently shaped quantum wells, U.P.B. Sci. Bull., *Series A*, 77 (4) (2015) 281-292
- [18] Ochalski T.J., Zuk J., Reginski K., Bugajski M., Photorefectance studies of InGaAs/GaAs/AlGaAs single quantum well laser structures, *Acta Physica Polonica A*, 94 (1998) 463-467.

Henderson's method approach to Kernel prediction in partially linear mixed models

Özge KURAN^{1*} , Seçil YALAZ¹ 

¹Dicle University, Faculty of Science, Department of Statistics, 21280, Diyarbakır / TURKEY

Abstract

In this article, we propose Kernel prediction in partially linear mixed models by using Henderson's method approach. We derive the Kernel estimator and the Kernel predictor via the mixed model equations (MMEs) of Henderson's that they give the best linear unbiased estimation (BLUE) of the fixed effects parameters and the nonparametric function computationally easier and the best linear unbiased prediction (BLUP) of the random effects parameters as by-products. Additionally, asymptotic property of the Kernel estimator is investigated. A Monte Carlo simulation study is supported to illustrate the performance of Kernel prediction in partially linear mixed models and then, we finalize the article with the help of conclusion and discussion part to summarize the findings.

Article info

History:

Received: 07.01.2020

Accepted: 15.06.2020

Keywords:

Henderson's method, Kernel estimator, Kernel predictor, partially linear mixed model, semiparametric model.

1. Introduction

The partially linear mixed models (PLMMs) can be viewed as a combination of the linear mixed models (LMMs) [1] and the partially linear models (PLMs) [2]. The PLMMs are popular in the analysis of correlated data including longitudinal and repeated measurement or clustered data over time by incorporating the between-subject and within-subject variations in many clinical and biomedical studies in recent years.

Let us consider the PLMMs

$$y_i = X_i\beta + g(T_i) + Z_iu_i + \varepsilon_i \quad i = 1, \dots, m \quad (1)$$

where y_i is an $n_i \times 1$ vector of response variables measured on subject i , β is a $p \times 1$ parameter vector of fixed effects, T_i is a random variable defined on $[0,1]$, the function $g(\cdot)$ is unknown function from \mathbb{R}^d to \mathbb{R}^1 , $X_i = (x_{i1}, \dots, x_{ip})^T$, $T_i = (t_{i1}, \dots, t_{id})^T$ and $Z_i = (z_{i1}, \dots, z_{iq})^T$ are $n_i \times p$, $n_i \times d$ and $n_i \times q$ known fixed and random effects design matrices, respectively, u_i random vector that the components of which are told random effects and ε_i is an $n_i \times 1$ random errors vector.

The posits, $u_i \stackrel{iid}{\sim} N_q(0, D)$ and $\varepsilon_i \stackrel{iid}{\sim} N_{n_i}(0, W_i)$, $i = 1, \dots, m$, where u_i and ε_i are independent, D and W_i are $q \times q$ and $n_i \times n_i$ known positive definite (pd) matrices are usually used.

When X_i 's are observable and under the assumptions of model (1), the conditional distribution of y_i given u_i is $y_i|u_i \sim N(X_i\beta + g(T_i) + Z_iu_i, W_i)$. Defining the conditional expectations which are also known as the kernel regressions with bandwidth h of y , X and Z as

$$\omega_y(T_i) = E(y_i|T_i) = \sum_{i=1}^n \omega_{ij}(t)y_i$$

*Corresponding author. Email address: ozge.kuran@dicle.edu.tr

<http://dergipark.gov.tr/csj> ©2020 Faculty of Science, Sivas Cumhuriyet University

$$\omega_x(T_i) = E(X_i|T_i) = \sum_{i=1}^n \omega_{ij}(t) X_i$$

$$\omega_z(T_i) = E(Z_i|T_i) = \sum_{i=1}^n \omega_{ij}(t) Z_i$$

where $\omega_{ij}(t) = K_h(t_{ij} - t) / \sum_{k=1}^n \sum_{l=1}^{n_k} K_h(t_{kl} - t)$, $K_h(\cdot) = K_h(\cdot/h)$ and $K(\cdot)$ is a Kernel function, the last expression could be written as

$$\omega_y(T_i) = \omega_x(T_i)\beta + \omega_z(T_i)u_i + g(T_i). \quad (2)$$

Subtracting equation (2) from equation (1), it is obtained that

$$y_i - \omega_y(T_i) = [X_i - \omega_x(T_i)]\beta + [Z_i - \omega_z(T_i)]u_i + \varepsilon_i$$

$$\tilde{y}_i = \tilde{X}_i\beta + \tilde{Z}_i u_i + \varepsilon_i. \quad (3)$$

Let $\tilde{y} = (\tilde{y}_1^T, \dots, \tilde{y}_m^T)^T$, $\tilde{X} = (\tilde{X}_1^T, \dots, \tilde{X}_m^T)^T$, $\tilde{Z} = \bigoplus_{i=1}^m \tilde{Z}_i$, where \bigoplus describes the direct sum, $u = (u_1^T, \dots, u_m^T)^T$ and $\varepsilon = (\varepsilon_1^T, \dots, \varepsilon_m^T)^T$. Then, equation (3) is obtained more compactly as

$$\tilde{y} = \tilde{X}\beta + \tilde{Z}u + \varepsilon \quad (4)$$

which implies that

$$\begin{bmatrix} u \\ \varepsilon \end{bmatrix} \sim N_{qm+n} \left(\begin{bmatrix} 0_{qm} \\ 0_n \end{bmatrix}, \begin{bmatrix} \mathcal{D} & 0 \\ 0 & W \end{bmatrix} \right)$$

where $n = \sum_{i=1}^m n_i$, $\mathcal{D} = I_m \otimes D$ and $W = \bigoplus_{i=1}^m W_i$ by \otimes indicating the Kronecker product. So, we derive $\tilde{y} \sim N(\tilde{X}\beta, V)$ where $V = \tilde{Z}\mathcal{D}\tilde{Z}^T + W$ in model (4).

There are the profile-kernel, backfitting, smoothing spline, penalized spline and local linear regression methodologies to estimate the nonparametric function in the PLMMs. Some of these methodologies were widespread for independent data, and some of them commonly used for correlated data. The asymptotic properties of profile-kernel estimators for the independent data were provided by [3], [4] and [5]. The bias problem of backfitting estimation was firstly discerned by [6]; see also [7] and [8]. Meanwhile, [8] demonstrated that the backfitting and kernel estimators share the same asymptotic behavior. [9] employed a semiparametric random intercept model (an extension of the PLMs) to examine the CD4 cell numbers in HIV seroconverters, where the nonparametric function is estimated by the backfitting method. [10] and [11] investigated PLMMs for longitudinal data and employed smoothing spline, while [12] and [13] employed the penalized spline to fit PLMMs. [14] characterized local linear regression in the framework of generalized PLMMs for longitudinal data.

[15]'s study is an extension of [9]'s model. [15] think a more general class of LMMs that the nonparametric component is estimated by the profile-kernel and backfitting methodologies. They work a natural extension of the linear mixed and semiparametric models called semiparametric mixed effect (or semiparametric linear mixed) model (SMEM) that uses parametric fixed effects to present the covariate effects and an arbitrary smooth function to model the time effect to account for the within subject correlation using random effects and its asymptotic behavior. To further highlighting the superiority of the methodology upon the backfitting, a comparison is also accomplished. They bring to an end that the kernel methodology rakes to have smaller bias and variance than the backfitting, asymptotically. Additionally, they demonstrate their theoretical results with the analysis of CD4 data in HIV disease and a small simulation study. They indicate that the SMEM is more stable and efficient than the linear mixed and semiparametric models. However, since [15] are obtained the profile-kernel and backfitting estimators under marginal model, they exclude the effect of the random effects in SMEM.

The principal goal of this article is to obtain Kernel predictors in the PLMMs by using [16]'s MMEs products. The plan of the article as follows. In Section 2, we recommend the Kernel prediction with the help of Henderson's MMEs and then, its asymptotic behavior is derived. In Section 3, a Monte Carlo simulation study is ensured to designate the theoretical outcomes. The article is finalized some summary and conclusions in Section 4.

2. Kernel Prediction in Partially Linear Mixed Models

In this section, we suggest the Kernel prediction in PLMMs via [16]'s MMEs different from [15]'s marginal model. Thus, we produce not only the estimation of the fixed effects and the nonparametric function but also the prediction of the random effects.

By following model (3) assumptions, u and \tilde{y} are jointly Gaussian distributed as

$$\begin{bmatrix} u \\ \tilde{y} \end{bmatrix} \sim N \left(\begin{bmatrix} 0 \\ \tilde{X}\beta \end{bmatrix}, \begin{bmatrix} \mathcal{D} & \mathcal{D}\tilde{Z}^T \\ \tilde{Z}\mathcal{D} & V \end{bmatrix} \right) \quad (5)$$

and then by using equation (5), the conditional distribution of \tilde{y} given u is $\tilde{y}|u \sim N(\tilde{X}\beta + \tilde{Z}u, W)$.

Following [16], we obtain the joint density of \tilde{y} and u given by

$$\begin{aligned} f(\tilde{y}, u) &= f(\tilde{y}|u)f(u) \\ &= (2\pi)^{-(n+qm)/2} |W|^{-1/2} |\mathcal{D}|^{-1/2} \exp \left\{ -\frac{1}{2} \left[(\tilde{y} - \tilde{X}\beta - \tilde{Z}u)^T W^{-1} (\tilde{y} - \tilde{X}\beta - \tilde{Z}u) \right. \right. \\ &\quad \left. \left. + u^T \mathcal{D}^{-1} u \right] \right\} \end{aligned} \quad (6)$$

where $|\cdot|$ designates a matrix determinate and the equations are similar to Henderson's MMEs.

Equation (6) is rewritten by taking the log-joint distribution of $f(\tilde{y}, u)$

$$\begin{aligned} \log f(\tilde{y}, u) &= \log f(\tilde{y}|u) + \log f(u) \\ &= -\frac{1}{2} \left\{ (n + qm) \log(2\pi) + \log |W| + \log |\mathcal{D}| \right. \\ &\quad \left. + \left[(\tilde{y} - \tilde{X}\beta - \tilde{Z}u)^T W^{-1} (\tilde{y} - \tilde{X}\beta - \tilde{Z}u) + u^T \mathcal{D}^{-1} u \right] \right\}. \end{aligned} \quad (7)$$

As the results of removing the fixed term, taking the log function into account and computing the partial derivatives of equation (7) in respond to the β and u to zero and using $\hat{\beta}_{Ke}$ and \hat{u}_{Kp} to demonstrate the Kernel estimator (Ke) and the Kernel predictor (Kp), the solutions are given as

$$\tilde{X}^T W^{-1} (\tilde{y} - \tilde{X} \hat{\beta}_{Ke}) - \tilde{X}^T W^{-1} \tilde{Z} \hat{u}_{Kp} = 0 \quad (8)$$

$$\tilde{Z}^T W^{-1} (\tilde{y} - \tilde{X} \hat{\beta}_{Ke}) - \tilde{Z}^T W^{-1} \tilde{Z} + \mathcal{D}^{-1} \hat{u}_{Kp} = 0. \quad (9)$$

Equations (8) and (9) are parallel to Henderson's MMEs obtained by [17] and [16], with a distinction that equations (8) and (9) are practiced to $\hat{\beta}_{Ke}$ and \hat{u}_{Kp} where Henderson's MMEs are practiced to the best linear unbiased estimator (BLUE) and the best linear unbiased predictor (BLUP).

Equations (8) and (9) can compactly be rewritten in matrix as

$$\begin{pmatrix} \tilde{X}^T W^{-1} \tilde{X} & \tilde{X}^T W^{-1} \tilde{Z} \\ \tilde{Z}^T W^{-1} \tilde{X} & \tilde{Z}^T W^{-1} \tilde{Z} + \mathcal{D}^{-1} \end{pmatrix} \begin{pmatrix} \hat{\beta}_{Ke} \\ \hat{u}_{Kp} \end{pmatrix} = \begin{pmatrix} \tilde{X}^T W^{-1} \tilde{y} \\ \tilde{Z}^T W^{-1} \tilde{y} \end{pmatrix}. \quad (10)$$

Using [18]'s approach, equation (10) can be written as

$$C\hat{\varphi} = \gamma^T W^{-1} \tilde{y} \quad (11)$$

where $\hat{\varphi} = (\hat{\beta}_{Ke}^T, \hat{u}_{Kp}^T)^T$, $\gamma = (\tilde{X}, \tilde{Z})$ and $C = \gamma^T W^{-1} \gamma + \mathfrak{D}^{**}$ with $\mathfrak{D}^* = \begin{bmatrix} I_p & 0 \\ 0 & \mathfrak{D} \end{bmatrix}$ and $G^{**} = \begin{bmatrix} I_p & 0 \\ 0 & \mathfrak{D}^{-1} \end{bmatrix}$ where the ‘+’ indicates the Moore–Penrose inverse.

By resolving equation (11), the following equation is found as

$$\hat{\varphi} = C^{-1} \gamma^T W^{-1} \tilde{y} \quad (12)$$

where C^{-1} is attained with the help of the inverse of the partitioned matrix (see [19]) as

$$C^{-1} = \begin{pmatrix} (\tilde{X}^T V^{-1} \tilde{X})^{-1} & -(\tilde{X}^T V^{-1} \tilde{X})^{-1} \tilde{X}^T V^{-1} \tilde{Z} \mathfrak{D} \\ -\mathfrak{D} \tilde{Z}^T V^{-1} \tilde{X} (\tilde{X}^T V^{-1} \tilde{X})^{-1} & (\tilde{Z}^T W^{-1} \tilde{Z} + \mathfrak{D}^{-1})^{-1} + \mathfrak{D} \tilde{Z}^T V^{-1} \tilde{X} (\tilde{X}^T V^{-1} \tilde{X})^{-1} \tilde{X}^T V^{-1} \tilde{Z} \mathfrak{D} \end{pmatrix}.$$

After algebraic simplifications and C^{-1} is replaced in equation (12), we suggest the Kernel estimator and the Kernel predictor, respectively, as

$$\hat{\beta}_{Ke} = (\tilde{X}^T V^{-1} \tilde{X})^{-1} \tilde{X}^T V^{-1} \tilde{y} \quad (13)$$

$$\hat{u}_{Kp} = \mathfrak{D} \tilde{Z}^T V^{-1} (\tilde{y} - \tilde{X} \hat{\beta}_{Ke}). \quad (14)$$

If β were known, the estimator of $g(t) = E(Y - X\beta | T = t)$ can be defined as

$$\hat{g}(t) = \sum_{i=1}^n \omega_{ij}(t) (y_i - X_i \hat{\beta}_{Ke}). \quad (15)$$

2.1. Asymptotic property of kernel estimator

In this subsection, we will examine the asymptotic property of Kernel estimator.

Theorem 2.1 Under the assumptions that the (y_i, X_i, T_i) are independent and identically distributed (i.i.d) triplets, $g^{(r)}(\cdot)$ is the r th derivative of any function $g(\cdot)$, v^{kl} is the (k, l) th element of V^{-1} , $f_k(t)$ is density of T_k , the Kernel density function $K(\cdot)$ is assumed to has mean 0, unit variance, $h \propto n^{-\alpha}$, $\frac{1}{5} \leq \alpha \leq \frac{1}{3}$ and $n \rightarrow \infty$ are held, $\hat{\beta}$ converges in distribution

$$\sqrt{n} \left\{ \hat{\beta} - \beta + \frac{h^2 b_1(\beta, g)}{2} \right\} \xrightarrow{D} N(0, V_k)$$

where the bias term $b_1(\beta, g) = A^{-1} E\{\tilde{X}^T V^{-1} g^{(2)}(t)\}$ and $V_k = A^{-1} E[(J_1 - J_2)^T V_0 (J_1 - J_2)] A^{-1}$ for $A = \lim_{n \rightarrow \infty} A_n = E(\tilde{X}^T V^{-1} \tilde{X})$, $V_0 = \text{Var}(y|x, t, z)$, $J_1 = V^{-1} \tilde{X}$, $J_2 = [J_{21}, \dots, J_{2n}]$, where $J_{2i} = [J_{2i1}, \dots, J_{2in}]^T$ is $J_{2ij} = \frac{|\sum_{k=1}^n \sum_{l=1}^n E(\tilde{X}_k V^{kl} | t_l = t_{ij}) f_j(t_{ij})|}{\sum_{l=1}^n f_l(t_{ij})}$ for $\mu_0 = E(y|x, t, z)$.

Proof. $\hat{\beta}_{Ke}$ is found as $\hat{\beta}_{Ke} = (\tilde{X}^T V^{-1} \tilde{X})^{-1} \tilde{X}^T V^{-1} \tilde{y}$ given by Eq. (13) where $\tilde{X} = X - \omega_x(T)$. Then,

$$\sqrt{n} \{\hat{\beta} - \beta\} = \sqrt{n} \left[\left(\sum_{i=1}^n \tilde{X}_i^T V_i^{-1} \tilde{X}_i \right)^{-1} \left(\sum_{i=1}^n \tilde{X}_i^T V_i^{-1} \tilde{y}_i \right) - \beta \right]$$

$$= \left[n^{-1} \tilde{X}_i^T V_i^{-1} \tilde{X}_i \right]^{-1} \left[\sqrt{n} n^{-1} \sum_{i=1}^n \tilde{X}_i^T V_i^{-1} (\tilde{y}_i - (\tilde{X}_i \beta + \tilde{g}(t_i) + \tilde{Z}_i u_i)) \right] = A_n^{-1} (\sqrt{n} \mathfrak{C}_n)$$

where $A = \lim_{n \rightarrow \infty} A_n = E(\tilde{X}^T V^{-1} \tilde{X})$,

$$\begin{aligned} \mathfrak{C}_n &= n^{-1} \sum_{i=1}^n \tilde{X}_i^T V_i^{-1} (y_i - (X_i \beta + \hat{g}(t_i) + g(t_i) - g(t_i) + Z_i u_i)) \\ &= n^{-1} \sum_{i=1}^n \tilde{X}_i^T V_i^{-1} (y_i - (X_i \beta + g(t_i) + Z_i u_i) - (\hat{g}(t_i) - g(t_i))) \\ &= n^{-1} \sum_{i=1}^n \tilde{X}_i^T V_i^{-1} (y_i - \mu_i) - n^{-1} \sum_{i=1}^n \tilde{X}_i^T V_i^{-1} (\hat{g}(t_i, \beta) - g(t_i)) + O_p(1) = \mathfrak{C}_{1n} - \mathfrak{C}_{2n} + O_p(1) \end{aligned}$$

where $\mu_i = X_i \beta + g(t_i) + Z_i u_i$ and $\mathfrak{C}_{1n} = n^{-1} \sum_{i=1}^n \tilde{X}_i^T V_i^{-1} (y_i - \mu_i) = n^{-1} \sum_{i=1}^n J_{1i}^T (y_i - \mu_i)$ for $J_{1i} = V_i^{-1} \tilde{X}_i$ and $\mathfrak{C}_{2n} = n^{-1} \sum_{i=1}^n \tilde{X}_i^T V_i^{-1} (\hat{g}(t_i, \beta) - g(t_i))$.

Since the derivation of the asymptotic distribution of $\sqrt{n} \mathfrak{C}_{1n}$ is easy, we now think the asymptotic distribution of $\sqrt{n} \mathfrak{C}_{2n}$. By following [4], \mathfrak{C}_{2n} is found as $\mathfrak{C}_{2n} = n^{-1} \sum_{i=1}^n J_{21i}^T (y_i - \mu_i) + \frac{h^2}{2} E \left(\tilde{X}_i^T V_i^{-1} g^{(2)}(t) \right) + O_p(1)$ where $J_{2i} = [J_{2i1}, \dots, J_{2in}]^T$ for $J_{2ij} = \frac{|\sum_{k=1}^n \sum_{l=1}^n E(\tilde{X}_k^T V_k^{-1} |t_l = t_{ij}) f_j(t_{ij})|}{\sum_{l=1}^n f_l(t_{ij})}$ and v^{kl} is the (k, l) th element of V^{-1} , $f_k(t)$ is density of T_k . Then,

$$\sqrt{n} \{\hat{\beta} - \beta\} = A^{-1} n^{-1/2} \left\{ \sum_{i=1}^n (J_{1i} - J_{2i}) (y_i - \mu_i) + \frac{(nh^4)^{1/2}}{2} b_1(\beta, g) \right\} + O_p(1)$$

where the bias term $b_1(\beta, g) = A^{-1} E\{\tilde{X}^T V^{-1} g^{(2)}(t)\}$. Equivalently, $\sqrt{n} \{\hat{\beta} - \beta + \frac{h^2 b_1(\beta, g)}{2}\} \xrightarrow{D} N(0, V_k)$ where $V_k = A^{-1} E[(J_1 - J_2)^T V_0 (J_1 - J_2)] A^{-1}$ for $V_0 = \text{Var}(y|x, t, z)$ and $\mu_0 = E(y|x, t, z)$. Thus, the proof of the Theorem 2.1 is completed.

3. A Monte Carlo Simulation Study

In this article, we will investigate a Monte Carlo simulation study to confront the performance of $\hat{\beta}_{Ke}$ and \hat{u}_{Kp} in respect of the estimated mean square error (EMSE) and the predicted mean square error (PMSE), respectively. Then mean square error (MSE) of successful models which have minimum EMSE and PMSE values are calculated to demonstrate the best model.

We get $m = 10, 30, 60$ subjects and $n_i = 10$ observations for every subject. By following [20], we choose $\beta = (\beta_1, \dots, \beta_p)^T$ as the normalized eigenvector corresponding to the largest eigenvalue of $\tilde{X}^T V^{-1} \tilde{X}$ so that $\beta^T \beta = 1$. The x_{ij} covariates are generated from the standard normal distribution and t_{ij} is generated from uniform distribution ($U(0,1)$). Then, the model is written for $p = 2$ fixed effects and $q = 2$ random effects as

$$y_{ij} = \beta_1 x_{ij1} + \beta_2 x_{ij2} + g(t_{ij}) + u_1 + u_2 \text{time}_{ij} + \varepsilon_i, \quad u_i \stackrel{iid}{\sim} N_q(0, \sigma^2 D), \quad \varepsilon_i \stackrel{iid}{\sim} N_{n_i}(0, \sigma^2 I_{n_i}), \quad i = 1, \dots, m$$

where $D = \begin{bmatrix} 1 & \rho \\ \rho & 1 \end{bmatrix}$ is the AR(1) process with $\rho = 0.30, 0.60, 0.90$ and time_{ij} indicates the time which was given as the same set of occasions, $\{\text{time}_{ij} = j \text{ for } i = 1, \dots, m, j = 1, \dots, n_i\}$. To simulate our results we thought both supersmooth and ordinary smooth functions. Hence we create 2 different functions g_1 and g_2 respectively given

as $S(t) = \begin{cases} -1, & t < -1 \\ t, & t \in [-1, 1] \\ 1, & t > 1 \end{cases}$ and $\text{erf}(t) = \frac{2}{\pi} \int_0^t e^{-s^2} ds$ while error function shows supersmooth function, $S(t)$ function shows ordinary smooth function. For kernel smoothing we use quartic kernel function $K(t) = \frac{15}{16}(1-t^2)^2 I(|t| \leq 1)$ and $h_n^{-1} = 1.2(\ln n)^{0.25}$.

Table 1. The estimated $\hat{\beta}, \hat{u}$ and the real β, u values

Function	Parameters	n = 100			n = 300			n = 600		
		$\rho = 0.30$	$\rho = 0.60$	$\rho = 0.90$	$\rho = 0.30$	$\rho = 0.60$	$\rho = 0.90$	$\rho = 0.30$	$\rho = 0.60$	$\rho = 0.90$
Partially Linear Mixed Model										
$g_1(t)$	β_1	-0.1383	-0.1997	-0.1779	0.5754	0.5554	0.5067	0.8250	0.8497	0.7731
		-0.2254*	-0.2258*	-0.2283*	0.6291*	0.6229*	0.6036*	0.7822*	0.7954*	0.7671*
	β_2	-1.0411	-1.0610	-1.0884	-0.8416	-0.7985	-0.7444	-0.6570	-0.6296	-0.6635
		-0.9743*	-0.9742*	-0.9736*	-0.7774*	-0.7823*	-0.7973*	-0.6231*	-0.6060*	-0.6415*
$g_2(t)$	β_1	-56.4091	-87.8467	-54.2041	-0.0772	-0.1754	-0.0542	-0.1229	-0.1970	-0.3093
		0.7973*	0.7973*	0.7973*	0.9931*	0.9931*	0.9931*	-2.3814*	-2.3814*	-2.3814*
	β_2	-58.8106	-88.1406	-52.1021	0.00496	0.1420	0.2580	-0.3973	-0.6017	-0.7800
		-0.3654*	-0.0287*	0.4413*	0.2255*	0.5351*	0.8607*	-1.1995*	-1.8357*	-2.3649*
$g_1(t)$	β_1	-0.1444	-0.1693	-0.1764	0.5657	0.5373	0.5031	0.7778	0.7937	0.7724
		-0.2254*	-0.2258*	-0.2283*	0.6195*	0.5968*	0.6289*	0.7715*	0.7806*	0.7735*
	β_2	-1.0363	-1.0880	-1.0700	-0.8335	-0.7994	-0.7533	-0.6752	-0.6439	-0.6585
		-0.9743*	-0.9742*	-0.9736*	-0.7850*	-0.8024*	-0.7775*	-0.6362*	-0.6251*	-0.6338*
$g_2(t)$	u_1	-63.0259	-79.1291	-15.3698	-0.0345	0.0026	-0.1398	-0.1075	0.0158	-0.1465
		0.7973*	0.7973*	0.7973*	0.9931*	0.9931*	0.9931*	-2.3814*	-2.3814*	-2.3814*
	u_2	-65.3904	-79.4588	-13.3486	0.0556	0.1601	0.2464	-0.4011	-0.5902	-0.7792
		-0.3654*	-0.0287*	0.4413*	0.2255*	0.5351*	0.8607*	-1.1995*	-1.8357*	-2.3649*
Partially Linear Model										
$g_1(t)$	β_1	-0.2087	-0.2341	-0.1724	0.5766	0.5346	0.5063	0.8058	0.7752	0.7208
		-0.2254*	-0.2258*	-0.2283*	0.6114*	0.6298*	0.6060*	0.7784*	0.7566*	0.7456*
	β_2	-1.0755	-1.0553	-1.0845	-0.8228	-0.8107	-0.7385	-0.6601	-0.7056	-0.7395
		-0.9743*	-0.9742*	-0.9736*	-0.7913*	-0.7767*	-0.7954*	-0.6278*	-0.6539*	-0.6664*
$g_2(t)$	u_1	-90.2572	-95.4439	-77.2981	-0.1160	-0.0520	-0.1182	-0.0695	-0.1697	-0.2989
		0.7973*	0.7973*	0.7973*	0.9931*	0.9931*	0.9931*	-2.3814*	-2.3814*	-2.3814*
	u_2	-92.6514	-95.7318	-75.1554	0.0450	0.1496	0.2557	-0.3843	-0.6070	-0.8016
		-0.3654*	-0.0287*	0.4413*	0.2255*	0.5351*	0.8607*	-1.1995*	-1.8357*	-2.3649*
$g_1(t)$	β_1	-0.1541	-0.1692	-0.2404	0.5682	0.5542	0.5147	0.7918	0.8142	0.6971
		-0.2254*	-0.2258*	-0.2283*	0.6071*	0.6203*	0.6363*	0.7658*	0.7953*	0.7353*
	β_2	-1.0571	-1.0746	-1.0626	-0.8326	-0.8039	-0.7587	-0.6698	-0.6155	-0.7268
		-0.9743*	-0.9742*	-0.9736*	-0.7947*	-0.7843*	-0.7714*	-0.6431*	-0.6062*	-0.6777*
$g_2(t)$	u_1	-38.7551	-62.1012	-52.8449	-0.0588	-0.1286	-0.1139	-0.0553	-0.0715	-0.1227
		0.7973*	0.7973*	0.7973*	0.9931*	0.9931*	0.9931*	-2.3814*	-2.3814*	-2.3814*
	u_2	-41.0706	-62.3697	-50.7557	0.0548	0.1475	0.2480	-0.3856	-0.5977	-0.7806
		-0.3654*	-0.0287*	0.4413*	0.2255*	0.5351*	0.8607*	-1.1995*	-1.8357*	-2.3649*
Linear Mixed Model										
$g_1(t)$	β_1	-0.1946	-0.1908	-0.2080	0.5691	0.5240	0.5144	0.7811	0.7967	0.7921
		-0.2254*	-0.2258*	-0.2283*	0.6167*	0.6100*	0.6275*	0.7675*	0.7764*	0.7786*
	β_2	-1.1265	-1.0509	-1.0505	-0.8322	-0.7817	-0.7523	-0.6636	-0.6746	-0.6294
		-0.9743*	-0.9742*	-0.9736*	-0.7872*	-0.7924*	-0.7581*	-0.6410*	-0.6303*	-0.6276*
$g_2(t)$	u_1	-71.1029	-78.1316	-33.6736	-0.1175	-0.1044	-0.1270	-0.0545	-0.1857	0.0943
		0.7973*	0.7973*	0.7973*	0.9931*	0.9931*	0.9931*	-2.3814*	-2.3814*	-2.3814*
	u_2	-73.5222	-78.4585	-31.6024	0.0490	0.1550	0.2521	-0.3860	-0.6089	-0.7374
		-0.3654*	-0.0287*	0.4413*	0.2255*	0.5351*	0.8607*	-1.1995*	-1.8357*	-2.3649*
$g_1(t)$	β_1	-0.1385	-0.1923	-0.2115	0.5774	0.5551	0.5047	0.7847	0.7872	0.7638
		-0.2254*	-0.2258*	-0.2283*	0.6302*	0.6138*	0.6357*	0.7520*	0.7719*	0.7609*
	β_2	-1.0250	-1.0495	-1.0657	-0.8485	-0.8072	-0.7500	-0.7276	-0.6632	-0.7011
		-0.9743*	-0.9742*	-0.9736*	-0.7765*	-0.7995*	-0.7719*	-0.6592*	-0.6357*	-0.6489*
$g_2(t)$	u_1	-27.8043	-52.6802	-9.3439	-0.1053	-0.0816	-0.0999	-0.1330	-0.1856	-0.2027
		0.7973*	0.7973*	0.7973*	0.9931*	0.9931*	0.9931*	-2.3814*	-2.3814*	-2.3814*
	u_2	-30.1215	-52.9815	-7.2430	0.0509	0.1576	0.2511	-0.3952	-0.6185	-0.7855
		-0.3654*	-0.0287*	0.4413*	0.2255*	0.5351*	0.8607*	-1.1995*	-1.8357*	-2.3649*

* demonstrates the real values.

The experiment is replicated 500 times by producing response variable. We compare our model with the partially linear models and the linear mixed models under the AR(1) process. The estimated $\hat{\beta}, \hat{u}$ and the real β, u values are compared in Table 1.

The EMSE for any estimator $\hat{\beta}$ of β and the PMSE for any predictor \hat{u} of u are computed for each m, n_i, ρ , and 500 replicated experiments, respectively, as

$$EMSE(\hat{\beta}) = \frac{1}{500} \sum_{r=1}^{500} (\hat{\beta}_{(r)} - \beta)^T (\hat{\beta}_{(r)} - \beta) \text{ and } PMSE(\hat{u}) = \frac{1}{500} \sum_{r=1}^{500} (\hat{u}_{(r)} - u)^T (\hat{u}_{(r)} - u)$$

where the subscript (r) demonstrates to the r th replication and the performances are given in Table 2.

Table 2. The EMSE and PMSE values

Function		$n = 300$			$n = 600$		
		$\rho = 0.30$	$\rho = 0.60$	$\rho = 0.90$	$\rho = 0.30$	$\rho = 0.60$	$\rho = 0.90$
Partially Linear Mixed Model							
$g_1(t)$	EMSE	0.0081	0.0132	0.0298	0.0037	0.0045	0.0059
	PMSE	1.1813	1.4730	1.3950	5.8783	6.5728	7.0004
$g_2(t)$	EMSE	0.0093	0.0173	0.0293	0.0050	0.0054	0.0060
	PMSE	1.1511	1.2358	1.7122	5.9866	7.3714	7.6027
Partially Linear Model							
$g_1(t)$	EMSE	0.0096	0.0141	0.0319	0.0039	0.0041	0.0093
	PMSE	1.2036	1.2510	1.5556	6.0365	6.6212	7.0593
$g_2(t)$	EMSE	0.0097	0.0127	0.0259	0.0043	0.0055	0.0105
	PMSE	1.1737	1.3550	1.6076	6.2039	6.8727	7.8799
Linear Mixed Model							
$g_1(t)$	EMSE	0.0092	0.0198	0.0252	0.0052	0.0041	0.0066
	PMSE	1.2895	1.3530	1.4792	6.2763	6.4763	8.9287
$g_2(t)$	EMSE	0.0078	0.0132	0.0289	0.0039	0.0049	0.0054
	PMSE	1.2951	1.3307	1.5378	5.8891	6.4500	7.4195

Then to compare successful models we compute MSE values which are given in Table 3 using the following equation

$$MSE = \frac{1}{500} \sum_{r=1}^{500} (\hat{y}_{(r)} - y)^T (\hat{y}_{(r)} - y).$$

Table 3. MSE values of models

Function	$n = 300$			$n = 600$		
	$\rho = 0.30$	$\rho = 0.60$	$\rho = 0.90$	$\rho = 0.30$	$\rho = 0.60$	$\rho = 0.90$
Partially Linear Mixed Model						
$g_1(t)$	0.8180	2.2366	6.6358	33.5532	76.8170	132.1835
$g_2(t)$	0.8920	3.0549	6.0778	33.1504	66.2158	120.4612
Linear Mixed Model						
$g_1(t)$	4.7880	9.5019	17.1337	55.4555	102.0681	170.6203
$g_2(t)$	4.5935	9.2114	16.8390	53.7372	101.2066	155.6432

Table 2 and 3 are generated under $n = 300, 600$ and $\rho = 0.30, 0.60, 0.90$ conditions. Since the estimated \hat{u} values are influenced from small samples sizes ($n = 100$), the difference is arisen between the estimated and the real values of u . And then, we have derived the EMSE, PMSE and MSE values for $n = 300, 600$.

We also investigate comparison between the finite sample and the asymptotic distributions of our estimator. In Figure 1 the ordinate is probability and the abscissa is $Z = (Var(\hat{g}(1, h)))^{-1/2} (\hat{g}(1, h) - E(\hat{g}(1, h)))$. The empirical c.d.f. of the estimator shown as a dashed line agrees very well with the normal c.d.f. shown as a solid line.

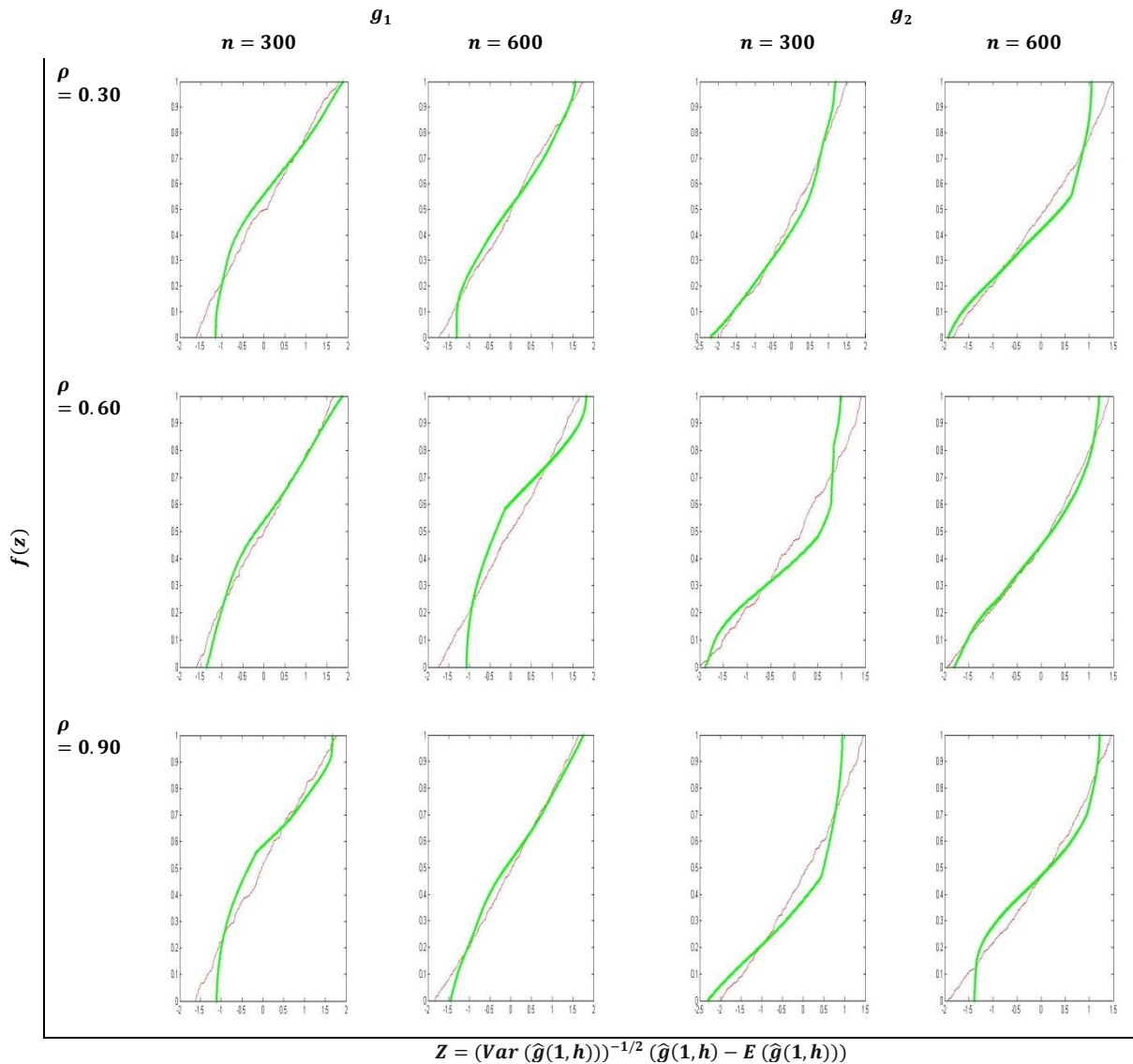


Figure 1. Comparison of the finite sample and asymptotic distributions of the estimators of functions.

4. Conclusion

This article presents a new approach which is called as Henderson's method approach to obtain the kernel estimator and predictor at the same time in PLMM. After the kernel estimator and the kernel predictor are suggested, asymptotic normality of the proposed estimator is also derived. Then, a Monte Carlo simulation study is done to support the theoretical results in the article.

The simulation study shows that the PLMMs have generally the best and the LMMs have the second best performances in resulting of having smaller EMSE and PMSE values. To compare the performances of the PLMMs and LMMs, we find their MSE values of the response variables. It is easily seen that PLMM has better MSE values which means that results show the superiority of the PLMMs when we think both estimators $\hat{\beta}$ and \hat{u} at the same time. We also investigate comparison between the finite sample and the asymptotic distributions of estimator \hat{g} of PLMM. This demonstrated that empirical c.d.f. of the estimator agrees very well with the normal c.d.f.


Acknowledgment

The authors would like to thank the editor and anonymous referees for their constructive comments.

References

- [1] Laird, N. M. and Ware, J. H., Random-effects models for longitudinal data, *Biometrics*, 38 (1982) 963-974.
- [2] Engle, R. F., Granger, C. W. J., Rice, J. and Weiss, A., Semiparametric estimates of the relation between weather and electricity sales, *J. Am. Stat. Assoc.*, 81 (1986) 310-320.
- [3] Severini, T. A. and Staniswalis, J. G., Quasi-likelihood estimation in semi-parametric models, *J. Am. Stat. Assoc.*, 89 (1994) 510-512.
- [4] Lin, X. and Carroll, R. J., Semiparametric regression for clustered data using generalised estimating equations, *J. Am. Stat. Assoc.*, 96 (2001) 1045–1056.
- [5] Wang, N., Marginal nonparametric kernel regression accounting for within-subject correlation, *Biometrika*, 90 (2003) 43–52.
- [6] Rice, J. A., Convergence rates for partially splined models, *Stat. Probabil. Lett.*, 4 (1986) 204–208.
- [7] Speckman, P. E., Regression analysis for partially linear models, *J. R. Stat. Soc. B.*, 50 (1988) 413–436.
- [8] Opsomer, J. D. and Ruppert, D., A root-n consistent backfitting estimator for semiparametric additive modeling, *J. Comput. Graph. Stat.*, 8 (1999) 715–732.
- [9] Zeger, S. L. and Diggle, P. J., Semi-parametric models for longitudinal data with application to CD4 cell numbers in HIV seroconverters, *Biometrics*, 50 (1994) 689–699.
- [10] Qin, G. Y. and Zhu, Z. Y., Robust estimation in generalized semiparametric mixed models for longitudinal data, *J. Multivar. Anal.*, 98 (2007) 1658–1683.
- [11] Qin, G. Y. and Zhu, Z. Y., Robustified maximum likelihood estimation in generalized partial linear mixed model for longitudinal data, *Biometrics*, 65 (2009) 52–59.
- [12] Li, Z. and Zhu, L., On variance components in semiparametric mixed models for longitudinal data, *Scand. J. Stat.*, 37 (2010) 442–457.
- [13] Zhang, D., Generalized linear mixedmodels with varying coefficients for longitudinal data, *Biometrics*, 60 (2004) 8–15.
- [14] Liang, H., Generalized partially linear mixed-effects models incorporating mismeasured covariates, *Ann. I. Stat. Math.*, 61 (2009) 27–46.
- [15] Taavoni, M. and Arashi, M., Kernel estimation in semiparametric mixed effect longitudinal modeling, *Stat. Papers*, (2019) <https://doi.org/10.1007/s00362-019-01125-8>.
- [16] Henderson, C. R., Estimation of genetic parameters. *Ann. I. Stat. Math.*, 21 (1950) 309–310 .
- [17] Henderson, C. R., Kempthorne, O., Searle, S. R., and Von Krosig, C. N., Estimation of environmental and genetic trends from records subject to culling, *Biometrics*, 15 (1959) 192–218.
- [18] Gilmour, A. R., Thompson, R., and Cullis, B. R., Average information REML: an efficient algorithm for variance parameter estimation in linear mixed models, *Biometrics*, 51 (1995) 1440–1450.
- [19] Searle, S. R., Matrix Algebra Useful for Statistics, New York: John Wiley and Sons, 1982.
- [20] Newhouse, J. P. and S. D. Oman., An evaluation of ridge estimators, *Rand Corporation R-716-PR*, (1971) 1–28.

Microbiological pollution and some physicochemical properties of sıkaraağaçlar creek in sinop (Black Sea-Turkey)

Ayşe GÜNDOĞDU^{1*} , Uğur ÇARLI² 

¹ Fisheries Faculty, Sinop University, Sinop, Turkey

² Scientific and Technological Researchs Application and Research Center, Sinop University, Sinop, Turkey

Abstract

Sırakaraağaçlar creek located in Akliman of Sinop city. It is born within the province of Sinop and discharges from the Akliman coastline to the Black Sea. The work continued from May 2014 to April 2015. Four stations were stated in the study. To determine the quality of water, some physicochemical features and microbiological analysis of creek water was determined. These are temperature, dissolved oxygen, pH, conductivity, biological oxygen demand, ammonium nitrogen, hydrogen sulfide, organic matter, total suspended solids parameters, and Total coliform and Fecal coliform values. When the T. coliform and F. coliform values of Sırakaraağaçlar Creek were examined seasonally, the minimum values were found as 35.88 ± 1.48 cfu/100ml and 27.33 ± 1.25 cfu/100ml at S1 station in Winter, and the maximum values were 1263.55 ± 184.57 cfu/100ml and 1020.22 ± 105.29 cfu/100ml at S4 station in Summer, respectively. The results obtained from the creek water were classified according to the regulations of Turkey's Surface Water Quality Management. It was evaluated whether the perimeter of the creek had any effect on the water source.

Article info

History:

Received:08.01.2020

Accepted:30.06.2020

Keywords:

Coliform,
River,
Physicochemical,
Sinop,
Black Sea.

1. Introduction

The quality of surface waters both flowing and stagnant is very important to the natural environment and humans, and for this reason, it should be assessed specific physical, biological, chemical and microbiological characteristics [1, 2]. Water is a specific and natural resource that is essential for all living organisms. It is both exhaustible and renewable resources, as when consumed or polluted in a given place and time, its quantity and quality can be restored under appropriate conditions [3]. Today, all water resources around the world are at risk of pollution and extinction. This situation can be attributed to tourism activities, domestic and industrial waste. Besides, it is possible to show climate changes and drought brought about by global warming. As a result of these negative factors, water resources are rapidly decreasing [4, 5]. For this reason, the protection of the proper water status and provision of sustainability is becoming increasingly important.

Water quality is deceived by both microbiological and physicochemical properties. Moreover, chemical and biochemical reactions such as decomposition, hydrolysis, dissolution, adsorption, sedimentation and

ion exchange, reduction, oxidation processes that are important control factors for surface and groundwater structure [6]. Evaluation of physicochemical parameters such as PH, conductivity, total suspended solids, alkalinity, hydrogen sulfide, organic matter, ammonium and nitrate are generally considered to be guiding principles and classify physicochemical water quality. In microbiological analysis, definition of indicator bacteria like Total coliform (T. coliform), Fecal coliforms (F. coliform), *Enterococcus*, *Fecal streptococci*, and *Escherichia coli* are generally performed to

evaluate the possibility of fecal contamination and to qualify the source for usable [7-9]. The total number of coliform bacteria is used as the most reliable indicator of water quality. Coliform bacteria may be found in human and animal intestines as well as in the environment. They may be indicative of potential fecal contamination. F. coliform and *E. coli* are found only in human and animal gut, and tests for their presence in the water are necessary to confirm fecal contamination of humans or other warm-blooded animals. [10, 11]. This kind of contamination means that any normal flora and pathogenic microorganisms that take place in the intestinal tract of these animals may also be formed [12]. The members of the genus *Escherichia* comprise more than 60% of the T.

coliforms and more than 90% of the F. coliforms. One of the most important coliform bacteria is *E. coli*. Several types of this species are opportunistic pathogens and may be the cause of the disease [13]. The indicator-microorganisms are coliform bacteria which are disunited into F. coliform and non-F. coliform. *E. coli* that is found in the normal flora in the human and other warm-blooded animals intestinal tract, it is feces type of Enterobacteria. The non-fecal type contains *Enterobacter aerogens* that are widely dispersed in nature and are sometimes found in the intestinal tract of warm-blooded organisms [12]. These bacteria are a part of the natural river mouth microflora and can be accumulated by shellfish during feeding [14, 15].

The microorganisms present in the water ecosystem are either mixed into the water from various ways or are formed according to the environmental conditions. Microorganisms can come to natural waters from the atmosphere and soil, and they can also be of industrial and domestic waste origin [16-18].

Microorganisms in water are grouped into three groups. Microorganisms naturally found in water: *Spirillum*, *Vibrio*, *Pseudomonas*, *Achromobacter*, *Chromobacter* species and some species of *Micrococcus* and *Sarcina*. Soil-based microorganisms: They are mixed with water as the water passes through the soil layers or as a result of washing the soil with. They are *Bacillus*, *Streptomyces* and saprophyte members of Enterobacteriaceae. Microorganisms of human and animal origin: Principles; *E. coli*, *Streptococcus faecalis*, *Clostridium perfringens* and other intestinal pathogens. Such microorganisms may cause harmful, dangerous, and disease-causing as well as cause changes in the biochemical structure of water resources [19-21]. High concentrations of sewage bacteria are a potential threat to human health in the event of sewage permeation into the environment. As intestinal bacteria, a special pathogenic property is exhibited by gram-negative Salmonella, including those that cause typhoid. [22, 23]. These microorganisms can cause many problems which are fever, nausea, vomiting, diarrhea, and they may also be the cause of death [24, 25].

Our study aims to assess the amount of T. coliform and F. coliform bacteria in the surface waters of Sırakaraağaçlar Creek. Further, an attempt to look for the correlation between the selected physicochemical variables of water quality and the quantitative occurrence of tested bacterial groups in these waters was determined. Surface water quality is of great importance for the economy due to microbiological indicators because legal standards are governing their monitoring and protection. Furthermore, to ensure the

sustainability of natural waters, it is necessary to continuously identify and monitor its properties.

2. Material and Methods

The study was conducted seasonally from May 2014 to April 2015. Four different stations were identified to represent Sırakaraağaçlar Creek. Water samples were collected in sterile brown bottles from each of the stations identified along the river and transported to the laboratory for analysis. Field surveys were conducted at the surface water of sampling stations in monthly periods, and some physical and chemical parameter measurements were performed.

2.1. Characteristics of the evaluation area

Karagöl-Aksaz Swamp is a swamp system formed when the front of an old gulf is closed with coastal dunes, and lagoon lakes that have been formed have turned into a terrestrial structure over time. The area of the area is approximately 300 ha. Karasu Stream feeds Karagöl Swamp, which started after Sinop Airport. The Aksaz Reeds, which is located in the northeast of Karagöl Swamp, feeds the Sırakaraağaçlar Creek, where smaller streams are also included. The swamp and reed unit distinguishes it from the sea with a coastal language of about 4100 m in length and up to 130 m in places [26]. The terrestrial area side of the dunes that make up the coastal language is covered with a rich dune vegetation (vegetation is the formation of reed, straw and similar plant groups or algae in the water growing in swamps). In the swamp and reed area, the wetland vegetation is enriched with the rise of the ground water level in the winter months [27, 28]. The average depth of the stream is 1.5 m, and the maximum depth is 2.5 m. While the bottom of stream has a muddy structure, its part opening to the sea has a sandy structure [29].

Four stations with different characteristics were determined in the Sırakaraağaçlar stream. S1 station: It is located in the Akliman area of Sinop where the creek meets the sea. In this region where the creek is poured into the sea, it is known that seawater occasionally enters from the creek mouth. The station is at the point where freshwater and saltwater mix, the sediment is covered with fine sand. It was chosen to reveal the effects of the sea on the stream and other environmental effects. S2 station: This station is located to the north-east of Aksaz swamp, the stream water is turbid, muddy and the surrounding area is covered with reeds. It is located within the settlements, also in the region where there are official institutions and various businesses and where maritime tourism

takes place. However, the settlement area is within the provincial borders of Sinop (central) and there is a sewage system. For this reason, domestic waste cannot be left to the S1 and S2 stations. S3 station: It is an area dominated by reeds and swamps. The water of the stream is turbid and muddy. S4 station: Although there is no settlement around the station, it is known that the village of Abalı is located 50-60 m away and the village does not have a sewage system. Domestic waste is mixed into the stream of Sıkaraağaçlar from this region. Moreover, it is known that there are agricultural lands around the village of Abalı, and animal husbandry is carried out (Figure 1).

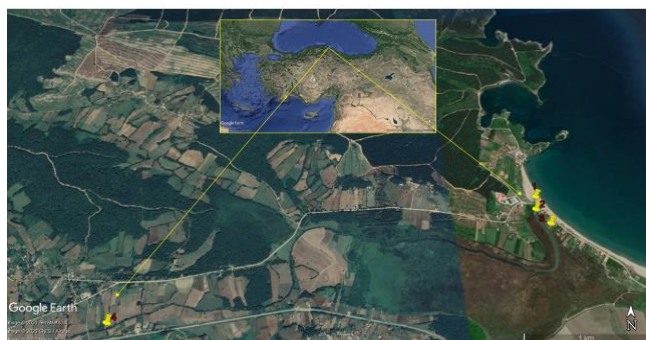


Figure 1. Sampling stations of Sirakaraağaçlar Creek (S1: 42°02'28.76"N-35°02'39.79"E, S2: 42°02'24.42"N-35°02'38.90"E, S3: 42°02'19.62"N-35°02'43.52"E and S4: 42°01'49.59"N-34°59'58.44"E).

2.2. Physicochemical Parameters

In the study, with the aim of determine the quality of water, temperature (°C), dissolved oxygen (DO, mg/L), pH, conductivity (µs/cm), biological oxygen demand (BOD₅, mg/L), ammonium nitrogen (NH₄⁺-N, mg/L), hydrogen sulfide (H₂S, mg/L), organic matter (OM, mg/L), total suspended solids (TSS, mg/L) parameters were selected. Temperature, DO, pH and conductivity measurements were performed with YSI Multiparameter (Professional Plus model) device in sampling areas. While taking the water samples, the sample containers were filled with a dip of 30-40 cm upside down relative to the water surface and held at 45° slopes. The other physicochemical analyses were held in laboratory conditions. Measurement and analysis of BOD₅, NH₄⁺-N, H₂S, OM and TSS were made by applying Standard Methods which are valid for waters. Parametric measurement results were obtained by using the Titrimetric method for BOD₅ and H₂S, Spectrophotometric method(RAYLEIGH UV-726) for NH₄⁺-N, Gravimetric method for OM and TAKM [30-33].

2.3. Microbiological Analysis

For microbial analysis of the creek, water samples were collected separately in sterile containers from stations. The sample cups were immersed upside down to a depth of 20-30 cm concerning the water surface, and filled with a 45° inclination. Microbiological analysis samples were transported to the laboratory under ice-cooled conditions. Total (T.) coliform and fecal (F.) coliform values (cfu/100 ml) were determined for microbial evaluation. To this end, samples reduced to a dilution of 10³ in 100 ml sterile sample cups were analyzed by membrane filtration method in triplicate. Water samples were filtered through strainers with pore diameter 0.45 µm utilizing a vacuum pump. Filter papers were placed on the prepared culture media and incubated at appropriate temperatures. In the study, ENDO agar for T. coliforms and m-FC agar nutrient pad systems for F. coliforms were used. The media containing the filters were evaluated after a 24 hour waiting period at 37± 0.1 °C for T. coliforms and 44.5±0.1 °C for F. coliforms. Dark red, metallic green colonies developed on ENDO agar were evaluated as T. coliform, and blue colonies grown on m-FC agar were F. coliform. T. coliform and F. coliform bacteria were detected at all stations, and the results were recorded as cfu/100 ml [34].

2.4. Statistical Analysis

Statistical analyses of water quality parameters are calculated with SPSS 22 and Minitab 18 program. Two-way ANOVA test was used to determine whether all parameters differ between stations and seasons. Tukey test was also used to determine the differences in the tests. Physicochemical parameters were found to be statistically significant according to P<0.05. Besides, correlation matrices were established to evaluate the relationships between the obtained results. Correlation coefficients between physicochemical parameters and coliform bacteria were evaluated.

3. Results and Discussion

Coliform bacteria and some physicochemical parameters (Figure 2, 3). of the Sirakaraağaçlar stream have been shown in Table 1-4. Microbiological evaluation of the creek was determined by investigating the presence of T. coliform and F. coliform bacteria. The minimum and maximum of the T. coliform values were found to be 30 - 245, 106-535, 87-439 and 128-1904 cfu/100 ml at S1, S2, S3 and S4 stations, respectively. Minimum and maximum of F. coliform levels were determined as 22-200, 90-452,

87-304 and 72-1394 cfu/100 ml in S1, S2, S3 and S4 stations, respectively. In this study, a statistically significant difference ($P < 0.05$) was found between the seasonal mean values, and also between the mean values of the stations (DO, BOD₅, NH₄⁺-N, OM, T. coliform and F. coliform). While values of temperature, pH and H₂S were significantly different from season to season, the conductivity was different from station to station ($P < 0.05$). Besides, the suspended solids did not show differences ($P > 0.05$) both in terms of stations and seasonally (Table 1-4). Correlation coefficients between physicochemical parameters and coliform bacteria are shown according to $P < 0.05$, $P \leq 0.01$ and $P \leq 0.001$ in Table 5.

The lowest and the highest temperature in Sırakaraağaçlar Creek was 12.45 °C and 26.98 °C at S3 station, respectively. It is known that the temperature value of the water source varies depending on climate, height, flow rate and bed structure of water source, atmospheric conditions [35]. Temperature, which is one of the main parameters in water quality studies, although it does not seem to make sense by itself, creates meaningful integrity with other parameters such as dissolved oxygen, biological oxygen need, pH, etc. [36]. Tepe and Mutlu [37] reported that the average temperature was 15.70 °C in Hatay Harbiye spring water. In another study, Bulut, Akçimen, Uysal, Küçükara, Savaşer, Tokatlı, Öztürk and Köse [38] showed that the optimum values were between 11.31 and 12.05 °C for temperature in the stations of Kestel Creek, and Yıldız [39] determined that the temperature was 13.19 °C in a conducted study on the Gelevera Creek of Giresun province. Our results were found to be parallel with the results of these studies conducted at different times in different regions.

When the seasonal variations of DO values of Sırakaraağaçlar Creek were examined, the lowest value was measured at S4 station with 1.56 mg/L in Summer (Figure 2). Since the S4 station is under the influence of the Abalı village sewage and agricultural areas located nearby, the oxygen level is quite low in the summer period. There are areas classified as marshes around the stream. In the region, animal husbandry is carried out, and animals have grazing areas. In our working period, we did not have access to any death information about fish or other species. But, Karslı [40] reported that fish (*A. Chantrei*) could not be obtained from the sampling area during the months of November-April due to the negative effects on the environment and water conditions in the study conducted in the Sırakaraağaçlar stream between June 2005 and May 2006. They emphasized that irregular

changes in the characteristics of the water in this region depending on the seasons negatively affect the fish population and the breeding amount. The highest value was detected at S1 station with 5.23 mg/L in Winter. It was determined that the DO values, seasonal air and water temperatures were affected by the change, and the highest concentration of DO in the water was in winter. This confirms that the solubility of gases is inversely proportional to temperature. Oxygen gas is the most important gas dissolved in water. The solubility of oxygen in water varies depending on temperature, salinity, photosynthetic activities and atmospheric pressure [41,42]. When the seasonal variations of DO values of Sırakaraağaçlar Creek are analyzed according to the Classes of Continental Water Resources, water quality in II. and IV. class (Table 6). According to the data of the World Health Organization (WHO), the DO value of river waters should be ≥ 5 mg/L. In our study, all DO data were found under the WHO standards [43]. According to the Water Framework Directive of the European Union, the DO value in the range of 2-6 mg/L is indicated as inadequacy [44]. DO values obtained as a result of our study correspond to this range. In this case, it can be considered that the DO values of the water source are low and may adversely affect the water ecosystem. DO concentration helps us to have an idea about the pollution potential of water, the amount of OM in it and the degree of self-cleaning of water [45]. In the study was conducted by Taşdemir and Göksu in Asi River [46], the amount of DO was determined between 2.6 and 9.9 mg/L. In the studies were carried out in Hatay Karamanlı Pond [47] and Trabzon İyidere River [48], they found average DO concentration of 9.31 mg/L and 11.10 mg/L, respectively. The DO values obtained from our study differ from the previous studies can be explained with the regional differences being effective. Additionally, it shows that environmental effects are high in the Sırakaraağaçlar stream and that it is facing a pollution problem.

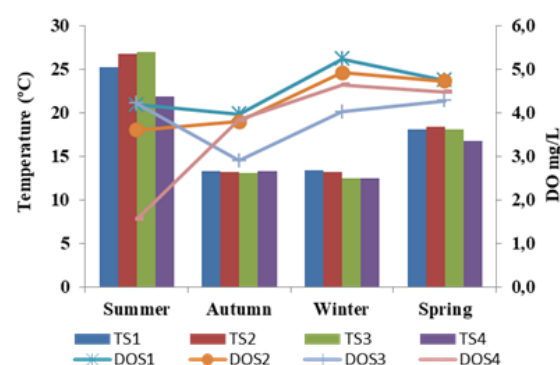


Fig. 2. Seasonal changes of temperatures and DO values of Creek.

Table 1. Values ($\bar{X} \pm \text{SD}$; min-max) of physicochemical parameters of Creek.

Stations	n	Summer	Autumn	Winter	Spring
Temperature (°C)	S1	9 25.21±0.92 ^{aA} (22.03-28.47)	13.30±0.90 ^{aB} (10.55-16.80)	13.37±0.60 ^{aB} (11.20-15.49)	18.13±0.24 ^{aC} (17.17-18.97)
	S2	9 26.80±0.40 ^{aA} (25.39-28.30)	13.21±0.82 ^{aB} (10.80-16.40)	13.24±0.59 ^{aB} (11.14-15.38)	18.44±0.46 ^{aC} (16.92-20.22)
	S3	9 26.98±0.39 ^{aA} (25.45-28.34)	13.13±0.80 ^{aB} (10.96-16.29)	12.45±0.42 ^{aB} (11.09-14.09)	18.11±0.61 ^{aC} (16.20-20.46)
	S4	9 21.85±0.36 ^{aA} (22.30-22.85)	13.27±0.76 ^{aB} (10.85-16.19)	12.50±0.43 ^{aB} (11.02-14.09)	16.79±0.19 ^{aC} (16.22-17.62)
DO (mg/L)	S1	9 4.18±0.25 ^{abA} (3.20-5.40)	3.97±0.40 ^{abB} (2.30-5.00)	5.23±0.06 ^{abC} (5.00-5.50)	4.75±0.09 ^{abC} (4.20-5.00)
	S2	9 3.60±0.06 ^{abA} (3.40-4.00)	3.80±0.30 ^{abB} (2.50-4.70)	4.92±0.07 ^{abC} (4.60-5.30)	4.72±0.15 ^{abC} (4.10-5.40)
	S3	9 4.22±0.61 ^{bA} (2.20-6.60)	2.90±0.33 ^{bB} (1.50-3.90)	4.02±0.08 ^{bC} (3.60-4.40)	4.28±0.18 ^{bC} (3.60-5.20)
	S4	9 1.56±0.24 ^{bA} (0.60-2.60)	3.84±0.19 ^{bB} (3.00-4.40)	4.64±0.07 ^{bC} (4.30-4.90)	4.48±0.09 ^{bC} (4.20-5.00)
pH	S1	9 8.11±0.12 ^{aA} (7.77-8.64)	7.57±0.06 ^{aB} (7.40-7.86)	7.19±0.01 ^{aC} (7.12-7.28)	7.29±0.14 ^{aC} (6.75-7.82)
	S2	9 8.37±0.04 ^{aA} (8.25-8.57)	7.64±0.07 ^{aB} (7.33-7.86)	7.14±0.02 ^{aC} (7.07-7.22)	7.37±0.13 ^{aC} (6.87-7.79)
	S3	9 8.32±0.02 ^{aA} (8.21-8.45)	7.63±0.08 ^{aB} (7.28-7.89)	7.15±0.02 ^{aC} (7.07-7.25)	7.31±0.12 ^{aC} (6.79-7.63)
	S4	9 7.79±0.01 ^{aA} (7.72-7.86)	7.78±0.10 ^{aB} (7.30-8.03)	7.15±0.03 ^{aC} (7.07-7.29)	7.25±0.13 ^{aC} (6.70-7.58)
Conductivity (µs/cm)	S1	9 612.57±122.70 ^{bA} (224.85-1067.18)	1004.71±31.01 ^{bA} (889.2-1102.11)	937.80±2.63 ^{bA} (928.65-946.96)	669.55±139.68 ^{bA} (110.80+955.37)
	S2	9 216.88±18.00 ^{cA} (178.6-288.88)	475.74±8.41 ^{cA} (444.60-502.50)	429.13±6.52 ^{cA} (408.80-453.55)	405.26±71.49 ^{cA} (119.32-554.80)
	S3	9 200.80±10.87 ^{dA} (176.7-244.29)	199.64±9.17 ^{dA} (173.20-234.96)	223.34±3.98 ^{dA} (208.20-235.60)	232.34±31.05 ^{dA} (110.85-315.9)
	S4	9 20.11±2.30 ^{aA} (11.18-26.7)	78.72±9.54 ^{aA} (57.70-116.89)	44.10±2.64 ^{aA} (34.86-53.26)	75.19±16.83 ^{aA} (8.30-115.52)
BOD ₅ (mg/L)	S1	9 1.02±0.16 ^{bA} (0.40-1.80)	3.10±0.41 ^{bB} (2.00-4.80)	2.05±0.04 ^{bA} (1.90-2.30)	2.24±0.34 ^{bA} (1.60-2.60)
	S2	9 1.15±0.24 ^{bA} (0.20-2.00)	4.02±0.29 ^{bB} (3.30-5.40)	3.15±0.05 ^{bA} (3.00-3.50)	3.13±0.17 ^{bA} (2.40-3.65)
	S3	9 1.06±0.21 ^{abA} (0.20-2.00)	2.14±0.26 ^{abB} (1.50-3.40)	1.28±0.02 ^{abA} (1.20-1.40)	1.43±0.10 ^{abA} (0.80-1.80)
	S4	9 0.84±0.14 ^{bA} (0.40-1.60)	4.42±0.51 ^{bB} (2.54-6.20)	2.33±0.02 ^{bA} (2.24-2.50)	2.82±0.13 ^{bA} (2.36-3.60)

A, B, C : The letters show differ between seasons ($P < 0.05$); a, b, c The letters show differ between stations ($P < 0.05$).

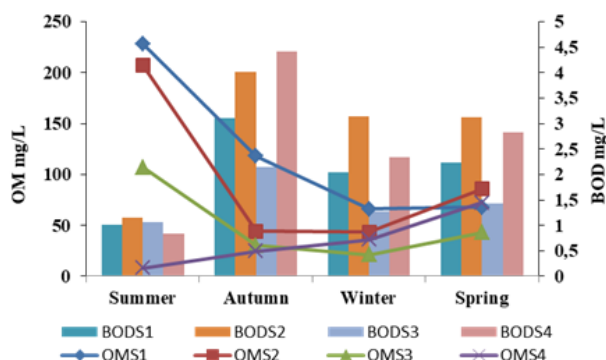
**Fig. 3.** Seasonal changes of OM and BOD₅ values of Creek.

Table 3. Values ($X \pm SD$; min-max) of T. coliform of Creek.

Stations	n	Summer	Autumn	Winter	Spring
T. Coliform (cfu/100ml)	S1	214.66 \pm 8.88 ^{aA}	98.22 \pm 4.10 ^{aB}	35.88 \pm 1.48 ^{aC}	83.22 \pm 3.53 ^{aB}
		(180-245)	(82-113)	(30-41)	(69-96)
	S2	470.77 \pm 16.14 ^{baA}	326.55 \pm 8.07 ^{bbB}	119.44 \pm 3.20 ^{bcC}	144.33 \pm 4.00 ^{bbB}
		(405-535)	(303-363)	(106-134)	(132-169)
	S3	337.66 \pm 27.91 ^{abA}	194.11 \pm 15.23 ^{abB}	132.55 \pm 12.5 ^{abC}	221.11 \pm 18.96 ^{abB}
		(241-439)	(140-256)	(87-183)	(158-298)
	S4	1263.55 \pm 184.57 ^{caA}	401.00 \pm 11.82 ^{cbB}	134.66 \pm 1.75 ^{ccC}	687.11 \pm 4.74 ^{cbB}
		(616-1904)	(358-452)	(128-144)	(673-708)

A, B, C : The letters show differ between seasons ($P < 0.05$); a, b, c The letters show differ between stations ($P < 0.05$).

Table 4. Values ($X \pm SD$; min-max) of F. coliform of Creek.

Stations	n	Summer	Autumn	Winter	Spring
F. Coliform (cfu/100ml)	S1	182.22 \pm 4.74 ^{aA}	76.77 \pm 5.10 ^{aB}	27.33 \pm 1.25 ^{aC}	50.22 \pm 1.36 ^{aB}
		(158-200)	(59-101)	(22-33)	(43-56)
	S2	430.11 \pm 7.40 ^{baA}	255.66 \pm 13.91 ^{bbB}	101.77 \pm 3.04 ^{bcC}	122.77 \pm 4.18 ^{bbB}
		(395-452)	(200-300)	(90-111)	(102-138)
	S3	276.55 \pm 11.29 ^{baA}	172.11 \pm 18.09 ^{bbB}	104.66 \pm 3.92 ^{bcC}	128.66 \pm 9.55 ^{bbB}
		(240-304)	(98-224)	(87-122)	(145-221)
	S4	1020.22 \pm 105.29 ^{daA}	380.33 \pm 11.43 ^{dbB}	86.22 \pm 2.94 ^{dcC}	539.11 \pm 13.86 ^{dbB}
		(629-1394)	(338-435)	(72-94)	(491-599)

A, B, C : The letters show differ between seasons ($P < 0.05$); a, b, c The letters show differ between stations ($P < 0.05$).

When the seasonal changes of pH values were examined according to the parameters of Sırakaraağaçlar Creek, the lowest value was 7.14 in winter and the highest value was 8.37 in summer, and both values were in S2 station. It can be stated that pH values are inversely proportional when compared with temperature values. pH values can vary depending on the amount of carbonate (CO_3^{2-}), bicarbonate (HCO_3^-), and free carbon dioxide (CO_2) in the water, but these changes can occur due to many factors. pH is inversely proportional to dissolved CO_2 and directly proportional to HCO_3^- . The critical value of the presence of CO_2 is pH 8 [32]. Therefore, in our study, CO_2 is active at pH 7.14 (winter), HCO_3^- is active at pH 8.37 (summer). In the study carried out in the stream of Sırakaraağaç, 11.36 and 5.01 mg/L CO_2 [49], 4.58 and 26.04 d ° H HCO_3^- values were obtained in the winter and summer seasons, respectively [50]. These results supported our study values. Oner and Celik [51], Şengün [52] and Dinçer [53] reported that pH values were 7.60 (in Gediz River), 7.42 (in Giresun Aksu Creek) and 7.92

(in Giresun Province Çanakçı Creek), respectively. In the studies carried out in river waters in different regions, it was found that the pH values were similar to our results. The pH of Sırakaraağaçlar Creek was in Class I and II Quality according to Continental Water Resources Quality Classification (Table 6).

Although the lowest conductivity was at S4 station with 20.11 $\mu\text{S}/\text{cm}$, the highest conductivity value was found at S1 station with 1004.71 $\mu\text{S}/\text{cm}$, and conductivity values generally changed below 1000 $\mu\text{S}/\text{cm}$, is shown in Table 1. Karşlı [40] found the average conductivity value in the Sakaryağaçlar stream as 12.25 $\mu\text{S}/\text{cm}$ in the summer season and 8.64 $\mu\text{S}/\text{cm}$ in the autumn season. According to WHO standards, conductivity should be 1000 $\mu\text{S}/\text{cm}$ in river waters [54]. The conductivity of water sources exceeding 1000 $\mu\text{S}/\text{cm}$ is considered as a sign of pollution [45]. It is known that the electrical conductivity varies depending on the salts dissolved in water, their density and water temperature [55]. When

the seasonal conductivity values of the stream were examined, it was found that the stations did not show a homogeneous distribution. The reason for this is primarily the difference in climatic conditions, the occasional merging of the water source with seawater, the variability of seasonal temperature and rainfall, the presence of other branches of the water supply can be shown. There are two most important reasons that affect our study results. The first of these, as the water level decreases in the late months of spring and in the summer, the mouth of the stream opening to the sea is closed, and the waters of the stream turn into freshwater in this period (station S1) [40]. The second reason is that precipitation varies according to the seasons. In Sinop province, the average of seasonal total rainfall between 1936-2019 was announced as 41.90 - 36.50 mm in spring-summer and 79.27 - 71.5 mm in autumn-winter, respectively [56]. The conductivity value was measured below expected due to the closed mouth of the stream in summer and the increase in precipitation in autumn. It was measured in studies that the conductivity value, which between 239 and 322 $\mu\text{S}/\text{cm}$ in Emiralem Creek [57] and between 28 and 450 $\mu\text{S}/\text{cm}$ in Trabzon province rivers [58]. Another study showed that the conductivity value of Ordu Ulugöl was 187.46 $\mu\text{S}/\text{cm}$ [59].

BOD₅ is the amount of oxygen that bacteria use to decompose OM under aerobic [32]. The correlation between BOD₅ and OM is negative, and statistically significant relative to $P \leq 0.05$ ($r = -0.326$). BOD₅ value was evaluated by many researchers in different regions. Verap, Serdar, Turan and Şahin [48], Dinçer [53] and Gedik, Verap, Ertuğrul and Fevzioğlu [60] evaluated that the average values of BOD₅ were 2.40 mg/L in Trabzon Iyidere, 1.85 mg/L in Rize storm Creek and 3.83 mg/L in Giresun Çanakçı Creek, respectively. Our findings were parallel with this study. In the Sırakaraağaçlar Creek, the lowest value (0.84 mg/L) and the highest value (4.42 mg/L) of BOD₅ were determined at S4 station, and it was found to be Class II in terms of water quality according to Continental water resources. When the seasonal BOD₅ values of the creek were examined, it was found that the BOD₅ values were low in summer and high in autumn. This is an indication that the solubility of the gases is inversely proportional to the temperature and the DO value decreases when the temperature increases. Due to the high temperatures during the summer, the decrease in DO value and the reduction of bacteria working in an aerobic environment, and the slowing or decreasing of the organic disintegration process can be shown as the cause [61, 62]. The increase in BOD₅ values towards autumn can be explained by the increased amount of DO due to

seasonal decreases in water temperature and an increase in precipitation. Water temperature is a parameter that affects the optimal living conditions of aquatic organisms, as well as many biochemical processes, while directly changing dissolved oxygen and many physicochemical properties (Figure 3) of water in aquatic environments [63].

When the seasonal changes of $\text{NH}_4^+\text{-N}$ values of Sırakaraağaçlar Creek were examined, the lowest value was 0.01 (mg/L) in S1, S2 and S3 stations, while the highest value was 0.33 (mg/L) in S4 station (Table 6). Ammonium is one of the nutrients that ensure the continuity of life. However, an excessive amount of nutrients in water resources causes pollution. In addition to providing the growth of algae in the water, it also adversely affects by reducing the amount of DO in the aquatic ecosystem [42]. When the $\text{NH}_4^+\text{-N}$ values in the water source were examined, it was observed that they were low in the autumn and winter seasons. This is because; the amount of DO increases due to reduced water temperatures, and nitrification events accelerate and NH_4 oxidizes during these seasons. Nitrification bacterial activity and concentrations rely on specific free ammonia concentration ($\text{NH}_3/\text{biomass}$ ratio), which is a function of temperature, pH, ammonium concentration and nitrification biomass concentration. Therefore, in the nitrification process, the temperature is a key parameter that produces two opposite effects. These are bacterial activation and free ammonia inhibition [64, 65]. At temperatures below 20°C, nitrification proceeds at a lower rate, but continues at temperatures below 10°C [66 - 68]. A temperature rise of 1°C in the range of 10-29°C causes a 2% increase in the nitrification rate [64]. However, microorganisms responsible for nitrification (Nitrobacter and Nitrosomonas) are extremely sensitive. They need a constant temperature of at least 12°C, a suitable C: N: P ratio and a sufficient amount of added oxygen. In our study, the possibility of nitrification may occur due to the pH being 7.15 - 7.78, the Nitrosomonas and Nitrobacter species being active at an optimum pH between 7 and 8 [69], and the temperature (12.45-13.37°C) is not too low. Also, some phytoplankton species absorb ammonium is an important factor in reducing ammonium amount. This is an indication that NH_4 is used in this cycle. $\text{NH}_4^+\text{-N}$ values were measured in the range of 0.11-20.04 mg/L in Afyon Akarçay and 0.02-1.98 mg/L in Asi river by Kıvrak, Uygun and Kalyoncu [70], and Taşdemir and Göksu [46], respectively. These results were found to be consistent with the $\text{NH}_4^+\text{-N}$ results in our study. According to the data of Turkey's Water Quality Management Regulation criteria Class of inland water

resources (Table 6), the water quality of Sirakaraağaçlar creek was class I (high-quality water) for BOD₅ and NH₄⁺-N values [71, 72].

H₂S is a colorless, toxic, volatile and flammable gas under normal conditions. SO₄⁻² ion in water sources is used as an oxygen source by sulphate reducing microorganisms in anaerobic environments, and S⁻² ion is formed as a result of biochemical reactions. The S⁻² ion reacts with hydrogen in water to form H₂S gas. In the study, when the H₂S values in the water source are examined, it is seen that the values are high in summer (Table 2). The reason for this is that the seasonal increase in water temperatures reduces the amount of dissolved oxygen. Moreover, the formation of oxygen-free products increases due to the fact that organic degradation is carried out by anaerobic bacteria [32,73]. In addition, H₂S may decrease if the DO value increases due to changes in water temperature. Since the final step of the S⁻² cycle is SO₄⁻², it is possible that a large proportion of the sulfur will be converted to sulfate owing to increased dissolved oxygen. S4 station is in the region where Abalı village domestic wastes are mixed, and agricultural activities and animal husbandry are carried out. Therefore, domestic wastes and animal droppings containing organic substances, various fertilizers used in agriculture and pesticides were added in the stream waters. In the excess of organic matter, since the oxygen utilization rate in the stream is greater than the supply of oxygen, anaerobic conditions have emerged at certain distances in the stream, and H₂S has formed together with other gases as decomposition product [33, 74]. Correlation values of H₂S were directly proportional to temperature and NH₄ (r = 0.878, r = 0.516, respectively; P ≤ 0.001), It was inversely proportional to DO and BOD₅ (r = -0.489, r = -0.650, respectively; P ≤ 0.001), and were found to be very important (Table 5).

Considering the results of the study (except S4 station), it was determined that the lowest values of OM changes were in Winter and the highest values were in Summer (Table 2). OM values in this study differed from the studies were made by Gedik, Versep, Ertuğrul and Fevzioğlu in Rize Fırtına Creek [61], and Dinçer in Giresun Çanakçı Creek [53]. In our study, OM values of the creek ranged from 0.27 to 644 mg/L. The fluctuations in the amounts of OM were decided, and it was concluded that this occurred due to seasonal changes of temperature, pH and precipitation. In 2014, Turkey in average rainfall of 641.6 kg/m², while 703.6 kg/m² (in 2015, 691.5 kg/m²) in average rainfall of Sinop was determined to be. It can be said that rains are very effective in the region [74, 75]. When the correlation values of OM were examined (Table 5), it

was found that it was directly proportional to temperature, TSS and pH (r=0.681, r=0.994 ve r=0.629, respectively), and they were statistically significant (P ≤ 0.001). TSS is known as the total of soluble and insoluble solids in water and they are suspended in water. It is generally composed of colloidal organic materials, sediment materials, sludge or clay minerals. Many substances (TSS) such as clay, organic substances, microscopic organisms, calcium carbonate, aluminum hydroxide, iron hydroxide can hang in the water. When organic substances break down, they can cause an increase in suspended substances that are soluble and have low solubility. Moreover, mixed organic substances (naphthalene and phenols etc.) and others can cause pH rise in water [76]. The area of the Sıkaraağaçlar Stream close to the sea is in the region where the swamps are most intense. Moreover, it is in the region where Tourism is effective because it is a residential area. For this reason, OM, TSS (except spring) and conductivity values were determined at the highest stations S1 and S2. Organic materials derived from detritus (rotting plant parts) predominate in marshes. The overall low permeability of soft fine-grained sediments limits the movement of water in the soft sediment layer [77] and causes the accumulation of organic substances.

Suspended solids are an important parameter for waters; as the amount of solids in the water increases, the permeability of the water decreases, and the solids cause adverse conditions for aquatic organisms [78]. Taşdemir and Göksu [46] found the TSS value as 1-381 mg/L in the Asi River, while Tepe and Mutlu [37] found the TSS value as 1.75 mg/L in Hatay Harbiye Spring water. TSS values in this study were established to be low values according to literature studies (Table 2). TSS values showed an increase and decrease in seasonal changes, and it can be said that it is due to water flow rate and precipitation. The reason for the fact that the TSS values in summer is higher compared to other seasons is that the evaporation and the input of urban wastewater are high. Correlation values of TSS were found to be directly proportional to temperature, pH, H₂S and OM (r=0.681, r=0.606, r=0.545 ve r=0.994, respectively), and this correlation (P ≤ 0.001) were to be very important statistically (Table 5). TSS values of the creek (Table 6), according to Turkey's Water Quality Management Regulations criteria according to internal water resources were clean water. According to the Eutrophication Control Limit Values data for lakes and marshes, the TSS value for natural protected areas is 5mg/L [71, 72].

Table 5.Correlation between Coliform Bacteria and Physicochemical Parameters.

	T.Coliform	F.Coliform	Temperature	DO	pH	Conductivity	BOD ₅	NH ₄ ⁺ -N	H ₂ S	OM
F.Coliform	0.985***									
Temperature	0.379**	0.38]**								
DO	-0.752***	-0.757***	-0.224							
pH	0.343*	0.404**	0.783***	-0.445**						
Conductivity	-0.554***	-0.535***	-0.154	0.429**	-0.138					
BOD ₅	-0.234	-0.188	-0.638***	0.280	-0.329*	0.139				
NH ₄ ⁺ -N	0.791***	0.732***	0.590***	-0.490***	0.255	-0.428**	-0.427**			
H ₂ S	0.545***	0.574***	0.878***	-0.489***	0.831***	-0.188	-0.650***	0.516***		
OM	-0.132	-0.083	0.681***	0.158	0.629***	0.336*	-0.326*	-0.000	0.570***	
TSS	-0.123	-0.076	0.681***	0.181	0.606***	0.335*	-0.308*	-0.026	0.545***	0.994***

P ≥ 0.05; (*)P ≤ 0.05; (**)P ≤ 0.01; (***)P ≤ 0.001

Table 6.Quality of Sırakaraağaçlar Creek according to inland water resources classes.

Water quality parameters	Water quality Classes				Sırakaraağaçlar Creek	
	Class I	Class II	Class III	Class IV	(Min.-Max.)	Class
Temperature (°C)	≤ 25	≤ 25	≤ 25	>30	(12.45 – 26.98)	I - III
DO (mg/L)	>8	6	3	<3	(5.23 - 1.26)	II - IV
pH	6.5-8.5	6.5-8.5	9	6-9 Outside	(7.14 - 8.37)	I - II
Conductivity ((μS/cm)	<400	1000	3000	>3000	(20.11 - 1004.71)	I-II
BOD ₅ (mg/L)	4	8	20	> 20	(0.84 - 4.42)	II
NH ₄ -N (mg/L)	0.2	1	2	< 2	(0.01 - 0.33)	I - II
OM (mg/L)	5	8	12	> 12	(8.20 – 228.41)	II - IV
TSS (mg/L)	5	Natural protected area and recreation			(0.014 - 0.415)	
T.Coliform (cfu)/100 mL	≤100	20000	100000	> 100000	(35.88 - 1263.55)	I - II
F.Coliform (cfu)/100 mL	≤10	200	2000	> 2000	(27.33 - 1020.22)	II - III

Class I: Clean. Class II: Slightly contaminated. Class III: Contaminated and Class IV: Highly contaminated.

Coliforms are a broad variety of bacteria. Coliform group of bacteria in the Enterobacteriaceae family, rod-shaped, non-spore-forming, gram-negative by fermentation of lactose at 35°C in 48 hours are bacteria that produce gas. Coliform bacteria are most frequently seen in the intestines of animals, as well as in plants and soil [34, 79]. The presence of F. coliform bacteria in water sources demonstrates that water is in contact with fecal waste, which designates that water sources are polluted with many harmful, dangerous and disease-causing bacteria, protozoa, parasites and viruses [34]. The lowest value of T. coliform and F. coliform in Sırakaraağaçlar Creek is monitored in S1 station with 33.88 and 27.33 cfu/100ml, respectively and the highest value is established in S4 station with 1263.55 and 1020.22 cfu/100ml, respectively. It was determined that there was a village settlement near the S4 station, there were agricultural areas and grazing areas of animals around the village. In addition, it is known that the sewage system of the village is mixed from this area into the stream. The reason why T.coliform and F. coliform values were higher than other stations was explained by the fact that human and animal origin wastes were mixed into the stream. Coliform amount in the Dicle river was found as $2.10-4.02 \log_{10}$ cfu/ml [80], whereas the amount of coliform and *E. coli* in the drinking water of Bitlis province was calculated to be in the range of 501-5000/100ml [81]. F.coliform load were found to be >1100/100ml in Çanakale Sarıçay Stream and Kahramanmaraş Aksu Creek by Çolakoğlu and Çakır [82], and Toroğlu, Toroğlu and Alaeddinoğlu [83], respectively. Coliform values were different from the results of previous studies. This was due to the difference in place and time.

The seasonal variation of F. coliforms was determined to be in parallel with T. coliforms. It is viewed that most of T. coliforms are generally occurred of F. coliforms, which are not wanted to be observed in the waters. Seasonal changes in Creek have also viewed both T. coliforms and F.coliforms contamination. This is an indication that creek is in contact with human and animal feces throughout the year. T. coliform and F. coliform load in Creek was identified to be higher in summer compared to other seasons. The reasons for the increase of coliform concentrations can be expressed as the increase of water temperature owing to seasonal temperature change, the formation of appropriate reproductive environment for microorganisms, the decrease in the amount of seasonal precipitation and the increase of water inflow from urban sewage into natural water resources. In the transition from summer to winter, the decrease in T. coliform and F. coliform loads was caused by the decrease in water temperature.

Moreover, the reduction in their load in the water was owing to increased precipitation. According to the results found from the study area, T. coliform value was discovered to be highest at S4 station in all seasons. The reason for this is the change in water flow rate and quantity, and also that the station is on the route of the animals. When seasonal T. coliform values of the stream were compared, S1 station was found to be lower than other stations. This situation was interpreted as the result of the increase in salinity value due to marine impact. One of the most important factors affecting our study results is that as the water level decreases in late spring and summer, the mouth of the creek closed to the sea and the waters of the stream turn into freshwater during this period [40]. The other is that the amount of precipitation in the region is high [74, 75]. When T. coliform and F. coliform correlation values ($P \leq 0.001$) were achieved (Tablo 6), it was decided that it was directly proportional with each other ($r = -0.985$) and with NH_4 ($r = -0.791$; $r = -0.732$, respectively), H_2S ($r = -0.545$; $r = -0.574$, respectively), inversely proportional with DO ($r = -0.752$; $r = -0.757$, respectively) and conductivity ($r = -0.554$; $r = -0.535$, respectively), and these relationships are quite important. The average value of physical parameters and coliforms were compared with “Environmental Legislation”, “Regulation on Water Pollution Control” and “Quality Criteria According to Classes of Inland Water Resources”, and were shown in Table 6 [71, 72] It was determined that Sırakaraağaçlar Creek were more or less (class II-IV) contaminated water in terms of DO parameter, and contaminated or highly contaminated water in terms of H_2S parameter, and slightly soiled or contaminated (class II-III) water in terms of T. coliform (class I-II) and F. coliform (class II-III) values.

4. Conclusions

In the developing world, due to the increase in environmental sensitivity, it is known that although necessary measures are taken for water pollution, it is not sufficient. It is very important to increase the studies on the quality and pollution of water resources and to determine the current conditions of water resources and the sources of pollutants. The water of Sırakaraağaçlar Creek passes through settlements and agricultural areas until it reaches the sea. If the current state of the water quality parameters of the water source is not improved and maintained, the possibility of an increase in pollution load is inevitable in the following years. Also, adverse conditions that may affect aquatic life and human health may arise in the ecosystem and water basin.

When the data obtained from this study were evaluated, it was determined that DO value of water source was low and H₂S, T. coliform and F. coliform values were high. This reinforces the possibility that eutrophication may start or increase in the water source. It is thought that the amount of suspended solids, temperature, the load of OM and other pollutants affect the low oxygen values in the water source. Controlling and continuous monitoring of these parameters supports the possibility that the DO value may naturally return to normal values. One of the measures that can be taken for hydrogen sulfide pollution, which is one of the pollution types in our study, is to correct the sewage infrastructure of the settlements around the creek. The second is to take measures to reduce a load of OM before the discharge of wastewater. The main source of coliform pollution is wastewater in sewers. These bacteria can cause serious diseases for human health. It is evident that the continuous monitoring of the coliform bacteria load of the water source and the installation of sewage treatment systems will be an effective measure to prevent pollution. The current status of Sırakaraağaçlar Creek should be monitored periodically and necessary measures ought to be taken to protect and improve it. In addition, the water source should be kept under control for the substances that may increase the load of suspended solids entering the water sources from the surrounding settlements and agricultural lands.

In order to ensure the sustainability of water resources; prevention of further degradation of aquatic environments, and improvement works, good protection of water resources for long-term use, further emphasizing the seriousness and importance of the issue should be among our goals. The idea of dissemination of the management concept on the basis of the river basin, which is the main objective of the European Union water framework directive, should be adopted. The quality of life and sustainability of aquatic organisms will be possible with the quality and cleanness of natural waters.

Acknowledgement

The data of the Master thesis “Investigation of some physicochemical and microbiological parameters in Karasu and Sırakaraağaçlar stream” was used. We owe our thanks for his contribution to Institute of the Natural Science of Sinop University.

Conflicts of interest

The authors state that did not have a conflict of interests.

References

- [1] Kanownik W. and Rajda W. Samooczyszczanie wody potoku Pychowickiego, *Zesz. Prob. Post. Nauk Rol.*, 561 (2011) 81–91.
- [2] Napieralska A. and Gołdyn R. Sanitary Analyses of Runoff Water a River, *Pol. J. Environ. Stud.*, 22 (2) (2013) 481–486.
- [3] Bogdal A., Kowalik T., Ostrowski K. and Skowron P. Seasonal variability of physicochemical parameters of water quality on length of Uszwica river, *J. Ecol. Eng.*, 17 (1) (2016) 161–170.
- [4] Küçük S. Investigation of Water Quality Parameters of the Büyük Menderes River for Fisheries, *Adü. Ziraat Derg.*, (2007) 7-13.
- [5] Gündoğdu A., Gültepe E., and Çarlı U. Determination of Anionic Detergent Concentration of Karasu Stream in Sinop (Turkey), *Turk. J. Agric.- Food Sci. Tech.*, 6-1 (2018) 112-123.
- [6] Wu J., Li P., Qian H., Duan Z. and Zhang X. Using correlation and multivariate statistical analysis to identify hydrogeochemical processes affecting the major ion chemistry of waters: a case study in Laoheba phosphorite mine in Sichuan, China, *Arab J. Geosci.*, 7 (2014) 3973–82.
- [7] Mostafa A.H., Al-Wasify R.S., Sayed A.M. and Haroun B.M. Microbiological and physicochemical evaluation of groundwater in Egypt, *Int. J. Environ. Sust.*, 2 (2013) 1-10.
- [8] Singh A.K., Das S., Singh S., Pradhan N., Gajamer V.R., Kumar S., Lepcha Y.D. and Tiwari H.K. Physicochemical Parameters and Alarming Coliform Count of the Potable Water of Eastern Himalayan State Sikkim: An Indication of Severe Fecal Contamination and Immediate Health Risk, *Front. Public Health*, 7 (2019) 174.
- [9] Hamzah A., Kipli S.H., Ismail S.R., Una R. and Sarmani S. Microbiological study in coastal water of Port Dickson, *Sains Malays.*, 40-2 (2011) 93-99.
- [10] WHO. Guidelines For Drinking Water Quality, Volume 2, Health Criteria and Other Supporting Information, Second ed., World Health Organization (WHO), Geneva, (1997) 65.
- [11] Abreu-Acosta N. and Vera L. Occurrence and removal of parasites, enteric bacteria and faecal contamination indicators in wastewater natural reclamation systems in Tenerife- Canary Islands, *Spain, Ecol. Eng.*, 37 (2011) 496-503.
- [12] Al-Bahry S., Mahmoud I.Y., Al-Belushi K.I.A., Elshafie A.E., Al-Harthy A. and Bakheit C.K. Coastal sewage discharge and its impact on fish with reference to antibiotic resistant enteric

- bacteria and enteric pathogens as bio-indicators of pollution, *Chemosphere*, 77 (2009) 1534–1539.
- [13] Berber I. and Avşar C. Investigating Some Microbial Pollution Parameters of Seawater and Mussels (*Mytilus galloprovincialis*, Lamarck 1819) of Sinop. Black Sea Coastal Zone, Turkey, *Sains Malays.*, 43 (12) (2014) 1835–1842.
- [14] Ward D.R. and Hackney C. Microbiology of marine food products, New York: Published by Van Nostrand Reinhold, 1991; 443.
- [15] Kilinc B. and Besler A. The occurrence of enteric bacteria in marine environment and pollution, *Mar. Sci. Tech. Bull.*, 3 (2) (2014) 39-43.
- [16] Elmanama A.A., Afifi S. and Bahr B. Seasonal and spatial variation in the monitoring parameters of Gaza Beach during 2002-2003, *Environ. Res.*, 101 (2006) 25-33.
- [17] Acehan G. Investigation of Microbiological Pollution Potential of Drinking Waters. Master Thesis, Cukurova University, Institute of Science, Adana, (2007) 235.
- [18] Elmacı A., Teksoy A., Topaç F.O., Özengin N. and Başkaya H.S. Monitoring of Seasonal Variation of Microbial Quality in Lake Uluabat. Uludağ University, *J. Eng.-Archit. Faculty*, 13 (1) (2008) 93-103.
- [19] Aksu H. Evaluation of Drinking Water Microbiological Risks. Istanbul and Water Symposium: Discussions and Forum, Istanbul, (2004).
- [20] Fakir Y. Investigation of water quality parameters in Denizli water supply network according to time and location. Master's Thesis, Pamukkale University, Institute of Science, Denizli, (2012) 142.
- [21] Ayaz E. Investigation on cryptosporidium parvum by using molecular technics in water samples collected from provinces of Giresun and Samsun. Master Thesis, Ordu University, Institute of Science, Ordu, (2015) 140.
- [22] Hagendorf U., Diehl K., Feuerpfeil I., Hummel A. and Szezyzyk R. Retention of microbiological organisms in constructed wetlands. In: Proceedings of the Seventh International Conference on Wetland Systems for Water Pollution Control., Gainesville: IWA and University of Floryda, (2000) 391.
- [23] Sigua G.C., Palhares J.C.P., Kich J.D., Mulinari M.R., Mattei R.M., Klein J.B., Müller S. and Plieske G. Microbiological Quality Assessment of Watershed Associated with Animal-Based Agriculture in Santa Catarina, Brazil, *Water Air Soil Pollut.*, 210 (2010) 307.
- [24] Salyers A.A. and Whitt D.D. Microbes and a human in imbalance: infectious diseases. In: Microbiology. Diversity, pathogenicity and environment. PWN, Warsaw, [In Polish], (2012).
- [25] Augustyn L., Babula A., Joniec J., Stanek-Tarkowska J., Hajduk E. and Kaniuczak J. Microbiological Indicators of the Quality of River Water, Used for Drinking Water Supply, *Pol. J. Environ. Stud.*, 25 (2) (2016) 511-519
- [26] Ozaner F.S. Sinop Batısındaki Ekosistemler ve İlginç Yerşekillerinin Jeomorfolojisi, Ekoturizm Yönünden Önemi. TÜBİTAK Yer Deniz Atmosfer Bilimleri ve Çevre Araştırma Grubu, Ankara, (1998) 19.
- [27] Ustaoglu S., Yardım Ö. and Tırlı A. General Characteristics and Conservation Problems of Wetlands (Sarıkum and Karagöl-Aksaz) in Sinop. Süleyman Demirel University, Protected Natural Areas Symposium, 8-10 September 2005, Isparta, (2005) 267.
- [28] GEUPD. T.C. Sinop Governorate, Environment and Urbanization Provincial Directorate (T.C.SGEUPD). Sinop province, 2018 Environmental Status Report. (2019).
- [29] Karşı Z. and Aral O. Population Age, Sex Structure and Growth of *Aphanius danfordii* (Boulenger, 1890) to Sirakaraağaçlar Stream, Turkey. *J. Anim. Vet. Adv.*, 9 (10) (2010) 1427-1431.
- [30] APHA. Standard methods for the examination of water and waste water. 19th edition. American Public Health Association (APHA) Inc., New York, (1965) 1193.
- [31] APHA. Standard Methods for the Examination of Water and Wastewater, 15th ed.; APHA (American Public Health Association): Washington, D.C, USA, (1981) 85- 99, 773-779, 786-828.
- [32] Egemen Ö. and Sunlu U. Water Quality, Ege University, İzmir, Turkey, E.Ü.F.F. Press., (1996) 153.
- [33] TSI. Drinking and Use Water Standards, Turkish Standards Institute: TSI (Türk Standartları Enstitüsü, İçme ve Kullanma Suları Standartları), (2005).
- [34] Halkman A.K. Food Microbiology Applications, Başak Typography (Gıda Mikrobiyolojisi Uygulamaları Merck., Ed: A. K. Halkman, Başak Matbaacılık), Ankara, Türkiye, 89 (124) (2005) 358.
- [35] Cirik S, Cirik Ş. Limnology. Ege University, Faculty of Fisheries Press, İzmir, Turkey, (2008) 166.
- [36] Gürel E., Determination of Porsuk Stream Water Quality, Master Thesis. Eskişehir Osmangazi University, Eskişehir, Turkey, (2011).

- [37] Tepe Y. and Mutlu E. Physico-Chemical Characteristics of Hatay Harbiye Spring Water. *D.Ü. Journal of the Institute of Science*, 6 (2004) 77-88.
- [38] Bulut C., Akçimen U., Uysal K., Küçükkara R., Savaşer S., Tokatlı C., Öztürk G.N. and Köse E. Water Quality Of Kestel Creek (Burdur) and Assesment For Salmonid Culture, *J. Sci. Technol. Dumlupınar Univ*, 28 (2012) 1-10.
- [39] Yıldız İ. Determination of the Water Quality and Pollution Level of Gelevera Creek. Master Thesis, Giresun University, Institute of Sciences, Department of Biology, Giresun, (2013) 92.
- [40] Karşı Z. Some Biological Characteries of the Mosquitofish (*Aphanius Chantrei*) Population In The Sırakarağaçlar Stream (Sinop-Aklıman). Master Thesis, Ondokuz Mayıs University Institute of Science, Samsun (2007) 45.
- [41] Gündoğdu A. Investigation of Anionic Detergents Pollution in shore of Sinop (Master's thesis). Ondokuz Mayıs University, Samsun, Turkey, (1995) 60.
- [42] Tayhan N. Periodic Monitoring of Physicochemical Water Quality of Uzuncayır Dam Lake (Tunceli) . Master Thesis, Tunceli University Institute of Science and Technology, Tunceli, (2012) 79.
- [43] WHO. World Health Organization (WHO). Diarrhoeal Disease. (2018).
- [44] EC. "Directive 2000/60/EC of the European Parliament and of the Council of 23 October 2000 establishing a framework for Community action in the field of water policy", Official Journal of the European Communities (EC), (2000).
- [45] Kara, C., Çömləkciöğlü, U. Karaçay (Kahramanmaraş)'ın Kirliliğinin Biyolojik ve Fiziko-Kimyasal Parametrelerle İncelenmesi, *KSÜ Fen ve Müh. Dergisi*, 7(1) (2004) 7.
- [46] Taşdemir, M. and Göksu, Z.L. Some Water Quality Criteria of Asi River (Hatay), *Ege J. Fish. Aquat. Sci.*, 18(1-2) (2001) 55-64.
- [47] Tepe Y., Mutlu E., Ateş A. and Başusta N. Water Quality of Samandağ Karamanlı Lake (Hatay),. *Turk. J. Aquat. Life*, 3 (2004) 408-414.
- [48] Verap B., Serdar O., Turan D. and Şahin C. Determination of Water Quality in terms of Physico-Chemical Structure of the River Iyidere (Trabzon), *Ecology*, 14(57) (2005) 26-35.
- [49] Gültepe E. Investigation of Anionic Detergent Pollution In Karasu and Sırakarağaçlar Stream. Master Thesis, *Sinop University Institute of Science Sinop*, (2016) 116.
- [50] Çarlı U. Investigation Ofsome Physico-Chemicaland Microbiological Parameters In Karasu and Sırakarağaçlar Stream. Master Thesis. Sinop University Institute of Science, Sinop, (2015) 136.
- [51] Oner O. and Celik A. Investigation of some pollution parameters in water and sediment samples collected from the lower Gediz river basin, *Ecology*, 20 (78) (2011) 48-52.
- [52] Şengün E. Determination of The Water Quality and Pollution Level of Aksu Creek. Master Thesis, Giresun University, Giresun, Turkey, (2013) p 66.
- [53] Dinçer S. Determination of the Water Quality and Pollution Level of Çanakçı Creek, Master's Thesis, Giresun University, Giresun, Turkey (2014).
- [54] Leong S.S., Ismail J., Nurdiyana A., Denil N.A., Shahrul R., Sarbini S.R., Wafri Wasli W. and Debbie A. Microbiological and Physicochemical Water Quality Assessments of River Water in an Industrial Region of the Northwest Coast of Borneo, *Water*, 10 (2018) 1648
- [55] Er C.B. Some physicochemical and microbiological properties of drinking water in Kilis province (Master's Thesis), Kilis 7 Aralık University, Kilis, Turkey, (2014).
- [56] MAFGDM., T.C. Ministry of Agriculture and Forestry General Directorate of Meteorology. General Statistical Data of Our Provinces 1936-1919. Retrieved June 03, 2020.
- [57] Sukatar A., Yorulmaz B., Ayaz D. and Barlas M. Investigation of Some Physio-chemical and Biological (Benthic Macroinvertebrata) Features of Emiralem Stream (Izmir-Menemen), *SDÜ. Fen Bil. Ens. Derg.*, 10 (3) (2006) 328-333.
- [58] Gültekin F., Ersoy A.F. Hatipoğlu E. and Celep S., Determination of Water Quality Parameters in Wet Season of Surface Water in Trabzon, *Ecology*, 21(82) (2012) 77-88.
- [59] Taş B., Candan, A.Y., Can, Ö. and Topkara, S. Ulugöl (ORDU)'nün Bazı Fiziko-Kimyasal Özellikleri, *Journal of Fisheries Sciences*, 4 (3) (2010) 254-263.
- [60] Gedik K., Verap B., Ertuğrul T. and Fevzioğlu S. Determination of Water Quality of Fırtına Stream (Rize) in terms of Physico-Chemical Structure, *Ecology*, 19-76 (2010) 25-35.
- [61] Egemen Ö. Environment and Water Pollution, .. İzmir, Turkey: EÜFF Press, 2000; 120.
- [62] Şakar S. Çevre Mikrobiyolojisi Ders Notları (2019–2020 Öğretim Yılı), Yıldız Teknik Üniversitesi İnşaat Fakültesi Çevre Mühendisliği Bölümü, İstanbul (2020) 138.
- [63] Hasançavuşoğlu Z. and Gündoğdu A. Investigation of Anionic Detergent Pollution in

- Sarıkum Lake (Sinop), *Turk. J. Agric.- Food Sci. Tech.*, 7 (11) (2019) 1825-1833.
- [64] Fdz-Polanco F., Villaverde S. and García P.A. Temperature effect on nitrifying bacteria activity in biofilters: Activation and free ammonia inhibition, *Wat. Sci. Tech.*, 30 (11) (1994) 121–130.
- [65] Kaplan D., Wilhelm R. and Abeliovich A. Interdependent environmental factors controlling nitrification in waters, *Water Science and Technology*. 42 (1–2) (2000) 167–172.
- [66] Schlegel H.G. *Allgemeine Mikrobiologie*, Newyork: Thieme Verlag, 1985; 571.
- [67] Kirmeyer G.J., Odell L.H., Jacangelo J., Wilczak A. and Wolfe R. Nitrification Occurrence and Control in Chloraminated Water Systems, Denver, Colo.: AwwaRF and AWWA, 1995;
- [68] Sivri N., Karaçam H. and Feyzioğlu M. Nitrifying Bacterial Activity In South Eastern Black Sea (Coast of Sürmene), *Tr. J. of Biology*, 22 (1998) 299-306.
- [69] EPA. Nitrification. U.S. Environmental Protection Agency Office of Ground Water and Drinking Water Standards and Risk Management Division, 1200 Pennsylvania Ave., NW Washington DC 20004. August 15 (2002).
- [70] Kıvrak E. Uygun A. and Kalyoncu H. Application of Diatom Indices to Assess Water Quality of the Akarçay Stream (Afyonkarahisar, Turkey). *AKU J. Sci.*, 12 (2012) 27-38.
- [71] SWQMR. Regulation on the surface water quality management, *Number of official gazette*: 29327 (2015).
- [72] SWQMR Regulation on the surface water quality management, *Number of official gazette*: 29797 (2016).
- [73] Öztürk M. Hydrogen sulfide gas formation in sewerage and Its effects on health. (Kanalizasyonda Hidrojen Sülfür Gazı Oluşumu ve Sağlık Üzerine Etkileri), *Ministry of Environment and Forestry*, Ankara, (2006) 13. Retrieved April 4, 2018.
- [74] SGEUPD. T.C. Sinop Governorate, Environment and Urbanization Provincial Directorate (T.C.SGEUPD), Sinop province, 2014 Environmental Status Report. (2015).
- [75] SGEUPD. T.C. Sinop Governorate, Environment and Urbanization Provincial Directorate (T.C.SGEUPD), Sinop province, 2015 Environmental Status Report. (2016).
- [76] Uslu O. and Türkman A. Water Pollution and Control. TC. Prime Ministry General Directorate of Environment Publications, Education series, (1987) 364.
- [77] EPA. US Environmental Protection Agenc, Region 2. Berry's Creek Study Are Proposed Plan. Part of the Ventron/Velsicol Superfund Site. New York, May (2018) 10007-1866. Retrieved June 4, 2020.
- [78] Dihkan M., Karslı F. and Güneroğlu A. Mapping Distribution of Total Suspended Matter Concentration In Coastal Black Sea Waters. Chamber of Survey and Cadastre Engineers (TMMOB), 13th Turkey Scientific and Technical Congress, Ankara, (2011).
- [79] Şengül F., Türkman A. Water and Wastewater Analysis. Chamber of Environmental Engineers (TMMOB), İzmir, (1998) 152.
- [80] Vural A. And Erkan M.E. 2006. Microbiological Quality Parameters in Fish of Dicle (Tigris) River Near Diyarbakır City, *Dicle Medical Journal*, 33(3) (2006) 153-156.
- [81] Alemdar S., Kahraman T., Ağaoğlu S. and Alişarlı M. Some Microbiological and Physicochemical Properties of Drinking Water in Bitlis District, *Ecology*, 19 (73) (2009) 29-38.
- [82] Çolakoğlu F.A. and Çakır F. Microbiological Quality in Sarıçay Stream, *Canakkale University Fisheries Faculty*, (2003) 305-312.
- [83] Toroğlu E., Toroğlu S. and Alaeddinoğlu F. Water Pollution in the Aksu River (Kahraman Maraş), *J. Geogr. Sci.*, 4(1) (2006) 93-103.

A research on antioxidant activity evaluation of waste lignocellulosic biomass: optimization using response surface methodology

Bahar MERYEMOĞLU^{1*} , Burcak KAYA ÖZSEL² , Berna NIS² 

¹ Central Research Laboratory, University of Cukurova, Adana, Turkey

² Department of Chemistry, Bursa Technical University, Bursa, Turkey

Abstract

In the present study, lignocellulosic biomass such as corn straw and sorghum were used as raw materials for a new, abundant, low-cost and natural antioxidant source to use in foods or medicinal materials as replacements for synthetic antioxidants such as butylated hydroxyanisole (BHA) and butylated hydroxytoluene (BHT). The effect of extraction temperature, extraction time, solvent volume on extraction yield, total phenol content and antioxidant activity were investigated and the results obtained by response surface methodology (RSM) were evaluated. Linear and quadratic models were revealed as a result of experiments. The fit of these models with predictions results were tested and optimal condition parameters were investigated. It was seen that different results were obtained because of structural differences between corn straw and sorghum. These results showed that the extraction temperature was the main positive linear effect on extraction yield. The solvent volume and temperature were found to important model terms for total phenol content. For antioxidant activity, the solvent volume was the main linear effect for sorghum where as it has a quadratic effect for corn straw biomass.

Article info

History:

Received:21.01.2020

Accepted:18.04.2020

Keywords:

Lignocellulosic biomass, phenolics, antioxidant activity, response surface methodology, optimization.

1. Introduction

In recent years, hundreds of herbal sources have been tested for antioxidant activity. The most important natural antioxidant sources are plants (oilseeds, cereals, vegetables, fruits, spices), animal products (peptides, amino acids and carotenoids), enzymes (glutathione peroxidase, superoxide dismutase and catalase) and some microorganisms [1]. In addition, due to the fact that phenolic compounds are natural antioxidant sources and have positive effects on health, the interest in fruit and vegetable products is increasing day by day.

Phenolics, composed of one or more aromatic rings bearing one or more hydroxyl groups, are found in almost every vegetable and fruit. Despite their structural diversity they have similar properties so can basically be categorised into several classes. The favourable effects derived from phenolic compounds have been attributed to their antioxidant activity due to the their ability scavenge free radicals from the body [2]. Besides vegetables and fruits, agricultural lignocellulosic biomass could be interesting and low-

cost natural sources of antioxidant phenolic compounds.

Lignocellulosic biomass composed of cellulose, hemicellulose, lignin and other extractives. These main extractives are aliphatic compounds (oils and waxes), terpenes (sterols and resins) and terpenoids, fatty acids, quinines, aldehydes, alcohols, coloring pigments, steroids and phenolic compounds [3]. Sorghum, as a lignocellulosic biomass, belongs to the Monocotyledon class of Gramine Familia. There are 113 species and represent over 40,000 genotypes [4]. It is the fifth most grown cereal plant in the world [5]. Sorghum is preferred due to the fact that high photosynthesis yield can easily be raised in all climatic conditions and does not require excessive irrigation and fertilizer. Corn, the industrial uses of which are very broad and generate large amounts of biomass residues. Corn straw production in 2014 was about 1661 Mt, highest among the three major types of crop straws (rice, wheat, corn) in the world [6]. Its chemical composition and low-cost make it an attractive feedstock to be used in production of high value products such as bioactive compounds.

*Corresponding author. Email address: meryemoglubahar@gmail.com

<http://dergipark.gov.tr/csj> ©2020 Faculty of Science, Sivas Cumhuriyet University

Studies on antioxidant activity are mainly focused on food in the human diet. Any study on lignocellulosic agro-wastes for antioxidant activity applications have not been reported yet in the literature. Therefore, in this study sorghum and corn straw, as lignocellulosic biomass residue, were extracted and investigated for an alternative non-food cheap antioxidant source for potential use in cosmetic, food and pharmaceutical industries.

Extraction is one of the most important step in antioxidant studies so effects of temperature, extraction time and solvent volume on extraction yield of phenolics from sorghum and corn straw were evaluated on the responses of total phenolic content and total antioxidant activity, optimal conditions were determined by using Response Surface Methodology (RSM).

2. Experimental

2.1. Extraction of lignocellulosic biomass

Sorghum and corn straw were used as biomass feedstocks. Sorghum was grown in Adana. It was harvested in autumn. The harvested plant was dried, grounded and used in extraction. Corn straw was obtained local supplier in Adana. The analytical data for lignocellulosic biomasses were given Table 1. The 7.5 g of grounded biomass was extracted with water:methanol (1:1) under reflux. After extraction, the solid residues were dried at 100 °C. The percentage of extraction was calculated as: (initial weight of biomass-weight of dried biomass)/(initial weight of biomass)*100.

UV-VIS Spectrophotometre: UV-1800 UV-VIS Spectrometer and UNICAM UV-VIS Spectrometer UV 2 pH meter: Adwa AD8000.

Table 1. Analytical data for lignocellulosic biomasses.

Analysis	wt %	
	Sorghum	Corn straw
C	39.75	47.80
H	5.22	6.89
N	0.85	2.01
S	0.11	0.48
O	54.07	34.76
Moisture	8.11	8.10
Ash	8.39	8.06
Cellulose	46.63	49.96
Hemicellulose	12.54	15.47
Lignin	18.95	15.09

2.2. Experimental design and optimization

In this study the optimization approach provided by the Box–Behnken design (BBD, Design Expert 7.0.0). The effect of various factors include temperature, extraction time and solvent volume on the extraction of phenolics from lignocellulosic biomass were investigated. The effect of experimental parameters on extraction yield, total phenolic content and antioxidant activity was investigated by response surface methodology (RSM). One of the greatest advantages of this method is to empirically demonstrate the effect of multiple experimental factors on the extraction efficiency by carrying out a few experimental studies. The 15 experimental run were carried out in this study. All experiment runs were carried out at least in duplicate. The range of factors used in the experimental run are given in Table 2.

Table 2. The ranges and levels of the factors in the experimental design

Factors	Semb.	Ranges and Coded Levels		
		-1	0	1
Temp. (°C)	A	60,00	80,00	100,00
Solvent volume (1:1) mL	B	75,00	112,50	150,00
Time (min)	C	30,00	45,00	60,00

2.3. Analysis

Total phenolic content of extracts were determined by Folin–Ciocalteu assay [7]. 100 and 150 µL samples were mixed with 2.5 mL of 10 times diluted Folin–Ciocalteu reagent and 5 ml of a 20% (w/v) anhydrous sodium carbonate solution. The mixture was vortexed for 30 s and kept at room temperature for 2h. Absorbance at 760 nm was recorded using a UV-VIS spectrophotometer (Agilent-Cary60). Gallic acid was used as a standard for calibration curve. The total phenolic content was expressed as gallic acid equivalents (mg gallic acid/g biomass).

Antioxidant capacity analysis was performed immediately after extraction [8]. Briefly, 1 mM, 1.5 mL DPPH was mixed with 50 and 250 µL sample solution and incubated for 105 min in dark covered with aluminum foil. Decrease of absorbance was monitored at 515 nm against a blank on a UV-VIS spectrometer (Agilent UV-Cary60).

The percentage of inhibition was calculated by the following equation:

$$\text{Inhibition\%} = (\text{Absorbance of control} - \text{Absorbance of sample}) / \text{Absorbance of control} \times 100$$

BHT (butylhydroxytoluene) was used as an antioxidant reference, inhibition percentage of sample was calculated using the graph by plotting BHT concentration against inhibition percentage and the results were given as mg BHT equivalent /g biomass)

3. Results and Discussion

In this study, the extraction parameters such as extraction temperature, solvent volume and extraction time were applied for the extraction of corn straw and sorghum. The optimization model has been developed for the highest percentage of extraction, total phenolic content and antioxidant activity by applying a 3-factor and 3-level Box–Behnken design (BBD). The variance analysis (ANOVA) was used to analyze data. The statistical significance of the quadratic effects of each factor on the responses was determined by using the Fischer (F-test) test at 95% confidence level. It has been decided whether the proposed model is a fitting approach to the real response of the system, provided that the insignificant and regressing variation caused by "lack of fit" is significant at the 95% level of confidence. In addition, the fit of the model was tested using the regression squared (R^2), the adjusted R -squared (R_{adj}). Experimental design and responses of the dependent variables were given Table 3. And also, Table 4 shows variance analysis of responses.

3.1. Model equation for the extraction yield

As a result of experiments on the extraction of corn straw and sorghum which were made in accordance with experimental designs, the extraction yields were subjected to regression analysis and the following equations were obtained;

$$\begin{aligned} \text{Extraction Yield}_{(\text{corn straw})} = & +13.34 + 2.31A + 0.88B - 0.20C + 7.500 \times 10^{-003}AB + 0.11AC + 1.02BC \\ & - 2.04A^2 + 0.096B^2 + 0.57C^2 \end{aligned} \quad (\text{Eq.1})$$

$$\begin{aligned} \text{Extraction Yield}_{(\text{sorghum})} = & +16.81 + 1.28A + 0.16B + 0.068C + 0.34AB + 1.37AC + \\ & + 0.31BC + 0.46A^2 + 0.37B^2 - 0.62C^2 \end{aligned} \quad (\text{Eq.2})$$

As can be seen in Eq.1, the positive value of coefficient A (2.31) indicates that the corn straw extraction yield increases with increasing the temperature from 60 °C

to 100 °C. The extraction temperature is the most significant parameter on extraction. While the B coefficient, solvent volume, was positive (0.88), indicating that the extraction yield increased with increasing the amount of solvent, the extraction time, C, has a negative value (-0.20) shows that the extraction yield will decrease with increasing time.

The fit of the model can be tested using the regression squared (R^2). The values of R^2 and R_{adj} found as a result of the variance analysis were 0.9328 and 0.8120, respectively for corn straw. These values provide a suitable approach for the relationship between the independent variables and the extraction yield of the proposed equation. The values of R^2 and R_{adj} were 0.9264 and 0.7938, respectively for sorghum. It was observed that all coefficients were positive and positively contributed to the sorghum extraction yield (Eq.2).

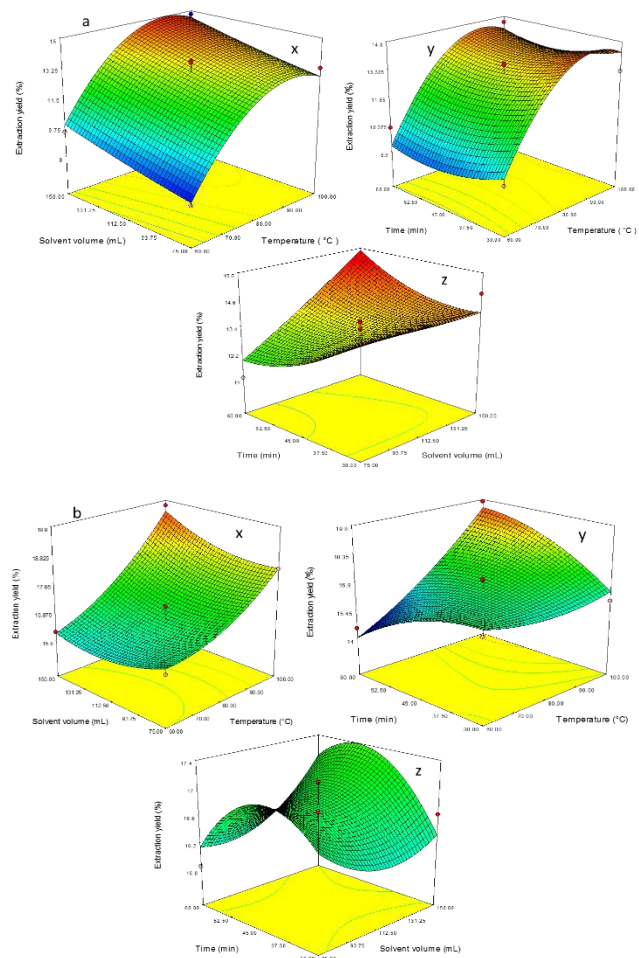


Fig.1. Response surface graphs for extraction yield a) corn straw b) sorghum

Table 3. Experimental design and responses of the dependent variables

Temperature (°C)	Solvent volume (1:1) mL	Time (min)	Corn Straw						Sorghum					
			Extraction yield		Total phenol content		Antioxidant activity		Extraction yield		Total phenol content		Antioxidant activity	
			Actual	Predicted	Actual	Predicted	Actual	Predicted	Actual	Predicted	Actual	Predicted	Actual	Predicted
80.00	112.50	45.00	13.59	13.34	3.47	3.59	2.15	2.42	17.09	16.81	7.53	8.16	16.66	16.64
80.00	75.00	30.00	14.88	14.35	2.73	3.06	1.85	1.97	17.16	16.64	6.35	6.92	11.33	14.24
80.00	150.00	60.00	15.18	15.71	5.46	5.13	3.54	3.42	16.57	17.09	8.40	7.84	22.60	19.69
60.00	112.50	60.00	10.24	9.25	3.16	3.19	2.90	2.99	14.55	14.06	6.64	6.75	8.88	10.91
80.00	75.00	60.00	11.09	11.90	2.48	2.50	1.44	1.29	15.86	16.15	5.83	6.09	6.27	6.14
100.00	75.00	45.00	13.28	12.82	2.42	2.12	1.52	1.49	18.39	18.42	6.53	6.07	4.23	3.35
60.00	75.00	45.00	8.04	8.21	2.11	2.06	1.61	1.67	16.34	16.53	5.45	5.09	6.42	4.52
80.00	112.50	45.00	13.67	13.34	3.64	3.59	2.69	2.42	16.25	16.81	8.59	8.16	17.32	16.64
60.00	112.50	30.00	9.51	9.87	2.52	2.24	2.57	2.39	16.34	16.66	6.77	6.57	7.86	6.85
100.00	150.00	45.00	14.77	14.60	4.52	4.57	2.91	2.85	19.61	19.41	8.64	9.01	6.92	8.82
100.00	112.50	60.00	14.46	14.10	2.95	3.23	2.16	2.34	19.69	19.36	6.76	6.96	4.55	5.56
100.00	112.50	30.00	13.28	14.27	3.65	3.62	2.80	2.71	16.00	16.49	9.85	9.75	11.78	9.75
80.00	150.00	30.00	14.89	14.07	4.02	4.00	2.39	2.54	16.63	16.33	9.88	9.62	11.58	11.71
60.00	150.00	45.00	9.50	9.96	2.90	3.20	2.97	3.00	16.20	16.17	6.14	6.60	9.20	10.08
80.00	112.50	45.00	12.77	13.34	3.65	3.59	2.41	2.42	17.10	16.81	8.36	8.16	15.95	16.64

Table 4. The variene analysis of responses

Responses		Sum of Squares	df	Mean Square	F Value	P Value Prob > F	
Corn straw	Extraction yield	71.03	9	7.89	7.72	0.0183	significant
	TPC	10.58	9	1.18	10.11	0.0101	significant
	BHT	4.85	9	0.54	8.94	0.0133	significant
Sorghum	Extraction yield	24.66	9	2.74	6.99	0.0227	significant
	TPC	25.92	9	2.88	6.58	0.0258	significant
	BHT	359.38	9	39.93	5.40	0.0389	significant

Response surface plots showing the effect of factors on extraction yield of corn straw and sorghum biomass presented in Fig. 1a and Fig. 1b. The interaction between solvent volume and extraction temperature at constant extraction time has a significant linear positive effect on corn straw extraction (Fig. 1.a.x). It was determined that the extraction yield of corn straw increased with increasing temperature. Similarly, when the effect of extraction time and temperature variables were examined, it was observed that the extraction time was not effective but the temperature was an important factor on the extraction yield of corn straw (Fig. 1.a.y). It has been found that maximum extraction yield will be achieved due to decrease in extraction time at constant temperature (Fig. 1.a.z). As presented Fig. 1.b.x, it was found that the temperature was an important factor for sorghum extraction yield and the solvent volume was not a significant factor on the sorghum extraction yield. Fig. 1.b.y shows the relationship between the extraction time and the temperature, it was observed that the sorghum extraction yield decreased due to the increase in the extraction time. It was seen that the maximum values for the extraction yield of sorghum was obtained when the time was 45-50 minutes, when the solvent volume was generally high at constant temperature.

3.2. Model equation for Total Phenolic Content (TPC)

The model equation for total phenolic content (TPC) obtained from the extractions of corn straw and sorghum show the total phenolic content (phenolic acids, polyphenols and flavonoids) value as a function of temperature, extraction time and solvent volume. The equations of the model are given below:

$$\begin{aligned} \text{TPC}_{(\text{corn straw})} \\ y = & +3.59 + 0.36A + 0.89B + 0.14C + 0.33AB - \\ & 0.33AC + 0.42BC - 0.60A^2 + 1.667 \times 10^{-003}B^2 + 0.084C^2 \end{aligned} \quad (\text{Eq.3})$$

$$\begin{aligned} \text{TPC}_{(\text{sorghum})} \\ y = & +8.16 + 0.85A + 1.11B - 0.65C + 0.36AB - 0.74AC - \\ & 0.24BC - 0.79A^2 - 0.68B^2 + 0.13C^2 \end{aligned} \quad (\text{Eq.4})$$

The R^2 and R_{adj} values of total phenolic content models of corn straw and sorghum extracts were 0.9229 and 0.8541 for corn straw and 0.9222 and 0.7821 for sorghum, respectively. When the model for corn straw was examined, it was observed temperature and solvent volume are significant model terms (Eq.3). The temperature and the solvent volume as well as the extraction time were found to be important model terms for sorghum (Eq.4).

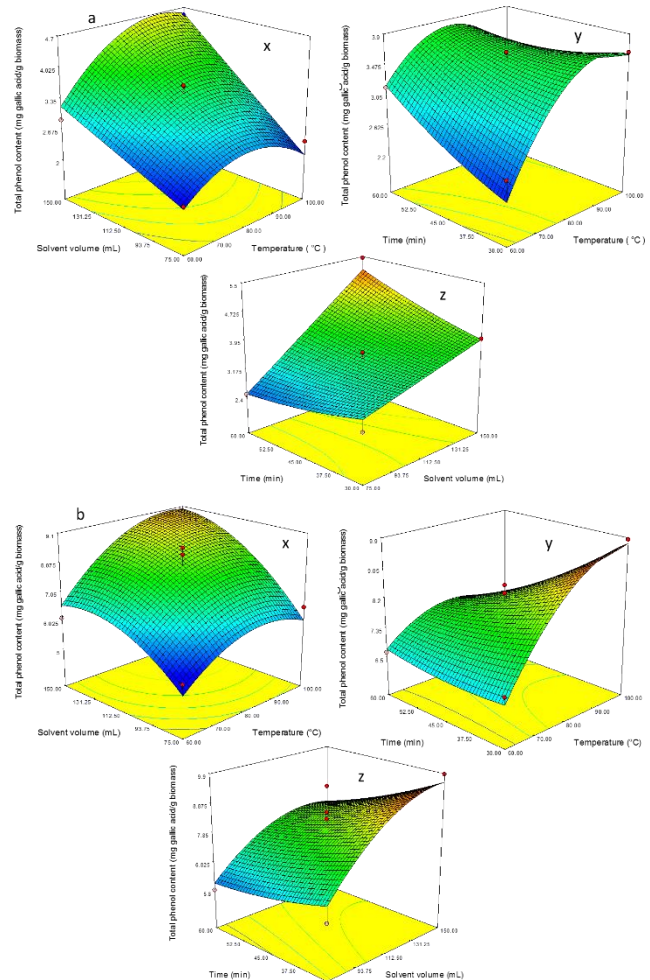


Fig. 2. Response surface graphs for total phenolic content a) corn straw b) sorghum

Figure 2 shows the three-dimensional graphs of the response surface of the total phenolic content values of corn straw and sorghum extracts against temperature, solvent volume and extraction time. When the total phenolic content value of corn straw extract was examined in terms of solvent volume and temperature factors, it was observed that the TPC value increased with increasing the amount of solvent, while the temperature was around 80 °C (Fig. 2.a.x). Some studies have shown that TPC values are lost because high temperatures damage the phenolic components [9-11]. The reason is explained by Prasad et al. (2011) as follow; the dielectric constant of the water at high temperature decreases and the solvent property changes and the phenolic substances can be extracted better [12]. High temperature also increases the solubility of phenolic substances, diffusion rate, extraction rate, decreases solvent viscosity and surface tension. However, high extraction temperatures can also lead to undesired results. For instance, degradation of phenolic substances arising from chemical and

enzymatic degradation or a reduction in total phenolic content is increased by the increase of the extraction temperature.

When the relationship between the extraction time and temperature were examined at a constant solvent volume, it was observed that the TPC was increased with an increasing of these two factors (Fig 2.a.y). Although TPC value of corn straw extract at a constant temperature increased with increasing solvent volume while extraction time did not change significantly (Fig 2.a.z). We have also examined the relation between solvent volume, extraction time and temperature on the value of total phenolic content of sorghum extract. The results showed that the TPC value increased while the amount of solvent and temperature increased at a constant extraction time (Fig. 2.b.x) On the other hand, we have found no significant effect of the extraction time on the TPC value while temperature increases (Fig.2.b.y). When we questioned the effect of solvent volume and extraction time, it was found that TPC value increased with increasing in amount of solvent and decreased with the increase in the extraction time (Fig.2.b.z). Some of the phenolic compounds are water-soluble, some are soluble in organic solvents and some are large insoluble polymers. For this reason, instead of using single solvent, a solvent with water and organic solvent mixture was used. The structure and composition of the material used, the type of heat treatment applied and the degree of temperature can lead to an increase in the amount of phenolic compounds [13]. It was seen that different results were obtained because of structural differences between corn straw and sorghum.

3.3. Model equation for antioxidant activity (BHT)

The equations of the model obtained as a result of the studies performed for the antioxidant activities of corn straw and sorghum extracts are given below;

Antioxidant activity (corn straw)

$$y = +2.42 - 0.083A + 0.67B + 0.054C + 7.500 \times 10^{-003}AB - 0.24AC + 0.39BC + 0.069A^2 - 0.23B^2 + 0.12C^2 \text{ (Eq.5)}$$

Antioxidant activity (sorghum)

$$y = +16.64 - 0.61A + 2.76B - 0.031C - 0.022AB - 2.06AC + 4.02BC - 7.31A^2 - 2.64B^2 - 1.06C^2 \text{ (Eq.6)}$$

The R^2 and R_{adj} values of antioxidant activities models of corn and sorghum extracts were 0.9415 ve 0.8361 for corn straw and 0.9068 ve 0.7390 for sorghum, respectively. Where R^2 is greater than 90%, the independent variables (temperature, solvent amount and extraction time) indicate that the value of antioxidant activity (BHT) is qualifiable. The effects of solvent amount on the antioxidant activity values of

corn straw and sorghum extracts were statistically significant. Solvent type and polarity are effective on single electron transfer and hydrogen atom transfer which are important in measuring antioxidant capacity [14]. There are different solvents used in the literature for antioxidant extraction. Solvents generally used in the extraction of medicinal herbs include methanol, ethanol, acetone, petroleum ether, hexane and their different concentrations.

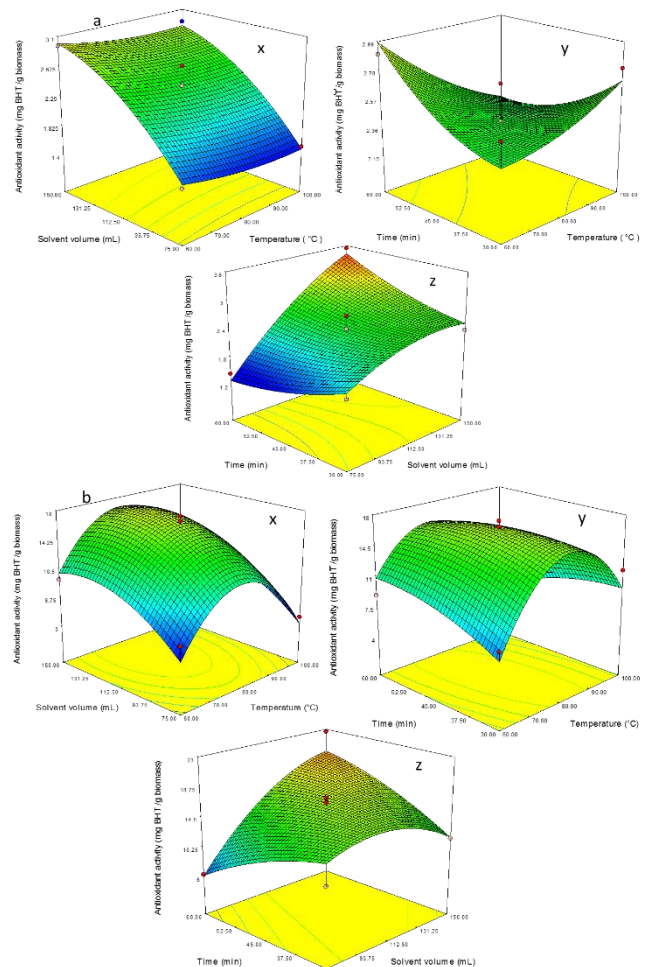


Fig. 3. Response surface graphs for antioxidant activity a) corn straw b) sorghum

Figure 3 shows the three-dimensional graphs of the response surface of the antioxidant activity values of corn straw and sorghum extracts against temperature, solvent amount and extraction time. When the antioxidant activity values of corn straw extracts were examined against the amount of temperature and solvent, antioxidant activity was directly affected by the amount of solvent (Fig 3.a.x). The change in temperature did not significantly affect the result. It can be said that the increase in the extraction time increases the antioxidant activity and decreases with the increase in temperature (Fig 3.a.y). According to Fig 3.a.z, the extraction time and the amount of solvent

had a positive effect on the antioxidant activity. The degree and time of the applied temperature can change the antioxidant properties (Calligaris ve ark., 2004). The Eq.5 and Eq.6 of antioxidant activities models of corn and sorghum extracts showed that the temperature has a negative effect on antioxidant activity.

This disparity may be attributed to differences in antioxidant capacity of phenolics. All phenolic compounds do not have same antioxidant capacity, for example tannins are known to have higher antioxidant activity as compared to other simple phenolics so increasing temperature not always resulted with increasing antioxidant capacity of extract despite of high levels of phenolics [15].

Some phenolic compounds and antioxidants can be destroyed and reduced by thermal treatment. In general, it is expected to decrease the amount of antioxidant activity and total phenolic content by thermal treatment [16]. When the surface graphs of the antioxidant activity for sorghum extracts were viewed, it was seen that the antioxidant activity increased to 80 °C and then started to decrease in Fig 3.b.x and Fig

3.b.y. Similar results have been found in other literature studies [17-20].

3.4. Verification experiments

The verification experiments were carried out using recommended optimal conditions derived from analysis of RSM for the factors; extraction temperature, extraction time and solvent volume. The experimental results were reasonably close to the predicted values verifying the validity of the RSM model (Table 3). The optimum extraction conditions to obtain high antioxidant yields with high antioxidant activities within the extraction parameters were: 77 °C (temperature), 150.0 mL (solvent volume), 60 min (time) and 90 °C (temperature), 150.0 mL (solvent) 50 min (time) for corn straw and sorghum, respectively. As shown in Table 5, predicted and experimental results were in harmony with each other. Therefore, it is suggested the models obtained can be used to optimise the process of antioxidant bioactive compounds extraction from lignocellulosics.

Table 5. The extraction yield, total phenol content and antioxidant activity found in recommended optimal conditions for corn straw and sorghum

Responses	Corn Straw		Sorghum	
	Predicted	Experimental	Predicted	Experimental
Extraction Yield (%)	15.39	14.31±1.32	18.45	19.49±1.55
TPC (mg gallic acid/g biomass)	5.08	4.32±0.28	8.60	8.59±0.32
Antioxidant activity (mg BHT /g biomass)	3.46	2.40±1.43	15.70	13.74±2.14

4. Conclusions

This study was designed to optimize extraction parameters on extraction yield, total phenol content and antioxidant activity from lignocellulosic biomass. A 3-factor and 3-level Box–Behnken design was applied to understand the effect extraction parameters (temperature, solvent volume and extraction time). The results showed that the extraction temperature was the main positive linear effect on extraction yield, the solvent volume and temperature were significant terms on total phenol content and the solvent amount has a linear positive effect for sorghum while it has quadratic effect for corn straw on antioxidant activity. The optimization model has been developed for the highest percentage of extraction, total phenol content and antioxidant activity. It was observed that recommended optimal conditions were in harmony with each other. With this study, it is thought that a standard for extraction of antioxidant plants which

have an important place in the field of medicine and pharmacy can be developed by using RSM.

Conflicts of interest

The authors state that did not have conflict of interests

References

- [1] Hall, III.C. :Source of natural antioxidants: oilseeds, nuts, cereals, legumes, animal products and microbial sources. Antioxidants in Food, Practical Applications, J Pokorny, N Yanislhlieva and M Gordon (eds), Cambridge: Woodhead Publishing Ltd., 2001; pp 169-219 .
- [2] Balasundram N., Sundram, K., Samman. S., Phenolic compounds in plants and agri-industrial by-products: Antioxidant activity, occurrence, and potential uses, *Food Chem.*, 99 (2006) 191–203.
- [3] Glasser W. G., Thermochemical biomass conversion processes are aimed for bio-fuels. In: Fundamentals of thermochemical biomass conversion, R. P. Overand, T. A. Mile, and L. K.

- Mudge (Eds.), New York: Elsevier Applied Science Publisher, 1985.
- [4] Icten O., Hydrogen Production from Sorghum by Aqueous Phase Reforming Process, Çukurova University, Master thesis, (2011).
- [5] Cardoso L.M., Montini T.A., Pinheiro S.S., Pinheiro-Sant'Ana H.M., Martino H.S.D., Moreira, A.V.B., Effects of processing with dry heat and wet heat on the antioxidant profile of sorghum, *Food Chem.*, 152 (2014) 210–217.
- [6] Liu H., Ou X., Yuan J., Yan X., Experience of producing natural gas from corn straw in China., *Resour Conserv Recy.*, 135 (2018) 216-224.
- [7] Caboni E., Tonelli M.G., Lauri P., Lacovacci P., Kevers C., Damiano C., Gaspar T., Biochemical aspects of almond microcuttings related to in vitro rooting ability, *Biol. Plant.*, 39 (1997) 91–97.
- [8] Prior R.L., Wu X., Schaich K., Standardized methods for the determination of antioxidant capacity and phenolics in foods and dietary supplements, *J Agr Food Chem.*, 53 (2005) 4290-4610.
- [9] Sun Y., Xu W., Zhang W., Hu Q., Zeng X., Optimizing the extraction of phenolic antioxidants from kudungcha made from Ilex kudingcha C.J. Tseng by using response surface methodology, *Sep Purif Technol.*, 78 (2011) 311–320.
- [10] Ballard T.S., Mallikarjunan P., Zhou K., O'Keefe S.F., Optimizing the extraction of phenolic antioxidants from peanut skins using response surface methodology, *J Agr Food Chem.*, 57 (2009) 3064–3072.
- [11] Cacace J., Mazza G., Optimization of extraction of anthocyanins from black currants with aqueous ethanol, *J Food Sci.*, 68(2003) 240–248.
- [12] Prasad K.N., Hassan F.A., Yang B., Kong K.W., Ramanan R.N., Azlan A., Ismail A., Response surface optimisation for the extraction of phenolic compounds and antioxidant capacities of underutilised *Mangifera pajang* Kosterm. Peels, *Food Chem.*, 128 (2011) 1121-1127.
- [13] Sakac M., Torbica A., Sedej I., Hadnadev M., Influence of breadmaking on antioxidant capacity of gluten free breads based on rice and buckwheat flours, *Food Res. Int.*, 44 (2011) 2806-2813.
- [14] Perez-Jimenez J. and Saura-Calixto F., Effect of solvent and certain food constituents on different antioxidant capacity assays, *Food Res. Int.*, 39 (2006) 791-800.
- [15] Dlamini N.R., Taylor J.R.N., Roon L.W., The effect of sorghum type and processing on the antioxidant properties of African sorghum-based foods, *Food Chem.*, 105 (2007) 1412–1419.
- [16] Raciye Meral., The Effects of Different Thermal Applications on Phenolics Compounds, Yüzüncü Yıl University, *Journal of The Institute of Natural & Applied Sciences* 21 (2016) 55-67.
- [17] Calligaris S., Manzocco L., Anese M., Nicoli M.C., Effect of heat-treatment on the antioxidant and pro-oxidant activity of milk, *Int. Dairy. J.*, 14 (2004) 421-427.
- [18] Choi Y., Lee S.M., Chun J., Lee H.B., Lee J., Influence of heat treatment on the antioxidant activities and polyphenolic compounds of Shiitake (*Lentinus edodes*) mushroom, *Food Chem.*, 99(2006) 381-387.
- [19] Gupta V., Nagar R., Effect of cooking, fermentation, dehulling and utensils on antioxidants present in pearl millet rabadi-a traditional fermented food, *J.Food.Sci. Technol.*, 47 (2010) 73-76.
- [20] Kim S.Y., Jeong S.M., Park W.P., Nam K.C., Ahna D.U., Lee S.C., Effect of heating conditions of grape seeds on the antioxidant activity of grape seed extract, *Food Chem.*, 97 (2006) 472-479.

Comparison of estimators under different loss functions for two-parameter bathtub - shaped lifetime distribution

Gülcan GENCER^{1*}  Kerem GENCER² 

¹ Selçuk University, Department of Statistics, Konya/TURKEY,

² Karamanoglu Mehmetbey University, Department of Computer Programming, Karaman/TURKEY,

Abstract

Chen is suggested a two-parameter distribution. This distribution can have increasing failure rate function or a bathtub-shaped that allows it to fit real lifetime data sets. The ML (Maximum Likelihood) and Bayes estimates of the parameters of Chen's distribution are constituted in this paper. The approximate values of Bayesian estimates are obtained by using the Tierney-Kadane approach. Two-parameter bathtub-shaped distribution's estimations are derived using Jeffrey's extension prior under General entropy, Squared and Linex loss functions. Besides, performances of ML and Bayes estimates are compared concerning MSE's (Mean Square Error) by using Monte Carlo simulation. As a result, it has been seen that approximate Bayes estimates obtained under linex loss function are better than others. Moreover, real data analysis for his distribution is presented.

Article info

History:

Received:29.01.2020

Accepted:01.07.2020

Keywords: Maximum Likelihood Estimation, Loss Functions, Bayes Estimation, Tierney Kadane's Approximation, Two-Parameter Bathtub-Shaped Lifetime Distribution.

1. Introduction

In this study, we have studied parameter estimation for a two-parameter lifetime distribution with either bathtub-shaped or increasing failure rate investigated by Chen [1]. Moreover, some distributions have been proposed with models for bathtub-shaped failure rates, such as Hjorth [2] and Mudholkar and Srivastava [3]. This distribution has been studied by many authors such as Sarhan et al. [4], Selim [5], Jung and Yung [6] Javadkhani et al. [7] and Faizan and Sana [8]. The new two-parameter lifetime distribution with increasing failure rate function bathtub-shaped compared with other models has some desirable properties, which has two parameters. For more details, see Lee et al. [9], Chen [1] and Wang [10]. In this paper, the cumulative distribution function (CDF), probability density function (pdf), reliability and hazard function of an X random variable having $\text{Chen}(\alpha, \beta)$ are as follows.

$$f(x) = \alpha\beta x^{\beta-1} \exp\left[\alpha\left(1 - \exp(x^\beta)\right) + x^\beta\right] \quad (1)$$

$$F(x) = 1 - \exp\left[\alpha\left(1 - \exp(x^\beta)\right)\right] \quad (2)$$

$$R(x) = \exp\left[\alpha\left(1 - \exp(x^\beta)\right)\right], \quad (3)$$

$$h(x) = \alpha\beta x^{\beta-1} \exp(x^\beta), \quad (4)$$

and where

*Corresponding author. Email address: gulcangencer@kmu.edu.tr

<http://dergipark.gov.tr/csj> ©2020 Faculty of Science, Sivas Cumhuriyet University

- if $\beta < 1$, $h(t)$ is bathtub function,
and
- if $\beta \geq 1$, $h(t)$ is increasing function.

The distribution has increasing failure rate function when $\alpha > 1$ and $\beta < 1$. Figure 1 present the failure rate functions for different values $\alpha = 2, \beta = 0.5, 1, 1.5$

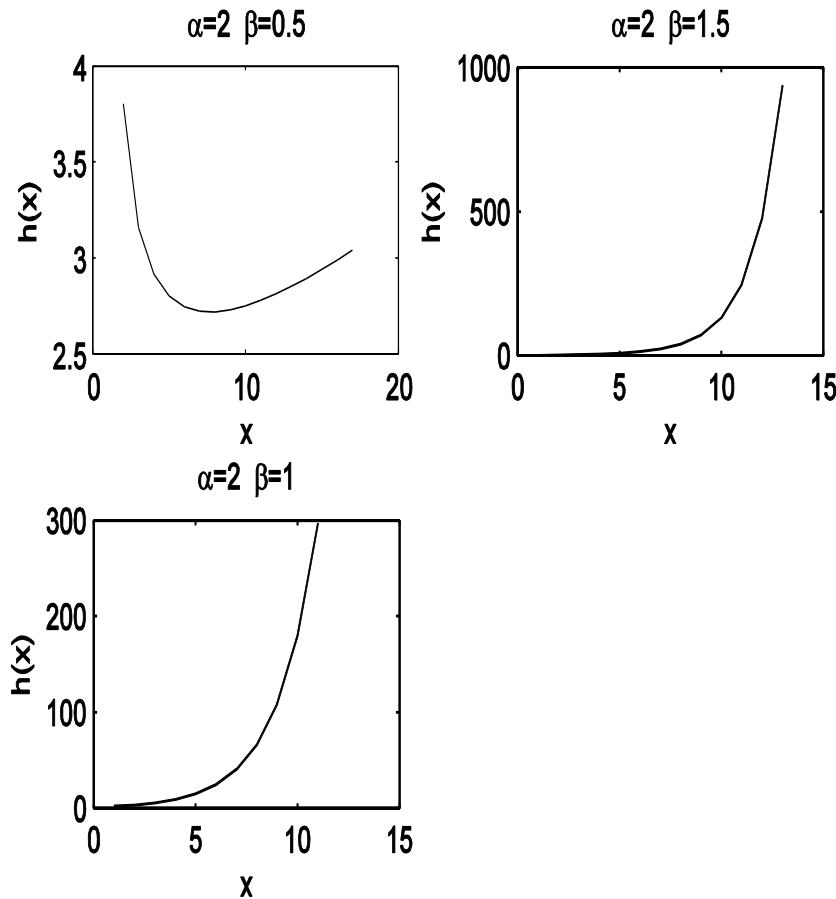


Figure 1. Failure rate functions of different parameters.

The primary objective of this study is to obtain the approximate Bayes estimators' samples under linex, general entropy and squared loss functions, following compare them in term of MSE's. The remaining text is arranged as follows. In Section 2, MLs for Chen distribution is given and the approximate Bayes estimators under different loss functions are derived by using Tierney's Kadane approximations. In section 4, using Monte Carlo simulation, Bayes estimations are compared with the ML in terms of MSE, and results are tabulated. A real data application is performed in Section 5. Finally, conclusion is given in the last section.

2. Methodology

2.1. Maximum likelihood estimation

Let X_1, X_2, \dots, X_n be the complete sample from independent random variables having Chen distribution with unknown α, β parameters. Then the log-likelihood function is given by,

$$L(\alpha, \beta | x) = \prod_{i=1}^n \alpha \beta \exp(x_i^\beta) \exp\left[\alpha \left(1 - e^{(x_i^\beta)}\right)\right] x_i^{\beta-1} \quad (5)$$

$$l(\alpha, \beta) = \ln\left(L(\alpha, \beta | x)\right) = n \ln \alpha + n \ln \beta + (\beta - 1) \sum_{i=1}^n \ln x_i + \sum_{i=1}^n x_i^\beta + \sum_{i=1}^n \alpha \left(1 - e^{(x_i^\beta)}\right) \quad (6)$$

Differentiating the log-likelihood function $\ell(\alpha, \beta | x)$ partially about unknown α, β parameters and after non-linear equations is attained. Newton-Raphson algorithm is one of the standard methods to determine the ML estimates of the two unknown parameters.

$$\frac{\partial l(\alpha, \beta)}{\partial \alpha} = 0 \Rightarrow \frac{n}{\alpha} + \sum_{i=1}^n \left(1 - e^{(x_i^\beta)}\right) = 0 \quad (7)$$

$$\frac{\partial l(\alpha, \beta)}{\partial \beta} = 0 \Rightarrow \frac{n}{\beta} + \sum_{i=1}^n (x_i^\beta \ln x_i) - \sum_{i=1}^n (\alpha x_i^\beta \ln x_i \exp(x_i^\beta)) + \sum_{i=1}^n (\ln x_i) = 0 \quad (8)$$

2.2. Bayesian estimation

For estimation of the parameters, prior distributions for these parameters is needed. In this study, as the prior distributions, Jeffrey's extension prior is used, and these are as follows [11].

$$\pi_1(\alpha) \propto \left(\frac{1}{\alpha}\right)^d \quad (9)$$

$$\pi_2(\beta) \propto \left(\frac{1}{\beta}\right)^d \quad (10)$$

The joint priors and posterior distributions of α, β parameters are

$$\pi(\alpha, \beta) \propto \left(\frac{1}{\alpha\beta}\right)^d \quad (11)$$

$$\begin{aligned} \pi(\alpha, \beta | x) &= \frac{f((\alpha, \beta); x)}{f(x)} \\ &= \frac{\alpha^n \beta^n \left(\exp \sum_{i=1}^n x_i^\beta\right) \exp\left[\sum_{i=1}^n \alpha (1 - \exp(x_i^\beta))\right] \prod_{i=1}^n x_i^{\beta-1} \left(\frac{1}{\alpha\beta}\right)^d}{\int_0^\infty \int_0^\infty \alpha^n \beta^n \left(\exp \sum_{i=1}^n x_i^\beta\right) \exp\left[\sum_{i=1}^n \alpha (1 - \exp(x_i^\beta))\right] \prod_{i=1}^n x_i^{\beta-1} \left(\frac{1}{\alpha\beta}\right)^d d\alpha d\beta} \end{aligned} \quad (12)$$

Squared error loss function is a symmetric function and introduced by Legendre [12] and Gauss [13]. Let any function of α and β be $s(\alpha, \beta) = s$.

The SLF is as follows:

$$Loss_1(\hat{s}_{Squared}, s) = (\hat{s}_{Squared} - s)^2 \quad (13)$$

The value which is minimize the expected value of SLF is expressed as,

$$\hat{s}_{Squared}(\alpha, \beta) = E[s(\alpha, \beta) | x] \quad (14)$$

In this case, Bayes estimator of $s(\alpha, \beta)$ under SLF is expressed as follows.

$$\hat{s}_{Squared}(\alpha, \beta) = E[s(\alpha, \beta) | x] = \frac{\int_0^\infty \int_0^\infty s(\alpha, \beta | x) e^{\left[\ell(\alpha, \beta | x) + \rho(\alpha, \beta)\right]} d\alpha d\beta}{\int_0^\infty \int_0^\infty e^{\left[\ell(\alpha, \beta | x) + \rho(\alpha, \beta)\right]} d\alpha d\beta} \quad (15)$$

where $\ell(\alpha, \beta | x)$ is a log-likelihood function, $\rho(\alpha, \beta | x)$ is the logarithm of joint prior distribution. The Linex loss function (LLF), which is an asymmetric function organized by Varian [14] and Zellner [15]. Let any function of α and β be $s(\alpha, \beta)$. LLF is defined as follows.

$$Loss_2(\Delta) \propto \exp(k\Delta) - k\Delta - 1; \quad k \neq 0, \quad (16)$$

where, $\Delta = \hat{s}(\alpha, \beta) - s(\alpha, \beta)$. Then, posterior mean of the linex loss function is given as:

$$E_\theta \left[Loss_2 \left(\hat{s} - s \right) \right] \propto \exp \left(k \hat{s} \right) E_\theta [\exp(-ks)] - k \left(\hat{s} - E_\theta(s) \right) - 1 \quad (17)$$

where $\hat{s} = \hat{s}(\alpha, \beta)$ and $s = s(\alpha, \beta)$. \hat{s}_{Linex} , which minimizes this posterior mean, is Bayes estimator of s and is expressed as,

$$\hat{s}_{Linex}(\alpha, \beta) = -\frac{1}{k} \ln E[\exp(-ks(\alpha, \beta)) | x] = -\frac{1}{k} \ln \left(\frac{\int_0^\infty \int_0^\infty \exp(-ks(\alpha, \beta)) e^{\left[\ell(\alpha, \beta | x) + \rho(\alpha, \beta)\right]} d\alpha d\beta}{\int_0^\infty \int_0^\infty e^{\left[\ell(\alpha, \beta | x) + \rho(\alpha, \beta)\right]} d\alpha d\beta} \right) \quad (18)$$

General entropy loss function (GLF) is an asymmetric function and suggested by Calabria and Pulcini [16]. Dey and Liao [17] studied with Bayes estimation under GLF. Let any function of α and β be $s(\alpha, \beta)$. GLF is denoted as,

$$Loss_3(\hat{s}, s) \propto \left(\frac{\hat{s}}{s} \right)^a - a \ln \left(\frac{\hat{s}}{s} \right) - 1 \quad (19)$$

Then, posterior mean of GLF is given as:

$$E_\theta \left[Loss_3 \left(\hat{s}, s \right) \right] \propto E \left(\frac{\hat{s}}{s} \right)^a - a E [\ln(\hat{s}) - \ln(s)] - 1 \quad (20)$$

where $\hat{s} = \hat{s}(\alpha, \beta)$ and $s = s(\alpha, \beta)$. Then, \hat{s}_{BGE} , which minimizes this posterior mean, is Bayes estimator of s and is expressed as follows.

$$s_{Entropy}^{\wedge}(\alpha, \beta) = \left\{ E \left\{ [s(\alpha, \beta)]^{-a} \middle| x \right\} \right\}^{-\frac{1}{a}}$$

$$= \left\{ \frac{\int_0^{\infty} \int_0^{\infty} [s(\alpha, \beta)]^{-a} e^{\left[\ell(\alpha, \beta | x) + \rho(\alpha, \beta) \right]} d\alpha d\beta}{\int_0^{\infty} \int_0^{\infty} e^{\left[\ell(\alpha, \beta | x) + \rho(\alpha, \beta) \right]} d\alpha d\beta} \right\}^{-\frac{1}{a}} \quad (21)$$

It is complicated to solve the equations (15), (18) and (21) in closed-form. Due to this reason, the Bayes Estimators of $s(\alpha, \beta)$ can be attained using Tierney-Kadane's approximation.

2.3. Tierney Kadane's approximation

Tierney and Kadane [18] are one of the most popular methods to find the approximate value of the mathematical explanations as to the odd of two integrals given in Equations (15), (18) and (21). This methods can be written as follows for a case with two parameters.

$$l(\alpha, \beta) = \frac{1}{n} \{ \rho(\alpha, \beta) + \ell(\alpha, \beta) \} \quad (22)$$

$$l^*(\alpha, \beta) = \frac{1}{n} \log s(\alpha, \beta) + l(\alpha, \beta) \quad (23)$$

where $s(\alpha, \beta)$ is any function of α and β , $\ell(\alpha, \beta | x)$ is defined in Eq., (6), $\rho(\alpha, \beta)$ is logarithm joint prior distribution and defined as follows.

$$\rho(\alpha, \beta) = \ln(\pi(\alpha, \beta)) = -m \ln(\alpha) - m \ln(\beta) \quad (24)$$

$$s_b^{\wedge}(\alpha, \beta) = E \left(s(\alpha, \beta) \middle| x \right) = \frac{\int e^{n l^*(\alpha, \beta)} d(\alpha, \beta)}{\int e^{n l(\alpha, \beta)} d(\alpha, \beta)}$$

$$= \left(\frac{\det \Sigma^*}{\det \Sigma} \right)^{1/2} \exp \left[n \left(l^*(\hat{\alpha}_l, \hat{\beta}_l) - l(\hat{\alpha}_l, \hat{\beta}_l) \right) \right] \quad (25)$$

Where $(\hat{\alpha}_l, \hat{\beta}_l)$ and $(\hat{\alpha}_l, \hat{\beta}_l)$ maximize $l^*(\alpha, \beta)$ and $l(\alpha, \beta)$, respectively. Σ^* And Σ are minus the inverse Hessians of $l^*(\alpha, \beta)$ and $l(\alpha, \beta)$ at $(\hat{\alpha}_l, \hat{\beta}_l)$ and $(\hat{\alpha}_l, \hat{\beta}_l)$. Σ is defined as,

$$\Sigma = \begin{bmatrix} -\partial^2 l / \partial \alpha^2 & -\partial^2 l / \partial \alpha \partial \beta \\ -\partial^2 l / \partial \alpha \partial \beta & -\partial^2 l / \partial \beta^2 \end{bmatrix}^{-1} \quad (26)$$

where l and partial derivatives are given as,

$$l(\alpha, \beta) = \frac{1}{n} \left[n \ln \alpha + n \ln \beta + (\beta - 1) \sum_{i=1}^n \ln x_i + \sum_{i=1}^n x_i^{\beta} + \sum_{i=1}^n \alpha \left(1 - e^{(x_i^{\beta})} \right) \right] - m \ln(\alpha) - m \ln(\beta) \quad (27)$$

$$\frac{\partial^2 \ell}{\partial \alpha^2} = \frac{1}{n} \left(-\frac{n}{\alpha^2} + \frac{m}{\alpha^2} \right) \quad (28)$$

$$\frac{\partial^2 \ell}{\partial \alpha \partial \beta} = \frac{1}{n} \sum_{i=1}^n \left(-x_i^{\beta} \ln x_i \exp(x_i^{\beta}) \right) \quad (29)$$

$$\frac{\partial^2 \ell}{\partial \beta^2} = \frac{1}{n} \left(-\frac{n}{\beta^2} + \frac{m}{\beta^2} + \sum_{i=1}^n \left(x_i^\beta \ln x_i^2 \right) + \sum_{i=1}^n \left(-\alpha x_i^\beta \ln x_i^2 \exp(x_i^\beta) - \alpha (x_i^\beta)^2 \ln x_i^2 \exp(x_i^\beta) \right) \right) \quad (30)$$

Bayes estimators for α, β parameters using Eq. (25) are found as follows.

i. If $s(\alpha, \beta) = \alpha$

$$\Sigma_1^* = \begin{bmatrix} -\partial^2 l_1^* / \partial \alpha^2 & -\partial^2 l_1^* / \partial \alpha \partial \beta \\ -\partial^2 l_1^* / \partial \alpha \partial \beta & -\partial^2 l_1^* / \partial \beta^2 \end{bmatrix}^{-1} \quad (31)$$

$$\hat{\alpha}_B = \left(\frac{\det \Sigma_1^*}{\det \Sigma} \right)^{1/2} \exp \left[n \left(l_1^* (\hat{\alpha}_{l_1}, \hat{\beta}_{l_1}) - l(\hat{\alpha}_l, \hat{\beta}_l) \right) \right] \quad (32)$$

where $l_1^*(\alpha, \beta) = \frac{1}{n} \log \alpha + l(\alpha, \beta)$.

The partial derivatives related to l_1^* are given as,

$$\frac{\partial^2 \ell_1^*}{\partial \alpha^2} = -\frac{1}{n\alpha^2} + \frac{1}{n} \left(-\frac{n}{\alpha^2} + \frac{m}{\alpha^2} \right) \quad (33)$$

$$\frac{\partial^2 \ell_1^*}{\partial \alpha \partial \beta} = -\frac{1}{n} \sum_{i=1}^n \left(x_i^\beta \ln x_i \exp(x_i^\beta) \right) \quad (34)$$

$$\frac{\partial^2 \ell_1^*}{\partial \beta^2} = \frac{1}{n} \left(-\frac{n}{\beta^2} + \frac{m}{\beta^2} + \sum_{i=1}^n \left(x_i^\beta \ln x_i^2 \right) + \sum_{i=1}^n \left(-\alpha x_i^\beta \ln x_i^2 \exp(x_i^\beta) - \alpha (x_i^\beta)^2 \ln x_i^2 \exp(x_i^\beta) \right) \right) \quad (35)$$

ii. If $s(\alpha, \beta) = \beta$

$$\Sigma_2^* = \begin{bmatrix} -\partial^2 l_2^* / \partial \alpha^2 & -\partial^2 l_2^* / \partial \alpha \partial \beta \\ -\partial^2 l_2^* / \partial \alpha \partial \beta & -\partial^2 l_2^* / \partial \beta^2 \end{bmatrix}^{-1} \quad (36)$$

$$\hat{\beta}_B = \left(\frac{\det \Sigma_2^*}{\det \Sigma} \right)^{1/2} \exp \left[n \left(l_2^* (\hat{\alpha}_{l_2}, \hat{\beta}_{l_2}) - l(\hat{\alpha}_l, \hat{\beta}_l) \right) \right] \quad (37)$$

where $l_2^*(\alpha, \beta) = \frac{1}{n} \ln \beta + l(\alpha, \beta)$. The partial derivatives related to l_2^* are given as,

$$\frac{\partial^2 \ell_2^*}{\partial \beta^2} = -\frac{1}{n\beta^2} + \frac{1}{n} \left(-\frac{n}{\beta^2} + \frac{m}{\beta^2} + \sum_{i=1}^n \left(x_i^\beta \ln x_i^2 \right) + \sum_{i=1}^n \left(-\alpha x_i^\beta \ln x_i^2 \exp(x_i^\beta) - \alpha (x_i^\beta)^2 \ln x_i^2 \exp(x_i^\beta) \right) \right) \quad (38)$$

$$\frac{\partial^2 \ell_2^*}{\partial \alpha \partial \beta} = -\frac{1}{n} \sum_{i=1}^n \left(x_i^\beta \ln x_i \exp(x_i^\beta) \right) \quad (39)$$

3. Simulation study

In this section, simulation study (based on 10000 replications) is performed to investigate the performance of the ML and Bayes estimators under loss functions in that their estimated risks. ML and approximate Bayes Estimators by Tierney-Kadane's approximation are attained under linex, general, and squared loss functions for Chen distribution. Finally, we obtained results to use Monte Carlo Simulation in the simulation study. It has been taken samples of size $n=30, 50$, and 100 from Chen Distribution. MSE is defined at follows:

Let θ be the true parameter value and $\hat{\theta}_i$ be the estimation value in i^{th} replication. Then the MSE can be written as,

$$MSE = \frac{1}{10000} \sum_{i=1}^{10000} (\hat{\theta}_i - \theta)^2 \quad (40)$$

The simulation steps are as follows.

Step 1 : It is generated data from Chen Distribution with $\alpha=0.3, \beta=0.6, d=1.5$, $\alpha=0.5, \beta=0.7, d=0.5$ parameters for the sample size $n=30, 50, 100$.

Step 2: ML estimates for α, β are computed by solution of non-linear Eqs.(7-8) by using Newton Raphson Method.

Step 3 : Tierney-Kadane Bayes estimates for α, β parameters under different loss functions.

Step 4 : MSE are computed over 10000 replications by using Eq.(40).

4. Real Data Application

Here we consider the real data of the amount of annual rainfall (in inches) recorded at the Los Angeles Civic Center for the 50 years, from 1959 to 2009. (see the website of Los Angeles Almanac: www.laalmanac.com/weather/we08aa.htm). This data set has been studied by [16]. This data set has been analyzed to compare the Chen distribution with other distributions such as, Exponential Poisson (EP) [17], ALT-Exponential [18]. Probability density functions of these distributions are given by,

$$f(x)_{ALT-Exp} = \begin{cases} \frac{\lambda \exp\left(-\frac{x}{\gamma}\right)}{\gamma \log(1+\lambda) \left(1 + \lambda \left(1 - \exp\left(-\frac{x}{\gamma}\right)\right)\right)} I_R(x), & \lambda > 0, \lambda \neq 0 \\ \frac{1}{\gamma} \exp\left(-\frac{x}{\gamma}\right), & \lambda = 0 \end{cases} \quad (41)$$

$$f(x)_{EP} = \frac{\lambda \beta}{1 - \exp(-\lambda)} \exp(-\lambda - \beta x + \lambda \exp(-\beta x)) \quad (42)$$

The data is given in Table 1:

Table 1. Real data of the amount of annual rainfall (in inches) recorded at the Los Angeles Civic Center

8.180	4.850	18.790	8.380	7.930	13.680	20.440	22.000	16.580	27.470	7.740	12.320	7.170	21.260	14.920	14.350
7.210	12.300	33.440	19.670	26.980	8.960	10.710	31.280	10.430	12.820	17.860	7.660	2.480	8.081	7.350	11.990
21.000	7.360	8.110	24.350	12.440	12.400	31.010	9.090	11.570	17.940	4.420	16.420	9.250	37.960	13.190	3.210
13.530	9.080														

AIC values and parameter estimates are given in Table 2.

Table 2. Parameter estimates and AIC values for amount of annual rainfall

Distributions	Parameter Estimations	AIC	-2ℓ
EP	$\hat{\lambda} = 5.6391$ $\hat{\beta} = 0.0139$	376.6237	372.6237
ALT-Exp	$\hat{\lambda} = -0.9659$ $\hat{\gamma} = 6.1265$	354.7464	350.7464
Chen	$\hat{\alpha} = 0.0228$ $\hat{\beta} = 0.4716$	352.2795	348.2795

Furthermore, fitted cdfs plots are presented Figure 2.

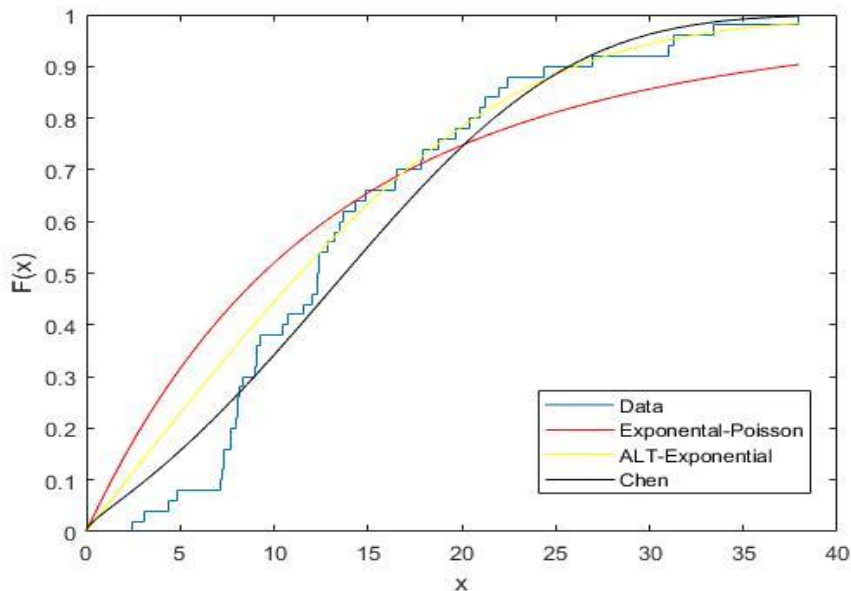


Figure 2. Fitted cdfs plots for amount of annual rainfall

5. Conclusion

As seen from Table 3-4, the performances of Bayes estimates for parameters for linex loss function are better than others regarding MSE's. Also, MSE's of ML and approximate Bayes estimates obtained under different loss functions are decreased when n is increased. Approximate Bayes estimators under LLF, GEL and SEL functions, obtained using the Tierney-Kadane method and ML's for Chen distribution with parameters are investigated. We found that Bayes estimates are superior to the corresponding ML's. The ML's of the unknown two parameters are computed by using the Newton Raphson method. The approximate estimators are compared with the ML's regarding MSE by using Monte Carlo simulation method. As a result, it has been seen that approximate Bayes estimates obtained under linex loss function are better than others. Moreover, a real data application is performed. We have concluded that the Chen distribution has to best fit other distributions according to AIC and -2ℓ .

Table 3. Mean Estimates and Mean Risk of ML's and Bayes Estimates for Chen Distribution ($\alpha=0.3, \beta=0.6, d=1.5$)

n	$\hat{\alpha}$	ML	Sq	Lin	Ent	ML	Sq	Lin	Ent
	$\hat{\beta}$	$k = -0.2, a = -0.3$				$k = -0.2, a = -0.3$			
30	α_{MSE}	0.036496	0.034277	0.007991	0.008813	0.036566	0.034335	0.007285	0.008312
	α_{ME}	0.469334	0.464269	0.463338	0.451248	0.468806	0.463751	0.464725	0.456754
	β_{MSE}	0.045399	0.041710	0.002406	0.003297	0.044800	0.041153	0.002204	0.003034
	β_{ME}	0.722669	0.711246	0.710468	0.705441	0.722169	0.710779	0.711356	0.707676
50	α_{MSE}	0.032192	0.031096	0.007202	0.008886	0.031451	0.030382	0.006492	0.008187
	α_{ME}	0.468114	0.465287	0.464730	0.457545	0.466363	0.463568	0.464125	0.459411
	β_{MSE}	0.021948	0.020653	0.001176	0.001884	0.021787	0.020510	0.001111	0.001783
	β_{ME}	0.677582	0.670943	0.670573	0.667976	0.676676	0.670063	0.670338	0.668473
100	α_{MSE}	0.029581	0.029116	0.006724	0.008983	0.029940	0.029470	0.006307	0.008419
	α_{ME}	0.466930	0.465626	0.465353	0.461798	0.008835	0.466902	0.467179	0.464840
	β_{MSE}	0.008760	0.008454	0.000475	0.000895	0.638284	0.635006	0.635118	0.634328
	β_{ME}	0.638561	0.635295	0.635161	0.634029	0.008835	0.008528	0.000467	0.000886

Table 4. Mean Estimates and Mean Risk of ML's and Bayes Estimates for Chen Distribution ($\alpha=0.5, \beta=0.7, d=0.5$)

n	$\hat{\alpha}$	ML	Sq	Lin	Ent	ML	Sq	Lin	Ent
	$\hat{\beta}$	$k = 0.6, a = 0.9$				$k = -0.6, a = -0.9$			
30	α_{MSE}	0.039525	0.035079	0.023698	0.097841	0.039666	0.035214	0.027175	0.116184
	α_{ME}	0.307212	0.319024	0.317330	0.303538	0.306991	0.318802	0.320275	0.317991
	β_{MSE}	0.024146	0.022595	0.008706	0.016173	0.023664	0.022156	0.007827	0.015459
	β_{ME}	0.736234	0.723560	0.721717	0.716852	0.735857	0.723191	0.724494	0.722846
50	α_{MSE}	0.036565	0.033940	0.022857	0.086401	0.036230	0.033619	0.025964	0.104714
	α_{ME}	0.312685	0.319802	0.318823	0.310570	0.012901	0.012708	0.004626	0.010706
	β_{MSE}	0.012534	0.012322	0.004575	0.010131	0.313620	0.320735	0.321634	0.320249
	β_{ME}	0.700241	0.692856	0.691968	0.689274	0.698462	0.691099	0.691799	0.690913
100	α_{MSE}	0.032944	0.031668	0.021317	0.074444	0.032971	0.031695	0.024481	0.093671
	α_{ME}	0.320800	0.324391	0.323904	0.319804	0.320732	0.324322	0.324781	0.324081
	β_{MSE}	0.007280	0.007476	0.002693	0.006893	0.007385	0.007579	0.002847	0.007647
	β_{ME}	0.665982	0.662368	0.662005	0.660786	0.665942	0.662327	0.662637	0.662245

ML:Maximum likelihood estimation. Sq:Bayes estimation under squared error loss function, Ent:Bayes estimation under general entropy loss function, Lin:Bayes estimation under linex loss function,

α_{MSE} : MSEs for α parameter, β_{MSE} : MSEs for β parameter

α_{ME} : Mean estimate for α parameter, β_{ME} : Mean estimate for β parameter

Conflicts of interest

There is no conflict of interest among the authors of the article.

References

- [1] Chen Z. M., A new two-parameter lifetime distribution with bathtub shape or increasing failure rate function, *Statistics & Probability Letters*, 49 (2), 2000, 155-161.
- [2] Hjorth U., A reliability distribution with increasing, decreasing, and bathtub-shaped failure rates,

Technometrics, 22 (1980) 99–107.

- [3] Mudholkar, G.S. and Srivastava, D.K., Exponentiated Weibull family for analyzing bathtub failure-rate data, *IEEE Trans. Rel.*, 42 (2) 1993 299–302.
- [4] Sarhan A.M., Hamilton D.C. and Smith, B., Parameter estimation for a two-parameter bathtub-shaped lifetime distribution, *Applied Mathematical Modelling*, 36(11) (2012) 5380-5392.
- [5] Selim M.A., Bayesian Estimations from the Two-Parameter Bathtub-Shaped Lifetime Distribution Based on Record Values, *Pakistan Journal of Statistics and Operation Research*, 8(2) (2012) 155-165.
- [6] Jung M. and Chung Y., Bayesian inference of three-parameter bathtub-shaped lifetime distribution. *Communications in Statistics Theory and Methods*, 47(17) (2018) 4229-4241.
- [7] Javadkhan N., Azhdari P. and Azimi R., On Bayesian estimation from two parameter Bathtub-Shaped lifetime distribution based on progressive first-failure-censored sampling, *International Journal of Scientific World*, 2 (1) (2014) 31-41.
- [8] Faizan M. and Sana, Bayesian Estimation and Prediction for Chen Distribution Based on Upper Record Values, *Journal of Mathematics and Statistical Science*, 6 (2018) 235-243.
- [9] Lee W. C., Wu J. W. and Yu, H. Y., Statistical inference about the shape parameter of the bathtub-shaped distribution under the failure-censored sampling plan, *Information and Management Sciences*, 18(2) (2007) 157-172.
- [10] Wang F. K., A note on a new two-parameter lifetime distribution with bathtub-shaped failure rate function, *International Journal of Reliability and Applications*, 3(1) (2002) 51-60.
- [11] Jeffreys H., Theory of Probability, Oxford at the Clarendon Press, 1948.
- [12] Legendre A., Nouvelles M'ethodes pour la D'etermination des Orbites des Com'etes, Paris: Courcier, 1805.
- [13] Gauss C.F., M'ethode des Moindres Carr'es. M'emoire sur la Combination des Observations, *Transl. J. Bertrand* (1955). Mallet-Bachelier, Paris, 1810.
- [14] Varian H. R., Variants in Economic Theory. Norhampton-USA: Edward Elgar, 2000.
- [15] Zellner A., Bayesian estimation and prediction using asymmetric loss functions, *Journal of the American Statistical Association*, 81(394) 1986, 446-451.
- [16] Asgharzadeh A., Abdi M. and Wu S.J., Interval estimation for the two-parameter bathtub-shaped lifetime distribution based on records, *Hacet. J. Math. Stat.*, 44 (2015) 399-416.
- [17] Kuş C., A new lifetime distribution, *Computational Statistics & Data Analysis*, 51 (9) (2007) 4497-4509.
- [18] Karakaya K., Kinaci I., Coşkun K. and Yunus A., A new family of distributions, *Hacettepe Journal of Mathematics and Statistics*, 46 (2) (2017) 303-314.



Neutrosophic triplets in some neutrosophic rings

Yılmaz ÇEVEN^{1,*} , Doğukan OZAN²

¹Süleyman Demirel University, Department of Mathematics, Isparta/ TURKEY

²Süleyman Demirel University, Graduate School of Natural and Applied Sciences, Isparta/ TURKEY

Abstract

In this paper, some mistakes about the neutrosophic triplets of some neutrosophic rings in the literature are pointed out and corrected. For this purpose, the neutrosophic triplets in neutrosophic rings $\langle Z \cup I \rangle$, $\langle Q \cup I \rangle$ and $\langle R \cup I \rangle$ where Z , Q and R denote the ring of integers, field of rationals and field of reals respectively are reinvestigated. It was claimed that $\langle Z \cup I \rangle$ has only trivial neutrosophic triplet in a paper which was recently published in Mathematics. But, as a result of the calculations, it was seen that $\langle Z \cup I \rangle$ has non-trivial neutrosophic triplets. Also neutrosophic triplets of the rings $\langle Q \cup I \rangle$ and $\langle R \cup I \rangle$ in the same literature was calculated incomplete.

Article info

History:

Received:05.02.2020

Accepted:20.07.2020

Keywords:

Neutrosophic ring,
Neutrosophic triplets,
Neutrosophic groups.

1. Introduction

The theories of neutrosophic set and neutrosophic triplets are introduced by F. Smarandache. The concept of neutrosophic set is a generalization of intuitionistic fuzzy sets [1]. F. Smarandache and M. Ali in [2, 3], for the first time, introduced the new notion of neutrosophic triplet group (NTG), which is another generalization of classical group. However, it is different from a group. In a NTG, the neutral element is different from the unit element of the classical group theory. By removing this restriction ([2,4]), it is defined neutrosophic extended triplet group (NETG) and the classical group is regarded as a special case of NETG. In [5], M. Ali, F. Smarandache and M. Khan introduced the concept of neutrosophic triplet ring and study some of its basic properties. Until now, for neutrosophic triplet group and neutrosophic triplet ring, some research articles (for example [3-7]) are published. But, at the same time, there are still some misunderstandings, mistakes about this new algebraic structure. In some papers, some authors clarified and corrected these misunderstandings and mistakes ([4,8,9]). This paper will clarify some misunderstandings, especially pointing out some erroneous conclusions in [7] and will try to give improved results.

2. Basic Concepts

In this section, we recall some of the basic concepts and properties associated with both neutrosophic triplets, neutrosophic groups and neutrosophic rings.

Definition 2.1 ([4]) Let N be a non-empty set together with a binary operation $*$. Then, N is called a neutrosophic extended triplet set if there exists a neutral of “a” (denoted by $\text{neut}(a)$) for any $a \in N$, and an opposite of “a” (denoted by $\text{anti}(a)$) for any $a \in N$, such that $\text{neut}(a) \in N$, $\text{anti}(a) \in N$ and

*Corresponding author. Email address: yilmazceven@sdu.edu.tr

<http://dergipark.gov.tr/csj> ©2020 Faculty of Science, Sivas Cumhuriyet University

$$a * \text{neut}(a) = \text{neut}(a) * a = a, \quad a * \text{anti}(a) = \text{anti}(a) * a = \text{neut}(a).$$

The triplet $(a, \text{neut}(a), \text{anti}(a))$ is called a neutrosophic extended triplet.

Definition 2.2 ([4]) Let $(N, *)$ be a neutrosophic extended triplet set. Then, N is called a neutrosophic extended triplet group (NETG), if the following conditions are satisfied:

- (1) $(N, *)$ is well-defined, i.e., $a * b \in N$, for all $a, b \in N$,
- (2) $(N, *)$ is associative, i.e., $(a * b) * c = a * (b * c)$ for all $a, b, c \in N$.

A NETG N is called a commutative NETG if $a * b = b * a$ for all $a, b \in N$.

Definition 2.3 ([5]) Let N be a neutrosophic extended triplet set together with two binary operations $*$ and $\#$. Then N is called a neutrosophic extended triplet ring (NETR) if the following conditions hold:

1. $(N, *)$ is a commutative neutrosophic triplet group,
2. $(N, \#)$ is well-defined and associative,
3. $a \# (b * c) = (a \# b) * (a \# c)$ and $(b * c) \# a = (b \# a) * (c \# a)$ for all $a, b, c \in N$.

Remark 1. A NETR in general is not a classical ring.

Let I denote the indeterminate which satisfies $I^2 = I$. \mathbb{Z} , \mathbb{Q} and \mathbb{R} denote the ring of integers, the field of rationals and the field of reals, respectively. The neutrosophic ring of integers, the field of neutrosophic rationals and the field of neutrosophic reals with usual addition and multiplication in all the three rings as the following, respectively:

$$\begin{aligned}\langle \mathbb{Z} \cup I \rangle &= \{a + bI : a, b \in \mathbb{Z}\}, \\ \langle \mathbb{Q} \cup I \rangle &= \{a + bI : a, b \in \mathbb{Q}\}, \\ \langle \mathbb{R} \cup I \rangle &= \{a + bI : a, b \in \mathbb{R}\}.\end{aligned}$$

3. Results and Discussion

In [7], the authors claimed that $\langle \mathbb{Z} \cup I \rangle$ has no non-trivial neutrosophic triplets. In this section, we find the neutrosophic triplets in rings $\langle \mathbb{Z} \cup I \rangle$, $\langle \mathbb{Q} \cup I \rangle$ and $\langle \mathbb{R} \cup I \rangle$. We see that $\langle \mathbb{Z} \cup I \rangle$ has non-trivial neutrosophic triplets.

Theorem 3.1 The neutrosophic triplets in ring $\langle \mathbb{Z} \cup I \rangle$ are as the following:

- i) $(0, 0, u + vI)$ where $u, v \in \mathbb{Z}$,
- (ii) $(I, I, u + (1 - u)I)$, $(-I, I, u - (1 + u)I)$ where $u \in \mathbb{Z}$,
- (iii) $(1, 1, 1)$ and $(-1, 1, -1)$,
- (iv) $(1 - 2I, 1, 1 - 2I)$ and $(-1 + 2I, 1, -1 + 2I)$,
- (v) $(1 - I, 1 - I, 1 + vI)$ and $(-1 + I, 1 - I, -1 + vI)$ for $v \in \mathbb{Z}$.

Proof. Let $a + bI \in \langle \mathbb{Z} \cup I \rangle$, $\text{neut}(a + bI) = x + yI$ and $\text{anti}(a + bI) = u + vI$ where $a, b, x, y, u, v \in \mathbb{Q}$. Then we have

$$(a + bI)(x + yI) = a + bI \tag{3.1}$$

and

$$(a + bI)(u + vI) = x + yI. \quad (3.2)$$

Using the Eq.(3.1), we get

$$ax = a \text{ and } ay + bx + by = b \quad (3.3)$$

and using the Eq. (3.2) we get

$$au = x \text{ and } av + bu + bv = y. \quad (3.4)$$

Hence we have the following cases:

a) If $a=0$ and $b=0$, using the Eqs. (3.3) and (3.4), we have $x=0, y=0$. Hence $\text{neut}(0+0I)=0+0I$ and $\text{anti}(0+0I)=u+vI$, where $u, v \in Z$. Then the elements $(0, 0, u+vI)$ where $u, v \in Z$ are neutrosophic triplets in $\langle Z \cup I \rangle$.

b) If $a=0$ and $b \neq 0$, using the Eqs. (3.3), (3.4), we have $x=0, y=1$ and $b(u+v)=1$. Hence $(b=1 \text{ and } v=1-u)$ or $(b=-1 \text{ and } v=-1-u)$. So we obtain $\text{neut}(I)=I$, $\text{anti}(I)=u+(1-u)I$, $\text{neut}(-I)=I$ and $\text{anti}(-I)=u-(1+u)I$ where $u \in Z$. Then the elements $(I, I, u+(1-u)I)$ and $(-I, I, u-(1+u)I)$ where $u \in Z$ are neutrosophic triplets in $\langle Z \cup I \rangle$.

c) If $a \neq 0$ and $b=0$, we have $x=1, y=0, v=0$ and $au=1$ using the Eqs. (3.3),(3.4). Hence it must be $a=u=1$ or $a=u=-1$. So we obtain $\text{neut}(1)=1$, $\text{anti}(1)=1$, $\text{neut}(-1)=1$ and $\text{anti}(-1)=-1$. Then the elements $(1,1,1)$ and $(-1,1,-1)$ are neutrosophic triplets in $\langle Z \cup I \rangle$.

d) Let $a \neq 0$ and $b \neq 0$. We have $x=1$ and $(a+b)y=0$ using the Eqs. (3.3). In this case, $y=0$ or $b=-a$.

d_i) If $y=0$, putting $x=1$ and $y=0$ in the Eqs. in (3.4), we get $au=1$ and $av+bu+bv=0$. Hence in case $a=u=1$ we have $b=v=-2$ and in case $a=u=-1$ we get $b=v=2$. So $(1-2I, 1, 1-2I)$ and $(-1+2I, 1, -1+2I)$ are neutrosophic triplets in $\langle Z \cup I \rangle$.

d_{ii}) If $b=-a$, putting $x=1$ and $b=-a$ in Eqs. in (3.4) we have $au=1$ and $y=-1$. Then neutrosophic triplets are $(1-I, 1-I, 1+vI)$ for $v \in Z$ when $a=u=1, y=-1$ and $(-1+I, 1-I, -1+vI)$ for $v \in Z$ when $a=u=-1, y=-1$.

Theorem 3.2 The neutrosophic triplets in the ring $\langle Q \cup I \rangle$ are as the following:

i) $(0, 0, u+vI)$ where $u, v \in Q$,

(ii) $(bI, I, u+vI)$ where $b \neq 0, u+v = \frac{1}{b}$ and $b, u, v \in Q$,

(iii) $\left(a, 1, \frac{1}{a}\right)$ where $a \neq 0$ and $a \in Q$,

(iv) $\left(a+bI, 1, \frac{1}{a} - \frac{b}{a(a+b)}I\right)$ where $a \neq 0, b \neq 0$ and $a+b \neq 0$,

(v) $\left(a-aI, 1-I, \frac{1}{a} + vI\right)$ where $a \neq 0, v \in Q$.

Proof. Let $a+bI \in Q \cup I$, $\text{neut}(a+bI)=x+yI$ and $\text{anti}(a+bI)=u+vI$ where $a, b, x, y, u, v \in Q$. Then the Eqs. (3.1)-(3.4) are true.

Hence we have the following cases:

a) If $a=0$ and $b=0$, using the Eqs. (3.3) and (3.4), we have $x=0, y=0$. Hence $\text{neut}(0+0I)=0+0I$ and $\text{anti}(0+0I)=u+vI$, where $u, v \in Q$. Then the elements $(0, 0, u+vI)$ where $u, v \in Q$ are neutrosophic triplets in $\langle Q \cup I \rangle$.

b) If $a=0$ and $b \neq 0$, using the Eqs. (3.3), (3.4), we have $x=0, y=1$ and $b(u+v)=1$. Hence we get $u+v=\frac{1}{b}$. So we obtain $\text{neut}(bI)=I$, $\text{anti}(bI)=u+vI$ where $u+v=\frac{1}{b}$. Then the elements $(bI, I, u+vI)$ where $u+v=\frac{1}{b}$ are neutrosophic triplets in $\langle Q \cup I \rangle$.

c) If $a \neq 0$ and $b=0$, we have $x=1, y=0, v=0$ and $au=1$ using the Eqs. (3.3), (3.4). Hence it must be $u=\frac{1}{a}$. So we obtain $\text{neut}(a)=1$, $\text{anti}(a)=\frac{1}{a}$. Then the elements $\left(a, 1, \frac{1}{a}\right)$ where $a \neq 0$ and $a \in Q$ are neutrosophic triplets in $\langle Q \cup I \rangle$.

d) Let $a \neq 0$ and $b \neq 0$. We have $x=1$ and $(a+b)y=0$ using the Eqs. (3.3). In this case, $y=0$ or $a+b=0$.

d_i) If $y=0$ and $a+b \neq 0$, putting $x=1$ and $y=0$ in the Eqs. in (3.4), we get $au=1$ and $av+bu+bv=0$. Hence we have $u=\frac{1}{a}$ and $v=-\frac{b}{a(a+b)}$. So $\text{neut}(a+bI)=1$ and $\text{anti}(a+bI)=\frac{1}{a}-\frac{b}{a(a+b)}I$. That is, the elements

$\left(a+bI, 1, \frac{1}{a}-\frac{b}{a(a+b)}I\right)$ where $a \neq 0, b \neq 0$ and $a+b \neq 0$ are neutrosophic triplets in $\langle Q \cup I \rangle$.

d_{ii}) If $b=-a$ and $y \neq 0$, putting $x=1$ and $b=-a$ in Eqs. in (3.4), we have $au=1$ and $y=-1$. Then neutrosophic triplets are $\left(a-aI, 1-I, \frac{1}{a}+vI\right)$ where $a \neq 0$.

Remark 3.3 According to Theorem 3.2 (v), Example 1 in [7] is missing. The elements $\left(a-aI, 1-I, \frac{1}{a}-\frac{1}{a}I\right)$ are neutrosophic triplets. But the elements $\left(a-aI, 1-I, \frac{1}{a}+vI\right)$ for $a, v \in Q$ and $a \neq 0$ which contain the elements $\left(a-aI, 1-I, \frac{1}{a}-\frac{1}{a}I\right)$ are neutrosophic triplets. According to Example 1 in [7], the element $\left(2-2I, 1-I, \frac{1}{2}+4I\right)$ is not a neutrosophic element. But this is a neutrosophic element. Also, since $a \in Q^*$, the elements $\left(a-aI, 1-I, \frac{1}{a}-\frac{1}{a}I\right)$ contain the elements $\left(\frac{1}{a}-\frac{1}{a}I, 1-I, a-aI\right)$. That is, no need to write the elements $\left(\frac{1}{a}-\frac{1}{a}I, 1-I, a-aI\right)$ as new neutrosophic triplets. Same is valid for $\left(aI, I, \frac{I}{a}\right)$ and $\left(\frac{I}{a}, I, aI\right)$, $\left(a+bI, 1, \frac{1}{a}-\frac{b}{a(a+b)}I\right)$ and $\left(\frac{1}{a}-\frac{b}{a(a+b)}I, 1, a+bI\right)$.

Remark 3.4 In $Q \cup I$, for any $0 \neq a \in Q$, $\text{neut}(a-aI)=1-I$ and $\text{anti}(a-aI)=\left\{\frac{1}{a}+vI : v \in Q\right\}$. Hence the collection of the neutrosophic triplets of $Q \cup I$ with neutral $1-I$ is the set

$$N = \left\{ \left(a-aI, 1-I, \frac{1}{a}+vI \right) : a, v \in Q \text{ and } a \neq 0 \right\}.$$

So the set M in Theorem 3 in [7] is not true. Actually $M \subset N$. The set N is not a group under component-wise product.

Theorem 3.5 The set of the neutrosophic triplets of $Z \cup I$ with neutral 1 is a commutative group of order 4 under component-wise product.

Proof. The set is

$$N = \{(1,1,1), (-1,1,-1), (1-2I,1,1-2I), (-1+2I,1,-1+2I)\}.$$

It is easily seen that the set N is closed under component-wise product. $(1,1,1)$ is the identity element, the inverse of every element is itself. Also, the set is associative.

In this paper, some mistakes about the neutrosophic triplets of neutrosophic rings in [7] are pointed out and corrected. For this purpose, the neutrosophic triplets in neutrosophic rings $\langle Z \cup I \rangle$, $\langle Q \cup I \rangle$ and $\langle R \cup I \rangle$ are reinvestigated. As a result of the calculations, it was seen that $\langle Z \cup I \rangle$ has non-trivial neutrosophic triplets. Also neutrosophic triplets of the rings $\langle Q \cup I \rangle$ and $\langle R \cup I \rangle$ in [7] was calculated incomplete. In this paper, we gave all neutrosophic triplets in those rings.

Conflicts of interest

The authors state that they did not have a conflict of interest.

References

- [1] Smarandache, F., Neutrosophic set-A generalization of the intuitionistics fuzzy sets, *Int. J. Pure Appl. Math.* 3 (2005) 287–297.
- [2] Smarandache, F., Neutrosophic Perspectives: Triplets, Duplets, Multisets, Hybrid Operators, Modal Logic, Hedge Algebras, and Applications, Brussels, Belgium: Pons Publishing House, 2017.
- [3] Smarandache, F. and Ali, M., Neutrosophic triplet group, *Neural Comput. Appl.* 29 (2018) 595–601.
- [4] Zhang, X., Hu, Q., Smarandache, F. and An, X., On Neutrosophic Triplet Groups: Basic Properties, NT-Subgroups, and Some Notes, *Symmetry*, 10 (2018).
- [5] Ali, M., Smarandache, F. and Khan, M., Study on the Development of Neutrosophic Triplet Ring and Neutrosophic Triplet Field, *Mathematics*, 6 (46) (2018)
- [6] Bal, M., Shalla, M.M., Olgun, N., Neutrosophic triplet cosets and quotient groups, *Symmetry*, 10 (2018) 126.
- [7] Kandasamy W. B., V., Kandasamy, I. and Smarandache, F., Neutrosophic Triplets in Neutrosophic Rings, *Mathematics*, 7 (2019) 563.
- [8] Çeven, Y., Smarandache, F., Correction: Ali, M., et al. Study on the Development of Neutrosophic Triplet Ring and Neutrosophic Triplet Field, *Mathematics*, 7 (2019) 565.
- [9] Smarandache, F., Ali, M., Neutrosophic Triplet Group (revisited), *Neutrosophic sets and Systems*, 26 (2019) 1-12.

Lacunary \mathcal{I} -invariant convergence

Uğur ULUSU^{1,*} , Fatih NURAY¹ 

¹ Afyon Kocatepe University, Department of Mathematics, Afyonkarahisar/TURKEY

Abstract

In this study, firstly, we introduce the notion of lacunary invariant uniform density of any subset E of the set \mathbb{N} (the set of all natural numbers). Then, as associated with this notion, we give the definition of lacunary \mathcal{I}_σ -convergence for real sequences. Furthermore, we examine relations between this new type convergence notion and the notions of lacunary invariant summability, lacunary strongly q -invariant summability and lacunary σ -statistical convergence which are studied in this area before. Finally, introducing the notions of lacunary \mathcal{I}_σ^* -convergence and \mathcal{I}_σ -Cauchy sequence, we give the relations between these notions and the notion of lacunary \mathcal{I}_σ -convergence.

Article info

History:

Received: 16.02.2020

Accepted: 26.06.2020

Keywords:

Lacunary sequence,
 \mathcal{I} -convergence,
Invariant convergence,
Statistical
convergence,
 \mathcal{I} -Cauchy sequence.

1. Introduction and Background

Let σ be a mapping such that $\sigma: \mathbb{N}^+ \rightarrow \mathbb{N}^+$ (the set of all positive integers). A continuous linear functional φ on ℓ_∞ , the space of real bounded sequences, is said to be an invariant mean or a σ -mean if it satisfies the following conditions:

- i. $\varphi(x_n) \geq 0$, when the sequence (x_n) has $x_n \geq 0$ for all $n \in \mathbb{N}$,
- ii. $\varphi(e) = 1$, where $e = (1, 1, 1, \dots)$ and
- iii. $\varphi(x_{\sigma(n)}) = \varphi(x_n)$ for all $(x_n) \in \ell_\infty$.

The mappings σ are assumed to be one-to-one and such that $\sigma^m(n) \neq n$ for all $m, n \in \mathbb{N}^+$, where $\sigma^m(n)$ denotes the m th iterate of the mapping σ at n . Thus, φ extends the limit functional on c , the space of convergent sequences, in the sense that $\varphi(x_n) = \lim x_n$ for all $(x_n) \in c$.

In the case σ is translation mappings $\sigma(n) = n + 1$, the σ -mean is often called a Banach limit.

The space V_σ , the set of bounded sequences whose invariant means are equal, can be shown that

$$V_\sigma = \left\{ (x_k) \in \ell_\infty : \lim_{m \rightarrow \infty} \frac{1}{m} \sum_{k=1}^m x_{\sigma^k(n)} = L, \text{ uniformly in } n \right\}.$$

Several authors studied on the notions of invariant mean and invariant convergent sequence (for examples, see [1-8]).

The notion of strongly σ -convergence (it is denoted by $[V_\sigma]$) was introduced by Mursaleen [9]. Then this notion, using a positive real number p , was generalized by Savaş [10] (it is denoted by $[V_\sigma]_p$).

By a lacunary sequence, we mean an increasing integer sequence $\theta = \{k_r\}$ such that

$$k_0 = 0 \text{ and } h_r = k_r - k_{r-1} \rightarrow \infty \text{ as } r \rightarrow \infty.$$

The intervals determined by θ is denoted by $I_r = (k_{r-1}, k_r]$ (see, [11]).

Throughout the study, $\theta = \{k_r\}$ will be taken as a lacunary sequence.

*Corresponding author. Email address: ulusu@aku.edu.tr

<http://dergipark.gov.tr/csj> ©2020 Faculty of Science, Sivas Cumhuriyet University

The set of lacunary strongly σ -convergence sequences was defined by Savaş [12] as below:

$$L_\theta = \left\{ (x_k): \lim_{r \rightarrow \infty} \frac{1}{h_r} \sum_{k \in I_r} |x_{\sigma^k(n)} - L| = 0, \text{ uniformly in } n \right\}.$$

Recently, Pancaroğlu and Nuray [13] defined the notions of lacunary invariant summability and lacunary strongly q -invariant summability as follows.

A sequence (x_k) is said to be lacunary invariant summable to L if

$$\lim_{r \rightarrow \infty} \frac{1}{h_r} \sum_{k \in I_r} x_{\sigma^k(n)} = L,$$

uniformly in n .

A sequence (x_k) is said to be lacunary strongly q -invariant summable ($0 < q < \infty$) to L if

$$\lim_{r \rightarrow \infty} \frac{1}{h_r} \sum_{k \in I_r} |x_{\sigma^k(n)} - L|^q = 0,$$

uniformly in n and it is denoted by $x_k \rightarrow L([V_{\sigma\theta}]_q)$.

The idea of statistical convergence was introduced by Fast [14] and then studied by several authors (for example, see [15-17]). In one of these studies, Savaş and Nuray [18] defined the notion of lacunary σ -statistical convergence as below.

A sequence (x_k) is said to be lacunary σ -statistical convergent to L if for every $\varepsilon > 0$,

$$\lim_{r \rightarrow \infty} \frac{1}{h_r} |\{k \in I_r: |x_{\sigma^k(n)} - L| \geq \varepsilon\}| = 0,$$

uniformly in n , where the vertical bars denote the number of elements in the enclosed set.

The idea of \mathcal{I} -convergence which is a generalization of the statistical convergence notion was introduced by Kostyrko et al. [19]. Some properties of this notion and similar notions which are noted following studied by several authors (for examples, see [20-22]).

A family of sets $\mathcal{I} \subseteq 2^{\mathbb{N}}$ is called an ideal iff

- i. $\emptyset \in \mathcal{I}$,
- ii. For each $E, F \in \mathcal{I}$, we have $E \cup F \in \mathcal{I}$,
- iii. For each $E \in \mathcal{I}$ and each $F \subseteq E$, we have $F \in \mathcal{I}$.

An ideal $\mathcal{I} \subseteq 2^{\mathbb{N}}$ is called non-trivial if $\mathbb{N} \notin \mathcal{I}$ and a non-trivial ideal $\mathcal{I} \subseteq 2^{\mathbb{N}}$ is called admissible if $\{n\} \in \mathcal{I}$ for each $n \in \mathbb{N}$.

All ideals in this study will be assumed to be admissible in $2^{\mathbb{N}}$ (the power set of \mathbb{N}).

An admissible ideal $\mathcal{I} \subset 2^{\mathbb{N}}$ has property (AP) if for every countable family of mutually disjoint sets $\{E_1, E_2, \dots\}$ belonging to \mathcal{I} , there exists a countable family of sets $\{F_1, F_2, \dots\}$ such that the symmetric differences $E_i \Delta F_i$ is a finite for each $i \in \mathbb{N}$ and $F = \bigcup_{i=1}^{\infty} F_i \in \mathcal{I}$.

A family of sets $\mathcal{F} \subseteq 2^{\mathbb{N}}$ is called a filter iff

- i. $\emptyset \notin \mathcal{F}$,
- ii. For each $E, F \in \mathcal{F}$, we have $E \cap F \in \mathcal{F}$,
- iii. For each $E \in \mathcal{F}$ and each $F \supseteq E$, we have $F \in \mathcal{F}$.

There is a filter $\mathcal{F}(\mathcal{I})$ corresponding with \mathcal{I} such that $\mathcal{F}(\mathcal{I}) = \{M \subset \mathbb{N}: (\exists E \in \mathcal{I})(M = \mathbb{N} \setminus E)\}$ for any ideal $\mathcal{I} \subseteq 2^{\mathbb{N}}$.

A sequence (x_k) is said to be \mathcal{J} -convergent to L if for every $\varepsilon > 0$, the set

$$E(\varepsilon) = \{k \in \mathbb{N} : |x_k - L| \geq \varepsilon\}$$

belongs to \mathcal{J} and it is denoted by $\mathcal{J} - \lim x_k = L$.

A sequence (x_k) is said to be \mathcal{J}^* -convergent to L if there exists a set $M = \{m_1 < m_2 < \dots < m_k < \dots\} \in \mathcal{F}(\mathcal{J})$ such that

$$\lim_{k \rightarrow \infty} x_{m_k} = L$$

and it is denoted by $\mathcal{J}^* - \lim x_k = L$.

The notions of \mathcal{J} -Cauchy sequence and \mathcal{J}^* -Cauchy sequence were introduced by Nabiev et al. [23]. Similar notions were studied in [24], too.

A sequence (x_k) is called an \mathcal{J} -Cauchy sequence if for every $\varepsilon > 0$, there exists an $N = N(\varepsilon) \in \mathbb{N}$ such that

$$F(\varepsilon) = \{k \in \mathbb{N} : |x_k - x_N| \geq \varepsilon\} \in \mathcal{J}.$$

A sequence (x_k) is called an \mathcal{J}^* -Cauchy sequence if there exists a set $M = \{m_1 < m_2 < \dots < m_k < \dots\} \in \mathcal{F}(\mathcal{J})$ such that

$$\lim_{k, p \rightarrow \infty} |x_{m_k} - x_{m_p}| = 0.$$

Lately, Nuray et al. [25] introduced the notions of \mathcal{J}_σ -convergence and \mathcal{J}_σ^* -convergence for real sequences. Also, they gave some relations between these notions and the notions which are studied in this area before.

2. Main Results

In this section, firstly, we introduce the notion of lacunary invariant uniform density of any subset E of the set \mathbb{N} . After that, associate with this notion, we give the definition of lacunary \mathcal{J}_σ -convergence for real sequences. Furthermore, we examine relations between this new type convergence notion and the notions of lacunary invariant summability, lacunary strongly q -invariant summability and lacunary σ -statistical convergence which are studied in this area before.

Definition 2.1 Let $\theta = \{k_r\}$ be a lacunary sequence, $E \subseteq \mathbb{N}$ and

$$s_r := \min_n \{|E \cap \{\sigma^m(n) : m \in I_r\}|\}, \quad S_r := \max_n \{|E \cap \{\sigma^m(n) : m \in I_r\}|\}.$$

If the following limits exist

$$\underline{V}_\theta(E) := \lim_{r \rightarrow \infty} \frac{s_r}{h_r} \quad \text{and} \quad \overline{V}_\theta(E) := \lim_{r \rightarrow \infty} \frac{S_r}{h_r},$$

then they are called a lower lacunary invariant uniform density and an upper lacunary invariant uniform density of the set E , respectively. If $\underline{V}_\theta(E) = \overline{V}_\theta(E)$, then $V_\theta(E) = \underline{V}_\theta(E) = \overline{V}_\theta(E)$ is called the lacunary invariant uniform density of the set E .

The class of all $E \subset \mathbb{N}$ with $V_\theta(E) = 0$ will be denoted by $\mathcal{J}_{\sigma\theta}$. Note that $\mathcal{J}_{\sigma\theta}$ is an admissible ideal.

Definition 2.2 A sequence (x_k) is lacunary \mathcal{J}_σ -convergent to L if for every $\varepsilon > 0$, the set

$$E(\varepsilon) := \{k \in \mathbb{N} : |x_k - L| \geq \varepsilon\}$$

belongs to $\mathcal{J}_{\sigma\theta}$, i.e., $V_\theta(E(\varepsilon)) = 0$ and we write $\mathcal{J}_{\sigma\theta} - \lim x_k = L$.

The class of all lacunary \mathcal{J}_σ -convergent sequences will be denoted by $\mathfrak{J}_{\sigma\theta}$.

It can be easily verified that if $\mathcal{J}_{\sigma\theta} - \lim x_k = L_1$ and $\mathcal{J}_{\sigma\theta} - \lim y_k = L_2$, then

- i. $\mathcal{J}_{\sigma\theta} - \lim (x_k + y_k) = L_1 + L_2$ and
- ii. $\mathcal{J}_{\sigma\theta} - \lim (\alpha x_k) = \alpha L_1$ (α is a constant).

Theorem 2.1 Let $(x_k) \in \ell_\infty$. If (x_k) is lacunary \mathcal{J}_σ -convergent to L , then this sequence is lacunary invariant summable to L .

Proof. Let $n \in \mathbb{N}$ be arbitrary and $\varepsilon > 0$. Also, we assume that $(x_k) \in \ell_\infty$ and (x_k) is lacunary \mathcal{J}_σ -convergent to L .

Now, we calculate

$$T_\theta(n) := \left| \frac{1}{h_r} \sum_{m \in I_r} x_{\sigma^m(n)} - L \right|.$$

For every $n = 1, 2, \dots$, we have

$$T_\theta(n) \leq T_\theta^{(1)}(n) + T_\theta^{(2)}(n),$$

where

$$T_\theta^{(1)}(n) := \frac{1}{h_r} \sum_{\substack{m \in I_r \\ |x_{\sigma^m(n)} - L| \geq \varepsilon}} |x_{\sigma^m(n)} - L|$$

and

$$T_\theta^{(2)}(n) := \frac{1}{h_r} \sum_{\substack{m \in I_r \\ |x_{\sigma^m(n)} - L| < \varepsilon}} |x_{\sigma^m(n)} - L|.$$

For every $n = 1, 2, \dots$, it is obvious that $T_\theta^{(2)}(n) < \varepsilon$. Since $(x_k) \in \ell_\infty$, there exists a $\lambda > 0$ such that

$$|x_{\sigma^m(n)} - L| \leq \lambda \quad (m \in I_r, n = 1, 2, \dots)$$

and so we have

$$\begin{aligned} T_\theta^{(1)}(n) &= \frac{1}{h_r} \sum_{\substack{m \in I_r \\ |x_{\sigma^m(n)} - L| \geq \varepsilon}} |x_{\sigma^m(n)} - L| \leq \frac{\lambda}{h_r} |\{m \in I_r : |x_{\sigma^m(n)} - L| \geq \varepsilon\}| \\ &\leq \lambda \frac{\max \{|\{m \in I_r : |x_{\sigma^m(n)} - L| \geq \varepsilon\}|\}}{h_r} \\ &= \lambda \frac{S_r}{h_r}. \end{aligned}$$

Hence, due to our assumption, the sequence (x_k) is lacunary invariant summable to L .

In general, the converse of Theorem 2.1 does not hold. For example, let (x_k) be the sequence defined as follows:

$$x_k := \begin{cases} 1 & , \quad \text{if } k_{r-1} < k < k_{r-1} + [\sqrt{h_r}] \text{ and } k \text{ is an even integer,} \\ 0 & , \quad \text{if } k_{r-1} < k < k_{r-1} + [\sqrt{h_r}] \text{ and } k \text{ is an odd integer.} \end{cases}$$

When $\sigma(n) = n + 1$, this sequence is lacunary invariant summable to $\frac{1}{2}$ but it is not lacunary \mathcal{J}_σ -convergent.

In [25], Nuray et al. gave some relations between the notions of \mathcal{J}_σ -convergence and $[V_\sigma]_p$ -convergence and they showed that these notions are equivalent for bounded sequences. Now, we will give analogous theorems which are state relations between the notions of lacunary \mathcal{J}_σ -convergence and lacunary strongly q -invariant summability, and we will show that these notions are equivalent for bounded sequences.

Theorem 2.2 If a sequence (x_k) is lacunary strongly q -invariant summable to L , then this sequence is lacunary \mathcal{I}_σ -convergent to L .

Proof. Let $0 < q < \infty$ and $\varepsilon > 0$. Also, we assume that $x_k \rightarrow L([V_{\sigma\theta}]_q)$. For every $n = 1, 2, \dots$, we have

$$\begin{aligned} \sum_{m \in I_r} |x_{\sigma^m(n)} - L|^q &\geq \sum_{\substack{m \in I_r \\ |x_{\sigma^m(n)} - L| \geq \varepsilon}} |x_{\sigma^m(n)} - L|^q \\ &\geq \varepsilon^q |\{m \in I_r : |x_{\sigma^m(n)} - L| \geq \varepsilon\}| \\ &\geq \varepsilon^q \max_n \{|\{m \in I_r : |x_{\sigma^m(n)} - L| \geq \varepsilon\}|\} \end{aligned}$$

and so

$$\begin{aligned} \frac{1}{h_r} \sum_{m \in I_r} |x_{\sigma^m(n)} - L|^q &\geq \varepsilon^q \frac{\max_n \{|\{m \in I_r : |x_{\sigma^m(n)} - L| \geq \varepsilon\}|\}}{h_r} \\ &= \varepsilon^q \frac{S_r}{h_r}. \end{aligned}$$

Hence, due to our assumption, $\mathcal{I}_{\sigma\theta} - \lim x_k = L$.

Theorem 2.3 Let $(x_k) \in \ell_\infty$. If (x_k) is lacunary \mathcal{I}_σ -convergent to L , then this sequence is lacunary strongly q -invariant summable to L .

Proof. Let $0 < q < \infty$ and $\varepsilon > 0$. Also, we assume that $(x_k) \in \ell_\infty$ and $\mathcal{I}_{\sigma\theta} - \lim x_k = L$. Since $(x_k) \in \ell_\infty$, there exists a $\lambda > 0$ such that $|x_{\sigma^m(n)} - L| \leq \lambda$ ($m \in I_r$, $n = 1, 2, \dots$) and so we have

$$\begin{aligned} \frac{1}{h_r} \sum_{m \in I_r} |x_{\sigma^m(n)} - L|^q &= \frac{1}{h_r} \sum_{\substack{m \in I_r \\ |x_{\sigma^m(n)} - L| \geq \varepsilon}} |x_{\sigma^m(n)} - L|^q + \frac{1}{h_r} \sum_{\substack{m \in I_r \\ |x_{\sigma^m(n)} - L| < \varepsilon}} |x_{\sigma^m(n)} - L|^q \\ &\leq \lambda \frac{\max_n \{|\{m \in I_r : |x_{\sigma^m(n)} - L| \geq \varepsilon\}|\}}{h_r} + \varepsilon^q \\ &\leq \lambda \frac{S_r}{h_r} + \varepsilon^q. \end{aligned}$$

Hence, due to our assumption, $x_k \rightarrow L([V_{\sigma\theta}]_q)$.

Theorem 2.4 Let $(x_k) \in \ell_\infty$. Then, (x_k) is lacunary \mathcal{I}_σ -convergent to L if and only if this sequence is lacunary strongly q -invariant summable to L .

Proof. This is an immediate consequence of Theorem 2.2 and Theorem 2.3.

Now, without proof, we will state a theorem that gives a relation between the notions of lacunary \mathcal{I}_σ -convergence and lacunary σ -statistical convergence.

Theorem 2.5 A sequence (x_k) is lacunary \mathcal{I}_σ -convergent to L if and only if this sequence is lacunary σ -statistical convergent to L .

Remark 2.1 By combining Theorem 2 in [18] and Theorem 5 in [25], we obtain that $\mathfrak{I}_{\sigma\theta} = \mathfrak{I}_\sigma$ for every lacunary sequence $\theta = \{k_r\}$, where \mathfrak{I}_σ is the class of all \mathcal{I}_σ -convergent sequences.

Finally, introducing the notions of lacunary \mathcal{I}_σ^* -convergence and lacunary \mathcal{I}_σ -Cauchy sequence, we will give the relations between these notions and the notion of lacunary \mathcal{I}_σ -convergence.

Definition 2.3 A sequence (x_k) is lacunary \mathcal{J}_σ^* -convergent to L if there exists a set $M = \{m_1 < m_2 < \dots < m_k < \dots\} \in \mathcal{F}(\mathcal{J}_{\sigma\theta})$ such that

$$\lim_{k \rightarrow \infty} x_{m_k} = L.$$

In this case, we write $\mathcal{J}_{\sigma\theta}^* - \lim x_k = L$.

Theorem 2.6 If a sequence (x_k) is lacunary \mathcal{J}_σ^* -convergent to L , then this sequence is lacunary \mathcal{J}_σ -convergent to L .

Proof. Let $\varepsilon > 0$. Also, we assume that $\mathcal{J}_{\sigma\theta}^* - \lim x_k = L$. Then, there exists a set $H \in \mathcal{J}_{\sigma\theta}$ such that for $M = \mathbb{N} \setminus H = \{m_1 < m_2 < \dots < m_k < \dots\}$ we have

$$\lim_{k \rightarrow \infty} x_{m_k} = L$$

and so there exists a $k_0 \in \mathbb{N}$ such that $|x_{m_k} - L| < \varepsilon$ for every $k > k_0$. Hence, it is obvious that for every $\varepsilon > 0$

$$E(\varepsilon) = \{k \in \mathbb{N} : |x_k - L| \geq \varepsilon\} \subset H \cup \{m_1 < m_2 < \dots < m_{k_0}\}.$$

Since $\mathcal{J}_{\sigma\theta} \subset 2^{\mathbb{N}}$ is admissible,

$$H \cup \{m_1 < m_2 < \dots < m_{k_0}\} \in \mathcal{J}_{\sigma\theta}$$

and so we have $E(\varepsilon) \in \mathcal{J}_{\sigma\theta}$. Consequently, $\mathcal{J}_{\sigma\theta} - \lim x_k = L$.

The converse of Theorem 2.6 holds if the ideal $\mathcal{J}_{\sigma\theta}$ has the property (AP).

Theorem 2.7 Let the ideal $\mathcal{J}_{\sigma\theta}$ be with the property (AP). If a sequence (x_k) is lacunary \mathcal{J}_σ -convergent to L , then this sequence is lacunary \mathcal{J}_σ^* -convergent to L .

Proof. Let the ideal $\mathcal{J}_{\sigma\theta}$ be with the property (AP) and $\varepsilon > 0$. Also, we assume that $\mathcal{J}_{\sigma\theta} - \lim x_k = L$. Then, for every $\varepsilon > 0$ we have

$$E(\varepsilon) = \{k \in \mathbb{N} : |x_k - L| \geq \varepsilon\} \in \mathcal{J}_{\sigma\theta}.$$

Denote E_1, E_2, \dots, E_n as following

$$E_1 := \{k \in \mathbb{N} : |x_k - L| \geq 1\} \text{ and } E_n := \left\{k \in \mathbb{N} : \frac{1}{n} \leq |x_k - L| < \frac{1}{n-1}\right\},$$

where $n \geq 2$ ($n \in \mathbb{N}$). Note that $E_i \cap E_j = \emptyset$ ($i \neq j$) and $E_i \in \mathcal{J}_{\sigma\theta}$ (for each $i \in \mathbb{N}$). Since $\mathcal{J}_{\sigma\theta}$ has the property (AP), there exists a set sequence $\{F_n\}_{n \in \mathbb{N}}$ such that the symmetric differences $E_i \Delta F_i$ are finite (for each $i \in \mathbb{N}$) and $F = \bigcup_{j=1}^{\infty} F_j \in \mathcal{J}_{\sigma\theta}$. Now, to complete the proof, it is enough to prove that

$$\lim_{\substack{k \rightarrow \infty \\ k \in M}} x_k = L, \tag{2.1}$$

where $M = \mathbb{N} \setminus F$. Let $\zeta > 0$. Choose $n \in \mathbb{N}$ such that $\frac{1}{n+1} < \zeta$. Then, we have

$$\{k \in \mathbb{N} : |x_k - L| \geq \zeta\} \subset \bigcup_{i=1}^{n+1} E_i.$$

Since the symmetric differences $E_i \Delta F_i$ ($i = 1, 2, \dots, n+1$) are finite, there exists a $k_0 \in \mathbb{N}$ such that

$$\left(\bigcup_{i=1}^{n+1} E_i\right) \cap \{k \in \mathbb{N} : k > k_0\} = \left(\bigcup_{i=1}^{n+1} F_i\right) \cap \{k \in \mathbb{N} : k > k_0\}. \tag{2.2}$$

If $k > k_0$ and $k \notin F$, then

$$k \notin \bigcup_{i=1}^{n+1} F_i \text{ and by (2.2) } k \notin \bigcup_{i=1}^{n+1} E_i.$$

This implies that

$$|x_k - L| < \frac{1}{n+1} < \zeta$$

and so (2.1) holds. Consequently, $\mathcal{J}_{\sigma\theta}^* - \lim x_k = L$.

Definition 2.4 A sequence (x_k) is a lacunary \mathcal{J}_{σ} -Cauchy sequence if for every $\varepsilon > 0$, there exists an $N = N(\varepsilon) \in \mathbb{N}$ such that the set

$$B(\varepsilon) = \{k \in \mathbb{N} : |x_k - x_N| \geq \varepsilon\}$$

belongs to $\mathcal{J}_{\sigma\theta}$, i.e., $V_{\theta}(B(\varepsilon)) = 0$.

Definition 2.5 A sequence (x_k) is a lacunary \mathcal{J}_{σ}^* -Cauchy sequence if there exists a set $M = \{m_1 < m_2 < \dots < m_k < \dots\} \in \mathcal{F}(\mathcal{J}_{\sigma\theta})$ such that

$$\lim_{k,p \rightarrow \infty} |x_{m_k} - x_{m_p}| = 0.$$

The proof of the following theorems are similar to the proof of theorems in [23], so we omit them.

Theorem 2.8 If a sequence (x_k) is lacunary \mathcal{J}_{σ} -convergent, then this sequence is a lacunary \mathcal{J}_{σ} -Cauchy sequence.

Theorem 2.9 If a sequence (x_k) is a lacunary \mathcal{J}_{σ}^* -Cauchy sequence, then this sequence is a lacunary \mathcal{J}_{σ} -Cauchy sequence.

Theorem 2.10 Let the ideal $\mathcal{J}_{\sigma\theta}$ be with the property (AP). Then, the notions of lacunary \mathcal{J}_{σ} -Cauchy sequence and lacunary \mathcal{J}_{σ}^* -Cauchy sequence coincide.

Acknowledgement

The work was supported by grants from AKUBAP (16.KARİYER.62).

Conflicts of interest

The authors state that did not have conflict of interests.

References

- [1] Raimi R.A., Invariant means and invariant matrix methods of summability, *Duke Math. J.*, 30(1) (1963) 81-94.
- [2] Schaefer P., Infinite matrices and invariant means. *Proc. Amer. Math. Soc.*, 36(1) (1972) 104-110.
- [3] Mursaleen M., On finite matrices and invariant means, *Indian J. Pure Appl. Math.*, 10 (1979) 457-460.
- [4] Savaş E., Strongly σ -convergent sequences, *Bull. Calcutta Math.*, 81 (1989) 295-300.
- [5] Mursaleen M. and Edely O.H.H., On the invariant mean and statistical convergence, *Appl. Math. Lett.*, 22(11) (2009) 1700-1704.
- [6] Başarır M. and Konca Ş., On some lacunary almost convergent double sequence spaces and Banach limits, *Abstr. Appl. Anal.*, 2012 (2012).
- [7] Pancaroğlu N. and Nuray F., On invariant statistically convergence and lacunary invariant statistical convergence of sequences of sets, *Prog. Appl. Math.*, 5(2) (2013) 23-29.
- [8] Nuray F. and Uluslu U., Lacunary invariant statistical convergence of double sequences of sets, *Creat. Math. Inform.*, 28(2) (2019) 143-150.
- [9] Mursaleen M., Matrix transformation between some new sequence spaces, *Houston J. Math.*, 9 (1983) 505-509.
- [10] Savaş E., Some sequence spaces involving invariant means, *Indian J. Math.*, 31 (1989) 1-8.
- [11] Fridy J.A., and Orhan C., Lacunary statistical convergence, *Pacific J. Math.*, 160(1) (1993) 43-51.
- [12] Savaş E., On lacunary strong σ -convergence, *Indian J. Pure Appl. Math.*, 21(4) (1990) 359-365.
- [13] Pancaroğlu N. and Nuray F., Statistical lacunary invariant summability, *Theoretical Math. Appl.*, 3(2) (2013)

71-78.

- [14] Fast H., Sur la convergence statistique, *Colloq. Math.*, 2(3-4) (1951) 241-244.
- [15] Šalát T., On statistically convergent sequences of real numbers, *Math. Slovaca*, 30(2) (1980) 139-150.
- [16] Fridy J.A., On statistical convergence, *Analysis*, 5(4) (1985) 301-314.
- [17] Rath D. and Tripathy B.C., On statistically convergent and statistically Cauchy sequences, *Indian J. Pure Appl. Math.*, 25(4) (1994) 381-386.
- [18] Savaş E. and Nuray F., On σ -statistically convergence and lacunary σ -statistically convergence, *Math. Slovaca*, 43(3) (1993) 309-315.
- [19] Kostyrko P., Šalát T. and Wilczyński W., \mathcal{I} -convergence, *Real Anal. Exchange*, 26(2) (2000) 669-686.
- [20] Kostyrko P., Macaj M., Šalát T., Sleziak M., \mathcal{I} -convergence and external \mathcal{I} -limits points, *Math. Slovaca*, 55 (2005) 443-464.
- [21] Sever Y., Ulus U. and Dündar E., On strongly \mathcal{I} and \mathcal{I}^* -lacunary convergence of sequences of sets, *AIP Conf. Proc.*, 1611(1) (2014) 357-362.
- [22] Konca Ş., Weighted lacunary \mathcal{I} -statistical convergence, *Iğdır Univ. J. Inst. Sci. & Tech.*, 7(1) (2017) 267-277.
- [23] Nabiev A., Pehlivan S. and Gürdal M., On \mathcal{I} -Cauchy sequences, *Taiwanese J. Math.*, 11(2) (2007) 569-576.
- [24] Dems K., On \mathcal{I} -Cauchy sequences, *Real Anal. Exchange*, 30(1) (2004) 123-128.
- [25] Nuray F., Gök H., Ulus U., \mathcal{I}_σ -convergence, *Math Commun.*, 16 (2011) 531-538.

On some geometric properties of normalized Wright functions

Evrir TOKLU^{1,*} , Neslihan KARAGÖZ² 

¹ Department of Mathematics, Ağrı İbrahim Çeçen University, Ağrı, TURKEY

² Graduate School of Naturel and Applied Science, Ağrı İbrahim Çeçen University, Ağrı, TURKEY

Abstract

The main purpose of the present paper is to determine the radii of lemniscate starlikeness, lemniscate convexity, Janowski starlikeness and Janowski convexity of normalized Wright functions. The key tools in the proof of our main results are the infinite product representation of Wright function and some properties of real zeros of Wright function and its derivative.

Article info

History:

Received:19.03.2020

Accepted:24.08.2020

Keywords:

Wright function,
radii of lemniscate
starlikeness and
convexity,
radii of Janowski
starlikeness and
convexity.

1. Introduction and Main Results

By \mathbb{D}_r we mean the open disk $\{z \in \mathbb{C} : |z| < r\}$ with the radius $r > 0$ and let $\mathbb{D} = \mathbb{D}_1$. Let $f: \mathbb{D}_r \rightarrow \mathbb{C}$ be the function defined by

$$f(z) = z + \sum_{n \geq 2} a_n z^n \quad (1)$$

where r is less or equal than the radius of convergence of the above power series. Let \mathcal{A} denote the class of all functions $f(z)$ of the form (1) which are analytic and normalized by the conditions $f(0) = f'(0) - 1 = 0$ in the open disk \mathbb{D}_r . By \mathcal{S} we mean the subclass of \mathcal{A} consisting of functions which are univalent in \mathbb{D}_r . A function $f \in \mathcal{A}$ is said to be starlike function if $f(\mathbb{D}_r)$ is starlike domain with the respect to the origin, meaning that for each $z \in \mathbb{D}_r$ the segment between the origin and $f(z)$ lie in $f(\mathbb{D}_r)$. Moreover, the function f , defined by (1), is said to be convex function in \mathbb{D}_r if f is univalent in \mathbb{D}_r , and the image domain $f(\mathbb{D}_r)$ is a convex domain, meaning that it is starlike domain with respect to each of its points. A function $f \in \mathcal{A}$ is subordinate to a function $g \in \mathcal{A}$, written as $f(z) \prec g(z)$, if there exist a Schwarz function w with $w(0) = 0$ and $|w(z)| < 1$ such that $f(z) = g(w(z))$. In addition, we know that if g is a univalent function, then $f(z) \prec g(z)$ if and only if $f(0) = g(0)$ and $f(\mathbb{D}) \subset g(\mathbb{D})$. It is clear that various subclasses of starlike and convex functions can be unified by using the concept of subordination. Let φ be analytic function, then by $S^*(\varphi)$ we mean the class of all analytic functions satisfying $1 + \frac{zf'(z)}{f(z)} \prec \varphi(z)$. Moreover, we denote the class of all analytic functions satisfying $1 + \frac{zf''(z)}{f'(z)} \prec \varphi(z)$ by $\mathcal{K}(\varphi)$. It is worth mentioning that these classes give a unified presentation of several famous subclasses of starlike and convex functions. For instance, if we take $\varphi(z) = \sqrt{1+z}$, we get the classes of lemniscate starlike and lemniscate convex functions denoted by $S_L^* := S^*(\sqrt{1+z})$ and $\mathcal{K}_L := \mathcal{K}(\sqrt{1+z})$, respectively. Lemniscate starlike functions introduced and investigated by Sokół and Stankiewicz [15].

We denote the radius of lemniscate starlikeness of function f by the real number

$$r_L^*(f) = \sup \left\{ r > 0 \mid \left| \left(\frac{zf'(z)}{f(z)} \right)^2 - 1 \right| < 1 \text{ for } z \in \mathbb{D}_r, 0 \leq r \leq 1 \right\}.$$

In addition, the radius of lemniscate convexity of function f is given by the real number

*Corresponding author. Email address: evrintoklu@gmail.com

$$r_L^c(f) = \sup \left\{ r > 0 \mid \left| \left(\frac{zf''(z)}{f'(z)} \right)^2 - 1 \right| < 1 \text{ for } z \in \mathbb{D}_r, 0 \leq r \leq 1 \right\}.$$

If we take $\varphi(z) = \frac{1+Az}{1+Bz}$ for $-1 \leq B < A \leq 1$, we have the classes of Janowski starlike and Janowski convex functions denoted by $S^*[A, B] := S^*\left(\frac{1+Az}{1+Bz}\right)$ and $\mathcal{K}[A, B] := \mathcal{K}\left(\frac{1+Az}{1+Bz}\right)$, respectively. Recall here that Janowski function is defined in the form $\frac{1+Az}{1+Bz}$ for $-1 \leq B < A \leq 1$. For comprehensive knowledge on Janowski starlike and Janowski convex functions one may refer to [10].

The real number

$$r_{A,B}^*(f) = \sup \left\{ r > 0 \mid \left| \frac{\left(\frac{zf'(z)}{f(z)} \right) - 1}{A - B \left(\frac{zf'(z)}{f(z)} \right)} \right| < 1 \text{ for } z \in \mathbb{D}_r, 0 \leq r \leq 1 \right\}$$

is called as the radius of Janowski starlikeness of the function f .

Moreover, the real number

$$r_{A,B}^c(f) = \sup \left\{ r > 0 \mid \left| \frac{\frac{zf''(z)}{f'(z)}}{A - B \left(1 + \frac{zf''(z)}{f'(z)} \right)} \right| < 1 \text{ for } z \in \mathbb{D}_r, 0 \leq r \leq 1 \right\}$$

is called as the radius of Janowski convexity of the function f .

Because of the fact that special functions play a key role in solving many problems in mathematics, applied mathematics and physics they have received a great deal of attention by many researchers from geometric function theory field (see the recent papers [1-5,7,9,17] and the references therein). In addition, for comprehensive knowledge on the radius problems of some special functions, one may consult on the works [6,10,13,16,18]. Recently, in [14] the authors investigated some geometric properties such that the radii of lemniscate starlikeness and lemniscate convexity, Janowski starlikeness and Janowski convexity of Bessel functions.

Inspired by the above mentioned papers, our main goal in the present paper is to ascertain the radii of starlikeness and convexity associated with lemniscate of Bernoulli and the Janowski function of normalized Wright functions.

Let us take a look the Wright function represented by

$$\phi(\rho, \beta, z) = \sum_{n \geq 0} \frac{z^n}{n! \Gamma(n\rho + \beta)},$$

where $\rho > -1$ and $z, \beta \in \mathbb{C}$. For further knowledge on Wright function one may refer to the studies [11] and [19]. Furthermore, it is worth mentioning here that Wright function is an entire function of z for $\rho > -1$. This means that some properties of the entire functions can be also used for Wright function.

With the aid of [9] we know that if $\rho > 0$ and $\beta > 0$, then the function $z \mapsto \lambda_{\rho, \beta}(z) = \phi(\rho, \beta, -z^2)$ has infinitely many zeros which are all real. If we denote the n th positive zero of the function $z \mapsto \phi(\rho, \beta, -z^2)$ by $\lambda_{\rho, \beta, n}$, under the same conditions the infinite product representation

$$\Gamma(\beta) \phi(\rho, \beta, -z^2) = \prod_{n \geq 1} \left(1 - \frac{z^2}{\lambda_{\rho, \beta, n}^2} \right) \quad (2)$$

holds, and this product is uniformly convergent on compact subsets of the complex plane. Moreover, let $\zeta'_{\rho, \beta, n}$ be the n th positive zero of $\Psi'_{\rho, \beta}$, where $\Psi_{\rho, \beta}(z) = z^\beta \lambda_{\rho, \beta}(z)$, then between any two positive zeros of $\lambda_{\rho, \beta}$ (or the positive real zeros of the function $\Psi_{\rho, \beta}$) there must be precisely one of $\Psi'_{\rho, \beta}$. That is, the zeros satisfy the following inequalities

$$\zeta'_{\rho, \beta, 1} < \lambda_{\rho, \beta, 1} < \zeta'_{\rho, \beta, 2} < \lambda_{\rho, \beta, 2} < \dots$$

We can readily observe that the function $z \mapsto \phi(\rho, \beta, -z^2)$ is not included in the class \mathcal{A} , and thus first we perform some natural normalization. Now we deal with three functions deriving from $\phi(\rho, \beta, \cdot)$:

$$f_{\rho,\beta}(z) = \left(z^\beta \Gamma(\beta) \phi(\rho, \beta, -z^2) \right)^{\frac{1}{\beta}}, \quad (3)$$

$$g_{\rho,\beta}(z) = z \Gamma(\beta) \phi(\rho, \beta, -z^2), \quad (4)$$

$$h_{\rho,\beta}(z) = z \Gamma(\beta) \phi(\rho, \beta, -z). \quad (5)$$

Clearly these functions are in the class \mathcal{A} . There is no doubt it is possible to obtain infinitely many other normalizations, that is the reason why we focus on the above mentioned ones is the fact that we oftenly encounter with their particular cases in terms of Bessel functions in the literature.

1.1. Lemniscate starlikeness and lemniscate convexity of normalized Wright functions

In the present section we deal with the radii of starlikeness and convexity associated with lemniscate of Bernoulli of the normalized Wright functions. It is important to emphasize here that it is said to be lemniscate starlike of a normalized analytic function f if the quantity $\frac{zf'(z)}{f(z)}$ lies in the region bounded by the right half of the lemniscate of Bernoulli $|w^2 - 1| = 1$.

Theorem 1. Let $\rho > 0$ and $\beta > 0$. Then the following assertions are valid.

- a. The radius of lemniscate starlikeness $r_L^*(f_{\rho,\beta})$ is the smallest positive root of the following transcendental equation

$$r^2 \left(\lambda'_{\rho,\beta}(r) \right)^2 - 2\beta \lambda'_{\rho,\beta}(r) \lambda_{\rho,\beta}(r) - \beta^2 \left(\lambda_{\rho,\beta}(r) \right)^2 = 0.$$

- b. The radius of lemniscate starlikeness $r_L^*(g_{\rho,\beta})$ is the smallest positive root of the following transcendental equation

$$r^2 \left(\lambda'_{\rho,\beta}(r) \right)^2 - 2r \lambda'_{\rho,\beta}(r) \lambda_{\rho,\beta}(r) - \left(\lambda_{\rho,\beta}(r) \right)^2 = 0.$$

- c. The radius of lemniscate starlikeness $r_L^*(h_{\rho,\beta})$ is the smallest positive root of the following transcendental equation

$$r \left(\lambda'_{\rho,\beta}(\sqrt{r}) \right)^2 - 4\sqrt{r} \lambda'_{\rho,\beta}(\sqrt{r}) \lambda_{\rho,\beta}(\sqrt{r}) - \left(\lambda_{\rho,\beta}(\sqrt{r}) \right)^2 = 0.$$

Proof. Owing to the Weierstrassian canonical representation of the function $z \mapsto \lambda_{\rho,\beta}(z)$ given in Eq. (2) we get

$$\frac{z \lambda'_{\rho,\beta}(z)}{\lambda_{\rho,\beta}(z)} = - \sum_{n \geq 1} \frac{2z^2}{\lambda_{\rho,\beta,n}^2 - z^2}. \quad (6)$$

Bearing in mind the normalizations presented in Eqs. (3)-(5) and by making use of Eq. (6) we obtain the following equations

$$\frac{zf'_{\rho,\beta}(z)}{f_{\rho,\beta}(z)} = 1 + \frac{1}{\beta} \left(\frac{z \lambda'_{\rho,\beta}(z)}{\lambda_{\rho,\beta}(z)} \right) = 1 - \frac{1}{\beta} \sum_{n \geq 1} \frac{2z^2}{\lambda_{\rho,\beta,n}^2 - z^2}, \quad (7)$$

$$\frac{zg'_{\rho,\beta}(z)}{g_{\rho,\beta}(z)} = 1 + \frac{z \lambda'_{\rho,\beta}(z)}{\lambda_{\rho,\beta}(z)} = 1 - \sum_{n \geq 1} \frac{2z^2}{\lambda_{\rho,\beta,n}^2 - z^2}, \quad (8)$$

$$\frac{zh'_{\rho,\beta}(z)}{h_{\rho,\beta}(z)} = 1 + \frac{1}{2} \left(\frac{\sqrt{z} \lambda'_{\rho,\beta}(\sqrt{z})}{\lambda_{\rho,\beta}(\sqrt{z})} \right) = 1 - \sum_{n \geq 1} \frac{z}{\lambda_{\rho,\beta,n}^2 - z}. \quad (9)$$

By means of Eqs. (7), (8) and (9), we deduce that the following inequalities

$$\begin{aligned} \left| \left(\frac{zf'_{\rho,\beta}(z)}{f_{\rho,\beta}(z)} \right)^2 - 1 \right| &\leq \frac{1}{\beta^2} \left(\sum_{n \geq 1} \frac{2|z|^2}{\lambda_{\rho,\beta,n}^2 - |z|^2} \right) \left(\sum_{n \geq 1} \frac{2|z|^2}{\lambda_{\rho,\beta,n}^2 - |z|^2} + 2\beta \right) \\ &= \left(\frac{|z| f'_{\rho,\beta}(|z|)}{f_{\rho,\beta}(|z|)} \right)^2 - 4 \left(\frac{|z| f'_{\rho,\beta}(|z|)}{f_{\rho,\beta}(|z|)} \right) + 3, \end{aligned}$$

$$\begin{aligned}
\left| \left(\frac{zg'_{\rho,\beta}(z)}{g_{\rho,\beta}(z)} \right)^2 - 1 \right| &\leq \left(\sum_{n \geq 1} \frac{2|z|^2}{\lambda_{\rho,\beta,n}^2 - |z|^2} \right) \left(\sum_{n \geq 1} \frac{2|z|^2}{\lambda_{\rho,\beta,n}^2 - |z|^2} + 2 \right) \\
&= \left(\frac{|z|g'_{\rho,\beta}(|z|)}{g_{\rho,\beta}(|z|)} \right)^2 - 4 \left(\frac{|z|g'_{\rho,\beta}(|z|)}{g_{\rho,\beta}(|z|)} \right) + 3, \\
\left| \left(\frac{zh'_{\rho,\beta}(z)}{h_{\rho,\beta}(z)} \right)^2 - 1 \right| &\leq \left(\sum_{n \geq 1} \frac{|z|}{\lambda_{\rho,\beta,n}^2 - |z|} \right) \left(\sum_{n \geq 1} \frac{|z|}{\lambda_{\rho,\beta,n}^2 - |z|} + 2 \right) \\
&= \left(\frac{|z|h'_{\rho,\beta}(|z|)}{h_{\rho,\beta}(|z|)} \right)^2 - 4 \left(\frac{|z|h'_{\rho,\beta}(|z|)}{h_{\rho,\beta}(|z|)} \right) + 3,
\end{aligned}$$

hold true for $|z| < \lambda_{\rho,\beta,1}$, $\rho > 0$ and $\beta > 0$.

For convenience, we deal with the function $z \mapsto \phi_{\rho,\beta}$ which collectively corresponds the functions $f_{\rho,\beta}$, $g_{\rho,\beta}$ and $h_{\rho,\beta}$. Assume that r^* is the smallest positive root of the equation

$$\left(\frac{r\phi'_{\rho,\beta}(r)}{\phi_{\rho,\beta}(r)} \right)^2 - 4 \left(\frac{r\phi'_{\rho,\beta}(r)}{\phi_{\rho,\beta}(r)} \right) + 2 = 0,$$

then the inequality

$$\left| \left(\frac{r\phi'_{\rho,\beta}(r)}{\phi_{\rho,\beta}(r)} \right)^2 - 1 \right| \leq 1$$

is valid for $|z| < r^*$. With the help of Eqs. (7)-(9), it is deducible that the zeros of the above mentioned equation for the functions $f_{\rho,\beta}$, $g_{\rho,\beta}$ and $h_{\rho,\beta}$ coincide with those of equations, respectively

$$\begin{aligned}
r^2 \left(\lambda'_{\rho,\beta}(r) \right)^2 - 2\beta \lambda'_{\rho,\beta}(r) \lambda_{\rho,\beta}(r) - \beta^2 \left(\lambda_{\rho,\beta}(r) \right)^2 &= 0, \\
r^2 \left(\lambda'_{\rho,\beta}(r) \right)^2 - 2r \lambda'_{\rho,\beta}(r) \lambda_{\rho,\beta}(r) - \left(\lambda_{\rho,\beta}(r) \right)^2 &= 0
\end{aligned}$$

and

$$r \left(\lambda'_{\rho,\beta}(\sqrt{r}) \right)^2 - 4\sqrt{r} \lambda'_{\rho,\beta}(\sqrt{r}) \lambda_{\rho,\beta}(\sqrt{r}) - \left(\lambda_{\rho,\beta}(\sqrt{r}) \right)^2 = 0.$$

This means that the radii of lemniscate starlikeness $r_L^*(f_{\rho,\beta})$, $r_L^*(g_{\rho,\beta})$ and $r_L^*(h_{\rho,\beta})$ are the smallest positive roots of the above equations, respectively.

To complete the proof we must show that each of the above equations have a unique roots in the open interval $(0, \lambda_{\rho,\beta,1})$. To do this, let us take into consideration the functions $F_{\rho,\beta}$, $G_{\rho,\beta}$, $H_{\rho,\beta}: (0, \lambda_{\rho,\beta,1}) \rightarrow \mathbb{R}$ defined by

$$\begin{aligned}
F_{\rho,\beta}(r) &= \left(\frac{rf'_{\rho,\beta}(r)}{f_{\rho,\beta}(r)} \right)^2 - 4 \left(\frac{rf'_{\rho,\beta}(r)}{f_{\rho,\beta}(r)} \right) + 2, \\
G_{\rho,\beta}(r) &= \left(\frac{rg'_{\rho,\beta}(r)}{g_{\rho,\beta}(r)} \right)^2 - 4 \left(\frac{rg'_{\rho,\beta}(r)}{g_{\rho,\beta}(r)} \right) + 2, \\
H_{\rho,\beta}(r) &= \left(\frac{rh'_{\rho,\beta}(r)}{h_{\rho,\beta}(r)} \right)^2 - 4 \left(\frac{rh'_{\rho,\beta}(r)}{h_{\rho,\beta}(r)} \right) + 2.
\end{aligned}$$

It is obvious that the above mentioned functions are strictly increasing functions of r since

$$\begin{aligned}
F'_{\rho,\beta}(r) &= \frac{2}{\beta} \sum_{n \geq 1} \frac{4r\lambda_{\rho,\beta,n}^2}{(\lambda_{\rho,\beta,n}^2 - r^2)^2} \left(1 + \frac{1}{\beta} \sum_{n \geq 1} \frac{2r^2}{\lambda_{\rho,\beta,n}^2 - r^2} \right) > 0, \\
G'_{\rho,\beta}(r) &= \sum_{n \geq 1} \frac{4r\lambda_{\rho,\beta,n}^2}{(\lambda_{\rho,\beta,n}^2 - r^2)^2} \left(1 + \sum_{n \geq 1} \frac{2r^2}{\lambda_{\rho,\beta,n}^2 - r^2} \right) > 0,
\end{aligned}$$

$$H'_{\rho,\beta}(r) = 2 \sum_{n \geq 1} \frac{\lambda_{\rho,\beta,n}^2}{(\lambda_{\rho,\beta,n}^2 - r)^2} \left(1 + \sum_{n \geq 1} \frac{r}{\lambda_{\rho,\beta,n}^2 - r} \right) > 0.$$

We can readily evaluate the limits

$$\lim_{r \searrow 0} F_{\rho,\beta}(r) = \lim_{r \searrow 0} G_{\rho,\beta}(r) = \lim_{r \searrow 0} H_{\rho,\beta}(r) = -1 < 0$$

and

$$\lim_{r \nearrow \lambda_{\rho,\beta,1}} F_{\rho,\beta}(r) = \lim_{r \nearrow \lambda_{\rho,\beta,1}} G_{\rho,\beta}(r) = \lim_{r \nearrow \lambda_{\rho,\beta,1}} H_{\rho,\beta}(r) = \infty.$$

This means that the lemniscate starlikeness radii of the functions $f_{\rho,\beta}$, $g_{\rho,\beta}$ and $h_{\rho,\beta}$, denoted by $r_{\mathcal{L}}^*(f_{\rho,\beta})$, $r_{\mathcal{L}}^*(g_{\rho,\beta})$ and $r_{\mathcal{L}}^*(h_{\rho,\beta})$ are, respectively, the unique zeros of $F_{\rho,\beta}(r)$, $G_{\rho,\beta}(r)$ and $H_{\rho,\beta}(r)$ in the open interval $(0, \lambda_{\rho,\beta,1})$.

Theorem 2. Let $\rho > 0$ and $\beta > 0$. Then the following assertions are valid.

- a. The radius of lemniscate convexity $r_{\mathcal{L}}^c(f_{\rho,\beta})$ is the smallest positive root of the following transcendental equation

$$\left(\frac{z\Psi''_{\rho,\beta}(z)}{\Psi'_{\rho,\beta}(z)} + \left(\frac{1}{\beta} - 1 \right) \frac{z\Psi'_{\rho,\beta}(z)}{\Psi_{\rho,\beta}(z)} \right)^2 - 2 \left(\frac{z\Psi''_{\rho,\beta}(z)}{\Psi'_{\rho,\beta}(z)} + \left(\frac{1}{\beta} - 1 \right) \frac{z\Psi'_{\rho,\beta}(z)}{\Psi_{\rho,\beta}(z)} \right) - 1 = 0.$$

- b. The radius of lemniscate convexity $r_{\mathcal{L}}^c(g_{\rho,\beta})$ is the smallest positive root of the following transcendental equation

$$\left(\frac{r^2\lambda''_{\rho,\beta}(r) + 2r\lambda'_{\rho,\beta}(r)}{\lambda_{\rho,\beta}(r) + r\lambda'_{\rho,\beta}(r)} \right)^2 - 2 \left(\frac{r^2\lambda''_{\rho,\beta}(r) + 2r\lambda'_{\rho,\beta}(r)}{\lambda_{\rho,\beta}(r) + r\lambda'_{\rho,\beta}(r)} \right) - 1 = 0.$$

- c. The radius of lemniscate convexity $r_{\mathcal{L}}^c(h_{\rho,\beta})$ is the smallest positive root of the following transcendental equation

$$\left(\frac{3\sqrt{r}\lambda'_{\rho,\beta}(\sqrt{r}) - r\lambda''_{\rho,\beta}(\sqrt{r})}{4\lambda_{\rho,\beta}(\sqrt{r}) + 2\sqrt{r}\lambda'_{\rho,\beta}(\sqrt{r})} \right)^2 - 2 \left(\frac{3\sqrt{r}\lambda'_{\rho,\beta}(\sqrt{r}) - r\lambda''_{\rho,\beta}(\sqrt{r})}{4\lambda_{\rho,\beta}(\sqrt{r}) + 2\sqrt{r}\lambda'_{\rho,\beta}(\sqrt{r})} \right) - 1 = 0.$$

Proof

- a. It is easy to obtain the following equality (see [9, Theorem 5])

$$1 + \frac{zf''_{\rho,\beta}(z)}{f'_{\rho,\beta}(z)} = 1 + \frac{z\Psi''_{\rho,\beta}(z)}{\Psi'_{\rho,\beta}(z)} + \left(\frac{1}{\beta} - 1 \right) \frac{z\Psi'_{\rho,\beta}(z)}{\Psi_{\rho,\beta}(z)}.$$

In view of [9] the infinite product representations

$$\Psi_{\rho,\beta}(z) = \frac{z^\beta}{\Gamma(\beta)} \prod_{n \geq 1} \left(1 - \frac{z^2}{\zeta_{\rho,\beta,n}^2} \right) \text{ and } \Psi'_{\rho,\beta}(z) = \frac{z^{\beta-1}}{\Gamma(\beta)} \prod_{n \geq 1} \left(1 - \frac{z^2}{\zeta'_{\rho,\beta,n}} \right)$$

are valid, where $\zeta_{\rho,\beta,n}$ and $\zeta'_{\rho,\beta,n}$ are the n th positive roots of $\Psi_{\rho,\beta}$ and $\Psi'_{\rho,\beta}$, respectively. By taking the logarithmic derivative on both sides of the above equalities we get

$$1 + \frac{zf''_{\rho,\beta}(z)}{f'_{\rho,\beta}(z)} = 1 - \sum_{n \geq 1} \frac{2z^2}{\zeta_{\rho,\beta,n}^2 - z^2} - \left(\frac{1}{\beta} - 1 \right) \sum_{n \geq 1} \frac{2z^2}{\zeta_{\rho,\beta,n}^2 - z^2}. \quad (10)$$

Assume that $\beta \in (0, 1]$, then $\frac{1}{\beta} - 1 \geq 0$. With the help of Eq. (10) and triangle inequality for $|z| < \zeta'_{\rho,\beta,1} < \zeta_{\rho,\beta,1}$, we arrive at

$$\left| \left(1 + \frac{zf''_{\rho,\beta}(z)}{f'_{\rho,\beta}(z)} \right) - 1 \right| \leq \left(\sum_{n \geq 1} \frac{2|z|^2}{\zeta_{\rho,\beta,n}^2 - |z|^2} + \left(\frac{1}{\beta} - 1 \right) \sum_{n \geq 1} \frac{2|z|^2}{\zeta_{\rho,\beta,n}^2 - |z|^2} \right)^2$$

$$+2\left(\sum_{n \geq 1} \frac{2|z|^2}{\zeta_{\rho,\beta,n}'^2 - |z|^2} + \left(\frac{1}{\beta} - 1\right) \sum_{n \geq 1} \frac{2|z|^2}{\zeta_{\rho,\beta,n}^2 - |z|^2}\right).$$

By virtue of Eq. (10), the above inequality gives

$$\left| \left(1 + \frac{zf_{\rho,\beta}''(z)}{f_{\rho,\beta}'(z)}\right)^2 - 1 \right| \leq \left(\frac{|zf_{\rho,\beta}''(|z|)|}{f_{\rho,\beta}'(|z|)} \right)^2 - 2 \left(\frac{|zf_{\rho,\beta}''(|z|)|}{f_{\rho,\beta}'(|z|)} \right). \quad (11)$$

Moreover, owing to the relation [8, Lemma 2.1]

$$\left| \frac{z}{a-z} - \lambda \frac{z}{b-z} \right| \leq \frac{|z|}{a-|z|} - \lambda \frac{|z|}{b-|z|} \quad (12)$$

for $|z| \leq r < a < b$ and $0 \leq \lambda < 1$ we conclude that the inequality given in Eq. (11) are valid for the case when $\beta > 1$ as well. This means that the inequality obtained in Eq. (11) is valid for $\beta > 0$ and $|z| < \zeta'_{\rho,\beta,1}$. Therefore, the function $f_{\rho,\beta}(z)$ lemniscate convex for $|z| < r_1$, where r_1 is the smallest positive root of

$$\left(\frac{rf_{\rho,\beta}''(r)}{f_{\rho,\beta}'(r)} \right)^2 - 2 \left(\frac{rf_{\rho,\beta}''(r)}{f_{\rho,\beta}'(r)} \right) - 1 = 0. \quad (13)$$

In order to complete the proof we must show that the above equation has a unique root in the open interval $(0, \zeta'_{\rho,\beta,1})$. To achieve our goal, let us take into account the function $u_{\rho,\beta}: (0, \zeta'_{\rho,\beta,1}) \rightarrow \mathbb{R}$ defined by

$$u_{\rho,\beta}(r) = \left(\frac{rf_{\rho,\beta}''(r)}{f_{\rho,\beta}'(r)} \right)^2 - 2 \left(\frac{rf_{\rho,\beta}''(r)}{f_{\rho,\beta}'(r)} \right) - 1.$$

It is easy to see that this function is strictly increasing for $\beta > 0$ since

$$u'_{\rho,\beta}(r) > \left(8r \sum_{n \geq 1} \left(\frac{\zeta_{\rho,\beta,n}'^2}{(\zeta_{\rho,\beta,n}'^2 - r^2)^2} - \frac{\zeta_{\rho,\beta,n}^2}{(\zeta_{\rho,\beta,n}^2 - r^2)^2} \right) \right) \times \\ \left(2r^2 \sum_{n \geq 1} \left(\frac{1}{\zeta_{\rho,\beta,n}'^2 - r^2} - \frac{1}{\zeta_{\rho,\beta,n}^2 - r^2} \right) \right) > 0$$

Here we tacitly used the relation $\zeta_{\rho,\beta,n}^2(\zeta_{\rho,\beta,n}'^2 - r^2)^2 < \zeta_{\rho,\beta,n}'^2(\zeta_{\rho,\beta,n}^2 - r^2)^2$ for $r < \sqrt{\zeta_{\rho,\beta,n}\zeta'_{\rho,\beta,n}}$ and $\beta > 0$. Also it is simple to evaluate the limits

$$\lim_{r \searrow 0} u_{\rho,\beta}(r) = -1 < 0 \text{ and } \lim_{r \nearrow \zeta'_{\rho,\beta,1}} u_{\rho,\beta}(r) = \infty.$$

In light of all explanations above mentioned, it is deducible that the root is unique in the open interval $(0, \zeta'_{\rho,\beta,1})$ and the radius of lemniscate convexity of the function $f_{\rho,\beta}(z)$, represented by $r_L^c(f_{\rho,\beta})$, is the unique root of Eq. (13) in the open interval $(0, \zeta'_{\rho,\beta,1})$.

- b.** We now focus on determining the radii of lemniscate convexity of normalized Wright function $g_{\rho,\beta}(z)$. Taking into account [9, Theorem 5], the infinite product representation of the function $g'_{\rho,\beta}(z)$ can be stated as

$$g'_{\rho,\beta}(z) = \prod_{n \geq 1} \left(1 - \frac{z^2}{\vartheta_{\rho,\beta,n}^2} \right),$$

where $\vartheta_{\rho,\beta,n}$ is the n th positive zero of the function $g'_{\rho,\beta}(z)$. By taking the logarithmic derivative of the above equality we get

$$1 + \frac{zg_{\rho,\beta}''(z)}{g'_{\rho,\beta}(z)} = 1 - \sum_{n \geq 1} \frac{2z^2}{\vartheta_{\rho,\beta,n}^2 - z^2}.$$

With the similar approach of the proof of Theorem 1, for $|z| < \vartheta_{\rho,\beta,1}$ we get

$$\left| \left(1 + \frac{zg''_{\rho,\beta}(z)}{g'_{\rho,\beta}(z)} \right)^2 - 1 \right| \leq \left(\frac{zg''_{\rho,\beta}(z)}{g'_{\rho,\beta}(z)} \right)^2 - 2 \left(\frac{zg''_{\rho,\beta}(z)}{g'_{\rho,\beta}(z)} \right).$$

Therefore, it follows that the radius of lemniscate convexity $r_L^c(g_{\rho,\beta})$ is the unique positive root of the equation

$$\left(\frac{rg''_{\rho,\beta}(r)}{g'_{\rho,\beta}(r)} \right)^2 - 2 \left(\frac{rg''_{\rho,\beta}(r)}{g'_{\rho,\beta}(r)} \right) - 1 = 0 \quad (14)$$

in $(0, \vartheta_{\rho,\beta,1})$. To complete the proof we must show that the above equation has a unique root in the open interval $(0, \vartheta_{\rho,\beta,1})$. To achieve our goal, let us take into consideration the function $v_{\rho,\beta}: (0, \vartheta_{\rho,\beta,1}) \rightarrow \mathbb{R}$ defined by

$$v_{\rho,\beta}(r) = \left(\frac{rg''_{\rho,\beta}(r)}{g'_{\rho,\beta}(r)} \right)^2 - 2 \left(\frac{rg''_{\rho,\beta}(r)}{g'_{\rho,\beta}(r)} \right) - 1$$

which is strictly increasing in the same interval since

$$v'_{\rho,\beta}(r) = 8r \left(\sum_{n \geq 1} \frac{\vartheta_{\rho,\beta,n}^2}{(\vartheta_{\rho,\beta,n}^2 - r^2)^2} \right) \left(\sum_{n \geq 1} \frac{2r^2}{(\vartheta_{\rho,\beta,n}^2 - r^2)^2} + 1 \right) > 0.$$

Also it can be observed that

$$\lim_{r \searrow 0} v_{\rho,\beta}(r) = -1 < 0 \text{ and } \lim_{r \nearrow \vartheta_{\rho,\beta,1}} v_{\rho,\beta}(r) = \infty.$$

That means that the radius of lemniscate convexity $r_L^c(g_{\rho,\beta})$ is the unique root of Eq. (14) in the open interval $(0, \vartheta_{\rho,\beta,1})$.

c. In [9] it is shown that the infinite product representation of the function $h'_{\rho,\beta}(z)$ can be stated as

$$h'_{\rho,\beta}(z) = \prod_{n \geq 1} \left(1 - \frac{z}{\tau_{\rho,\beta,n}} \right),$$

where $\tau_{\rho,\beta,n}$ is the n th positive zero of the function $h'_{\rho,\beta}$. As a result of mimicking the same evaluations in the part (b), it is deducible that the radius of lemniscate convexity $r_L^c(h_{\rho,\beta})$ is the unique root of equation stated in the part (c) of the theorem.

1.2. Janowski starlikeness and Janowski convexity of normalized Wright functions

In the present section we focus on finding out the radii of Janowski starlikeness and Janowski convexity of the normalized Wright functions $f_{\rho,\beta}(z)$, $g_{\rho,\beta}(z)$ and $h_{\rho,\beta}(z)$. It is important to mention here that it is said to be Janowski starlike of a normalized analytic function f if the quantity $\frac{zf'(z)}{f(z)}$ lies in the disc whose diametric end points are $\frac{1-A}{1-B}$ and $\frac{1+A}{1+B}$ for $-1 \leq B < A \leq 1$.

Theorem 3. Let $\rho > 0$ and $\beta > 0$. Then the following assertions are valid.

a. The radius of Janowski starlikeness $r_{A,B}^*(f_{\rho,\beta})$ is the smallest positive root of the equation

$$\frac{r\lambda'_{\rho,\beta}(r)}{\lambda_{\rho,\beta}(r)} + \beta \left(\frac{A-B}{1+|B|} \right) = 0$$

b. The radius of Janowski starlikeness $r_{A,B}^*(g_{\rho,\beta})$ is the smallest positive root of the equation

$$\frac{r\lambda'_{\rho,\beta}(r)}{\lambda_{\rho,\beta}(r)} + \frac{A-B}{1+|B|} = 0.$$

c. The radius of Janowski starlikeness $r_{A,B}^*(h_{\rho,\beta})$ is the smallest positive root of the equation

$$\frac{\sqrt{r}\lambda'_{\rho,\beta}(\sqrt{r})}{\lambda_{\rho,\beta}(\sqrt{r})} + 2\frac{A-B}{1+|B|} = 0.$$

Proof. In order to ascertain the radius of Janowski starlikeness of the normalization $f_{\rho,\beta}(z)$ of $\phi(\rho,\beta,\cdot)$ presented in Eq. (3), we need to find a positive real number r^* such that

$$\left| \frac{\frac{zf'_{\rho,\beta}(z)}{f_{\rho,\beta}(z)} - 1}{A - B \frac{zf'_{\rho,\beta}(z)}{f_{\rho,\beta}(z)}} \right| < 1, \quad \text{for } |z| < r^*.$$

In light of Eq. (7) and by making use of triangle inequality, it can readily be seen that the inequality

$$\left| \frac{\frac{zf'_{\rho,\beta}(z)}{f_{\rho,\beta}(z)} - 1}{A - B \frac{zf'_{\rho,\beta}(z)}{f_{\rho,\beta}(z)}} \right| \leq \frac{\frac{1}{\beta} \sum_{n \geq 1} \frac{2|z|^2}{\lambda_{\rho,\beta,n}^2 - |z|^2}}{A - B - |B| \frac{1}{\beta} \sum_{n \geq 1} \frac{2|z|^2}{\lambda_{\rho,\beta,n}^2 - |z|^2}}, \text{ for } |z| < \lambda_{\rho,\beta,1}$$

is valid for $\beta > 0$ with equality at $z = |z| = r$. It is clear that the above inequality gives

$$\left| \frac{\frac{zf'_{\rho,\beta}(z)}{f_{\rho,\beta}(z)} - 1}{A - B \frac{zf'_{\rho,\beta}(z)}{f_{\rho,\beta}(z)}} \right| \leq \frac{1 - \frac{zf'_{\rho,\beta}(z)}{f_{\rho,\beta}(z)}}{A - B + |B| \left(\frac{zf'_{\rho,\beta}(z)}{f_{\rho,\beta}(z)} - 1 \right)}. \quad (15)$$

Let r^* denote the smallest positive root of the equation

$$\frac{rf'_{\rho,\beta}(r)}{f_{\rho,\beta}(r)} + \frac{A-B}{1+|B|} - 1 = 0, \quad (16)$$

then the inequality given in Eq. (15) implies that the function $f_{\rho,\beta}(z)$ is Janowski starlike for $|z| < r^*$. In order to complete the proof we must show that the above equation has a unique root in the open interval $(0, \lambda_{\rho,\beta,1})$. To achieve our goal, let us take into consideration the function $u_{\rho,\beta}: (0, \lambda_{\rho,\beta,1}) \rightarrow \mathbb{R}$ defined by

$$u_{\rho,\beta}(r) = \frac{rf'_{\rho,\beta}(r)}{f_{\rho,\beta}(r)} + \frac{A-B}{1+|B|} - 1.$$

Since

$$u'_{\rho,\beta}(r) = -\frac{1}{\beta} \sum_{n \geq 1} \frac{4r\lambda_{\rho,\beta,n}^2}{(\lambda_{\rho,\beta,n}^2 - r^2)^2} < 0$$

the function $u_{\rho,\beta}$ is strictly decreasing on $(0, \lambda_{\rho,\beta,1})$. Also we can readily obtain that

$$\lim_{r \nearrow \lambda_{\rho,\beta,1}} u_{\rho,\beta}(r) = -\infty \text{ and } \lim_{r \searrow 0} u_{\rho,\beta}(r) = \frac{A-B}{1+|B|} > 0.$$

Therefore, we draw conclusion that the Janowski starlikeness radius of $f_{\rho,\beta}$, denoted by $r_{A,B}^*(f_{\rho,\beta})$, is the unique zero of Eq. (16) in the open interval $(0, \lambda_{\rho,\beta,1})$ which is desired result.

It is clear that the similar results can also be obtained for the normalizations $g_{\rho,\beta}$ and $h_{\rho,\beta}$ given in Eqs. (4) and (5), respectively for $\beta > 0$. Hence, the radii of Janowski starlikeness $r_{A,B}^*(g_{\rho,\beta})$ and $r_{A,B}^*(h_{\rho,\beta})$ are the unique roots of the equations stated in the parts (b) and (c) of the theorem, respectively.

Theorem 4. Let $\rho > 0$ and $\beta > 0$. Then the following assertions are valid.

- a. The radius of Janowski starlikeness $r_{A,B}^c(f_{\rho,\beta})$ is the smallest positive root of the equation

$$\frac{r\Psi''_{\rho,\beta}(r)}{\Psi'_{\rho,\beta}(r)} + \left(\frac{1}{\beta} - 1\right) \frac{r\Psi'_{\rho,\beta}(r)}{\Psi_{\rho,\beta}(r)} + \frac{A-B}{1+|B|} = 0.$$

- b. The radius of Janowski starlikeness $r_{A,B}^c(g_{\rho,\beta})$ is the smallest positive root of the equation

$$\frac{r^2 \lambda''_{\rho,\beta}(r) + 2r \lambda'_{\rho,\beta}(r)}{\lambda_{\rho,\beta}(r) + r \lambda'_{\rho,\beta}(r)} + \frac{A - B}{1 + |B|} = 0.$$

c. The radius of Janowski starlikeness $r_{A,B}^c(h_{\rho,\beta})$ is the smallest positive root of the equation

$$\frac{3\sqrt{r} \lambda'_{\rho,\beta}(\sqrt{r}) - r \lambda''_{\rho,\beta}(\sqrt{r})}{4\lambda_{\rho,\beta}(\sqrt{r}) + 2\sqrt{r} \lambda'_{\rho,\beta}(\sqrt{r})} + \frac{A - B}{1 + |B|} = 0.$$

Proof When taking into consideration definition of Janowski convex function in the open disk \mathbb{D}_r , for the function $f_{\rho,\beta}$, we deduce that the inequality

$$\left| \frac{\frac{zf''_{\rho,\beta}(z)}{f'_{\rho,\beta}(z)}}{A - B \left(1 + \frac{zf''_{\rho,\beta}(z)}{f'_{\rho,\beta}(z)}\right)} \right| < 1$$

must be valid for $|z| < r$. By using Eq. (10), It can be readily seen that for $0 \leq \beta < 1$ the function $f_{\rho,\beta}(z)$ satisfies the inequality

$$\left| \frac{\frac{zf''_{\rho,\beta}(z)}{f'_{\rho,\beta}(z)}}{A - B \left(1 + \frac{zf''_{\rho,\beta}(z)}{f'_{\rho,\beta}(z)}\right)} \right| \leq \frac{\sum_{n \geq 1} \frac{2z^2}{\zeta_{\rho,\beta,n}^2 - z^2} + \left(\frac{1}{\beta} - 1\right) \sum_{n \geq 1} \frac{2z^2}{\zeta_{\rho,\beta,n}^2 - z^2}}{A - B + |B| \left(\sum_{n \geq 1} \frac{2z^2}{\zeta_{\rho,\beta,n}^2 - z^2} + \left(\frac{1}{\beta} - 1\right) \sum_{n \geq 1} \frac{2z^2}{\zeta_{\rho,\beta,n}^2 - z^2}\right)},$$

for $|z| < \zeta'_{\rho,\beta,1}$ with $z = |z| = r$. With the help of inequality (12), the above mentioned inequality holds good for $\beta \geq 1$ as well. Due to Eq. (10), by putting $|z|$ in place of z , we obtain

$$\left| \frac{\frac{zf''_{\rho,\beta}(z)}{f'_{\rho,\beta}(z)}}{A - B \left(1 + \frac{zf''_{\rho,\beta}(z)}{f'_{\rho,\beta}(z)}\right)} \right| \leq \frac{-\frac{|z|f''_{\rho,\beta}(|z|)}{f'_{\rho,\beta}(|z|)}}{A - B + |B| \frac{|z|f''_{\rho,\beta}(|z|)}{f'_{\rho,\beta}(|z|)}}$$

for $\beta > 0$. Therefore, we draw conclusion that the radius of Janowski convexity $r_{A,B}^c(f_{\rho,\beta})$ is the smallest positive root of the equation

$$\frac{rf''_{\rho,\beta}(r)}{f'_{\rho,\beta}(r)} + \frac{A - B}{1 + |B|} = 0. \quad (17)$$

In order to complete our proof, we must show that Eq. (17) has a unique root in the open interval $(0, \zeta'_{\rho,\beta,1})$. To achieve our purpose, let us take into consideration the function $u_{\rho,\beta}: (0, \zeta'_{\rho,\beta,1}) \rightarrow \mathbb{R}$, defined by

$$u_{\rho,\beta}(r) = \frac{rf''_{\rho,\beta}(r)}{f'_{\rho,\beta}(r)} + \frac{A - B}{1 + |B|}$$

which is continuous on $(0, \zeta'_{\rho,\beta,1})$ and is strictly decreasing in $(0, \zeta'_{\rho,\beta,1})$ since

$$u'_{\rho,\beta}(r) < 4r \sum_{n \geq 1} \left(\frac{\zeta_{\rho,\beta,n}^2}{(\zeta_{\rho,\beta,n}^2 - r^2)^2} - \frac{\zeta_{\rho,\beta,n}^2}{(\zeta_{\rho,\beta,n}^2 - r^2)^2} \right) < 0.$$

Here we used tacitly the interlacing property $\zeta_{\rho,\beta,n}^2 (\zeta_{\rho,\beta,n}^2 - r^2)^2 < \zeta_{\rho,\beta,n}^2 (\zeta_{\rho,\beta,n}^2 - r^2)^2$ for $r < \sqrt{\zeta_{\rho,\beta,n} \zeta'_{\rho,\beta,n}}$ and $\beta > 0$. We can also observe that

$$\lim_{r \searrow 0} u_{\rho,\beta}(r) = \frac{A - B}{1 + |B|} > 0 \text{ and } \lim_{r \nearrow \zeta'_{\rho,\beta,1}} u_{\rho,\beta}(r) = -\infty.$$

Consequently, the radius of Janowski starlikeness of the function $f_{\rho,\beta}$, denoted by $r_{A,B}^c(f_{\rho,\beta})$, is the unique positive root of Eq. (17) in the open interval $(0, \zeta'_{\rho,\beta,1})$. This completes the proof.

Since the results given in part (b) and part (c) can readily be obtained by imitating the same evaluations in the part (a) of the theorem and by bearing in mind the infinite product representations of the functions $g'_{\rho,\beta}(z)$ and $h'_{\rho,\beta}(z)$ (see [9]) we omit the proof of part (b) and part (c).

Conflicts of interest

The authors state that did not have conflict of interests.

References

- [1] Aktaş, İ. and Baricz, Á., Bounds for radii of starlikeness of some q –Bessel functions, *Results Math.*, 72(1-2) (2017) 947-963.
- [2] Aktaş, İ., Baricz, Á. and Orhan H., Bounds for the radii of starlikeness and convexity of some special functions, *Turk J Math*, 42(1) (2018) 211–226.
- [3] Aktaş, İ., Baricz, Á. and Yağmur, N., Bounds for the radii of univalence of some special functions, *Math. Inequal. Appl.*, 20(3) (2017) 825–843.
- [4] Aktaş, İ., Baricz, Á. and Singh, S., Geometric and monotonic properties of hyper-Bessel functions, *Ramanujan J.*, 51(2) (2020) 275-295.
- [5] Aktaş İ., Toklu, E. and Orhan, H., Radii of uniform convexity of some special functions, *Turk J Math*, 42(6) (2018) 3010-3024.
- [6] Ali, R.M., Jain, N.K. and Ravichandran, V., Radii of starlikeness associated with the lemniscate of Bernoulli and the left-half plane, *Appl. Math. Comput.*, 218(11) (2012) 6557–6565.
- [7] Baricz, Á. and Prajapati, A., Radii of starlikeness and convexity of generalized Mittag-Leffler functions, *Math. Commun.*, 25 (2020) 117-135.
- [8] Baricz, Á. and Szász, R., The radius of convexity of normalized Bessel functions of the first kind, *Anal. Appl.*, 12(5) (2014) 485-509.
- [9] Baricz, Á., Toklu, E. and Kadioğlu, E., Radii of starlikeness and convexity of Wright functions., *Math. Commun.*, 23 (2018) 97-117.
- [10] Goodman, A.W., Univalent functions. Vol. I, Mariner Publishing Co., Inc., Tampa, FL, 1983.
- [11] Gorenflo, R., Luchko, Y. and Mainardi, F., Analytical properties and applications of the Wright function, *Fract. Calc. Appl. Anal.*, 2(4) (1999) 383-414.
- [12] Janowski, W., Extremal problems for a family of functions with positive real part and for some related families, *Ann. Polon. Math.*, 23 (1970/1971) 159–177.
- [13] Madaan, V., Kumar, A. and Ravichandran, V., Lemniscate Convexity and Other Properties of Generalized Bessel Functions, *Stud. Sci. Math. Hun.*, 56(4) (2019) 404-419.
- [14] Madaan, V., Kumar, A. and Ravichandran, V., Radii of starlikeness and convexity of Some Entire Functions, *Bull. Malays. Math. Sci. Soc.*, (2020).
- [15] Sokół, J. and Stankiewicz, J., Radius of convexity of some subclasses of strongly starlike functions, *Zeszyty Nauk. Politech. Rzeszowskiej Mat.*, 19 (1996) 101–105.
- [16] Toklu, E., Radii of starlikeness and convexity of q –Mittag-Leffler functions, *Turk J Math*, 43(5) (2019) 2610-2630.
- [17] Toklu, E., Aktaş, İ. and Orhan, H., Radii problems for normalized q –Bessel and Wright functions, *Acta Univ Sapientiae Mathematica*, 11(1) (2019) 203-223.
- [18] Verma, S. and Ravichandran, V., Radius problems for ratios of Janowski starlike functions with their derivatives, *Bull. Malays. Math. Sci. Soc.*, 40(2) (2017) 819–840.
- [19] Wright, E.M., On the coefficients of power series having exponential singularities, *J. Lond. Math. Soc.*, (1933) 71-79.

The comparison of inflammatory markers in pentylenetetrazole-induced acute epileptic seizure model and chronic epilepsy model in rats

Ahmet Şevki TAŞKIRAN^{1,*}  Yaşar TAŞTEMUR² 

¹Sivas Cumhuriyet University, School of Medicine, Department of Physiology, Sivas/ TURKEY

²Sivas Cumhuriyet University, School of Medicine, Department of Anatomy, Sivas/ TURKEY

Abstract

Recent studies have provided important evidence that neuroinflammation has an effective role in epilepsy pathophysiology. However, it is not clear that the occurrence of neuroinflammation is related to one epileptic seizure or repeating seizures. Therefore, we aimed to investigate the comparison of inflammatory markers in pentylenetetrazole-induced acute epileptic seizure model and chronic epilepsy model in rats. In this study, 18 male Wistar albino rats were used. The animals divided into three groups as control, acute epileptic seizure model and chronic epilepsy model. Inflammatory markers (TNF- α , IL-1 β , COX-1, and COX-2) were measured by using ELISA methods in the cortical and hippocampal brain regions after completing the epileptic model procedure. Statistical evaluation of the data was performed by one-way ANOVA and multiple comparisons were determined by the Tukey test. Statistical significance was defined at $p < 0.05$. Obtained data show that there was significant increase in inflammatory markers in chronic epilepsy model compared to the control and acute epileptic seizure model ($p < 0.05$). In conclusion, this study may suggest that inflammatory system is related to epileptogenesis process rather than only one epileptic seizure.

Article info

History:

Received: 11.05.2020

Accepted: 25.08.2020

Keywords:

Epilepsy,
Seizure,
Pentylenetetrazole,
Inflammation, Rats.

1. Introduction

Epilepsy is a neurological disorder characterized by spontaneous recurrent seizures, resulting in cognitive and psychological consequences [1]. About 70 million people are affected by epilepsy in worldwide. Epileptic seizure, which is the unique clinical sign of epilepsy, is seen as a result of increased, rapid and abnormal local electrical discharges of neurons in the cerebral cortex. During the seizure, short-term and temporary behavioral abnormalities appear in consciousness, behavior, emotion, movement or perception functions [2]. Traumatic brain injuries, hypoxia or febrile seizures can lead to neuronal deaths and dysfunctional synaptic modifications that can cause spontaneous recurrent seizures [3]. Since approximately one-third of patients with epilepsy do not respond to current medical treatment, they have progressive cognitive disorders and may need surgical treatment to prevent recurrence of seizures [4].

Neuroinflammation is a complex event involving the activation of microglia, astrocytes and endothelial cells participating in the blood brain barrier, infiltration of plasma proteins and immune system cells into the brain

tissue, and the interaction of inflammation-related mediators with the brain tissue [5]. Neuroinflammation findings are found in many central nervous system diseases, and neuroinflammation is often associated with epilepsy. Numerous evidence has been obtained with clinical and experimental research that neuroinflammation increases seizure frequency and severity [6]. Recurrent seizures are also seen in autoimmune diseases and encephalitis patients accompanied by severe and prolonged neuroinflammation, and neuroinflammation findings are frequently encountered in anticonvulsant drug-resistant epilepsies [7]. These findings have demonstrated the importance of neuroinflammation in the pathogenesis of epilepsy and have demonstrated the importance of elucidating these mechanisms in developing antiepileptogenic therapy.

Pentylenetetrazole (PTZ), a tetrazole derivative, is a chemical agent in the class of 'systemic' experimental convulsants. PTZ exerts its effect by blocking the GABAA chloride ionophore complex. Also PTZ, affects various neurotransmitter systems, such as gabaergic and glutamatergic systems [8]. Therefore, it is often used to create an acute or chronic animal epilepsy model. Parenterally administered PTZ has convulsive effects in mice, rats, cats and primates. PTZ

*Corresponding author. Email address: ahmettaskiran@cumhuriyet.edu.tr
<http://dergipark.gov.tr/csj> ©2020 Faculty of Science, Sivas Cumhuriyet University

initially produces myoclonic stresses, then causes generalized tonic-clonic seizures [9]. Single-dose (45-80 mg/kg) PTZ causes acute epileptic seizures, while repeated subacute dose PTZ (20-35 mg/kg) produces the chronic epileptic model which is meaning completing epileptogenesis process. epileptogenesis refers that transform from normal brain to epileptic brain by pathophysiological.

Several studies have shown important evidence that neuroinflammation has an effective role in epilepsy pathophysiology. However, it is not clear that the occurrence of neuroinflammation is related to one epileptic seizure or repeating seizures. Therefore, we aimed to investigate the comparison of inflammatory markers in pentylenetetrazole-induced acute epileptic seizure model and chronic epilepsy model in rats.

2. Materials and Methods

2.1. Animals

The experiments were performed using adult male Wistar rats weighing 230-250 g (n = 18). The animals were fed a standard laboratory diet and water ad libitum, kept at $22 \pm 2^\circ\text{C}$ with a 12-h light/dark cycle in a closed room which has lighting system controlled

by timers. Animals were acclimatized to laboratory conditions before the test. All experiments were carried out blindly between 09:00 and 17:00 h (n = 6 in each experimental group in the study). The Cumhuriyet University Animal Ethics Committee approved the experimental protocols (Approval Number: 65202830-050.04.04-371).

2.2. Drugs

Pentylenetetrazole (PTZ), (Sigma-Aldrich Co., St Louis, MO, USA) was dissolved in physiological saline. Each drug solution was prepared freshly on the days of the experiments.

2.3. Experimental protocol

The animals were divided into three groups as Group 1 (Control; n = 6); rats were treated with 1 ml/kg single dose of physiological saline intraperitoneally (i.p.), Group 2 (Acute epileptic seizure model; n = 6); rats were administered with single dose of i.p. PTZ (45 mg/kg), Group (Chronic epilepsy model; n = 6); rats were given with repeated doses of i.p. PTZ (35 mg/kg) every Monday, Wednesday and Friday day for 12 times. The animals were sacrificed by decapitation after 24 hours. The brain tissue obtained from the animals underwent biochemical assessment (Figure 1).

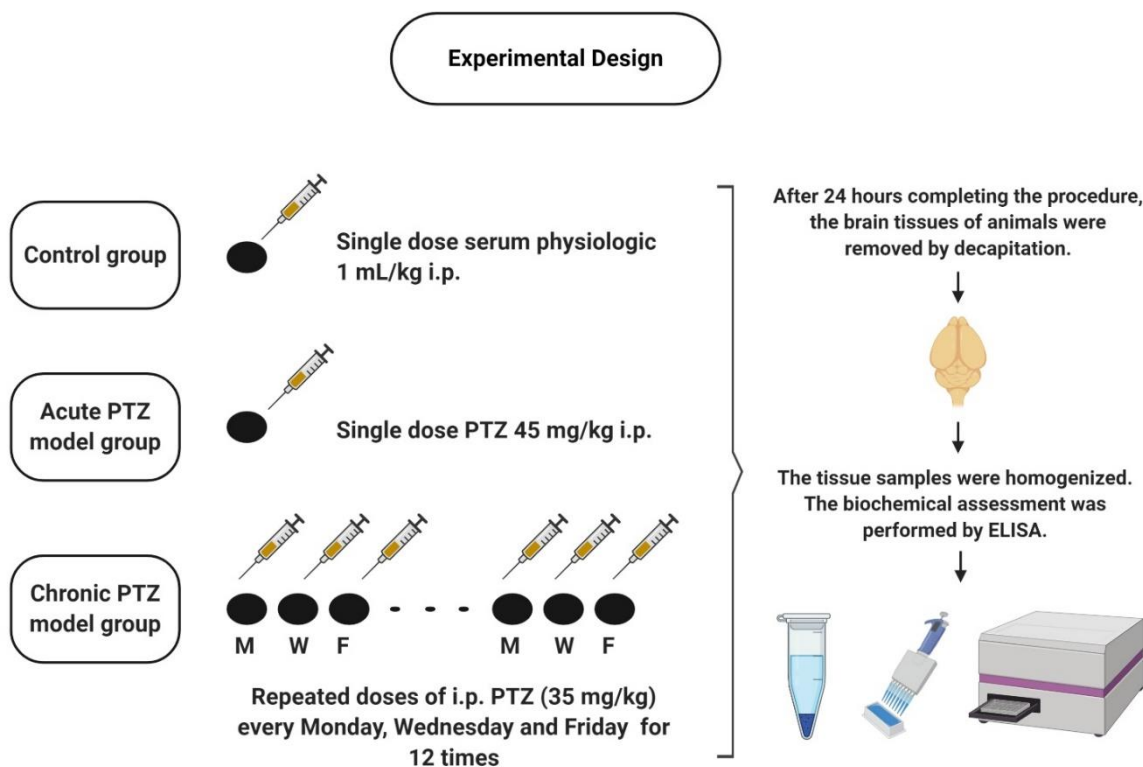


Figure 1. Experimental design (created by BioRender).

2.4. Biochemical assesment

2.4.1 Preparation of brain tissue homogenates

After mixing the brain tissue samples (both cortex and hippocampus area of the brain by separating) of the animals with a cold phosphate-buffered saline solution, the tissue samples were homogenized using a mechanical homogenizer (Analytik Jena speedmill plus, Jena, Germany). The homogenates were centrifuged at 4000 rpm for 10 min at a temperature of 4°C. Then, the supernatants were obtained and stored in ice until biochemical analysis. Bradford protein assay kit (Merck, Germany) was used to determination of total protein levels in samples [10].

2.4.2 Measurement of Tumor Necrosis Factor Alpha (TNF- α), Interleukin-1 Beta (IL-1 β) Cyclooxygenase-1 (COX-1) and Cyclooxygenase-2 (COX-2)

The levels of TNF- α , IL-1 β , COX-1 and COX-2 from brain supernatants were measured using rat ELISA commercial kits (Shanghai Sunred Biological Technology, Shanghai, China). The operation protocols were according to manufacturer's instructions. In brief, standard and tissue samples were added in plate and incubated for 60 min at 37 ° C. After washing step, staining solutions were added and incubated for 15 minutes at 37 ° C. Stop solution was added and read at 450 nm. There were standard curves used to calculate for all these kits. The coefficients of variation within and between plates were less than %10.

2.5. Statistical analysis

The data are expressed as mean \pm standart error of mean (SEM). The one-way ANOVA followed by Tukey posthoc test was used to compare the study data. The p -value of < 0.05 indicated a statistical significance.

3. Results and Discussion

3.1. Proinflammatory cytokines in acute and chronic PTZ models

Cytokines are proteins that regulate the inflammatory process. They are produced by neurons and glial cells during brain inflammation [11]. In a clinical study, IL-1 β and TNF- α levels in febrile seizures have been shown to increase [12].

TNF- α increases α -amino-3-hydroxy-5-ethylisoxazole-4-propionic acid (AMPA) receptors,

which increase glutamatergic transmission. Increased AMPA receptors cause excessive calcium intake and neurotoxicity in neurons. In addition, TNF- α induces GABA receptor endocytosis. Through these mechanisms, TNF- α causes an increase in excitation and a decrease in inhibition. This means a tendency to seizure [13,14]. In this study, we found that there is increase in TNF- α levels chronic PTZ models in cortex and hippocampus compared to control (Figure 2 A-B; $p<0,01$). However, the acute PTZ-induced seizures did not affect TNF- α levels in both cotex and hippocampus compared to control (Figure 2 A-B; $p>0,05$). Therefore, there was statical different in TNF- α levels between acute and chronic model in hippocampus (Figure 2 A-B; $p<0,05$). These findings show that TNF- α raises after epileptogenesis and is not related to acute epileptic seizures.

Our findings of TNF- α levels in acute PTZ model is coherent one of the previous study [15]. On the other hand, some studies have shown the increase in TNF- α levels after a single PTZ induced seizures dose in total brain and serum in contrast to our study [16,17]. It can be related to using the different doses of PTZ or collecting different parts of the tissues such as total brain and serum in these studies. Moreover, our findings of TNF- α levels in chronic PTZ models is consistent of the previous study performed in both mice and rat chronic PTZ models in hippocampus [18,19]. However, in contrast to our study, one of the study heve suggested that there is no changing in TNF- α levels in hippocampus after chronic PTZ model [20,21]. It can be explained the collecting time of tissues after last PTZ injection.

Proinflammatory cytokine IL-1 β is expressed in active microglia and astrocytes. IL-1 β increases glutamate release from astrocytes and reduces the reuptake of glutamate. By these ways, IL-1 β increases glutamate levels in neuronal synapses and causes neuronal hyperexcitability. It has been suggested that IL-1 β gives rise to seizures by activation of the GluN2B subunit of the N-methyl D-aspartate (NMDA) receptor and increasing regulation of NMDA receptors on postsynaptic cells [22]. In this study, we show that there is increase in IL-1 β levels chronic PTZ models in the cortex (Figure 2 C; $p<0,05$) and hippocampus (Figure 2 D; $p<0,001$), also in hippocampal region of acute PTZ model (Figure 2 D; $p<0,05$) compared to the control. However, the acute PTZ-induced seizures did not affect IL-1 β levels in the cotex region compared to the control (Figure 2 C; $p>0,05$). Moreover, there was statical different in IL-1 β levels between acute and chronic model in only hippocampal region (Figure 2 D; $p<0,05$). These findings show that IL-1 β raises after acute epileptic seizures and chronic. It can be

Show that IL-1 β may be associated with the both epileptic seizure and epileptogenesis.

Our findings of IL-1 β levels in acute and chronic PTZ models is consistent one of the previous studies which are carried out in rat and mice brain [15,20,23]. According to our findings, it may be suggested that TNF- α is associated with epileptogenesis, while IL-1 β

is related to both acute seizure and epileptogenesis. This also may explain the relationship between TNF and AMPA, and also between IL-1 β and NMDA. Because recent studies have shown that AMPA is the dominant role in epileptogenesis, while NMDA has an important role in both acute seizure and epileptogenesis [24,25].

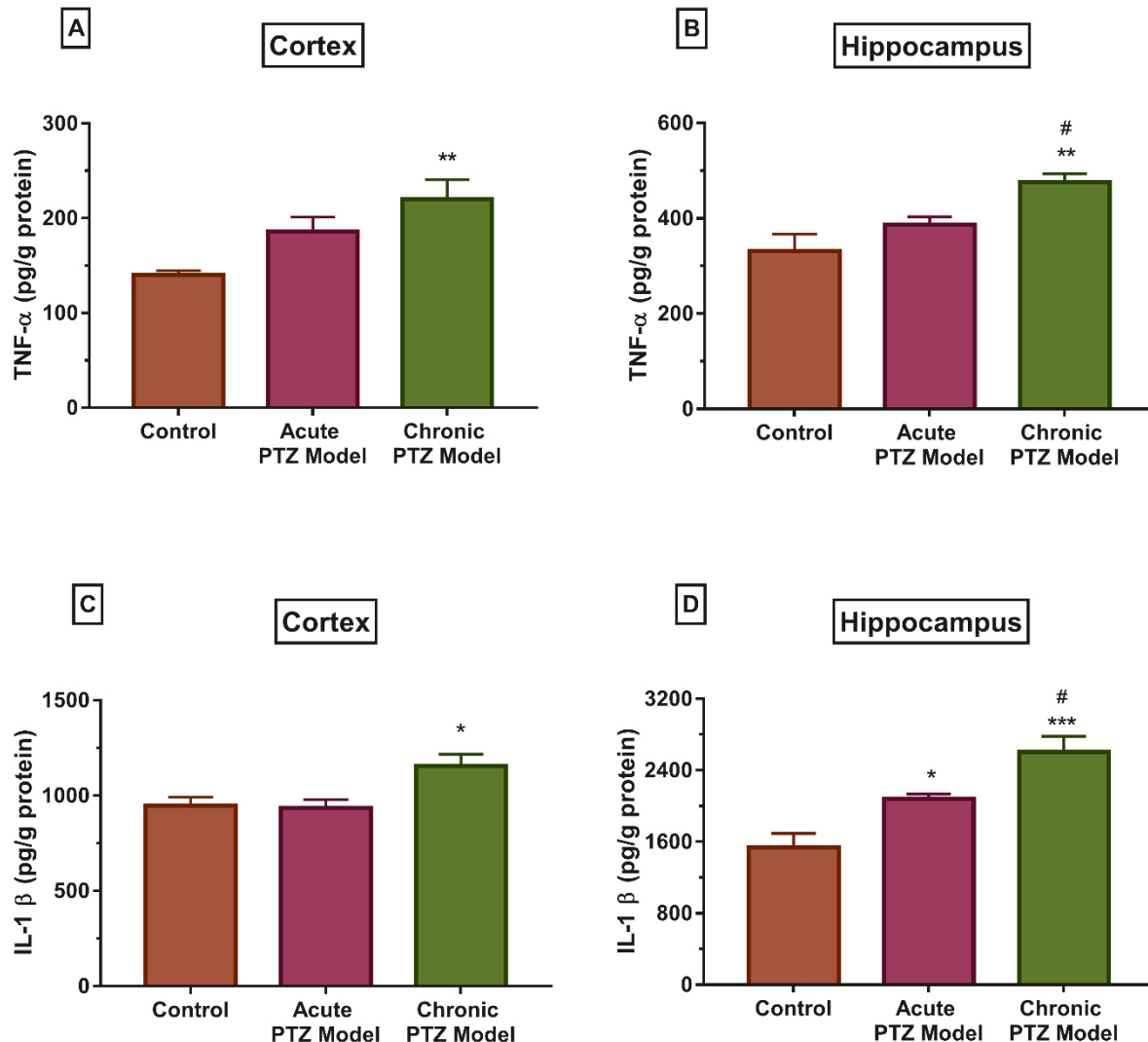


Figure 2. Proinflammatory cytokines in acute and chronic PTZ models in the cortex and hippocampus. * $p < 0,05$, ** $p < 0,01$ and *** $p < 0,001$ compared to control. # $p < 0,05$ compared to acute PTZ model.

3.2. Inflammatory enzymes in acute and chronic PTZ models

COX-1 and COX-2 are isoenzymes that catalyze the conversion of arachidonic acid into prostaglandins. It has been reported that COX-1 and COX-2, are induced in humans and experimental animals after seizures. COX-1 studies in animal models of seizures/epilepsy, it has shown that the selective COX-1 inhibitor slowed the development of epilepsy in electrical amygdala

kindling in mouse model [26]. Moreover, aspirin, which inhibit the activity of both COX-1 and COX-2, reduced seizures in the absence epilepsy model, in the zebrafish seizure model, and in the pilocarpine-induced epilepsy model [27,28]. However, there is no study in acute and chronic models induced by PTZ in rodents. In our study, we assert that there is increase in COX-1 levels in chronic PTZ models in cortex and hippocampus compared to control and acute PTZ model (Figure 3 A-B; $p < 0,001$). However, the acute

PTZ-induced seizures did not change COX-1 levels in both cortex and hippocampus compared to control and acute PTZ model (Figure 3 A-B; $p>0,05$). To the best of our knowledge, it was the first study is about COX-1 expression after two different models of PTZ in the English language. It has been suggested that COX-1 may be related closely to epileptogenesis and may be a new target for epileptogenesis.

Because COX-2 is considered the inducible expressed isoform responsible for propagating the inflammatory response, several studies have been predominantly exploring the COX-2 isoform as the most suitable target for pharmacological intervention in epilepsy studies [29,30]. However, the role of COX-2 inhibition

on epileptogenesis and/or seizure suppression remains controversial. Treatment with nimesulide, a COX-2 selective inhibitor, prior to electrical kindling, had antiepileptogenic effects in rodents [31,32]. On the other hand, proconvulsant effects of COX-2 inhibitor have also been shown in kainic acid-induced seizure model [33,34]. In addition to these studies, we found that there is increase in COX-2 levels chronic PTZ models in the cortex and hippocampus (Figure 3 C-D; $p<0,001$), also in hippocampal region of acute PTZ model (Figure 3 D; $p<0,001$) compared to the control. Nonetheless, the acute PTZ-induced seizures did not alter COX-2 levels in the cortex region compared to the control (Figure 2 C; $p>0,05$).

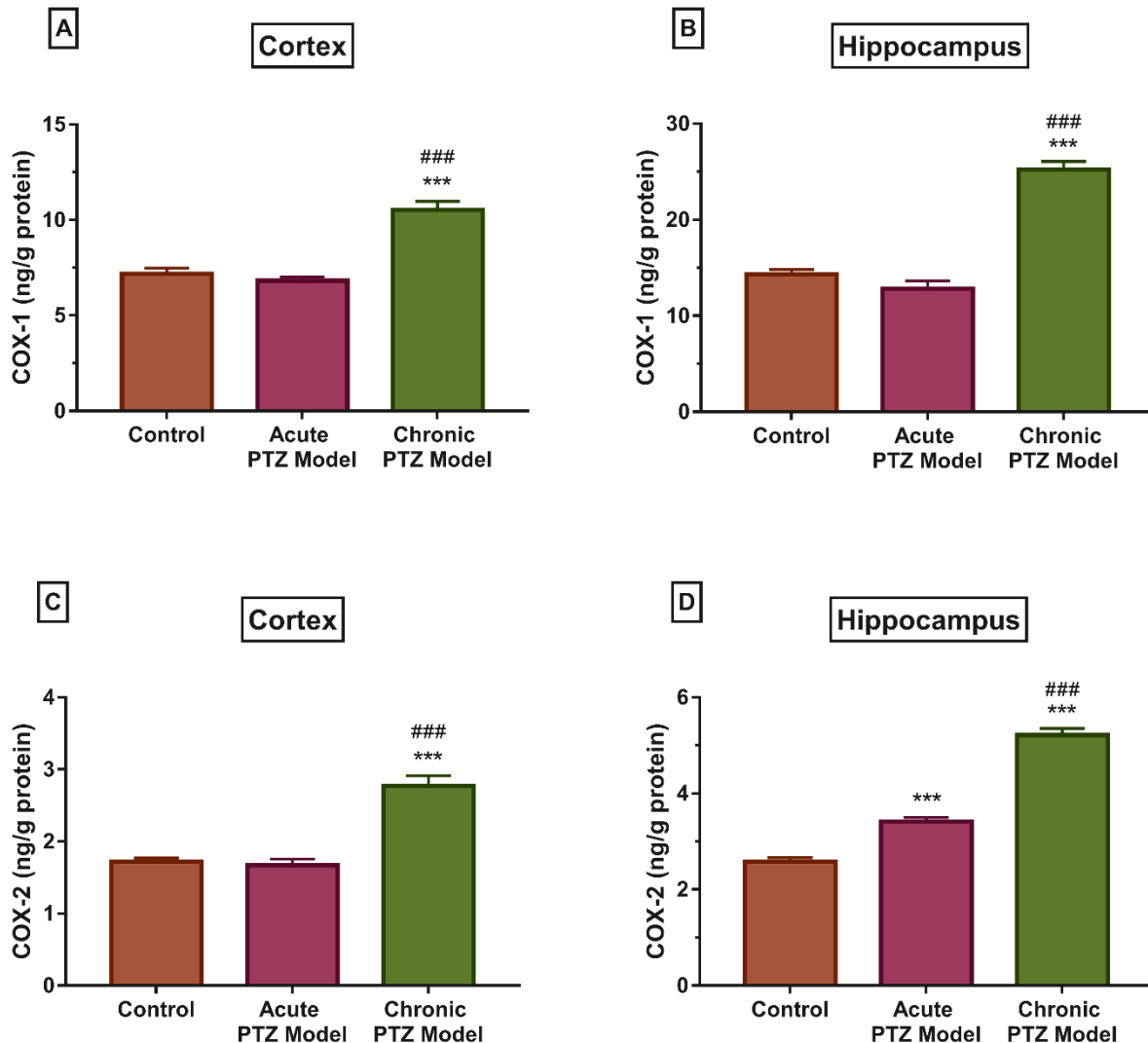


Figure 3. Inflammatory enzymes in acute and chronic PTZ models in the cortex and hippocampus. *** $p<0,001$ compared to control. ### $p<0,05$ compared to acute PTZ model.

4. Conclusion

In conclusion, based on the literature background and our study inflammation system is relevant epileptogenesis rather than acute epileptic occurring. Regulating inflammatory reactions in the brain and targeting inflammatory mediators may be effective therapeutic strategies to prevent or stop epileptogenesis process in the nervous system. Therefore, controlling inflammation may reduce the risk of developing epilepsy. Nevertheless, further researches are needed to clarify the role of inflammation in the pathogenesis of epilepsy.

Acknowledgment

The authors thank the institution for using the facilities of the Sivas Cumhuriyet University.

Conflicts of interest

Sample sentences if there is no conflict of interest: The authors state that did not have conflict of interests

References

- [1] Karabulut S., Bayramov R., Korkmaz Bayramov K., Filiz A.K., Taskiran A.S. and Ozdemir E. Effect of the allopregnanolone and allotetrahydrodeoxycorticosteron on spike-wave discharges in the EEG of absence epilepsy rat models, *Gen Physiol Biophys.*, 37 (2) (2018) 205-211.
- [2] Jackson C.F., Makin S.M., Marson A.G. and Kerr M. Pharmacological interventions for epilepsy in people with intellectual disabilities, *Cochrane Database Syst Rev.*, 3(9) (2015) CD005399
- [3] Akkaya R., Gümüş E., Akkaya B., Karabulut S., Gülmez K., Karademir M., Taştumur Y. and Taşkıran A.Ş. Wi-Fi decreases melatonin protective effect and increases hippocampal neuronal damage in pentylenetetrazole induced model seizures in rats, *Pathophysiology*, 26 (3-4) (2019) 375-379.
- [4] Wiebe S., Blume W.T., Girvin J.P. and Eliasziw M. Effectiveness and Efficiency of Surgery for Temporal Lobe Epilepsy Study Group. A randomized, controlled trial of surgery for temporal-lobe epilepsy, *N Engl J Med.*, 345 (5) (20013) 11-8.
- [5] Dey A., Kang X., Qiu J., Du Y. and Jiang J. Anti-Inflammatory Small Molecules To Treat Seizures and Epilepsy: From Bench to Bedside, *Trends Pharmacol Sci.*, 37 (6) (2016) 463-484.
- [6] Vezzani A., Aronica E., Mazarati A. and Pittman Q.J. Epilepsy and brain inflammation, *Exp Neurol.*, 244 (2013) 11-21.
- [7] Rana A. and Musto A.E. The role of inflammation in the development of epilepsy, *J Neuroinflammation.*, 15 (1) (2018) 144.
- [8] Shimada T. and Yamagata K. Pentylenetetrazole-Induced Kindling Mouse Model, *J Vis Exp.*, 12 (136) (2018) 56573.
- [9] Romualdi P., Lesa G., Donatini A., Balboni G., Tomatis R. and Ferri S. Alterations in vasoactive intestinal polypeptide-related peptides after pentylenetetrazole-induced seizures in rat brain, *Eur J Pharmacol.*, 229 (2-3) (1992) 149-153.
- [10] Kruger N.J. The Bradford method for protein quantitation, *Methods Mol Biol.*, 32 (1994) 9-15.
- [11] Alyu F. and Dikmen M. Inflammatory aspects of epileptogenesis: Contribution of molecular inflammatory mechanisms, *Acta Neuropsychiatr.*, 29 (1) (2017) 1-16.
- [12] Scorza C.A., Marques M.J.G., Gomes da Silva S., Naffah-Mazzacoratti M.D.G., Scorza F.A. and Cavalheiro E.A. Status epilepticus does not induce acute brain inflammatory response in the Amazon rodent *Proechimys*, an animal model resistant to epileptogenesis, *Neurosci. Lett.*, 668 (2018) 169-173.
- [13] Stellwagen D. and Malenka R.C. Synaptic scaling mediated by glial TNF- α . *Nature.*, 440 (7087) (2006) 1054-1059.
- [14] Galic M.A., Riazi K. and Pittman Q.J. Cytokines and brain excitability, *Front. Neuroendocrino.*, 33 (1) (2012) 116-125.
- [15] Dede F., Karadenizli S., Özsoy Ö.D., Eraldemir F.C., Şahin D. and Ateş N. The Effects of Adenosinergic Modulation on Cytokine Levels in a Pentylenetetrazole-Induced Generalized Tonic-Clonic Seizure Model, *Neuroimmunomodulation.*, 24 (1) (2017) 54-59.
- [16] Golechha M., Sarangal V., Bhatia J., Chaudhry U., Saluja D. and Arya D.S. Naringin ameliorates pentylenetetrazol-induced seizures and associated oxidative stress, inflammation, and cognitive impairment in rats: possible mechanisms of neuroprotection, *Epilepsy Behav.*, 41(2014) 98-102.
- [17] Chen L., Liu X., Wang H. and Qu M. Gastrodin Attenuates Pentylenetetrazole-Induced Seizures by Modulating the Mitogen-Activated Protein Kinase-Associated Inflammatory Responses in Mice, *Neurosci Bull.*, 33 (3) (2017) 264-272.

- [18] Mansoor S.R., Hashemian M., Khalili-Fomeshi M., Ashrafpour M., Moghadamnia A.A. and Ghasemi-Kasman M. Upregulation of klotho and erythropoietin contributes to the neuroprotection induced by curcumin-loaded nanoparticles in experimental model of chronic epilepsy, *Brain Res Bull.*, 142 (2018) 281–288.
- [19] Ahmadian S.R., Ghasemi-Kasman M., Pouramir M. and Sadeghi F. Arbutin attenuates cognitive impairment and inflammatory response in pentylenetetrazol-induced kindling model of epilepsy, *Neuropharmacology.*, 146 (2019) 117–127.
- [20] Muke S., Kaikini A., Peshattiwar V., Bagle S., Dighe V. and Sathaye S. Neuroprotective Effect of Coumarin Nasal Formulation: Kindling Model Assessment of Epilepsy, *Front Pharmacol.*, 9 (2018) 992.
- [21] Hoda U., Agarwal N.B., Vohora D., Parvez S. and Raisuddin S. Resveratrol suppressed seizures by attenuating IL-1 β , IL-1-Ra, IL-6, and TNF- α in the hippocampus and cortex of kindled mice, *Nutr Neurosci.*, 20 (9) (2017) 497–504.
- [22] Postnikova T., Zubareva O., Kovalenko A., Kim K., Magazanik L. and Zaitsev A. Status epilepticus impairs synaptic plasticity in rat hippocampus and is followed by changes in expression of NMDA receptors, *Biochem Mosc.*, 82 (3) (2017) 282–290.
- [23] Singh N., Saha L., Kumari P., Singh J., Bhatia A., Banerjee D. and Chakrabarti A. Effect of dimethyl fumarate on neuroinflammation and apoptosis in pentylenetetrazol kindling model in rats, *Brain Res Bull.*, 144 (2019) 233–245.
- [24] Sutula T., Koch J., Golarai G., Watanabe Y. and McNamara J.O. NMDA receptor dependence of kindling and mossy fibersprouting: evidence that the NMDA receptor regulates pattern-ing of hippocampal circuits in the adult brain, *J. Neurosci.*, 16 (1996) 7398-7406.
- [25] Davoudi M., Shojaei A., Palizvan M.R., Javan M. and Mirnajafi-Zadeh J. Comparison between standard protocol and a novel window protocol for induction of pentylenetetrazol kindled seizures in the rat, *Epilepsy Res.*, 106 (1-2) (2013) 54–63.
- [26] Tanaka S., Nakamura T., Sumitani K., Takahashi F., Konishi R., Itano T. and Miyamoto O. Stage- and region-specific cyclooxygenase expression and effects of a selective COX-1 inhibitor in the mouse amygdala kindling model, *Neurosci Res.*, 65 (1) (2009) 79-87.
- [27] Ma L., Cui X.L., Wang Y., Li X.W., Yang F., Wei D. and Jiang W. Aspirin attenuates spontaneous recurrent seizures and inhibits hippocampal neuronal loss, mossy fiber sprouting and aberrant neurogenesis following pilocarpine-induced status epilepticus in rats, *Brain Res.*, 1469 (2012) 103-113.
- [28] Barbalho P.G., Lopes-Cendes I. and Maurer-Morelli C.V. Indomethacin treatment prior to pentylenetetrazole-induced seizures downregulates the expression of il1b and cox2 and decreases seizure-like behavior in zebrafish larvae, *BMC Neurosci.*, 17 (2016) 12.
- [29] Kulkarni S.K. and Dhir A. Cyclooxygenase in epilepsy: from perception to application, *Drugs Today (Barc.)*, 45(2) (2009) 135-154.
- [30] Citraro R., Leo A., Marra R., De Sarro G. and Russo E. Antiepileptogenic effects of the selective COX-2 inhibitor etoricoxib, on the development of spontaneous absence seizures in WAG/Rij rats, *Brain Res Bull.*, 113 (2015) 1-7.
- [31] Tu B. and Bazan N.G. Hippocampal kindling epileptogenesis upregulates neuronal cyclooxygenase-2 expression in neocortex, *Exp Neurol.*, 179 (2) (2003) 167-175.
- [32] Takemiya T., Suzuki K., Sugiura H., Yasuda S., Yamagata K., Kawakami Y. and Maru E. Inducible brain COX-2 facilitates the recurrence of hippocampal seizures in mouse rapid kindling, *Prostaglandins Other Lipid Mediat.*, 71(3-4) (2003) 205-216.
- [33] Baik E.J., Kim E.J., Lee S.H. and Moon C. Cyclooxygenase-2 selective inhibitors aggravate kainic acid induced seizure and neuronal cell death in the hippocampus, *Brain Res.*, 843 (1-2) (1999) 118-129.
- [34] Kim H.J., Chung J.I., Lee S.H., Jung Y.S., Moon C.H. and Baik E.J. Involvement of endogenous prostaglandin F2alpha on kainic acid-induced seizure activity through FP receptor: the mechanism of proconvulsant effects of COX-2 inhibitors, *Brain Res.*, 1193 (2008) 153-161.

Equality of internal angles and vertex points in conformal hyperbolic triangles

Ümit TOKEŞER^{1,*}  Ömer ALSAN² 

¹ Department of Mathematics, Faculty of Science and Arts, Kastamonu University, 37100, Kastamonu, Turkey

² Zeytinburnu Anatolian High School, 34100, Istanbul, Turkey

Abstract

In this article, by using the conformal structure in Euclidean space, the conformal structures in hyperbolic space and the equality of the internal angles and vertex points of conformal triangles in hyperbolic space are given. Especially in these special conformal triangles, the conformal hyperbolic equilateral triangle and the conformal hyperbolic isosceles triangle, the internal angles and vertices are shown.

Article info

History:

Received: 14.04.2020

Accepted: 01.09.2020

Keywords:

Conformal hyperbolic triangle, Conformal hyperbolic isosceles triangle, Conformal hyperbolic equilateral triangle

1. Introduction

The set $H_0^n = \{x \in R_1^{n+1} : \langle x, x \rangle = -1\}$ is also called the n-dimensional unit pseudo-hyperbolic space. Two connected components of space H_0^n are $H_{0,+}^n$ and $H_{0,-}^n$; each of these components can be taken as the model of n-dimensional hyperbolic space. Based on the literature, we will consider the positive component as a model of hyperbolic space; that is $H_{0,+}^n = H^n \subset R_1^{n+1}$ [1,2,8].

First, we remember the concepts of lines and triangles in the hyperbolic plane.

As for $\alpha: \mathbb{R} \rightarrow H^n$ and $x, y \in H^n$, curve

$$\alpha(t) = (\cosh t)x + (\sinh t) \frac{(y + \langle x, y \rangle x)}{\|y + \langle x, y \rangle x\|}$$

is called *line through* x, y of H^n [9].

Similarly for $\alpha: \mathbb{R} \rightarrow H^n$ and $x, y \in H^n$,

$$\alpha(t) = (\cosh t)x + (\sinh t) \frac{(y - \cosh t_1 x)}{\sinh t_1}, \quad t \in [0, t_1]$$

curve segment is called *the line segment of* H^n *limited to* x, y [9].

x, y, z , three of which are three points on the same hyperbolic line;

*Corresponding author. Email address: utokeser@kastamonu.edu.tr

<http://dergipark.gov.tr/csj> ©2020 Faculty of Science, Sivas Cumhuriyet University

$$\alpha(t) = (\cosh t)x + (\sinh t) \frac{(y - \cosh t_1 x)}{\sinh t_1}, \quad t \in [0, t_1]$$

$$\beta(s) = (\cosh s)y + (\sinh s) \frac{(z - \cosh s_1 y)}{\sinh s_1}, \quad s \in [0, s_1]$$

$$\gamma(u) = (\cosh u)z + (\sinh u) \frac{(x - \cosh u_1 z)}{\sinh u_1}, \quad u \in [0, u_1]$$

the combination of the $\alpha(t_1) = \beta(0)$, $\beta(s_1) = \gamma(0)$ ve $\gamma(u_1) = \alpha(0)$ segmented line segments is called the hyperbolic triangle, and the hyperbolic zone bounded by the triangle is called the *hyperbolic triangular zone* [9].

Ω is hyperbolic triangle with P_1, P_2, P_3 vertex points;

$$M = \begin{bmatrix} -1 & -\cosh \varphi_{12} & -\cosh \varphi_{13} \\ -\cosh \varphi_{12} & -1 & -\cosh \varphi_{23} \\ -\cosh \varphi_{13} & -\cosh \varphi_{23} & -1 \end{bmatrix}$$

matrix is called *egde matrix* of Ω [4].

P_i, P_j two vertices of Ω ;

$$\cosh \varphi_{ij} = -\langle P_i, P_j \rangle$$

the real number φ_{ij} in the property $\cosh \varphi_{ij} = -\langle P_i, P_j \rangle$ is called *edge length limited by P_i, P_j* of Ω [4].

Definition 1. The edges of the P_i, P_j, P_k -pointed Ω hyperbolic triangle through P_k point are also

$$\alpha: IR \rightarrow H^n,$$

$$\beta: IR \rightarrow H^n;$$

the θ_{ij} angle, which is to be $\langle \alpha'(t) \big|_{P_k}, \beta'(s) \big|_{P_k} \rangle = \cos \theta_{ij}$, is called *the internal angle of Ω at point P_k* [9].

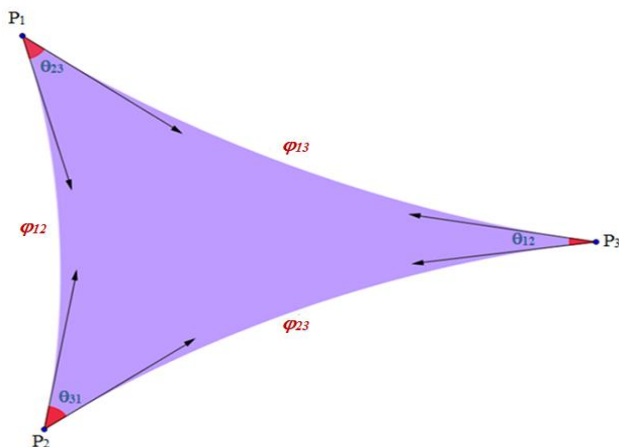


Figure 1. Triangle in Hyperbolic Space

2. Conformal Triangles in Hyperbolic Space

Definition 2. The set $\{P \in H^2 : \langle m, P \rangle = -\cosh r\}$, as $m \in H^2$ and $r \in \mathbb{R}^+$, is called *the m -centered r hyperbolic circle in H^2* [9].

Definition 3. Let Ω be the hyperbolic triangle with P_1, P_2, P_3 vertex points. If there are real numbers $r_1, r_2, r_3 \in \mathbb{R}^+$ as $\varphi_{ij} = r_i + r_j$ with an edge length φ_{ij} limited to P_i, P_j ; Ω is called *conformal hyperbolic triangle* [9].

Theorem 4. Let Ω be hyperbolic triangle with P_1, P_2, P_3 vertex points. Ω to be conformal if and only if

$$r_i > \ln \sqrt{2}, \quad i = 1, 2, 3 \quad (2.1)$$

where $r_1, r_2, r_3 \in \mathbb{R}^+$ [9].

Now, we give edge matrices for conformal hyperbolic triangles. These matrices play very important roles throughout the paper for calculations.

Lemma 5. Edge matrix of conformal hyperbolic triangles, edge matrix of conformal hyperbolic equilateral triangles and edge matrix of conformal hyperbolic isosceles triangles as follows

$$M = \begin{bmatrix} -1 & -\cosh(r_1 + r_2) & -\cosh(r_1 + r_3) \\ -\cosh(r_1 + r_2) & -1 & -\cosh(r_2 + r_3) \\ -\cosh(r_1 + r_3) & -\cosh(r_2 + r_3) & -1 \end{bmatrix} \quad (2.2)$$

$$\tilde{M} = \begin{bmatrix} -1 & -\cosh(r_1 + r_2) & -\cosh(r_1 + r_2) \\ -\cosh(r_1 + r_2) & -1 & -\cosh(r_1 + r_2) \\ -\cosh(r_1 + r_2) & -\cosh(r_1 + r_2) & -1 \end{bmatrix} \quad (2.3)$$

$$\hat{M} = \begin{bmatrix} -1 & -\cosh(r_1 + r_2) & -\cosh(r_1 + r_2) \\ -\cosh(r_1 + r_2) & -1 & -\cosh(r_2 + r_3) \\ -\cosh(r_1 + r_2) & -\cosh(r_2 + r_3) & -1 \end{bmatrix} \quad (2.4)$$

respectively [9].

From [4]

$$\cos \theta_{ij} = \frac{M_{ij}}{\sqrt{M_{ii} M_{jj}}}, \quad i \neq j; \quad i, j = 1, 2, 3 \quad (2.5)$$

and from equation (8) in [5], we can define

$$\sin \theta_{ij} = \frac{\sqrt{-|M|}}{\sqrt{M_{ii} M_{jj}}}, \quad i \neq j; \quad i, j = 1, 2, 3. \quad (2.6)$$

3. Equality of Internal Angles and Vertex Points in Conformal Hyperbolic Triangles

In this section, using the expressions of the internal angles and vertex points, we defined in Definition 1, equality of internal angles to vertex points of the conformal hyperbolic triangle and special conformal hyperbolic triangles will be shown.

Now, in Eq. 2.5

$$\cos \theta_{ij} = \frac{M_{ij}}{\sqrt{M_{ii}M_{jj}}}, \quad i \neq j; \quad i, j = 1, 2, 3$$

was given.

$$\text{As } \sin P_k = \frac{\sqrt{-|M|}}{\sqrt{(-M_{ii})(-M_{jj})}}, \quad i \neq j, i \neq k, j \neq k; \quad i, j, k = 1, 2, 3 \quad . \quad (3.1)$$

It is

$$\cos \theta_{12} = \frac{M_{12}}{\sqrt{M_{11}M_{22}}}$$

if M_{11}, M_{12} and M_{22} from Eq. 2.2 are calculated and replaced,

$$\cos \theta_{12} = \frac{\cosh(r_1 + r_3)\cosh(r_2 + r_3) - \cosh(r_1 + r_2)}{\sqrt{\sinh^2(r_2 + r_3)\sinh^2(r_1 + r_3)}}$$

is obtained.

Similarly, if M_{11}, M_{12} and $|M|$ are used at Eq 3.1, calculated from Eq 2.2,

$$\sin P_3 = \frac{\sqrt{-|M|}}{\sqrt{M_{11}M_{22}}}$$

$$\sin P_3 = \frac{\sqrt{4 \sinh r_1 \sinh r_2 \sinh r_3 \sinh(r_1 + r_2 + r_3)}}{\sqrt{\sinh^2(r_2 + r_3)\sinh^2(r_1 + r_3)}}$$

would be. From here

$$\theta_{12} = \arccos \left(\frac{\cosh(r_1 + r_3)\cosh(r_2 + r_3) - \cosh(r_1 + r_2)}{\sqrt{\sinh^2(r_2 + r_3)\sinh^2(r_1 + r_3)}} \right),$$

$$P_3 = \arcsin \left(\frac{\sqrt{4 \sinh r_1 \sinh r_2 \sinh r_3 \sinh(r_1 + r_2 + r_3)}}{\sqrt{\sinh^2(r_2 + r_3)\sinh^2(r_1 + r_3)}} \right) \quad (3.2)$$

are obtained.

We calculate the cosine of the right side of Eq 3.2. It would be

$$\begin{aligned}
 & \cos \left(\arcsin \left(\frac{\sqrt{4 \sinh r_1 \sinh r_2 \sinh r_3 \sinh (r_1 + r_2 + r_3)}}{\sqrt{\sinh^2 (r_2 + r_3) \sinh^2 (r_1 + r_3)}} \right) \right) \\
 &= \sqrt{1 - \sin^2 \left(\arcsin \left(\frac{\sqrt{4 \sinh r_1 \sinh r_2 \sinh r_3 \sinh (r_1 + r_2 + r_3)}}{\sqrt{\sinh^2 (r_2 + r_3) \sinh^2 (r_1 + r_3)}} \right) \right)} \\
 &= \sqrt{1 - \left(\frac{\sqrt{4 \sinh r_1 \sinh r_2 \sinh r_3 \sinh (r_1 + r_2 + r_3)}}{\sqrt{\sinh^2 (r_2 + r_3) \sinh^2 (r_1 + r_3)}} \right)^2} \\
 &= \frac{\sqrt{\sinh^2 (r_1 + r_2) \sinh^2 (r_1 + r_3) - 4 \sinh r_1 \sinh r_2 \sinh r_3 \sinh (r_1 + r_2 + r_3)}}{\sinh (r_1 + r_2) \sinh (r_1 + r_3)}.
 \end{aligned}$$

When necessary calculations are made, we get

$$\sinh^2 (r_1 + r_2) \sinh^2 (r_1 + r_3) - 4 \sinh r_1 \sinh r_2 \sinh r_3 \sinh (r_1 + r_2 + r_3) = (\cosh (r_1 + r_3) \cosh (r_2 + r_3) - \cosh (r_1 + r_2))^2$$

Thus,

$$\theta_{12} = P_3$$

equation is obtained. By using similar method

$$\theta_{23} = P_1$$

and

$$\theta_{13} = P_2$$

are obtained [6].

3.1. Equality of internal angles and vertex points in the conformal hyperbolic equilateral triangle

Definition 6. Let Ω be a hyperbolic triangle with P_1, P_2, P_3 vertex points, $\theta_{12}, \theta_{13}, \theta_{23}$ dihedral angles and $\varphi_{12}, \varphi_{13}, \varphi_{23}$ edge lengths. Let $\Omega \in H^2$; if $\theta_{12} = \theta_{13} = \theta_{23}$, $\varphi_{12} = \varphi_{13} = \varphi_{23}$ and $\theta_{12} < \frac{\pi}{3}$, Ω is called *equilateral hyperbolic triangle* [7].

Now, in Eq. 2.5

$$\cos \theta_{ij} = \frac{\tilde{M}_{ij}}{\sqrt{\tilde{M}_{ii} \tilde{M}_{jj}}}, \quad i \neq j; \quad i, j = 1, 2, 3$$

was given.

Including

$$\sin P_k = \frac{\sqrt{-|\tilde{M}|}}{\sqrt{(-\tilde{M}_{ii})(-\tilde{M}_{jj})}}, \quad i \neq j, i \neq k, j \neq k; \quad i, j, k = 1, 2, 3. \quad (3.3)$$

If $\tilde{M}_{11}, \tilde{M}_{12}$ and \tilde{M}_{22} are calculated and replaced from Eq. 2.3;

$$\cos \theta_{12} = \frac{\cosh(r_1 + r_2)(\cosh(r_1 + r_2) - 1)}{\sqrt{\sinh^4(r_1 + r_2)}}$$

is obtained.

Similarly, if $\tilde{M}_{11}, \tilde{M}_{12}$ and $|\tilde{M}|$ calculated from Eq. 2.3 used in Eq. 3.3, it becomes as

$$\sin P_3 = \frac{\sqrt{-|\tilde{M}|}}{\sqrt{\tilde{M}_{11} \tilde{M}_{22}}}$$

$$\sin P_3 = \frac{\sqrt{(\cosh(r_1 + r_2) - 1)^2 (\cosh(r_1 + r_2) + 1)}}{\sqrt{\sinh^4(r_1 + r_2)}}.$$

Here,

$$\theta_{12} = \arccos \left(\frac{\cosh(r_1 + r_2)(\cosh(r_1 + r_2) - 1)}{\sqrt{\sinh^4(r_1 + r_2)}} \right),$$

$$P_3 = \arcsin \left(\frac{\sqrt{(\cosh(r_1 + r_2) - 1)^2 (\cosh(r_1 + r_2) + 1)}}{\sqrt{\sinh^4(r_1 + r_2)}} \right) \quad (3.4)$$

are obtained.

We calculate the cosine of the right side of Eq. 3.4 as follow,

$$\begin{aligned} & \cos \left(\arcsin \left(\frac{\sqrt{(\cosh(r_1 + r_2) - 1)^2 (\cosh(r_1 + r_2) + 1)}}{\sqrt{\sinh^4(r_1 + r_2)}} \right) \right) \\ &= \sqrt{1 - \sin^2 \left(\arcsin \left(\frac{\sqrt{(\cosh(r_1 + r_2) - 1)^2 (\cosh(r_1 + r_2) + 1)}}{\sqrt{\sinh^4(r_1 + r_2)}} \right) \right)} \\ &= \sqrt{1 - \left(\frac{\sqrt{(\cosh(r_1 + r_2) - 1)^2 (\cosh(r_1 + r_2) + 1)}}{\sqrt{\sinh^4(r_1 + r_2)}} \right)^2} \\ &= \frac{\sqrt{\sinh^2(r_1 + r_2) - (\cosh(r_1 + r_2) - 1)^2 (\cosh(r_1 + r_2) + 1)}}{\sinh^2(r_1 + r_2)}. \end{aligned}$$

We get

$$\sinh^2(r_1 + r_2) - (\cosh(r_1 + r_2) - 1)^2 (\cosh(r_1 + r_2) + 1) = \cosh^2(r_1 + r_2) (\cosh(r_1 + r_2) - 1)^2$$

when necessary calculations are made. Thus

$$\theta_{12} = P_3$$

equality is obtained. By using similar method

$$\theta_{23} = P_1$$

and

$$\theta_{13} = P_2$$

are obtained [6].

3.2. Equality of internal angles and vertex points in the conformal hyperbolic isosceles triangle

Definition 7. Let Ω be a hyperbolic triangle with P_1, P_2, P_3 vertex points, $\theta_{12}, \theta_{13}, \theta_{23}$ dihedral angles and $\varphi_{12}, \varphi_{13}, \varphi_{23}$ edge lengths. Let $\Omega \in H^2$; if $\theta_{12} = \theta_{13}$ and $2\theta_{12} < \pi - \theta_{23}$, Ω is called *isosceles hyperbolic triangle* [7].

Now, in Eq. 2.5

$$\cos \theta_{ij} = \frac{\hat{M}_{ij}}{\sqrt{\hat{M}_{ii} \hat{M}_{jj}}}, \quad i \neq j; \quad i, j = 1, 2, 3$$

was given.

Including

$$\sin P_k = \frac{\sqrt{-|\hat{M}|}}{\sqrt{(-\hat{M}_{ii})(-\hat{M}_{jj})}}, \quad i \neq j, i \neq k, j \neq k; \quad i, j, k = 1, 2, 3 \quad (3.5)$$

If $\hat{M}_{11}, \hat{M}_{22}$ and \hat{M}_{22} are calculated and replaced from Eq. 2.4;

$$\cos \theta_{12} = \frac{\cosh(r_1 + r_2)(\cosh(r_2 + r_3) - 1)}{\sqrt{\sinh^2(r_2 + r_3) \sinh^2(r_1 + r_2)}}$$

is obtained.

Similarly, if $\hat{M}_{11}, \hat{M}_{22}$ and $|\hat{M}|$ calculated from Eq. 2.4 used in Eq. 3.5, it becomes as

$$\sin P_3 = \frac{\sqrt{-|\hat{M}|}}{\sqrt{\hat{M}_{11} \hat{M}_{22}}}$$

$$\sin P_3 = \frac{\sqrt{4 \sinh r_1 \sinh^2 r_2 \sinh(r_1 + r_2)}}{\sqrt{\sinh^2(r_2 + r_3) \sinh^2(r_1 + r_2)}}.$$

Here,

$$\theta_{12} = \arccos \left(\frac{\cosh(r_1 + r_2)(\cosh(r_2 + r_3) - 1)}{\sqrt{\sinh^2(r_2 + r_3) \sinh^2(r_1 + r_2)}} \right),$$

$$P_3 = \arcsin \left(\frac{\sqrt{4 \sinh r_1 \sinh^2 r_2 \sinh(r_1 + r_2)}}{\sqrt{\sinh^2(r_2 + r_3) \sinh^2(r_1 + r_2)}} \right) \quad (3.6)$$

are obtained.

We calculate the cosine of the right side of Eq. 3.6 as follow,

$$\begin{aligned} & \cos \left(\arcsin \left(\frac{\sqrt{4 \sinh r_1 \sinh^2 r_2 \sinh(r_1 + r_2)}}{\sqrt{\sinh^2(r_2 + r_3) \sinh^2(r_1 + r_2)}} \right) \right) \\ &= \sqrt{1 - \sin^2 \left(\arcsin \left(\frac{\sqrt{4 \sinh r_1 \sinh^2 r_2 \sinh(r_1 + r_2)}}{\sqrt{\sinh^2(r_2 + r_3) \sinh^2(r_1 + r_2)}} \right) \right)} \\ &= \sqrt{1 - \left(\frac{\sqrt{4 \sinh r_1 \sinh^2 r_2 \sinh(r_1 + r_2)}}{\sqrt{\sinh^2(r_2 + r_3) \sinh^2(r_1 + r_2)}} \right)^2} \\ &= \frac{\sqrt{\sinh^2(r_2 + r_3) \sinh^2(r_1 + r_2) - 4 \sinh r_1 \sinh^2 r_2 \sinh(r_1 + r_2)}}{\sinh^2(r_2 + r_3) \sinh^2(r_1 + r_2)}. \end{aligned}$$

We get

$$\sinh^2(r_2 + r_3) \sinh^2(r_1 + r_2) - 4 \sinh r_1 \sinh^2 r_2 \sinh(r_1 + r_2) = \cosh^2(r_1 + r_2) (\cosh(r_2 + r_3) - 1)^2$$

when necessary calculations are made. Thus

$$\theta_{12} = P_3$$

equality is obtained. By using similar method,

$$\theta_{23} = P_1$$

and

$$\theta_{13} = P_2$$

are obtained [6].

References

- [1] Asmus, I., Duality Between Hyperbolic and de-Sitter Geometry, New York: Cornell University, 2008; pp 1-32.
- [2] O'neil, B., Semi-Riemannian Geometry, London: Academic Press, 1983; pp 46-49, 54-57, 108-114, 143-144.
- [3] Suarez-Peiro, E., A Schlafli Differential Formula for Implices in Semi-Riemannian Hyperquadrics, Gauss-Bonnet Formulas for Simplices in the de Sitter Sphere and the Dual Volume of a Hyperbolic Simplex, *Pacific Journal of Mathematics*, 194(1) (2000) 229.
- [4] Karlıga, B., Edge matrix of hyperbolic simplices, *Geom. Dedicata*, 109 (2004) 1-6.

- [5] Karlığa, B., Yakut, A.T., Vertex angles of a simplex in hyperbolic space H^n , *Geom. Dedicata*, 120 (2006) 49-58.
- [6] Alsan, Ö., Conformal Triangles, M.Sc. Thesis, Kastamonu University Institute of Science and Technology, Kastamonu, 2015.
- [7] Karlığa, B., Savaş, M., “Field Formulas Based on Edge Lengths of Hyperbolic and Spherical Triangles”, Seminar of Mathematics Department, Gazi University, Ankara, (2006) 1-6.
- [8] Ratcliffe, J.G., “Foundations of Hyperbolic Manifolds”, , Berlin: Springer-Verlag, 1994.
- [9] Tokeşer, Ü., “Triangles in Spherical Hyperbolic and de-Sitter Planes”, Ph.D. Thesis, Gazi University Institute of Science and Technology, Ankara 2013.

Isotherm, kinetic and thermodynamic studies for the adsorption of methylene blue on almond leaf powder

Adnan ALDEMİR^{1,*} Ali Rıza KUL²

¹Van Yüzüncü Yıl University, Faculty of Engineering, Chemical Engineering Department, 65080, Van

²Van Yüzüncü Yıl University, Faculty of Science, Chemistry Department, 65080, Van

Abstract

In this study almond leaf powder (ALP) was used as an adsorbent for the methylene blue (MB) removal. The initial MB concentration, interaction time and temperature effects were investigated in a batch experimental system. The equilibrium data was modelled using Langmuir, Freundlich and Temkin adsorption isotherms, while kinetic parameters were determined using the pseudo first order (PFO), pseudo second order (PSO) and intra-particle diffusion (IPD) models. It was noted that the Freundlich model was the most convenient option compared to the Langmuir and Temkin models. The Freundlich model coefficients increased as the temperature increased, proving that adsorption process is favorable at higher temperatures. The results also indicated that the experimental and calculated q_e values were close to each other, which shows that this process fits the PSO kinetic model with higher R^2 values than other two models. Kinetic constants became closer to both temperatures and the initial concentrations and q_e values increased with the increase in the concentration of MB. The initial MB concentration increased from 10 to 60 mg/L, while the adsorption capacity on ALP increased from 1.46 to 9.24 mg/g, 1.61 to 9.71 mg/g and 1.89 to 10.71 mg/g for 298, 308 and 323 K, respectively. Gibbs free energy, enthalpy and entropy of this separation process were determined as -1737.1 J/mol, 14.776 kJ/mol and 55.413 J/mol, respectively. Results of this study showed that ALP can be an alternative material for dye removal.

Article info

History:

Received:15.04.2020

Accepted:02.07.2020

Keywords:

Almond leaf powder,
Dye adsorption,
Methylene blue,
Isotherm model,
Kinetic coefficient,
Thermodynamic
parameters

1. Introduction

Removing hazardous compounds from wastewater are one of the most serious environmental challenges faced by humans today [1]. This matter has received considerable attention due to the fact that most organic dyestuffs are hazardous to humans, animals and other organisms [2]. Dyes are generally utilized to impart color in different industries [3]. Commercial dyes can be classified in several ways including chemical structure, color and application methods. They are generally classified as cationic, anionic and non-ionic. The different classes of dyes and their effects are given in [4-7]. Dyes have stable and complex structures and low biodegradability. They are toxic to organisms living in waters and prejudicial to photosynthetic activities and some dyes have harmful effects in humans. Owing to their harmful effects, removals of dyes from aqueous solutions have been studied extensively by researchers [8-9].

A variety of chemical and biological treatment technologies are applied to wastewaters [10-12]. Among these is the adsorption technique which is relatively economical, flexible, efficient, has a simple design and has been proved to be an effective technique in treating colorized wastewaters [13]. The performance of adsorption is related to the adsorbent materials. Activated carbon, which is commonly used adsorbent, has high operational costs and after it has been used the water is required to be regenerated [14]. This limitation has encouraged the search for different adsorbents, such as natural materials, biosorbents and waste materials from industrial or agricultural processes. Natural wastes have been favored as adsorbents due to being low in cost, high in efficiency, non-hazardous to nature and locally available materials [15,16].

There are many studies in the literature that have used various agri-food materials, such as peanut hulls, pineapple stems, garlic peels, rice, wheat and coffee husks, banana and orange peels and peach gum, for the depollution of aqueous solutions [16-18]. However,

*Corresponding author. Email address: adnanaldemir@yyu.edu.tr
<http://dergipark.gov.tr/csaj> ©2020 Faculty of Science, Sivas Cumhuriyet University

the need to find new materials that easily available, low-cost and environmentally friendly are still existing. Consequently, various kinds of leaves have been utilized as bioadsorbents in the dyes removal applications for removal of dyes from wastewaters [19].

MB has been continually investigated by researchers and has used for adsorption studies regarding organic contaminants in aqueous solutions [20]. MB has a wide application area such as cotton and wool dyes, paper stock coating and analytical reagents. Although not exactly poisonous, MB can have damaging effects on humans and animals [21,22]. Thus, Removal of MB from aqueous solutions is extremely important. Various leaf-based adsorbents were investigated for MB adsorption and some of them provided well-suited [23-27].

The interference among the adsorbent and adsorbate molecules is explained with adsorption isotherms. The nature of the adsorbate can change the amount that can be adsorbed, the adsorbent affect and the adsorption isotherm profile shape. The different isotherms were used to investigate the results [28]. According to the Langmuir isotherm, adsorption of the monolayer and all active sites on the surface of the adsorbent are equal in energy. The Freundlich isotherm clarifies the multilayer adsorption behavior, while the Temkin isotherm describes the interaction of solute molecules in the aqueous phases with heterogeneous solid surfaces [29]. The effect of temperature on adsorption was determined by analyzing thermodynamic parameters including Gibbs free energy (ΔG), entropy (ΔS) and enthalpy (ΔH). The kinetic mechanism of adsorption was explained using calculated different equations including PFO, PSO and IPD models [30]. The purpose of this study is investigated the adsorption capacity of ALP for MB which is selected as the adsorbate on account of the fact that it is a commonly used dye. Adsorption techniques were suggested by examining the isotherms, kinetics and thermodynamic of MB adsorption on ALP.

2. Materials and Methods

2.1. Adsorbent

ALP, used in adsorption experiments, was made from leaves of the almond trees (*Prunus dulcis*) growing on the Akdamar Island located in Van Lake, Turkey. The collected almond leaves were washed with deionized water to remove impurities and were dried at 90 °C in an oven for 24 h. The scales of almond leaves were reduced and blended in food processor. The emergent powder was sieved and particles below 150 μm were collected.

2.2. Adsorbate

In this study, MB, a cationic dye, was used as the adsorbate which formula is $\text{C}_6\text{H}_{18}\text{N}_3\text{SCl}\cdot 3\text{H}_2\text{O}$ and the molecular weight is 319.85 g/mol. MB was purchased from Merck Chemicals Company and stock dye solution was prepared for experiments.

2.3. Adsorption experiments

Within the scope of batch experiments, which were carried out in a temperature-controlled water bath, 2 g ALP was treated with 500 mL of MB solution. Different MB concentrations (10, 20, 30, 40, 50, 60 mg/L) in the solution of MB determined for 200 min while the pH was gradually adjusted by adding either H_2SO_4 or NaOH solutions (0.1 M). All of the experiments were carried out in triplicate at the same conditions at temperatures of 298 K, 308 K and 323 K and the average values were taken to represent the results when calculating the overall data. For UV/VIS spectrophotometer (PG Instruments Ltd. T80 model) a calibration curve was obtained by plotting among absorbance and certain concentrations of the dye solution at a maximum 660 nm wavelength. This calibration curve was used to measure unknown MB concentration. The dye adsorption capacity of adsorbent was analyzed using the equation given below:

$$q_e = (C_0 - C_e)V/m \quad (1)$$

where V was the solution volume (L), C_0 and C_e were initial and equilibrium concentration of the dye (mg/L) and W was adsorbent mass (g). Data obtained from batch experiments were used in isotherm, kinetic and thermodynamic calculations to design the MB removal with ALP.

3. Results and Discussion

3.1. Adsorption isotherm studies

Many different models are used to identify the adsorption of dyes on solid surfaces. In this research three isotherm models, Freundlich, Langmuir and Temkin, where selected to investigate the interactions between dye and adsorbent. These models were applicable for the descriptions of the experimental results obtained at three different temperatures. The parameters of these isotherm models were calculated using linear form of their equations [31]. The amount of MB adsorbed per unit by samples (q_e) and equilibrium concentrations (C_e) for three temperatures are given in Figure 1. It was determined that adsorption

efficiency increased with the increase in initial MB concentration.

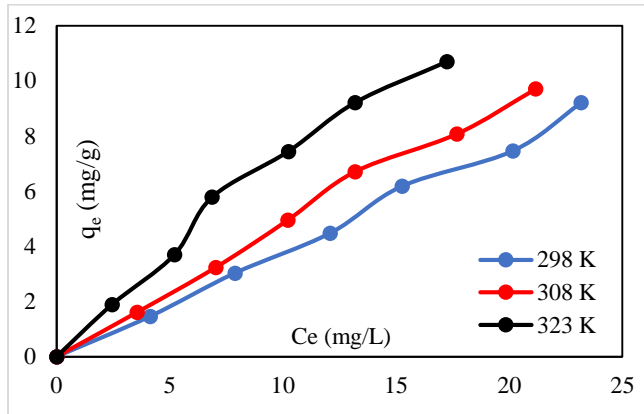


Figure 1. Adsorption isotherms of MB on ALP for different temperatures

The Langmuir isotherm model has some assumptions for the adsorption occurrence on a homogenous surface without interaction between adsorbates in the plane of the surface. Langmuir isotherm model is given Eq. (2);

$$q_e = (q_m K_L C_e) / (1 + K_L C_e) \quad (2)$$

where q_m is maximum capacity of adsorption (mg/g), K_L is Langmuir constant (L/g). q_m and K_L values were determined from plot of the C_e/q_e versus C_e , respectively. Langmuir isotherm results for MB adsorption on ALP at 298, 308, 323 K are given in Figure 2.

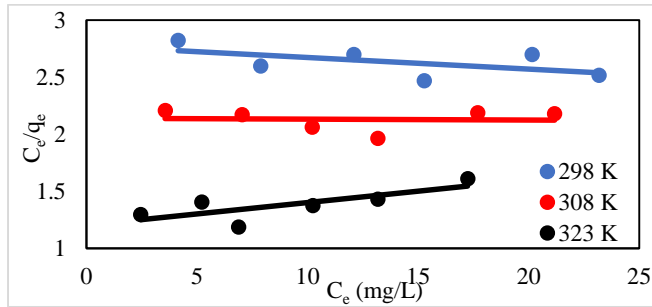


Figure 2. Langmuir isotherms of MB adsorption on ALP at different temperatures

The Freundlich isotherm model is based on adsorption on heterogeneous surfaces. Freundlich isotherm model is given Eq. (3);

$$q_e = K_F C_e^{1/n} \quad (3)$$

where K_F is a Freundlich constant (L/g), $1/n$ is an empirical parameter. K_F and n values were found from intercept and slope of the plot between $\ln q_e$ against $\ln C_e$, respectively. The Freundlich isotherm results for MB adsorption on ALP at 298, 308 and 323 K are given in Figure 3.

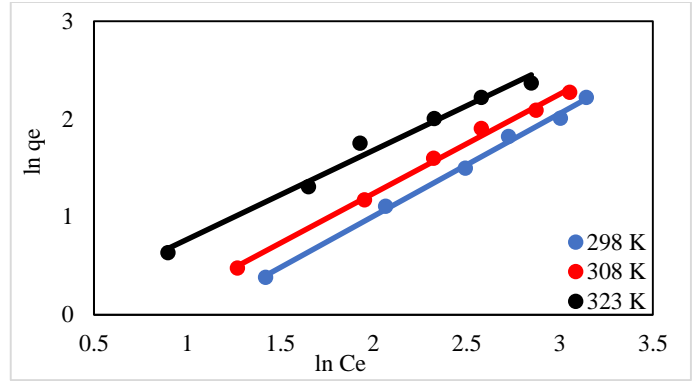


Figure 3. Freundlich isotherms of MB adsorption on ALP at different temperatures

The Temkin isotherm model describes interactions of solute molecules on solid surfaces. This isotherm is based on the concept that heat of adsorption decreases when the solid surface is covered. Temkin isotherm model is given with Eq. (4);

$$q_e = B \ln(K_T C_e) \quad (4)$$

where K_T and B constants are evaluated from the plot. B illustrates constant related to heat of adsorption, which is calculated with Eq. (5);

$$B = RT/b_T \quad (5)$$

where $1/b_T$ symbolizes adsorption potential; R means gas constant (8.314 J/kmol); and T is temperature in Kelvin (K). Temkin isotherm results for MB adsorption on ALP at 298, 308 and 323 K are given in Figure 4.

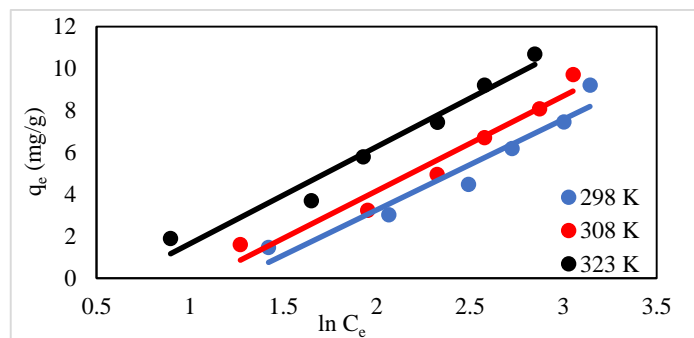


Figure 4. Temkin isotherms of MB adsorption on ALP at different temperatures

The calculated parameters of Langmuir, Freundlich and Temkin isotherms are shown in Table 1. Freundlich model was more fitting compared to the other two models with regards to the determined coefficients. The values of K_F and n were increased when the temperature increase and adsorption was also

increased with the higher temperatures. The R^2 values of the three isotherm models were high, however the R^2 values of the Freundlich model were higher than other two models. The q_m values of adsorbents produced from different leaves for MB removal

calculated using the Langmuir isotherm model are given in Table 2 and different adsorbents used for MB removal including agricultural and industrial wastes are given in [32].

Table 1. Isotherm model parameters of MG adsorption on ALP at different temperatures

Temp	Langmuir			Freundlich			Temkin		
K	K_L	q_m	R^2	n	K_F	R^2	K_T	b_T	R^2
	(L/g)	(mg/g)			(L/g)		(L/g)	(J/mol)	
298	0.0165	50.251	0.3099	0.9534	0.3394	0.9967	0.6231	898.517	0.8519
308	0.0253	98.039	0.2869	0.9841	0.4522	0.9955	0.6545	814.228	0.8847
323	0.0374	125.013	0.5833	1.0978	0.8697	0.9947	0.7561	712.541	0.8447

Table 2. Adsorption capacity of different leaf powders on MB

Adsorbent	q_m (mg/g)	References
Plane leaves powder	114.9	[1]
Lotus leaves powder	221.7	[24]
Date palm leaves powder	58.1	[25]
Oil palm leaves powder	103.2	[26]
Neem leaves powder	19.6	[27]
Weeping pillow leaves powder	60.9	[30]
Gulmohar leaves powder	186.2	[33]
Almond leaves powder	125.0	This study

3.2. Temperature and adsorption thermodynamics

The temperature effect on MB adsorption was determined by carrying out the same experiments at three different temperatures. The results of the experiments indicated that dye adsorption capacity decreased with the rise in temperature. A thermodynamic investigation was conducted to determine the significance of the adsorption process. ΔG° , ΔH° and ΔS° parameters were used for detecting any heat alterations in the adsorption process regarding MB and ALP [11]. These parameters were calculated with Eq. (6) – (9);

$$K_c = C_{Ads} / C_e \quad (6)$$

$$\Delta G^\circ = -RT \ln K_c \quad (7)$$

$$\Delta G^\circ = \Delta H^\circ - (T \Delta S^\circ) \quad (8)$$

$$\ln K_c = (\Delta S^\circ / R) - (\Delta H^\circ / (RT)) \quad (9)$$

where, K_c is equilibrium constant, C_{Ads} is dye amount (mg) adsorbed by ALP per liter of the solution at equilibrium, the adsorbent of adsorbent per unit liter of solution. The ΔH° and ΔS° parameters were analyzed from slope and intercept of the $\ln K_c$ versus $1/T$ plot. From the graphical representation, according to Eq. (9), namely $\ln K_c$ vs $1/T$, a straight line is

obtained in Figure 5 and thermodynamic parameters were illustrated in Table 3. The thermodynamic parameters of MB adsorption on ALP were calculated with using Equations 6-9. The ΔG° values for MB on ALP were obtained as -1.7371, -2.2912 and -3.1224 kJ/mol for 298 K, 308 K and 323 K, respectively. The ΔH° and ΔS° values of MB adsorption on ALP were determined as 14.776 kJ/mol and 55.413 kJ/mol.K, respectively. ΔG° values showed feasibility and spontaneous nature of adsorption, while negative ΔG° values indicated that adsorption was physisorption. The decrease in absolute values of ΔG° with the increase in temperature shows that this separation process is constructive at low temperatures. The positive ΔH° value is showed that process is endothermic and the positive ΔS° value is verified the affinity of ALP on MB.

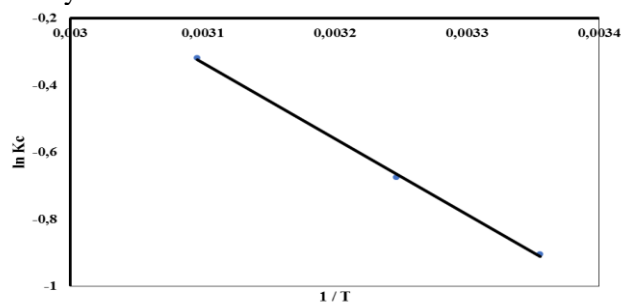


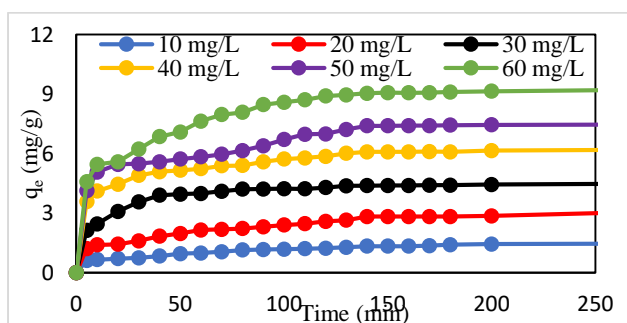
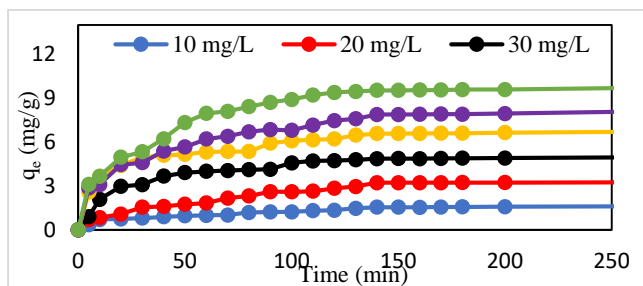
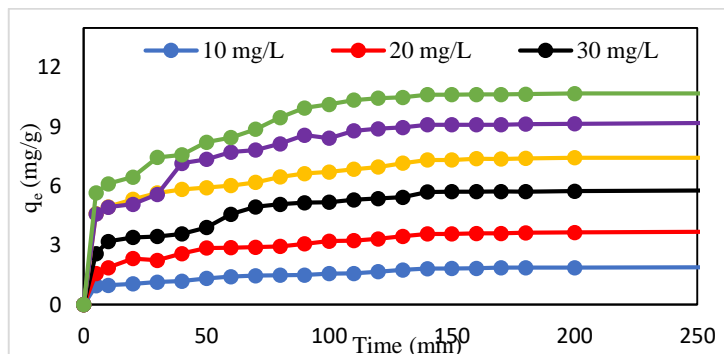
Figure 5. $\ln K_c$ versus $1/T$ plot for MB adsorption on ALP

Table 3. Thermodynamic parameters of MB adsorption on ALP

Temp (K)	ΔG° (kJ/mol)	ΔH° (kJ/mol)	ΔS° (J/mol.K)	R^2
298	-1.7371	14.776	55.413	0.999
308	-2.2912			
323	-3.1224			

3.3. Effect of initial concentrations and contact time on adsorption

Time is one of the most significant factors used in planning and operating of treatment. In Figures 6-8, MB removal from the solutions is extremely fast at the initial period, while the velocity in final period reaches of balance decreases. The equilibrium time in dye adsorption was found as 120 min for MB removal from the solutions. Figures 6-8 show that increase in initial concentration of MB caused an increment in the adsorption capacity for all three temperatures. As the initial MB concentration increased from 10 to 60 mg/L, capacity of MB adsorption on ALP increased from 1.46 to 9.24 mg/g, 1.61 to 9.71 mg/g and 1.89 to 10.71 mg/g for 298 K, 308 K and 323 K, respectively. This data shows that initial concentration plays a critical role in adsorption capacity, which provides a driving force for the adsorption. According to the experimental results, the maximum dye adsorption rate was obtained with 60 mg/L initial dye concentration. In the present study, MB adsorption on ALP has similarity. When the results of the present study were compared to those in the literature, it was determined that dye adsorption capacity of ALP is good and it may be a novel material used as an inexpensive adsorbent for dye removal.

**Figure 6.** Effect of time and concentration of MB removal with ALP at 298 K**Figure 7.** Effect of time and concentration of MB removal with ALP at 308 K**Figure 8.** Effect of time and concentration of MB removal with ALP at 323 K

3.4. Adsorption kinetics studies

Kinetic models were applied to check the experimental results of adsorbates adsorption on adsorbents. Adsorption kinetics of dyes is important when choosing the best test circumstances for the separation process [33]. In the present study, the kinetics of MB were calculated by using PFO, PSO and IPD models. The best-suited model was chosen depending on the R^2 coefficient values. The models were examined according to the experimental data at varied temperatures and initial MB concentrations.

PFO kinetic model can be the first for the characterization of liquid-solid adsorption systems depending on solid capacity [33]. PFO kinetic model is given with Eq. (10);

$$\ln(q_e - q_t) = \ln q_e - k_1 t \quad (10)$$

where q_e and q_t (mg/g) values are the adsorption capacities at equilibrium and at time, respectively, and k_1 (min^{-1}) is the rate constant. PFO constants were determined from slope and intercept of the plot which prepared the $\ln(q_e - q_t)$ against t values.

The PSO kinetic model, which can be explained with the chemical bond formation between the adsorptive site and solute molecule, is a rate-limiting step based on adsorption capacity. The equation for the PSO model is given with Eq. (11);

$$t/q_t = 1/(k_2 q_e^2) + (t/q_e) \quad (11)$$

where k_2 is the rate of adsorption (g/mg min), q_e is the amount of adsorbate that adsorbed on the adsorbent at

equilibrium (mg/g) and q_t is the amount of dye adsorbed at any time (mg/g). k_2 and q_e values were determined from intercept and slope of the plot of t/q_t vs t , respectively.

IPD model was used as the rate controlling step, it was determined that the adsorption of the dyes was more gradual. According to this model the chemical or physical bond designed between solute. The equation for this model was suggested by Weber and Morris and was created by testing possibility of IPD as a rate limiting step. The IPD kinetic model is given with Eq. (12);

$$q_t = k_{ipd} t^{0.5} + C \quad (12)$$

where k_{ipd} (mg/g min^{1/2}) is the IPD constant and C gives an idea on the boundary thickness. A plot of q_t against $t^{0.5}$ at different MB concentrations gave two phases of linear plots [33].

PFO, PSO and IPD kinetic parameters are given in Table 4. Experimental results showed that R^2 coefficients of PSO were higher than 0.99 with the experimental and analyzed q_e values were very close to each other. This determined that the process best fit the PSO kinetic model. Moreover, for most dye adsorption systems kinetic data are most often better represented by PSO model. Experimental and calculated q_e values of 323 K were higher than the 298 K and 308 K values. Accordingly, it can be said that the q_e values increased with the increase in concentration of MB. When kinetic constants were compared, it was seen that the constant values were closer to both temperatures and concentrations of the PSO model [33]. This result showed that MG adsorption kinetics on ALP result from the PSO model and that the step of rate-limiting can be the dye chemisorption.

Table 4. PFO, PSO and IPD kinetic parameters of MB adsorption on ALP

Kinetic Model	Temp (K)	Kinetic Coefficients	10 (mg/L)	20 (mg/L)	30 (mg/L)	40 (mg/L)	50 (mg/L)	60 (mg/L)
PFO kinetic model	298	$q_{e \text{ exp}}(\text{mg/g})$	1.465	3.032	4.478	6.183	7.468	9.205
	308	$q_{e \text{ exp}}(\text{mg/g})$	1.613	3.245	4.948	6.705	8.078	9.708
	323	$q_{e \text{ exp}}(\text{mg/g})$	1.888	3.698	5.783	7.445	9.205	10.693
	298	$k_1(\text{min}^{-1})$	0.0152	0.0137	0.0206	0.0219	0.0283	0.0235
		$q_{e \text{ cal}}(\text{mg/g})$	1.138	1.987	2.143	3.353	5.509	6.102
		R^2	0.9483	0.9567	0.9467	0.9577	0.9153	0.9857
	308	$k_1(\text{min}^{-1})$	0.0192	0.0228	0.0241	0.0219	0.0209	0.0238
		$q_{e \text{ cal}}(\text{mg/g})$	1.651	3.159	4.033	4.761	6.736	7.844
		R^2	0.9431	0.8729	0.9734	0.9621	0.9668	0.9754
	323	$k_1(\text{min}^{-1})$	0.0235	0.0204	0.0251	0.0232	0.0258	0.0326
		$q_{e \text{ cal}}(\text{mg/g})$	1.845	2.844	5.023	5.441	6.821	10.477
		R^2	0.9122	0.9621	0.9509	0.9461	0.9781	0.9661
PSO kinetic model	298	$k_2(\text{min}^{-1})$	0.0268	0.0236	0.0213	0.0185	0.0106	0.0091
		$q_{e \text{ cal}}(\text{mg/g})$	1.547	3.168	4.585	6.349	7.800	9.634
		R^2	0.9933	0.9938	0.9992	0.9978	0.9931	0.9967
	308	$k_2(\text{min}^{-1})$	0.0176	0.0162	0.0129	0.0108	0.0062	0.0054
		$q_{e \text{ cal}}(\text{mg/g})$	1.787	3.852	5.322	7.018	8.658	10.482
		R^2	0.9962	0.9985	0.9944	0.9946	0.9919	0.9934
	323	$k_2(\text{min}^{-1})$	0.0261	0.0161	0.0101	0.0126	0.0083	0.0073
		$q_{e \text{ cal}}(\text{mg/g})$	2.010	3.887	6.165	7.711	9.709	11.299
		R^2	0.9952	0.9959	0.9958	0.9915	0.9923	0.9965
IPD kinetic model	298	$k_{ipd}(\text{mg/g.min}^{0.5})$	0.0825	0.1681	0.2167	0.2788	0.3533	0.4747
		$C(\text{mg/g})$	0.3164	0.6756	1.8343	2.6997	2.9587	3.2733
		R^2	0.9326	0.9273	0.7231	0.7218	0.7725	0.8147
	308	$k_{ipd}(\text{mg/g.min}^{0.5})$	0.1015	0.2299	0.3004	0.3533	0.4786	0.5983
		$C(\text{mg/g})$	0.2217	0.3892	1.1801	2.2021	2.8702	3.1965
		R^2	0.9497	0.9577	0.8519	0.8298	0.9053	0.8805
	323	$k_{ipd}(\text{mg/g.min}^{0.5})$	0.1016	0.1985	0.3199	0.3391	0.4944	0.5606
		$C(\text{mg/g})$	0.5385	1.1052	1.7043	2.1541	3.0591	3.7434
		R^2	0.8872	0.8701	0.8629	0.7453	0.8247	0.8217

4. Conclusion

In this work, MB adsorption on ALP was examined at various experimental conditions. The data obtained showed that adsorption of MB on ALP augmented with the rise in initial MB concentration, contact time and temperature. As the initial MB concentration changed from 10 to 60 mg/L, MB adsorption capacity on ALP enlarged from 1.46 to 9.24 mg/g, 1.61 to 9.71 mg/g and 1.89 to 10.71 mg/g for 298 K, 308 K and 323 K, respectively. The equilibrium time for MB removal with ALP was determined at 120 min.

Isotherm studies showed that Freundlich model was more suitable for MB adsorption on ALP than Langmuir and Temkin models. Parameters of all three isotherm models increased when temperature increased. In addition, it was determined that adsorption was positively affected by higher temperatures. The R^2 values of the Freundlich model for MB removal with ALP were higher than those of the other two model. q_m values of ALP were found to be 50.25, 98.04, 125.01 mg/g for 298 K, 308 K and 323 K, respectively. This result indicates that adsorption process is of an endothermic nature.

Kinetic studies showed that process of MB adsorption was best suited to PSO model and suggested that the step of rate-limiting could be the dye chemisorption. The R^2 coefficients were higher than 0.99 with the experimental and evaluated q_e values very close to each other. The kinetic constants were closer to both temperatures and concentrations, while the q_e values increased with the increase in MB concentration. Furthermore, IPD constant (k_{ipd}) and monolayer concentration (C) values increased with the upturn in temperature.

Thermodynamic parameters determined that MB adsorption on ALP occurred as an endothermic reaction. The negative ΔG° values indicated that adsorption was physisorption, while the ΔG° values suggested that adsorption was feasible and spontaneous. The absolute values of ΔG° decreased with the increase in temperature, which shows that this separation process is constructive at low temperatures. The positive values of ΔH° and ΔS° demonstrated that adsorption process was endothermic and affinity of ALP for MB. The results of the experiments clearly determined that ALP is an efficient adsorbent for the removal of MB from aqueous solution. In conclusion, ALP can be used as a prospective adsorbent for the removal of dyes in wastewaters.

Acknowledgment

The authors thanks to Van Yüzüncü Yıl University, Scientific Research Projects Commission (YYÜ BAP)

for the financial support of this research under the FAP-2019-8615 grant number.

Conflicts of interest

The authors state that did not have conflict of interests.

References

- [1] Peydayesh M., Rahbar-Kelishami A., Adsorption of methylene blue onto platanus orientalis leaf powder: kinetic, equilibrium and thermodynamic studies, *J. Ind. Eng. Chem.*, 21 (2015) 1014-1019.
- [2] Weng C. H., Lin Y. T., Tzeng T. W., Removal of methylene blue from aqueous solution by adsorption onto pineapple leaf powder, *J. Hazard. Mater.*, 170(1) (2009) 417-424.
- [3] Kallel F., Chaari F., Bouaziz F., Bettaieb F., Ghorbel R., Chaabouni S. E., Sorption and desorption characteristics for the removal of a toxic dye, methylene blue from aqueous solution by a low cost agricultural by-product, *J. Mol. Liq.*, 219 (2016) 279-288.
- [4] Gupta V. K., Suhas., Application of low-cost adsorbents for dye removal, a review, *J. Environ. Manage.*, 90 (2009) 2313-2342.
- [5] Yagub M. T., Sen T. K., Afroze S., Ang H. M., Dye and its removal from aqueous solution by adsorption, a review, *Adv. Colloid Interface Sci.*, 209 (2014) 172-184.
- [6] Forgacs E., Cserhati T., Oros G., Removal of synthetic dyes from wastewaters, a review, *Env. Int.*, 30 (2004) 953-971.
- [7] Zhou Y., Lu J., Zhou Y., Liu Y., Recent advances for dyes removal using novel adsorbents, a review, *Env. Poll.*, 252 (2019) 352-365.
- [8] Bouaziz F., Koubaa M., Kallel F., Chaari F., Driss D., Ghorbel R. E., Chaabouni S. E., Efficiency of almond gum as a low-cost adsorbent for methylene blue dye removal from aqueous solutions, *Ind. Crops and Products*, 74 (2015) 903-911.
- [9] Kausar A., Iqbal M., Javeda A., Aftab K., Nazli Z. H., Bhatti H. N., Nouren S., Adsorption using clay and modified clay, a review, *J. Mol. Liq.*, 256 (2018) 395-407.
- [10] Mahmoodi N. M., Hayati B., Arami M., Lan C., Adsorption of textile dyes on pine cone from colored wastewater: kinetic, equilibrium and thermodynamic studies, *Desalination*, 268(1-3) (2011) 117-125.
- [11] Debnath S., Ballav N., Maity A., Pillay K., Competitive adsorption of ternary dye mixture using pine cone powder modified with β -cyclodextrin, *J. Mol. Liq.*, 225 (2017) 679-688.

- [12] Miyah Y., Lahrichi A., Idrissi M., Khalil A., Zerrouq F., Adsorption of methylene blue dye from aqueous solutions onto walnut shells powder: Equilibrium and kinetic studies, *Surfaces and Interfaces*, 11 (2018) 74-81.
- [13] Singh N. B., Nagpal G., Agrawal S., Rachna., Water purification by using adsorbents, a review, *Env. Tech. & Innov.*, 11 (2018) 187-240.
- [14] Jin Y., Zeng C., Lü Q-F, Yu Y., Efficient adsorption of methylene blue and lead ions in aqueous solutions by 5-sulfosalicylic acid modified lignin, *Int. J. Biol. Macromol.*, 123 (2019) 50-58.
- [15] De Gisi S., Lofrano G., Grassi M., Notarnicola M., Characteristics and adsorption capacities of low-cost sorbents for wastewater treatment, a review, *Sust. Materials Tech.*, 9 (2016) 10-40.
- [16] Değermenci G. D., Değermenci N., Ayvaoğlu V., Durmaz E., Çakır D., Akan E., Adsorption of reactive dyes on lignocellulosic waste; characterization, equilibrium, kinetic and thermodynamic studies, *J. Clean. Prod.*, 225 (2019) 1220-1229.
- [17] Bouaziz F., Koubaa M., Kallel F., Ghorbel R. E., Chaabouni S. E. Adsorptive removal of malachite green from aqueous solutions by almond gum: kinetic study and equilibrium isotherms, *Int. J. Biol. Macromol.*, 105(1) (2017) 56-65.
- [18] Adegoke K. A., Bello, O. S., Dye sequestration using agricultural wastes as adsorbents, *Water Resour. Ind.*, 12 (2015) 8-24.
- [19] Bulgariu L., Escudero L. B., Bello O. S., Iqbal M., Nisar J., Adegoke K. A., Alakhras F., Kornaros M., Anastopoulos I., The utilization of leaf-based adsorbents for dyes removal, a review, *J. Mol. Liq.*, 276 (2019) 728-747.
- [20] Bedin K. C., Martins A. C., Cazetta A. L., Pezoti O., Almeida V. C., KOH-activated carbon prepared from sucrose spherical carbon: adsorption equilibrium, kinetic and thermodynamic studies for methylene blue removal, *Chem. Eng. J.*, 286 (2016) 476-484.
- [21] Hamed M. M., Ahmed I. M., Metwally S. S., Adsorptive removal of methylene blue as organic pollutant by marble dust as eco-friendly sorbent, *J. Ind. Eng. Chem.*, 20(4) (2014) 2370-2377.
- [22] Liu T., Li Y., Du Q., Sun J., Jiao Y., Yang G., Wang Z., Xia Y., Zhang W., Wang K., Zhu H., Wu D., Adsorption of methylene blue from aqueous solution by graphene, *Colloids Surf. B Bio.*, 90 (2012) 197-203.
- [23] Ojha A. K., Bulasara V. K., Adsorption characteristics of jackfruit leaf powder for the removal of Amido black 10B dye, *Env. Prog. & Sust. Energy*, 34(2) (2015) 461-470.
- [24] Han X., Wang W., Ma X., Adsorption characteristics of methylene blue onto low cost biomass material lotus leaf, *Chem. Eng. J.*, 171(1) (2011) 1-8.
- [25] Gouamid M., Ouahrani M. R., Bensaci M. B., Adsorption equilibrium, kinetics and thermodynamics of methylene blue from aqueous solutions using date palm leaves, *Enrgy. Proced.*, 36 (2013) 898-907.
- [26] Setiabudi H. D., Jusoh R., Suhaimi S. F. R. M., Masrur S. F., Adsorption of methylene blue onto oil palm (*Elaeis guineensis*) leaves: process optimization, isotherm, kinetics and thermodynamic studies, *J. Taiwan Inst. of Chem. Eng.*, 63 (2016) 363-370.
- [27] Bhattacharyya K., Sharma A., Kinetics and thermodynamics of methylene blue adsorption on neem leaf powder, *Dyes and Pigments*, 65(1) (2005) 51-59.
- [28] Franca A. S., Oliveira L. S., Ferreira M. E., Kinetics and equilibrium studies of methylene blue adsorption by spent coffee grounds, *Desalination*, 249(1) (2009) 267-272.
- [29] Rangabhashiyam S., Anu N., Nandagopal M. S. G., Selvaraju N., Relevance of isotherm models in biosorption of pollutants by agricultural by products, *J. Env. Chem. Eng.*, 2(1) (2014) 398-414.
- [30] Khodabandehloo A., Rahbar-Kelishami A., Shayesteh H., Methylene blue removal using salix babylonica (weeping willow) leaves powder as a low-cost biosorbent in batch mode: Kinetic, equilibrium, and thermodynamic studies, *J. Mol. Liq.*, 244 (2017) 540-548.
- [31] Rida K., Bouraoui S., Hadnine S., Adsorption of methylene blue from aqueous solution by kaolin and zeolite, *App. Clay. Sci.*, 83 (2013) 99-105.
- [32] Rafatullah M., Sulaiman O., Hashim R., Ahmad A., Adsorption of methylene blue on low-cost adsorbents, a review, *J. Hazard. Mater.*, 177(1-3) (2010) 70-80.
- [33] Ponnusami V., Gunasekar V., Srivastava S. N., Kinetics of methylene blue removal from aqueous solution using gulmohar (*Delonix regia*) plant leaf powder: Multivariate regression analysis, *J. Hazard. Mater.*, 169 (2009) 119-127.
- [34] Kul A., Koyuncu H., Adsorption of Pb(II) ions from aqueous solution by native and activated bentonite: Kinetic, equilibrium and thermodynamic study, *J. Hazard. Mater.*, 179 (2010) 332-339.

Computational study on molecular structure, vibrational spectrum analysis and acidity strength of P_4O_n ($n = 6-10$) phosphorus oxides with cage structure

Duran Karakaş^{1*} 

¹ Sivas Cumhuriyet University, Faculty of Science, Department of Chemistry, 58140, Sivas/TURKEY

Abstract

In this study, molecular structure, IR spectra and acidity strength of P_4O_n ($n = 6-10$) type phosphorus oxides with cage structure were investigated at the PBE1PBE/6-311+G(2d) level. Structural parameters and IR spectra of oxides were obtained from optimized structures. From the structural parameters and IR spectra, P_4O_6 and P_4O_{10} molecules were found in T_d symmetry, P_4O_7 and P_4O_9 molecules in C_{3v} symmetry and P_4O_8 molecule in C_{2v} symmetry. Symmetry labeling of the peaks in the IR spectra of oxides was performed. To predict the acidity strength of the oxides in the gas phase, the protonated species were optimized at the PBE1PBE/6-311+G(2d) level. Proton affinity values were calculated using the total energies of neutral and protonated species. Acidity strength ranking according to proton affinity values was obtained as $P_4O_6 < P_4O_7 < P_4O_8 < P_4O_9 < P_4O_{10}$.

Article info

History:

Received:16.04.2020

Accepted:06.08.2020

Keywords:

Computational study, phosphorus oxides, molecular structures, acidity strength.

1. Introduction

Tetraphosphorus hexaoxide (P_4O_6) is obtained from the reaction of white phosphorus (P_4) in tetrahedral geometry with a limited amount of oxygen, and tetrophosphorus decoxide (P_4O_{10}) from its reaction with excessive oxygen. It has been reported that intermediate compounds such as P_4O_7 , P_4O_8 and P_4O_9 can also be synthesized under controlled conditions [1,2].

The molecular structures of P_4O_6 and P_4O_{10} compounds have been determined in previous studies and have been found to have a white phosphorus structure [3,4]. P_4O_6 molecule is formed by the introduction of oxygen atoms between adjacent phosphorus atoms in the white phosphorus structure. The difference of P_4O_{10} molecule from P_4O_6 is that each phosphorus atom contains a terminal oxygen atom. In P_4O_7 , P_4O_8 and P_4O_9 compounds, one, two, and three of the phosphorus atoms have terminal oxygen atoms, respectively [5].

Phosphorus compounds and oxygen atoms give chemiluminescence reactions and form the basis of laser systems [6,7]. Therefore, P_4O_{10} is used in the development of high energy laser lenses [8]. Also, since these compounds contain cages, they are used as host materials for the vitrification of nuclear waste [9].

P_4O_{10} is a powerful dehydrating agent and is used in desiccators as desiccant. H_3PO_4 is formed as a result of the hydrolysis reaction of P_4O_{10} . Phosphoric acid is used in the pharmaceutical industry, oil industry, insecticide production and for various cleaning purposes. It is used in cola and baking powders in the food industry. It participates in the structure of DNA and RNA. It is found in the structure of all nucleotides. Phosphoric acid, an inorganic compound, is the group that imparts acidic properties to nucleic acids [10].

The acidity strength of a chemical species depends on two main factors: itself and its environment. The acidity force arising from the species itself is obtained from the proton affinity values measured in the gas phase. The higher the value of the proton affinity, the higher the basicity of the species, the weaker the conjugate acid [11].

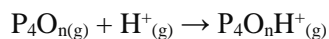
Molecular orbital theory can also be used to predict acidity or basicity of chemical species. According to the molecular orbital theory, the acidity of a molecule depends on LUMO energy and its basicity depends on HOMO energy. The species with low LUMO energy are acidic. The species with high HOMO energy and with non-binding molecular orbitals act as bases [12]. In this study, we aimed to predict the molecular structure and acidity strength of P_4O_n ($n=6-10$) type oxides. For this purpose, neutral phosphorus oxides

*Corresponding author. Email address: dkarakas@cumhuriyet.edu.tr

and their protonated species were optimized at the PBE1PBE/6-311+G(2d) level. Bond lengths, bond angles, IR spectra of neutral oxides were obtained from the optimized structures. Proton affinity of the oxides was calculated from the total energies of neutral and protonated species and acidity strength sequences were estimated.

2. Methods and techniques

Molecular structures of P_4O_n ($n = 6-10$) phosphorus oxides with cage type were drawn in GaussView 6.0.16 program [13]. Phosphorus oxides were optimized at PBE1PBE/6-311G(2d) level with the Gaussian 09: AS64L-G09RevD.01 program [14]. PBE1PBE is a pure functional of density functional theory (DFT) developed in 1996 by Perdew, Burke and Ernzerhof [15]. This functional was transformed into a hybrid functional by Adamo [16] and shown with the PBE1PBE keyword. This hybrid functional uses 25% exact exchange and 75% DFT exchange. It is known in the literature as PBE0 [16] and PBE hybrid [17]. 6-311+G(2d) is a basis set with high angular momentum. Such basis sets add multiple polarized functions per atom and diffuse functions to heavy atoms [18]. The reason for choosing such a level in this study is that the vibration spectra of P_4O_6 and P_4O_{10} oxides were studied by P. Carbonniere and C. Pouchan. In their study, benchmark analysis was done and PBE1PBE/6-311+G(2d) level was found as the best level [1]. Bond lengths, bond angles and vibrational spectrum analysis were performed from the optimized structures of neutral phosphorus oxides. To calculate the proton affinity of phosphorus oxides, a proton was added to the atom with the most negative charge and the total energy was calculated. As shown in Equation (1), the proton affinity in the energies of neutral and protonated species was determined [18].



$$PA = E(P_4O_n) - E(P_4O_nH^+) \quad (1)$$

3. Findings and Discussion

3.1. Optimized structures of phosphorus oxides

The structures of P_4O_n ($n = 6-10$) type phosphorus oxides drawn in GaussView 6.0.16 program were optimized in the gas phase at the level of PBE1PBE/6-311+G(2d) in Gaussian 09 calculation program. Optimized structures are given in Fig. 1 with atomic labeling. Bond lengths and bond angles obtained from the optimized structures in Fig. 1 are given in Table 1.

Experimental values in Table 1 are taken from reference [1]. Only one of the equivalent bond lengths and bond angles was shown.

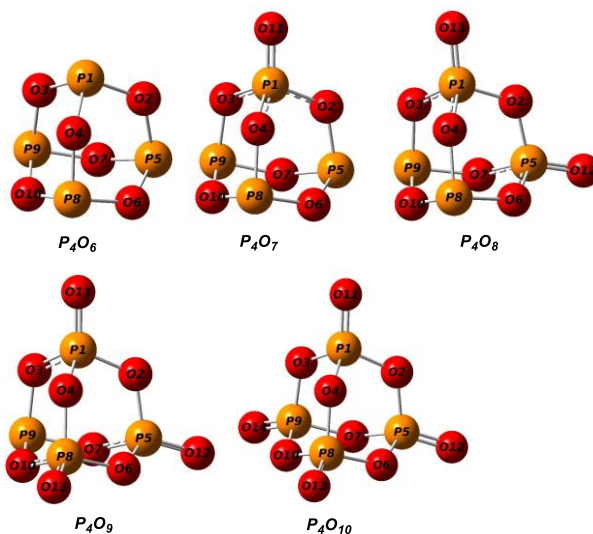


Fig. 1 Optimized structures of P_4O_n ($n = 6-10$) phosphorus oxides with cage type.

As seen in Fig. 1, P1-O11, P5-O12, P8-O13 and P9-O14 bonds show the bonding of terminal oxygen with phosphorus. These bonds are equivalent length and are shown in Table 1 as P1-O11 and their length is given as approximately 1.44 Å. Other P-O bonds belong to bridge oxygen. P-Ob bond lengths vary between 1.60-1.66 Å. This difference between P-Ot and P-Ob lengths is explained by the formation of π -bonds. π -bond is formed between terminal oxygen $p\pi$ -orbital and phosphorus atom $d\pi$ -orbital. π -bond formation causes the P-Ot bond to be shorter.

The change of P-Ob bond lengths between 1.60-1.66 Å in P_4O_7 and P_4O_8 is due to their distance from terminal oxygen. It can be seen from Table 1 and Figure 1 that the P-Ob bond, which is farther away from the terminal oxygen atom, is longer than the closer one.

As can be seen from Table 1, there are three types of bond angles for phosphorus oxides ranging from about 100, 115 and 122-127 degrees. Ob-P-Ob bond angles are approximately 100 degrees, Ob-P-Ot bond angles are about 115 degrees and P-Ob-P bond angles range from 122-127 degrees. These angles neither belong to the ideal tetrahedral geometry nor the ideal triangular plane. Therefore, the geometries of oxides are given by symmetry point groups. Considering the symmetry operation of the molecules, it was found that P_4O_6 and P_4O_{10} are in the T_d symmetry point group, P_4O_7 and P_4O_9 are in the C_{3v} symmetry point group and P_4O_8 in the C_{2v} symmetry point group.

Table 1 Molecular structure parameters of phosphorus oxides calculated at PBE1PBE/6-311+G(2d) level in gas phase

Molecule	Bond	Length (Å)	Exp. [1]	Bond	Angle (°)	Exp. [1]
P ₄ O ₆	P1-O2	1.654	1.638	O2-P1-O3	100.0	99.8
	-	-	-	P1-O2-P5	126.1	126.7
P ₄ O ₇	P1-O2	1.602	1.644	O2-P1-O3	103.0	-
	P5-O2	1.668	1.684	O2-P5-O6	99.3	-
	P5-O6	1.651	1.595	O2-P1-O11	115.3	-
	P1-O11	1.443	1.450	P1-O4-P8	124.1	-
	-	-	-	P5-O7-P9	126.6	-
P ₄ O ₈	P1-O2	1.612	1.633	O2-P1-O3	102.3	-
	P1-O3	1.601	1.668	O3-P1-O4	103.1	-
	P8-O4	1.665	1.576	O2-P1-O11	115.2	-
	P8-O10	1.649	1.596	O3-P1-O11	115.9	-
	P1-O11	1.440	1.414	P1-O2-P5	122.7	-
	-	-	-	P1-O4-P8	124.4	-
	-	-	-	P8-O10-P9	127.1	-
P ₄ O ₉	P1-O2	1.611	1.661	O2-P1-O3	102.3	-
	P1-O3	1.602	1.605	O2-P1-O4	102.1	-
	P1-O11	1.438	1.418	O2-P1-O11	115.6	-
	-	-	-	O3-P1-O11	116.7	-
	-	-	-	O3-P9-O7	99.2	-
	-	-	-	P1-O2-P5	122.9	-
	-	-	-	P1-O3-P9	124.5	-
P ₄ O ₁₀	P1-O2	1.610	1.604	O2-P1-O11	116.1	116.5
	P1-O11	1.436	1.429	O2-P1-O3	102.0	101.6
	-	-	-	P1-O2-P5	122.8	123.5

Table 2 Basic vibration modes of phosphorus oxides and IR active modes.

Molecule	Point group	Fundamental vibration modes	IR active modes	Peak number
P ₄ O ₆	T _d	1A ₁ +2E+2T ₁ +4T ₂	4T ₂	4
P ₄ O ₇	C _{3v}	7A ₁ +2A ₂ +9E	7A ₁ +9E	16
P ₄ O ₈	C _{2v}	10A ₁ +5A ₂ +7B ₁ +8B ₂	10A ₁ +7B ₁ +8B ₂	25
P ₄ O ₉	C _{3v}	7A ₁ +4A ₂ +11E	7A ₁ +11E	18
P ₄ O ₁₀	T _d	3A ₁ +3E+3T ₁ +6T ₂	6T ₂	6

3.2. IR spectra of phosphorus oxides and symmetry labeling of peaks

IR spectra were calculated at the optimization level and symmetry labeling of the peaks was performed to test the correctness of the molecular structure of phosphorus oxides. Symmetry species of the basic vibrational modes of molecules, IR active modes and expected peak numbers in the IR spectrum were obtained by symmetry application [19] and are given in Table 2.

As seen in Table 2, the vibration modes A₂, E and T₁ of the molecules in the T_d point group and A₂ vibration

modes of the molecules in the C_{3v} and C_{2v} point group are IR inactive. Peak intensities of vibration modes with IR inactive are zero. Therefore, IR inactive modes do not generate peaks. When the peak intensities of the vibration modes with IR active below a certain value, they do not generate peaks. Therefore, fewer peaks are observed in the IR spectrum than expected.

P₄O₆ and P₄O₁₀ molecules are in the T_d point group. In the T_d point group, only T₂ symmetry modes is IR active. Since the T₂ symmetry species is triple degenerate, four peaks are expected in the IR spectrum of the P₄O₆ molecule and six peaks in the IR spectrum of the P₄O₁₀ molecule

P_4O_7 and P_4O_9 molecules are in the C_{3v} point group. A_2 modes of molecules in C_{3v} point group are IR inactive, A_1 and E modes are IR active. E is a double degenerate symmetry type. Sixteen peaks are expected in the IR spectrum of P_4O_7 molecule and eighteen peaks in P_4O_9 . P_4O_8 molecule is in the C_{2v} point group. A_2 modes of molecules in the C_{2v} point group are IR inactive and other vibration modes are IR active. Therefore, 25 peaks are expected in the IR spectrum. In this study, IR spectra of the phosphorus oxides were calculated in gas phase at PBE1PBE/6-311+G(2d) level. Peaks with intensity greater than 10 km/mol [20] are given with their labels in Figure 2.

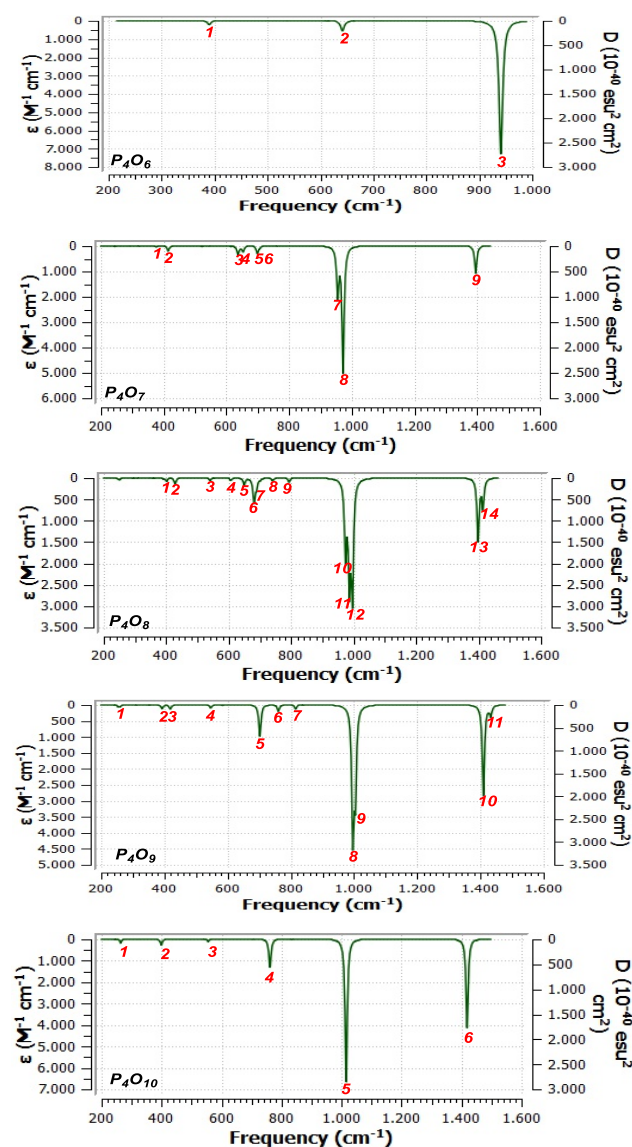


Fig. 2 IR spectra of phosphorus oxides calculated at PBE1PBE/6-311+G(2d) level.

As seen in Figure 2, while four peaks are expected in the IR spectrum of P_4O_6 molecule, three peaks are calculated. This is because the peak intensity of one of the vibration modes in the T_2 symmetry is greater than

zero but less than 10 km/mol. The same is true for other molecules except P_4O_{10} . In P_4O_{10} , the expected peak number was equal to the calculated peak number. The vibration modes, frequencies and symmetry labeling of the peaks in Figure 2 are given in Table 3.

As seen in Table 3, around 1400 cm^{-1} peaks were obtained for P_4O_7 , P_4O_8 , P_4O_9 and P_4O_{10} molecules. This peak belongs to the P-Ot stretching vibration. For P_4O_{10} , this peak was calculated comparatively at 1418 cm^{-1} and experimentally observed at 1406 cm^{-1} [21]. These results are quite compatible with each other. Since this bond is not in the P_4O_6 molecule, no IR peak around 1400 cm^{-1} was observed. Since the P-Ot bond has a double bond character, it occurs at high frequency, that is, in the double bond stretching region. Other P-Ob bonds have a single bond character. Therefore, it appeared at low frequency, that is, in the single bond stretching region.

Both the compatibility of molecular structure parameters with experimental values and IR spectrum analyzes show that the point groups and structures of molecules are determined correctly.

3.3 Proton affinities and acidity strengths of phosphorus oxides

Proton affinity was calculated for prediction the acidity strength of oxides. To calculate proton affinity, a proton was connected to the atom with the most negative charge, it was optimized and the total energy was calculated. The most negative formal charged atom was determined by considering Mulliken charges. Mulliken charges of atoms are given in Fig. 3.

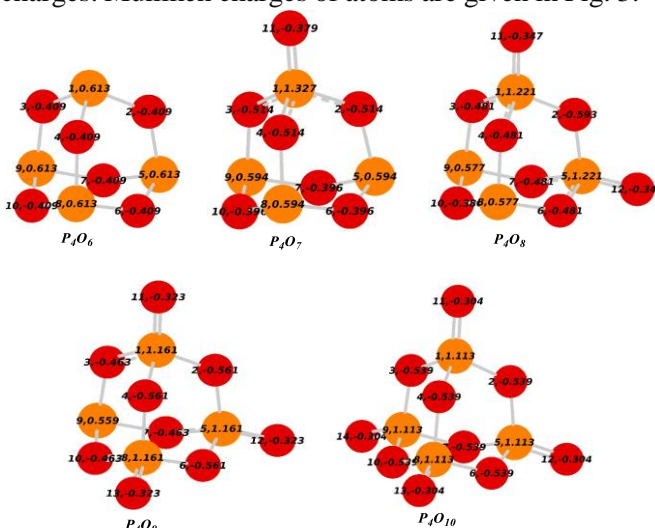


Fig. 3 Mulliken charges of atoms calculated at PBE1PBE/6-311+G(2d) level in gas phase.

As seen in Figure 3, P_4O_6 can be protonated from any oxygen atom and P_4O_{10} any of the bridge oxygen atoms. P_4O_7 can be protonated from one of the oxygen

atoms numbered with 2, 3 or 4, P_4O_8 oxygen atom numbered with 2, and P_4O_9 any of the oxygen atoms numbered with 2, 4 and 6. According to the Equation

(1), the proton affinity were calculated from the total energies of the neutral and protonated species and given in Table 4.

Table 3 Vibration modes, frequencies and symmetry labeling of phosphorus oxides computed at PBE1PBE/6-311+G(2d) level

Peak	Modes	Freq. (cm ⁻¹)	Symmetry	Peak	Modes	Freq. (cm ⁻¹)	Symmetry
P₄O₆				P₄O₉			
1	6,7,8	391.6	T ₂	1	6	259.9	A ₁
2	16,17,18	646.3	T ₂	2	11,12	392.2	E
3	22,23,24	942.6	T ₂	3	14	418.9	A ₁
P₄O₇				4	15	545.8	A ₁
1	8	375.5	A ₁	5	20,21	701.8	E
2	9,10	413.4	E	6	22	759.7	A ₁
3	16	635.8	A ₁	7	25,26	813.7	E
4	17,18	651.6	E	8	28,29	996.4	E
5	19,20	698.3	E	9	30	1003.8	A ₁
6	21	705.7	A ₁	10	31,32	1409.5	E
7	24	955.0	A ₁	11	33	1432.7	A ₁
8	25,26	972.3	E	P₄O₁₀			
9	27	1395.3	A ₁	1	6,7,8	264.4	T ₂
P₄O₈				2	11,12,13	400.8	T ₂
1	11	401.1	A ₁	3	18,19,20	555.8	T ₂
2	12	428.7	B ₁	4	22,23,24	769.6	T ₂
3	14	541.2	A ₁	5	30,31,32	1018.1	T ₂
4	16	606.3	A ₁	6	33,34,35	1418.4	T ₂
5	17	649.8	A ₁				
6	18	681.3	B ₂				
7	19	689.2	B ₁				
8	22	740.3	B ₁				
9	25	793.9	A ₁				
10	26	973.9	B ₂				
11	27	986.5	A ₁				
12	28	996.3	B ₁				
13	29	1398.6	B ₂				
14	30	1414.1	A ₁				

Table 4 Total energies and proton affinity (PA) of phosphorus oxides calculated at PBE1PBE/6-311+G(2d) level in gas phase

Molecule	E(neutral) (Hartree)	E(protonated) (Hartree)	PA (eV)
P ₄ O ₆	-1816.211019	-1816.495185	7.73
P ₄ O ₇	-1891.431078	-1891.701142	7.35
P ₄ O ₈	-1966.646769	-1966.894749	6.75
P ₄ O ₉	-2041.857303	-2042.089442	6.32
P ₄ O ₁₀	-2117.061515	-2117.277013	5.86

As can be seen from Table 4, as the number of terminal oxygen atoms increases, the proton affinity decreases. Acidity increases as proton affinity decreases. Because, according to the Lowry-Bronsted acid base definition, the acidity of a species depends on the tendency to give protons. According to this definition, the species that can give proton acts as acid and the

species that can take proton acts as base. The tendency to give protons is inversely proportional to the proton interest. According to the proton affinity values, the acidity strength of phosphor oxides with cage structure is as follows:



It can be said that the P_4O_{10} molecule is a strong dehydration agent and the formation of H_3PO_4 as a result of its hydrolysis is related to its acidity strength.

4. Conclusions

As a result of this study, molecular structures, molecular structure parameters and IR spectra of phosphorus oxides were calculated. Calculations were made at the PBE1PBE/6-311+G(2d) level. It was found that P_4O_6 and P_4O_{10} molecules are in the T_d point group, P_4O_7 and P_4O_9 molecules in the C_{2v} point group and P_4O_8 molecule in the C_{2v} point group. Symmetry labeling of the peaks in the IR spectra of the studied molecules was performed. Protonated species were also optimized at the computation level. Proton affinity values were calculated using the total energies of neutral and protonated species. Acidity strength ranking according to proton affinity values was obtained as $P_4O_6 < P_4O_7 < P_4O_8 < P_4O_9 < P_4O_{10}$.

References

- [1] Carbonniere, P., Pouchan, C. Vibrational spectra for P_4O_6 and P_4O_{10} systems: Theoretical study from DFT quartic potential and mixed perturbation-variation method, *Chemical Physics Letters*, 462(4-6) (2008) 169-172.
- [2] Mielke, Z., Andrews, L. Infrared spectra of phosphorus oxides in solid argon. *The Journal of Physical Chemistry*, 93(8) (1989) 2971-2976.
- [3] Jansen, M., Moebs, M. (1984). Structural investigations on solid tetra phosphorus hexa oxide, *Inorganic Chemistry*, 23(26), 4486-4488.
- [4] Beattie, I. R., Ogden, J. S., Price, D. D. The characterization of molecular vanadium oxide (V_4O_{10}), an analog of phosphorus oxide (P_4O_{10}). *Inorganic Chemistry*, 17(11) (1978) 3296-3297.
- [5] Sharma, B. D. Phosphorus (V) oxides, *Inorganic Chemistry*, 26(3) (1987) 454-455.
- [6] Fraser, M. E., Stedman, D. H. Spectroscopy and mechanism of chemiluminescent reactions between group V hydrides and ozone, *Journal of the Chemical Society, Faraday Transactions 1: Physical Chemistry in Condensed Phases*, 79(2) (1983) 527-542.
- [7] Harris, D. G., Chou, M. S., Cool, T. A. Experiments concerning phosphorus chemiluminescence, *The Journal of chemical physics*, 82(8) (1985) 3502-3515.
- [8] Karabulut, M., Marasinghe, G. K., Click, C. A., Metwalli, E., Brow, R. K., Booth, C. H., Campbell, J. H. XAFS investigation of platinum impurities in phosphate glasses, *Journal of the American Ceramic Society*, 85(5) (2002) 1093-1099.
- [9] Marasinghe, G. K., Karabulut, M., Ray, C. S., Day, D. E., Shuh, D. K., Allen, P. G., Haefner, D. Properties and structure of vitrified iron phosphate nuclear wasteforms, *Journal of Non-Crystalline Solids*, 263 (2000) 146-154.
- [10] Seidell, A., Linke, W. F. Solubilities of Inorganic and Organic Compounds/Supplement. Van Nostrand, (1952).
- [11] Speranza, M. The reactivity of heteroaromatic compounds in the gas phase, *In Advances in heterocyclic chemistry*, 40 (1986) 25-104. Academic Press.
- [12] Kaya, C. *İnorganik kimya 2*. Palme Yayıncılık (2011).
- [13] Dennington, R. D., Keith, T. A., Millam, J. M. (2016). GaussView 6.0. 16, Semichem. Inc., Shawnee Mission KS.
- [14] Gaussian09, R. A. (2009). M.J. Frisch, G.W. Trucks, H.B. Schlegel, G.E. Scuseria, M.A. Robb, J.R. Cheeseman, G. Scalmani, V. Barone, B. Mennucci, G.A. Petersson et al., Gaussian, Inc., Wallingford CT, 2013.
- [15] Perdew, J. P., Burke, K., Ernzerhof, M. Generalized gradient approximation made simple, *Physical review letters*, 77(18) (1996) 3865.
- [16] Adamo, C., Barone, V. Toward reliable density functional methods without adjustable parameters: The PBE0 model, *The Journal of chemical physics*, 110(13) (1999) 6158-6170.
- [17] Ernzerhof, M., Scuseria, G. E. Assessment of the Perdew–Burke–Ernzerhof exchange–correlation functional, *The Journal of chemical physics*, 110(11) (1999) 5029-5036.
- [18] Foresman, J.B., Frisch, A.E., *Exploring Chemistry with Electronic Structure Methods*, Sec. Ed., Gaussian, Inc., Pittsburg, PA, (1993).
- [19] Kaya, C., Karakaş, D. *Moleküler simetri*. Palme Yayıncılık, 2010.
- [20] Karakaş, D., Kariper, S. E. Theoretical investigation on the vibrational and electronic spectra of three isomeric forms of dicobalt octacarbonyl. *Journal of Molecular Structure*, 1062 (2014) 77-81.
- [21] Beattie, I. R., Livingston, K. M. S., Ozin, G. A., Reynolds, D. J. Single-crystal Raman spectra of arsenolite (As_4O_6) and senarmonite (Sb_4O_6). The gas-phase Raman spectra of P_4O_6 , P_4O_{10} , and As_4O_6 . *Journal of the Chemical Society A: Inorganic, Physical, Theoretical*, (1970) 449-451.

Evaluation of tetracycline, oxytetracycline and penicillin G residues in chicken meat samples by high performance liquid chromatography with pda detection

Fatoş Ayça ÖZDEMİR OLGUN^{1,*} Birsen DEMİRATA ÖZTÜRK¹

¹ Istanbul Technical University, Faculty of Science and Letters, Department of Chemistry, Maslak, Sariyer, Istanbul, Turkey

Abstract

Penicillin G, tetracycline and oxytetracycline are broad-spectrum antibiotics with considerably low side effects which are used in most of the poultries. Due to complex matrix effects, it is considerably difficult to isolate these compounds from other molecules (such as proteins and lipids) in order to analyze. In this study, a high performance liquid chromatography (HPLC) coupled with photodiode array (PDA) detector system was introduced for the determination of tetracycline, oxytetracycline and penicillin G residues in nine chicken breast samples. For the separation of tetracycline and oxytetracycline out of samples prior to the analysis, trichloroacetic acid (TCA) and McIlvaine buffer solutions were used while formic acid and phosphate buffer solutions were utilized for penicillin G using a solid phase extraction system. The peaks at the chromatograms were enlightened and recovery percentages were calculated using spiked samples (96.57% for penicillin G; 99.00% for oxytetracycline; 95.92% for tetracycline). LOD and LOQ values were calculated, respectively as 1.55 µg L⁻¹ and 5.20 µg L⁻¹ for tetracycline; 1.32 µg L⁻¹ and 4.39 µg L⁻¹ for oxytetracycline; 1.07 µg L⁻¹ and 3.60 µg L⁻¹ for penicillin G. With the proposed method, the determination of three antibiotic residues was performed in less than 15 minutes and applied successfully to real samples.

Article info

History:

Received:20.04.2020

Accepted:04.08.2020

Keywords:

Antibiotic residue, analysis, hplc-pda, solid phase extraction.

1. Introduction

Chicken meat is one of the most consumed meat products around the world, with its low-cost, high protein content and health-friendly properties [1]. Antibiotics are the compounds synthesized through bacteria or fungicide and employed for the medical treatments such as chemotherapeutic and prophylactic properties [2]. The first antibiotic treatment in animals was at 1940s for medical issues [3]. However, once their effects on growth and feed efficiency were discovered, chicken meat production industry accelerated their usage. Taking the advantage of anabolic effects of antibiotics, caused bacteria resistance both at animals and humans consuming animal products of these animals. Therefore, at the beginning of 1970s, European Union started to control these substances regarding to the maximum amount of metabolites (originated from veterinary pharmaceuticals) found in a food product, defined as maximum residue limits (MRL). There are many

reasons to monitor residues of antibiotics in animal products as; excess usage of antibiotics, marketing and slaughter of animals after a short time period of medical treatment, taking maximum efficiency by mixing the feed with antibiotics or misuse. Whatever the reason is, MRL of antibiotics found in animal products should be determined and evaluated with respect to regulations [4]. Most commonly used antibiotics in poultries are penicillin G, tetracycline and oxytetracycline that are broad-spectrum antibiotics with considerably low side effects [5,6]. Microbial or immunological assays seem to be the most preferred methods for monitoring MRL in meat samples, as they are low-cost and fast. However, the most important drawback is that they are too specific on one target analyze. There have been several studies on the determination of antibiotics in animal products using various methods such as LC, LC-MS/MS, HPLC and HPLC with fluorescence detection [7-12]. Liquid chromatographic methods with their simultaneous separation and minimum matrix effects especially in

*Corresponding author. Email address: ozdemirfa@itu.edu.tr

<http://dergipark.gov.tr/csj> ©2020 Faculty of Science, Sivas Cumhuriyet University

drug analyses, are the most preferred analytical techniques [13].

Sample preparation step is the most important part of providing a promising and accurate method in complex matrixes such as meat. Poultry meat, just as other meat samples, contain high amount of protein and lipid making the extraction part of the target molecules challenging [14]. Among many procedures, liquid extraction in combination with solid phase extraction (SPE) system was utilized, as it is suitable for tetracycline, oxytetracycline and penicillin G and ensures the accuracy.

In this study, determination of tetracycline, oxytetracycline and penicillin G by HPLC-PDA method with photo diode array detection system enabling to monitor both chromatogram and spectrum of a sample was used to analyze antibiotic residues in nine chicken breast samples. Solid phase extraction system was used to isolate the antibiotics out of real samples. Limit of detection, limit of quantification, recovery percentages were calculated in order to validate the method.

2. Materials and Methods

2.1. Chemicals and apparatus

Standards of tetracycline, oxytetracycline and penicillin G were all purchased from Aldrich. HPLC-grade solutions such as methanol, acetonitrile with citric acid monohydrate and ammonium acetate were purchased from E. Merck. J.T. Baker's oxalic acid dihydrate, trichloroacetic acid, disodiumhydrogen phosphate dihydrate, potassiumphosphate dibasic and potassium hydrogen phosphate were used for the experiments. Formic acid and Na salt of EDTA were purchased from Carlo Erba. During experiments, as it is required for the installation of HPLC, ultrapure water was used.

2.1.1. Preparation of Solutions

McIlvaine buffer solution (pH=4) was prepared dissolving 2.95 g of citric acid monohydrate and 3.43 g disodiumhydrogen phosphate dihydrate and 8.41 g etilendiamintetraacetic acid sodiumsalt in 250 mL ultra-pure water [15].

Phosphate buffer solution (pH=8.5) was prepared dissolving potassiumphosphate dibasic in 250 mL ultra-pure water.

Solutions to be used in sample preparation step were prepared as follows; 20% (w/v) TCA solution, 5% (v/v) MeOH solution, 0.1% (v/v) formic acid solution, 0.03 M methanolic oxalic acid solution, 0.025 M KH_2PO_4 solution.

Stock solutions of tetracycline, oxytetracycline and penicillin G at 1000 mgL^{-1} concentration levels were prepared in methanol and standard solutions at desired concentration levels were obtained by appropriate dilutions.

2.2. Sample preparation by solid phase extraction (SPE) system

Eight chicken breast samples of the most popular companies were purchased from local markets found in Istanbul, Turkey. The organic chicken breast sample was purchased from a local poultry farm found in a village of Catalca, Turkey. The samples were labeled with capital letters (from A to I) for a better understanding. Raw meat samples were minced with mechanic blender. For tetracycline and oxytetracycline; 2.0 mL of 20% TCA buffer solution and 20.0 mL McIlvaine buffer solution were added on the homogenized meat samples at 5.0 ± 0.1 g weight, respectively and allowed to mix for 5 min. using vortex mixer. The mixtures were centrifuged for 15 min at 3500 rpm and purified using SPE system [15]. C18 cartridge was washed with 10 mL of 5% methanol solution before extraction and the analytes were eluted using 0.01M methanolic oxalic acid solution. The solvent of the final solution was evaporated with rotary and the residue was dissolved in 2.5 mL methanol, filtered through 0.45 μm PTFE membrane filters in order to be analyzed with HPLC.

For Penicillin G, 2.0 mL 20% formic acid and 20.0 mL pH8.5 phosphate buffer solutions were added to the minced raw chicken breast samples and mixed for 5 min with the aid of homogenizer. The mixture was centrifuged for 15 min at 3500 rpm. and extracted using SPE system equipped with C18 cartridge that was washed with 3.0 mL methanol and 3.0 mL of 0.1% formic acid prior and latter to extraction process. Penicilline G was eluted with 3.0 mL acetonitrile and solvent was evoparated using rotary. The residue was dissolved in 2.5 mL methanol and filtered through 0.45 μm filter to prevent any possible blockage at HPLC tubing systems.

2.3. HPLC-PDA technique

For the determination of antibiotics, two different gradient elution programs were developed and carried out. For tetracycline and oxytetracycline, the mobile phase consisted of HPLC-grade methanol (mobile phase A), HPLC-grade acetonitrile (mobile phase B) and 0.03 M oxalic acid solution (mobile phase C). Penicillin G analysis with HPLC technique was performed using a different elution program involving 50% KH_2PO_4 (A) and HPLC-grade acetonitrile (B).

The injection volume and flow rate were kept at 20 μL and 1 mLmin^{-1} , respectively. The column temperature was set to 30°C for a stable procedure of analysis. The antibiotics may be determined at their own maximum absorption wavelength in agreement with the principle of diode array detector system, however for the mutual evaluation, the wavelength was adjusted to 351nm.

Calibration equations were obtained by graphing concentration values versus peak area. For the validation of the developed methods, the experiments were performed as three replicates and validation parameters such as; regression coefficients, limit of detection (LOD) and limit of quantification (LOQ) levels with recovery percentages were calculated.

3. Results and Discussion

3.1. Determination of tetracycline, oxytetracycline and penicillin G by conventional HPLC-PDA technique

As cited in literature and observed through experiments, it is a difficult task to monitor all three antibiotics in a chromatogram due to intricate

molecular structure of tetracycline [16]. Therefore another different gradient elution program was installed individually for penicillin G. Isocratic elution program with acetonitrile and methanol is the other option for elution, however it was proved to be inefficient resulting chromatograms with indefinite retention times and asymmetric peaks (with tails). The main reason of the peak asymmetry was explained with chelat formation of antibiotics (especially tetracycline) with metal ions [17]. In order to avoid these consequences, a third mobile phase, whether oxalic acid or phosphoric acid was employed in elution programs. Evaluating these concerns, the method described in experimental section was developed and applied to standard and sample solutions. For each antibiotic standard solution linear calibration graphs were obtained. Analyzing the data acquired from the calibration graphs, molar absorption coefficients, linear range and calibration equations were found and tabulated in Table 1. Validation parameters such as limit of detection (LOD) and limit of quantification (LOQ) values were calculated as 3 times and 10 times of standard deviations of blank solutions, divided by the slope of each calibration graph, respectively.

Table 1. The performance characteristics obtained with respect to HPLC-PDA method

Name	Retention Time	Calibration graph equation	Regression Coefficient	Molar absorption coefficient	Working Range (mgL^{-1})	LOD (μgL^{-1})	LOQ (μgL^{-1})
Tetra cycline	9.15±0.07	$A = (1.00 + 1.27 C_{\text{tetracycline}}) \times 10^5$	0.98	1.27×10^5	10-160	1.55	5.20
Oxy tetra cycline	8.03±0.06	$A = (7.13 + 1.46 C_{\text{oxytetracycline}}) \times 10^5$	1.00	1.46×10^5	10-160	1.32	4.39
Penicillin G	3.95±0.02	$A = (1.11 + 2.73 C_{\text{penicillin G}}) \times 10^5$	1.00	2.73×10^5	10-160	1.07	3.60

Table 2. Recovery percentage levels of chicken breast sample not including antibiotic residue

Added concentration of standard solution (mgL^{-1})	Penicillin G		Oxytetracycline		Tetracycline	
	Found concentration (mgL^{-1})	R% (recovery percentage)	Found concentration (mgL^{-1})	R% (recovery percentage)	Found concentration (mgL^{-1})	R% (recovery percentage)
					19.78±0.11	
20	19.43±0.08	97.15	19.83±0.06	99.17		98.90
	38.53±0.12				39.10±0.10	
40		96.32	39.12±0.08	97.82		97.76
	77.26±0.22					
80		96.57	79.20±0.18	99.00	76.74±0.15	95.92

The accuracy of the proposed assay was proved through recovery percentage calculation. For this purpose, the blank chicken breast sample (labeled as C) was spiked with standard solutions of tetracycline, oxytetracycline, penicillin G at 20 mgL⁻¹, 40 mgL⁻¹, 80 mgL⁻¹ concentration levels, after extraction step.

As displayed in Table 1 and Table 2, low LOD and LOQ values, high regression coefficients and recovery percentage levels approaching 100% define the accuracy and validation of the proposed method. The other factor defining the applicability of a method is its selectivity and easy operation. The proposed technique with no interference effects during analysis, may bring novelty to literature as accurate determination of antibiotic residues in chicken breast samples in a short period of time (12 min including column regeneration). Application of The Proposed Method To Real Samples

Sample preparation is an important step for the success of an assay. Solid phase extraction, 2/3 times faster replying when compared to liquid-liquid extraction [18] was preferred for sample analysis. Moreover, SPE has many advantages as fast sample preparation decreasing total time of analysis, obtaining samples at desired concentration levels and achieving high recovery percentages. Tetracycline-type of antibiotics is classified in amphoteric group of drugs that makes them difficult to isolate from the biological matrix. Methanolic oxalic acid was resorted to come over this drawback. Sample preparation procedure was summarized and schemed in Fig. 1.

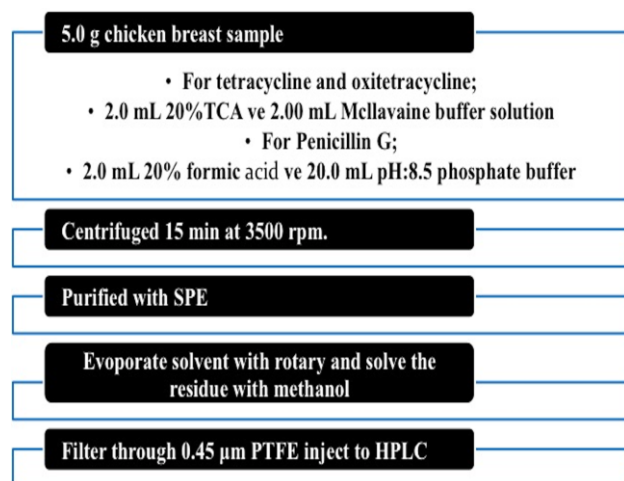


Figure 1. The flow chart of sample preparation

The chromatograms were obtained and figured (Fig. 2, Fig. 3) after sample preparation procedure followed by adequate analysis program. The amounts of residue

levels found (as 3 replicates) were tabulated in Table 3 with standard deviations.

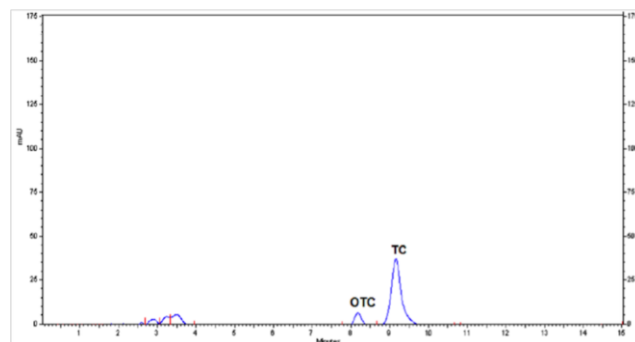


Figure 2. The chromatogram of sample F displaying peaks of oxytetracycline and tetracycline

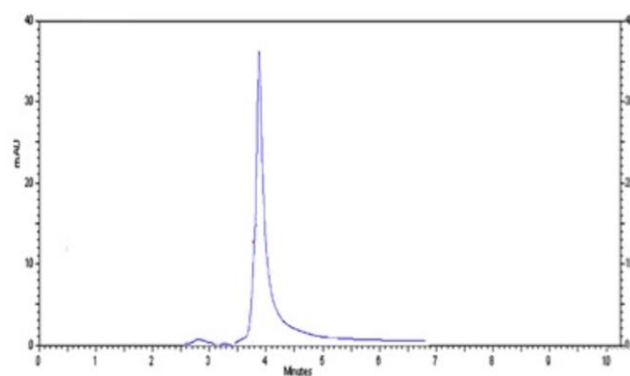


Figure 3. The chromatograms of sample F displaying peak Penicillin G

The peaks at the chromatograms of samples were identified with standard addition method and residue levels were quantified with the aid of calibration graphs. As shown in Table 3, 7 of 9 samples contain considerable amounts of antibiotic residues. Sample C that was purchased with organic label and H are the ones that do not include any type of antibiotic residue.

Amount of tetracycline and oxytetracycline were determined in raw chicken breast samples and compared with the limits of legislations. Penicillin G, which is also known as benzylpenicillin, was also investigated within this study. According to commission regulations on pharmacologically active substances and their classification regarding maximum residue limits in foodstuffs of animal origin, maximum residue levels should not exceed 100 µg for tetracycline and oxytetracycline and 50 µg for penicillin G at 1.0 kg chicken meat sample [19]. As it is displayed in Table 3, residue level of oxytetracycline seems to be over the limits while the others are approaching to the edge of limits.

Table 3. Amount of oxytetracycline, tetracycline and Penicillin G found in 1.0 kg raw chicken breast samples

Sample Name	Oxytetracycline (µg)	Tetracycline (µg)	Penicillin G (µg)
A	116.4 ±0.4	56.6 ±0.3	2.34±0.2
B	19.5 ±0.5	10.6±0.4	-
C	-	-	-
D	6.2 ±0.2	-	-
E	-	4.1±0.1	1.74±0.1
F	0.8±0.2	14.8 ±0.6	38.0±0.5
G	-	-	28.4±0.4
H	-	-	-
I	8.7±0.6	-	-

4. Conclusion

Antibiotics may be used in poultries not only for medical issues but also for feed efficiency and acceleration in growth. Unrelated with the main purpose, excess amount of antibiotic residue in meat products to be consumed is a major problem. Therefore, maximum residue levels must be evaluated. In this assay, a new method for the determination of antibiotic residue levels found in raw chicken meat,

with easy-to-operate and effective sample preparation step, was introduced. The method was validated by calculating LOD, LOQ levels (LOD=1.07; LOQ=3.60 for Penicillin G) and recovery percentages and successfully applied to real samples. Determination of three most used antibiotics may be performed in less than 15 minutes.

When compared to the literature summarized in Table 4, these LOD and LOQ values are quite sufficient as the method proposed in this study is very easy to install and cost-effective.

Table 4. Comparison of LOD and LOQ values found in the literature including the methods used and samples analyzed

Reference Number	Oxytetracycline		Tetracycline		Penicillin G		Method	Sample
	LOD	LOQ	LOD	LOQ	LOD	LOQ		
[14]	3.0 µgkg ⁻¹	10µgkg ⁻¹	3.0 µgkg ⁻¹	10µgkg ⁻¹	-	-	Turbo Flow LC-MS	Chicken meat
[20]	0.1 µgkg ⁻¹	1.0µgkg ⁻¹	0.1 µgkg ⁻¹	1.0µgkg ⁻¹	0.5 µgkg ⁻¹	5.0 µgkg ⁻¹	LC-MS-MS	milk
[11]	0.1 µgkg ⁻¹	-	0.3 µgkg ⁻¹	-	-	-	HPLC-couple with fluorescence detector	commercial tablets
[17]	4.4 µgkg ⁻¹	10 µgkg ⁻¹	5.0 µgkg ⁻¹	13µgkg ⁻¹	-	-	HPLC-DAD	chicken meat liver
[21]	-	-	7.9µgkg ⁻¹	14.6µgkg ⁻¹	-	-	LC-MS	chicken meat
[22]	-	-	-	-	7.4 µgkg ⁻¹	24.6 µgkg ⁻¹	Capillary Electrophoresis	chicken muscle
[23]	5µgkg ⁻¹	-	5µgkg ⁻¹	-	10µgkg ⁻¹	-	LC-MS-MS	chicken meat

Conflicts of interest

The authors state that did not have conflict of interests.

References

- [1] Inal T., Besin hijyeni, hayvansal gıdaların sağlık kontrolü, *Final Ofset*, (1992) 55-57.
- [2] Jayalakshmi K., Paramasivam M., Sasikala M., Tamilar V., Sumiyo A., *J. Entomol. Zool. Stud.*, 5 (2017) 1446-1451.
- [3] Mitchel J., Griffiths M. W., McEwen W. B., McNab A. J., Yee A., Antimicrobial drug residues in milk and meat; causes, concerns, prevalence, regulations, tests and test performance, *J Food Protect* 61(6) (1988) 742-756.

- [4] EC (1990) Council Directive 90/167/EEC of 26 March 1990 laying down the conditions governing the preparation, placing on the market and use of medicated feeding stuffs in the Community, Council Directive 90/167/EEC (1990). Offic J Eur Comm L92:42-48
- [5] Berrada H., Molto J.C., Manes J., Font G., Determination of Aminoglycoside and Macrolide Antibiotics in Meat by Pressurized Liquid Extraction and LC-ESI-MS., *J Sep Sci.*, 33 (2010) 522-529.
- [6] Percin Ozkorucuklu S., Uka B., Yildirim Bastemur G., Voltammetric Analysis of Cephalexin and Cefazolin in Pharmaceutical Formulations and Biological Samples., *JOTSCA*, 6(2) (2019) 217-224.
- [7] Young-Song J., Jung Hu S., Joo H., Hwang J. B., Kim M. O., Shin J. K., Cho D., Determination of Penicillin Residues in Livestock and Marine Products by LC/MS/MS, *WASET*, 81 (2011) 809-811.
- [8] Granelli K., Brazzell C., Rapid multi-residue screening of antibiotics in muscle and kidney by liquid chromatography-electrospray ionization-tandem mass spectrometry, *JACA.*, 585 (2007) 289-295.
- [9] Furusawa N., Simplified liquid-chromatographic determination of residues of tetracycline antibiotics in eggs, *Chromatographia*, 53 (2001) 47-50.
- [10] Schneider M. J., Braden S. E., Herrera I. R., Donoghue D. J., Simultaneous determination of fluoroquinolones and tetracyclines in chicken muscle using HPLC with fluorescence detection, *J Chromatography B*, 846 (2007) 8-13.
- [11] Lu H., Jiang Y., Li H., Chen F., Wong M., Simultaneous determination of oxytetra-cycline, doxycycline, tetracycline and chlortetracycline in tetracycline antibiotics by high-performance liquid chromatography with fluorescence detection, *Chromatographia*, 60(5-6), 259-264.
- [12] Cháfer-Pericás C., Maquieira A., Puchades R., Fast screening methods to detect antibiotic residues in food samples, *TrAC*, 29 (9) (2010) 1038-1049.
- [13] Yuvali D., Narin İ., Simultaneous determination of sulfachloropyridazine and trimethoprim in veterinary formulations by hplc, *Cumhuriyet Sci. J.*, 41(1) (2020) 239-244.
- [14] Bousova K., Senyuva H., Mitterdorf K., Quantitative multi-residue method for determination antibiotics in chicken meat using turbulent flow chromatography coupled to liquid-chromatography-tandem mass spectrometry, *J. Chrom. A*, 1274 (2013) 19- 27.
- [15] Tong J., Rao Q., Zhu Z., Jiang Z., Ding S., Simultaneous determination of five tetracycline and macrolide antibiotics in feeds using HPCE, *J. Sep. Sci.*, 32 (23-24) (2009) 4254-4260.
- [16] Aszalos A., Fast determination of tetracycline antibiotics in different fast determination of tetracycline antibiotics in different media by High-Performance Liquid Chromatography. *Chromatographia*, 20 (1985) 313-322.
- [17] Shalaby A. R., Salama N. A., Abouraya S. H., Mehaya F. M., Incidence of tetracycline residues in chicken meat and liver retailed to consumers, *Food Chem.*, 124 (2011) 1660-1666.
- [18] Zief M., Solid Phase Extraction for Sample Preparation, Phillipsburg: JT Baker (2005).
- [19] World Health Organization, 70th report of the Joint FAO/ WHO expert committee on food additives, *Geneva*, 21-29 October (2008).
- [20] Magon T., Silveira R., Galuch M. B., Fagan E. P., Feitoza F. D., Palombini S. V., Santos O. O., Visenteiner J. V., Simultaneous determination of four antibiotics in raw milk by UPLC-MS/MS using protein precipitation as sample preparation: Development, validation, and application in real samples, *J. Braz. Chem. Soc.*, 29 (2018) 2441-2448.
- [21] Cetinkaya F., Yibar A., Soyutemiz G. E., Okutan B., Ozcan A., Karaca M. Y., Determination of tetracycline residues in chicken meat by liquid chromatography-tandem mass spectrometry, *Food Addit. Contann. Part B Surveill*, 5 (2012) 9-45.
- [22] Kowalski P., Konieczna L., Determination of penicillin antibiotics in poultry muscle by capillary electrophoresis, *Bull Vet Inst Pulawy*, 51 (2007) 595-598.
- [23] Jammoul A., Darra N., Evaluation of antibiotic residues in chicken meat samples in Lebanon antibiotics, *Basel* , 8 (2019) 69.

UV-VIS spectrophotometric determination of magnesium after complexing with 8-hydroxy quinoline in sodium dodecyl sulphate micellar medium

Cemalettin UYAN ^{1*} , Ersin YILMAZ ¹ 

¹ Sivas Cumhuriyet University, Faculty of Science, Department of Chemistry, Sivas /TURKEY

Abstract

In this study, an alternative UV-VIS spectrophotometric method for determination of magnesium was proposed. The method is based on complexation with 8-hydroxyquinoline (oxin) in sodium dodecyl sulphate (SDS) micelle medium, the absorbance of the product was recorded at 390 nm. pH of the solution, the concentration of ligand and surfactant were critical parameters, which affect the absorbance measurements, and optimised. The molar absorptivity coefficient is $5 \times 10^2 \text{ Lmol}^{-1}\text{cm}^{-1}$, the Sandell's sensitivity is $0,052 \mu\text{gcm}^{-2}$, detection limit is $0,3 \text{ mgL}^{-1}$, quantification limit is $1,1 \text{ mgL}^{-1}$ and linear working range is $2-8 \text{ mgL}^{-1}$ at pH 12 and 390 nm. The proposed method was applied for determination of magnesium to some drug and mineral water samples, nearly good accuracy and reproducible values were obtained percent as recovery and relative standard deviation.

Article info

History:

Received:08.10.2019

Accepted:05.06.2020

Keywords:

Magnesium analysis,
UV-VIS
spectrophotometric
method,
8-hydroxyquinoline,
Sodium dodecyl
sulphate,
Micellar medium.

1. Introduction

Magnesium determination areas are great variety. These areas can be classified as water, industry, clinic, foods. Magnesium determinations were made by gravimetric, volumetric, atomic spectrophotometric, UV-VIS spectrophotometric, fluorimetric, electroanalytical and ion chromatographic method. Atomic absorption spectrophotometric (AAS) pathway is the best method for metal ions determination. However, because this instrument is expensive, not every routine analysis is available. The UV-VIS spectrophotometric methods are the most common. The conventional UV-VIS spectrophotometric determination of metal ions is based on the complexation of the metal ion with a ligand. UV-VIS spectrophotometric methods are divided into three in terms of the micro environment of the species where the signal is measured. These are: 1) Aqueous media 2) Organic solvent media (with liquid-liquid extraction) 3) Micellar media methods. Information about these studies were given in Table 1, Table 2 and Table 3.

While the direct aqueous medium method is more advantageous, the liquid-liquid extraction method has been developed in cases where the metal complex does

not dissolve in water or good peaks are obtained. One way for the same situations is to measure the signal in micelle. The micelle medium of a surfactant whose suitability is determined experimentally leads to improvement. The reason for this improvement can be explained as follows. The analyte species or its derivation is attached by micelle (held by the micelle), which changes the spectroscopic property of the different surrounding species by affecting the orbital energy levels, resulting in a better peak. The micelle media methods also have the following advantages: 1) Environmentalist; surfactants undergo biological degradation very quickly compared to organic solvents. 2) Cost of analysis is lower; in one assay, the surfactants are used in very small amounts relative to organic solvents. 3) The method is shorter and easier since no separation is required [1].

In this study, an alternative method for determination of magnesium in micelle medium is proposed. For mycelium, In this study, SDS as a surfactant and oxin as a ligand are used for the determination of Mg. In the literature, no studies have found these three together. With the realization of this study, we will present an alternative method of magnesium determination which can meet the demands of institutions that do not have AAS device because they do not have budgets.

*Corresponding author. Email address: cuyan@cumhuriyet.edu.tr

<http://dergipark.gov.tr/csj> ©2020 Faculty of Science, Sivas Cumhuriyet University

Table 1. UV-VIS Spectrophotometric determination of magnesium in aqueous medium

Ligant	pH	λ_{\max} (nm)	Detection limit (mg L ⁻¹)	$\epsilon \times 10^{-3}$ M ⁻¹ cm ⁻¹	Linear working range (mg L ⁻¹)	References
Eriochrom Black T	9.5-11.7	630	-	-	-	[2]
Chlorophospho-nazo III	7	699	-	-	-	[3]
Chromotrope 2R	10.8	570	-	-	-	[4]
Titan Yellow*	>12	545	-	2.8	-	[5]
Acid Chrome Black Special*	10	540	-	33	-	[5]
Calmagite	alkaline	520	-	-	0,0-36	[6]
1,8- dihydroxy- anthraquinone	-	510	-	-	0.25 - 2.00	[7]
Xylidyl Blue-1	alkaline	524	-	22	0-4	[8]
Terpiridine	3	668	-	-	-	[9]
Furfurin	9.5	540	0,075	9,2	0.8 – 4.3	[10]
CPC	10.5	570	0.24	-	0-20	[11]
Acid Chrome Blue K	-	540	-	9.3	0-2	[12]
Bromopyrogallo Red	9.4	RS- CWT**	-	-	0.2-3,2	[13]

* photometric

** Continuous wavelength transforms

Table 2. UV-VIS spectrophotometric determination of magnesium with liquid-liquid extraction

Ligant	Solvent	pH	λ_{\max} (nm)	Detection limit (mgL ⁻¹)	$\epsilon \times 10^{-3}$ M ⁻¹ cm ⁻¹	Linear working range mgL ⁻¹)	References
8-hydroxyquinoline*	Cloroform	11.2-11.3	380	-	5.6	-	[5]
PTTHA	Cloroform	9.5	590	-	2.8	-	[14]

* Photometric

Table 3. UV-VIS spectrophotometric determination of magnesium in micellar medium

Ligant	Surfactan	pH	λ_{\max} (nm)	Dedection limit (mgL ⁻¹)	$\varepsilon \times 10^{-3}$ M ⁻¹ cm	Linear working range (mgL ⁻¹)	References
Calmagite	Empigen BB	11.5	655	-	-	-	[15]
Xylidyl Blue -1	Brij 35	alkaline	505	-	-	0.0- 48	[16]
Bromopyrogallo l Red	Tween 80	10	570	0.03	-	0.5-3.5	[17]
Eriochrome Black T	CTAB	9.5	640	0.012	8.9	0.05-1.2	[18]

2. Materials and Methods

2.1. Tools and Equipment

UV-VIS Spectrophotometer: UV-1800 UV-VIS Spectrometer and UNICAM UV-VIS Spectrometer
UV 2 pH meter: Adwa AD8000.

2.2. Reagents

Solids of all reagents are of analytical purity. The solutions were prepared with double distilled water.

1) 375 ppm Oxin solution (pH 12): 0.0940 g of solid auxin was removed and transferred to a 250 mL beaker. It was diluted close to the adjustment line and the pH was 12. A 250 mL flask was then transferred to the flask and raised to the volume adjustment line with water. It was observed that the solution exceeding one week after preparation should not be used.

2) Sodiumdodecylsulfate (SDS): 5% (w / v). 5.0 g of SDS solid were dissolved in water and the volume was completed to 100 mL. To use this solution should not exceed a week.

3) pH 12 Glycine Buffer: Firstly, the following two solutions were prepared: 3-1) (0.2 M NH₂CH₂COOH + 0.2 M NaCl) solution: 1.5014 g of glycolic acid and 1.1688 g of NaCl were dissolved in a small amount of water in the same beaker and 100 mL of flask. the volume to 100 mL. 3-2) 0.2 M NaOH solution: 0.8 g of sodium hydroxide was dissolved in some pure water and then made up to 100 mL with volume of water. 54.6 mL of the second solution, 45.6 mL of the first solution were taken and mixed [4]. Alternatively, at various concentrations NaOH is added drop by drop to the first solution (prior to completion to 100 mL) until the pH is adjusted to pH 12.0 at a well-adjusted pH meter, then added to 100 mL with water.

4) 1000 mgL⁻¹ Mg (II) standard: 10.1411g (MgSO₄ 27H₂O solid was weighed and dissolved in water, was transferred to a 1 L balloon and the volume was completed with water to liter.

5) 100 mgL⁻¹ Mg (II) standard: It was prepared by diluting ten times before the previous one.

2.3. Recommended Method

A series of balloon of 10 mL each are collected. These are made in two groups, one for calibration curve and the other for samples. To each of the flasks in both groups were added 4 mL of oxin (375 mgL⁻¹), 1.5 mL of SDS (5% w / v), 1 mL of pH 12 glycine buffer, with the following four solution sequences, volumes and concentrations. For calibration, 200 - 400 - 600 - 800 µL of 100 mgL⁻¹ Mg (II) is added sequentially and each amount is parallel. 400 µL of the prepared sample is added to each of the balloons taken for the sample (at least three) and pre-added to the reagent. The solution levels are completed with double distilled water to the marking line, sealed and mixed.

Absorbance measurements of the solutions in the flasks at 390 nm are started without passing over the last addition. Absorbance measurements should be completed in less than 20 minutes, the first reading and the last reading should be between 10 and 15 minutes at most.

2.4. Preparation of samples

2.4.1. Preparation of magnesium sulfate ampoule sample 330 μL was taken from the original sample and diluted to 1 L.

2.4.2. Preparation of Magnesie Calsinee Saba sample

Some solid powder was transferred to a vessel and left in the etuv at 120°C . 0.600 g of this was weighed. 25 mL of 1 M HNO_3 was dissolved. 6 M NaOH was added to make the pH slightly basic. The solution was transferred to a 100 mL flask and the volume was completed to the marking line with double distilled water (Solution A). 2000 μL of this was transferred to a 50 mL flask and diluted to this volume (Solution B).

2.4.3. Preparation of Magnesie Calsinee Saba sample

One film tablet was taken and weighed. 31 mL of 1 M HNO_3 was added to the beaker and stirred for a long time. Filtered. It was made slightly basic so that the pH was between 8-9. The volume was made up to 250 mL with water (Solution A). 6,850 mL (6.0 mL + 850 μL) was taken and diluted to 100 mL (Solution B).

2.4.4. Preparation of magvital drug sample

One bowl was taken and the whole powder was transferred and weighed. Water was added to the beaker and mixed. Waited until the bubbles disappear in the water. To this solution, pH 3.4, 1 M HNO_3 was added dropwise to a pH of about 2 and heated. 6 M NaOH was added to make the pH slightly basic. The volume was completed to 250 mL (Solution A). 6.850 mL (6 mL + 850 μL) was taken and diluted to 100 mL (Solution B).

2.4.5. Preparation of water samples

The water sample mineral water was transferred to a beaker after the bottle was opened and waited until the exit of the gas bubbles was completed. The post is the same for both. Filtered. It was then taken up to a certain volume and acidified and heated, then made slightly basic to a pH of from about 8-9 to the same as that of the Mg standard. The solution is transferred to a flask which its volume was pre-determined, then is diluted.

3. Results and Discussion

3.1. Effect of SDS micelle on the spectrum of Mg-oxin complex

Critical micelle concentration (cmc) value of SDS is given as 8.1×10^{-3} M (0.23% (w / V) [18]. The volume to be added at least is 0.0162 mL, since the value added here is much larger than this value, the measuring medium will certainly be micelle.

When the spectra of the oxin buffer (glycine pH12) Mg st mixture were taken in one medium without SDS and the other with SDS micelle medium, respectively, Figure 1 and Figure 2 were obtained. As shown in the second figure, an analytical peak was obtained in SDS micelle medium.

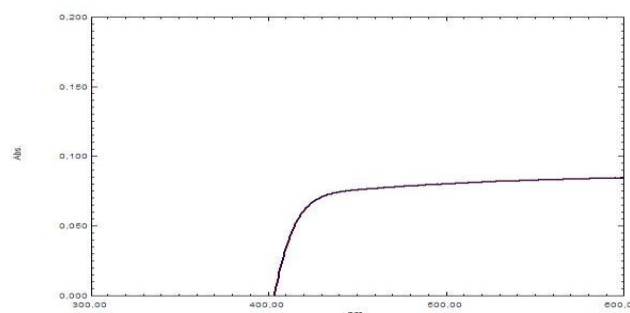


Figure 1. Spectrum of Mg-oxin complex in the absence of surfactant. 10 mL total volume Reactive additives in: 3 mL oxin (saturated in pure water), 1 mL buffer (pH 12) and 0.5 mL 100 ppm Mg (II)

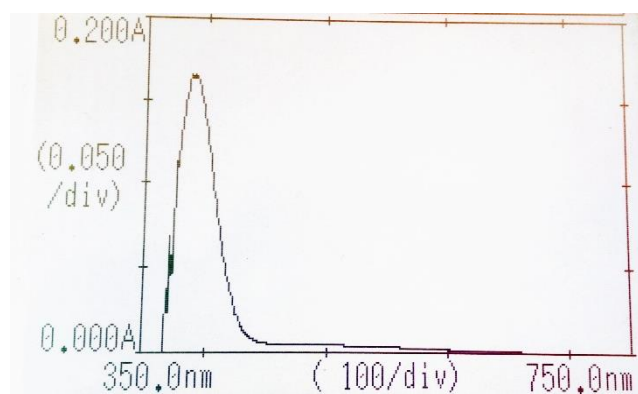


Figure 2. Spectrum of Mg-oxin complex in SDS micelle medium. Media composition: [Oxin] = 150 mgL^{-1} , [SDS] = 0.026 M (0.75% (w / v), pH = 11.5 -12, [Mg (II)] = 8 mgL^{-1}

3.2. pH effect

To determine the optimum pH, the following was followed: A series of 10 mL flasks were taken. To each flask 3 mL of saturated oxin, 2 mL of SDS (5% w / v), 1 mL of buffer (pH 2, 3, 4, 5, 6, 7, 8, 9, 10, 11, 12), 200

μL 100 mgL^{-1} Mg (II) standard was added. The solution volumes were made up to 10 mL with double distilled water. Blank solution was taken as reference; this was not prepared for all solutions, but individually prepared at each pH.

The spectra of each solution were taken separately. Peaks were not obtained from solutions of pH 2-8, Turbidity was observed at pH 8. Analytical peaks were obtained from pH 9 and above. Figure 3 was obtained when the absorbances measured at the wavelength peaking at each pH were plotted against pH. As shown in the graph, the absorbance at pH 12 is maximum. 12 was chosen as the optimum pH.

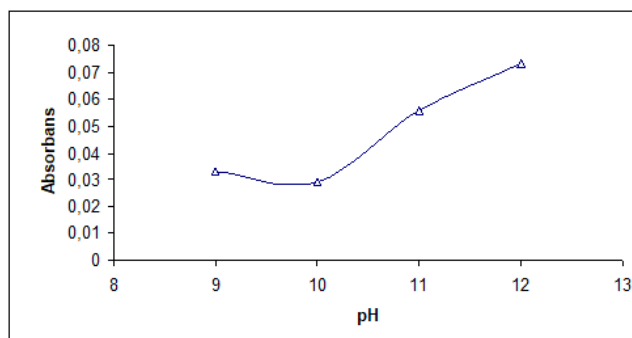


Figure 3. Effect of pH on absorbance. Media content: Oxin: Saturated diluted (in pure water) 3/10 after addition, SDS: 1% w / v (after addition), The pH values shown are those of the added buffers (initial), [Mg (II)] = 2 μgL^{-1} (after addition)

3.3. Effect of oxin concentration on absorbance

To determine the optimum oxin concentration, the reagents were added with the oxin volume variable and the others constant: The oxin reagent volume was predicted to be 4 mL before determining the optimum concentration. 1000 ppm oxin (0.01 M NaOH) solution in different volumes of 0.5, 1.0, 1.5, 2.0 mL was transferred to the balloons. 3.5-2 mL of double distilled water was added, each having a total volume of 4 mL. To each was added 2 mL of 5% SDS and 1 mL of buffer (pH12), 200 μL of 100 ppm Mg (II). The solution volumes were completed to 10 mL. Each volume was made in parallel. A different blank solution was used for each oxin concentration. The absorbances of the solutions were measured at peak wavelength. The mean of the parallel ones were taken. Figure 4 was obtained when the absorbance versus oxin volume was plotted.

According to the graph, the 1.5 mL volume is the optimal volume, which corresponds to a final concentration of 150 ppm after this dilution (completion to 10 mL). If the volume of oxin is taken

to 4 mL, the initial concentration corresponds to 375 ppm.

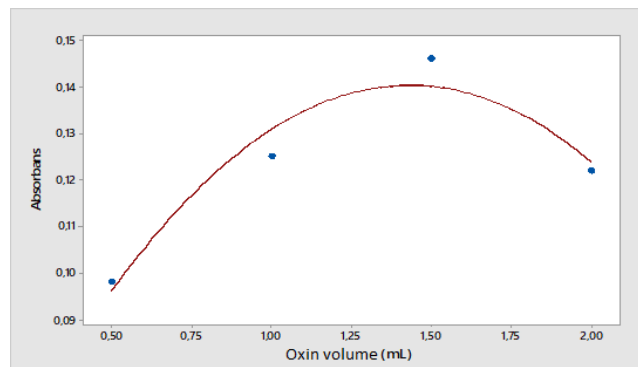


Figure 4. Effect of oxin concentration on absorbance. Solution additives in a volume of 10 mL: 1000 mgL^{-1} oxin (at 0.01 M NaOH) variable, 2 mL SDS (5%), 1 mL buffer (pH12 glycine), 200 μL 100 ppm Mg (II) standard

3.4. Effect of SDS concentration on absorbance

In order to determine the optimum SDS concentration, the reagents were added at this time with the variable SDS volume being variable and the others constant: 4 mL 375 ppm oxin (pH 12), 1-3 mL 5% SDS in different volumes, 1 mL pH 12 glycine buffer, 300 μL 100 ppm Mg standard was added. The solution volumes were completed to 10 mL. One blank was prepared for all as a reference. Figure 5 was obtained when the absorbance values measured at the peak giving wavelength were plotted against the added SDS volume.

There seems to be much deviation between the absorbances values in the graph. This is because the absorbance axis was scaled at very narrow intervals. In fact, there is not much deviation in absorbance. 1.5 mL was taken as the appropriate SDS concentration.

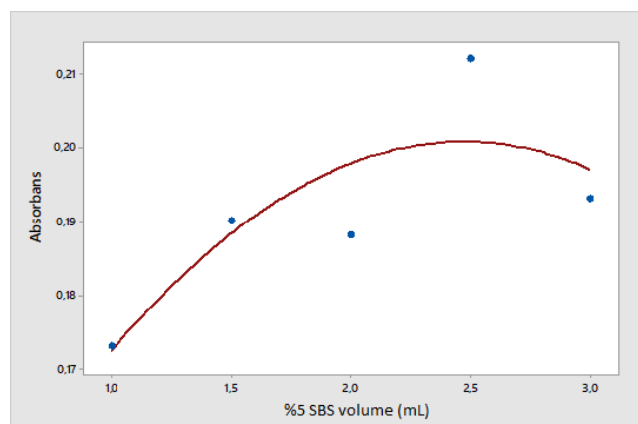


Figure 5. Effect of SDS concentration on absorbance. Additives in a volume of 10 mL : 4000 μL 375 mgL^{-1} oxin ;, SDS: different, 1000 μL Buffer (pH12 glycine), 100 mgL^{-1} , 300 μL , Mg (II) standard

3.5. Optimum wavelength

The peak wavelength varies according to the pH of the medium, and the lower the wavelength, the lower the wavelength. The pH in Figure 3 showing the effect of absorbance on the pH is not the pH of the medium, but the pH of the buffers used before addition. After addition, the pH drops slightly below that of the added buffer. As the ambient pH is lower than 12, the peak wavelength shifts from 392 to 365 nm. The amount of shear varies according to the concentration and pH of oxin used. Oxin has the lowest solubility in pure water and is about 45 mgL^{-1} . The saturated auxin solution in pure water is slightly acidic. The solubility of oxin increases at high pH. When saturated oxin (in pure water) is used, the pH decreases further. In experiments using this solution, peak wavelength was observed below 390 nm and absorbances were measured accordingly. When the oxin solution was adjusted to a pH of 12 and had a higher and optimal concentration, it was observed that the decrease in pH was less than 12 and the peak wavelength was 390 nm or close. This value corresponding to the optimal pH as the optimal wavelength was taken.

One way to reduce the pH drop after buffer addition is to increase the buffer capacity. In subsequent experiments, the buffer components were prepared in such a way that the concentrations of glycine and NaOH were doubled (the preparation given in Section 2.2 was this).

3.6. Stability and optimum reading time

When the balloons were last added, the levels were equalized and the absorbance signals were monitored after closing the mouths, the signals could not remain stable for a long time. As can be seen in Figure 6, in the spectrum band, there was a rise in ground (noise) over time, with higher concentrations. The spectra in the figure were taken approximately 30 min after the preparation of the solutions and starting at the lowest concentration (2 mgL^{-1}). Others were taken at about 5-10 minute intervals, with a higher concentration later. After 45 minutes, peak λ_{max} values also changed and the peak feature disappeared and turbidity occurred in the solution. The cloudiness was not observed in the empty trial solution; this shows us that clouding is not caused by coagulation of micelles.

Ground rise was not seen until the first 20 minutes. It is insignificant for the first 30 minutes. The start of the absorbance measurements of the solutions should not

exceed 20 minutes after the final solution component has been added and the levels have been equalized and the mouth closed, the measurement should be completed in 10, maximum 15 minutes.

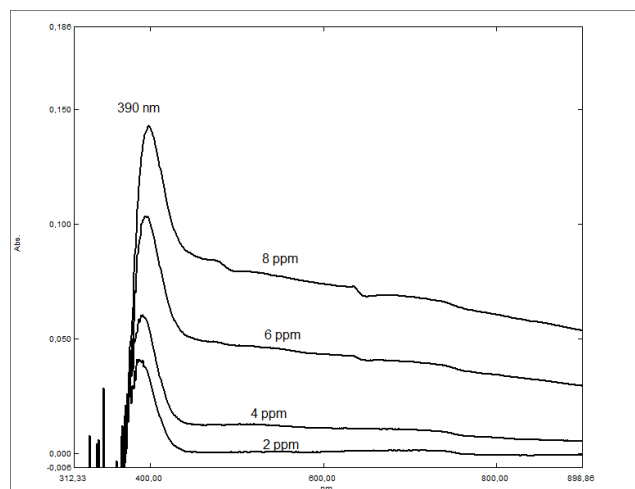


Figure 6. UV-VIS absorption spectrum according to the method and its variation over time. Media composition; [oxin] = 150 mgL^{-1} , [SDS] = 0.026 M (0.75% (w/v)), pH = 12, [Mg(II)] values indicated on the curve in the graph) Spectra began to be taken about 30 minutes after the last reagent was added, this process continued to be more concentrated later.

Table 4. Optimum values of critical factors in the measurement medium

Parametre	pH	SDS, % (w/v)	Oksin, mgL^{-1}	λ_{max} , nm	Time
Value	12	0,75	150	390	20 dak*

* This is the time after which the last reagent is added and the moment of equalizing the levels is taken as the starting point.

3.7. Interferences

Species that have been investigated are generally found in the measurement environment. These are sodium, potassium, calcium, chloride, carbonate, bicarbonate, sulfate ions. No interference effects of sulfate, carbonate bicarbonate and nitrate were observed. Other results was given in Table 5. As the tolerance limit, the species/analyte (w/w) ratio or the corresponding concentration that changed the absorbance by $\pm 5\%$ was accepted.

Observations up to 0.01 M to determine whether NaCl is interfering. No interference was observed. Precipitation was observed when KCl was 50 mgL^{-1} in the measuring medium. Observation of this turbidity even in the blank solution indicates that the turbidity is due to the cloud point state or peptidization or coagulation; it can also be said that KCl interference is

independent of Mg (II). The KCl value of 50 mgL⁻¹ corresponds to a concentration of 23.54 mgL⁻¹ K⁺ if calculated. Considering that the concentration in the original sample is at least 10-fold diluted to the final medium, the K⁺ ion concentration in the original sample is at least 235 mgL⁻¹. This value is above the K⁺ levels found in water and drug samples. As a result, it can be said that K⁺ and Na⁺ will not be at the level that will cause effect in the samples where the method is applied.

Since heavy metal ions can complex with oxin such as Mg, interference is expected when these ions are present. The concentrations of metal ions other than Ca(II), Mg (II) in water and drug are at ppb levels. Moreover, the method is much lower than they are subjected to dilution when applied, so that their interference is out of the question.

When the Ca / Mg ratio was above 2/1, it was observed that the absorbance increase exceeded $\pm 5\%$. This ratio was taken as the tolerance limit for Ca (II). Masking with tartrate, citrate and EDTA was used to remove Ca (II) interference, but none of them yielded a positive and consistent result.

Table 5. Tolerance limits of some species (which changes the absorbance by $\pm 5\%$) species / analyte ratios), (ppm / ppm)

Species	Tolerance limit	[Sp] / [Mg] (ppm/ppm)
NaCl	>0,01 M (>580 ppm)	> 145
KCl	50 ppm*	(Mg independent)
Ca(II)	-	2/1

*Coagulation limit

3.8. Calibration curve parameters

Table 7. Application of the proposed method to some water samples

Sample	Known conc., mgL ⁻¹	Ca/Mg	Found conc., mgL ⁻¹	% R	% RSD
Mineral water samples 1	317 ^b	0.13 ^c	332.8 \pm 34.8 ^a	105	11
Mineral water samples 2	108 ^b	2.2 ^c	136.8 \pm 6.8 ^a	126	5

^a n=5, % 90 confidence level, t= 2,13,

^bThe value given on the label.

^c Rate calculated from the values given on the packaging (w/w)

The parameters of a calibration curve obtained by taking the optimal values of each critical factor was given in Table 6.

Table 6. Calibration curve parameters (two repeat measurements for each concentration)

Parameter	Value
Linear regression equation (c as mgL ⁻¹)	A = 0.0194 c - 0.014
Correlation constant / r ²	0.9964
Measurement peak wavelength λ_{\max} (nm)	390
Molar absorption constant ϵ (Lmol ⁻¹ cm ⁻¹)	5 \times 10 ²
Sandell's sensitivity* (μ g cm ⁻²)	0.052
Detection limit 3 σ /m (μ g mL ⁻¹) (n=18)	0.3
Quantization limit 10 σ /m (μ g mL ⁻¹) (n=18)	1.1
Linear working range (mgL ⁻¹)	2 - 8
*Concentration rise which causes to an increase of 0,001 in absorbance in a spectrophotometer with 1 cm beam length [19]	

3.9. Calibration curve parameters

The accuracy and precision of the proposed method were tested by applying mineral water sample of two different brands and some Mg supplement drugs.

The composition of the mineral water sample is given on the packaging bottle. As these values were determined by the standard method in routine analysis sites, they were taken as the correct value or comparison value. The obtained data are given in Table 7.

Table 8. Application of the proposed method to some drug samples and testing the accuracy by analyte spiked method

Sample	Added Con., mgL ⁻¹	Conc. difference found, mgL ⁻¹	%R	% RSD
Mg-sulfat ampoule*	0	0.97 ± 0.49	-	11
	2	1.34 ± 0.00	67	0
	4	4.22 ± 0.16	106	0,9
	6	5.98 ± 6.18	100	23
Magnezya Calsinee**	0	2.54 ± 0.54	-	13
	2	1.86 ± 0.43	93	14
	4	3.92 ± 0.71	98	11
	6	5.05 ± 0.59	84	7
Magosit*	0	2.03 ± 1.62	-	20
	2	1.86 ± 1.59	93	19
	4	4.64 ± 1.46	116	7
	6	5.88 ± 0.16	98	0,6
Magvital*	0	0.58 ± 1.63	-	63
	4	4.23 ± 1.14	106	6
	6	4.97 ± 2.11	83	10

* n=2, % 90 convedence level, t= 6,31, \bar{x} : Mean volues

** n=3, % 90 güven düzeyi, t= 2,92

The analyte spiked method or standard addition / method was used to determine the accuracy for the drugs. For this, the following path was followed. Equal amounts (200 µL) of the prepared sample solution were added to each of a series of 10 mL each flask. On top of that, 0 - 600 µL of 100 ppm Mg (II) standard was added for each volume to be measured again. Other procedures were performed according to Section 2.3. The obtained data are given in Table 8.

When the method was applied to water samples, accuracy was positive with 5% recovery in Kızılay Erzincan mineral water sample while accuracy was lower with 126% recovery in Beypazarı mineral water sample (Table 7). This is due to the Ca / Mg ratio of 0.13 / 1 Kızılay Erzincan mineral water Ca (II) is not interference. The other is the Beypazarı mineral water with a Ca / Mg ratio of 2.2 / 1, which is above the tolerance limit. The error rate in this example is therefore higher than the previous water sample.

Accuracy values as percent recovery are mostly positive when the method is applied to magnesium supplementation drugs that do not contain Ca(II) according to the propectus information. The repeatability values are unfortunately not the same (Table 8).

4. Conclusions

As a result, the applicability of this method is limited by Ca (II) interference. The method can be applied to

magnesium-supplementing drugs which do not contain Ca (II). When applied to water samples, it may give error results due to Ca (II) interference.

Conflicts of interest

The authors state that did not have conflict of interests

References

- [1] Pramaura, E. and Pelizetti, E., Surfactants in Analytical chemistry, Chapter 4, Hardbound, 2008; pp 203-211.
- [2] Young A., Sweet T. R. and Baker B. B. Simultaneous Spectrophotometric Determination of Calcium and Magnesium, *Analytical Chemistry*, 27(3) (1955) 356-359.
- [3] Ferguson J. W., Richard J. J., O'laughlin J. W. and Banks C. V. Simultaneous Spectrophotometric Determination of Calcium and Magnesium with Chlorophosphonazo III, *Analytical Chemistry*, 36 (4) (1964) 796-799.
- [4] Shibata S. Uchiumi, A., Saski S. and Goto K. Spectrophotometric determination of magnesium with chromotrope 2R: Application to zinc and aluminum alloys, *Analytica Chimica Acta*, 44 (2) (1969) 345-352.
- [5] Lurie, J., Handbook of Analytical Chemistry, MIR publishers, Moskow: (1975); pp 261 - 326,
- [6] Khayam-Bashi H., Liu TZ. and Walter V. Measurement of Serum Magnesium with a Centrifugal Analyzer, *Clin. Nephrol.*, 46 (1977) 326-331.
- [7] Ceba M., R., Fernándezgutiérrez A. and Mahedero M. C. 1,8-dihydroxyanthraquinone-Mg (II)

- complex: II. Spectrophotometric study, Determination of Mg(II), *Microchemical Journal*, 27 (1982) 339-344.
- [8] Xing Q. and Ying Z. Rapid analysis of cation-exchangeable property in acidic soil: III. Sensitive spectrophotometric determination of microgram amounts of exchangeable magnesium with xylydyl Blue I in the presence of CTAB, *Microchemical Journal*, (33) (3) (1986) 364-370.
- [9] Peerzada N. and Kozlik E., Spectrophotometric Determination of Magnesium with 2,2',6',2" Terpyridine, *Analytical Letters*, (23) (6) (1990) 1087 – 1093.
- [10] Idriss K. A., Sedaira H. and Ahmed H. M. An Insight into the Solution Equilibria of Magnesium (II) with Purpurin and Spectrophotometric Determination of Magnesium, *Talanta*, 54(2) (2001) 369-375.
- [11] Tesfaldet Z. O., Staden J. F. and Stefan R. I. Spectrophotometric determination of magnesium in pharmaceutical preparations by cost-effective sequential injection Analysis, *Talanta*, (64) (2004) 981-988
- [12] Fangqin C., Yaning Z., Huimin C. and Chuan D. UV spectrophotometric determination of magnesium and calcium in brine from salt lake, *Inorganic Chemicals Industry*, 13 (2006) 11-21.
- [13] Afkhami A., Madrakian T. and Abbasi M. T. Simultaneous determination of calcium, magnesium and zinc in different foodstuffs and pharmaceutical samples with continuous wavelet transforms, *Food Chemistry*, (109) (3) (2008) 660–669.
- [14] Dallali N. and Agrawal Y. K. Solvent Extraction and Spectrophotometric Determination of Magnesium by Paratoly 1-2-Thenohydroxamic Acid and Quinalizarin, *Iran. J. Chem. & Chem. Eng.*, (23) (1) (2004) 65-71.
- [15] Abernethy M. and Fowler R. T., Micellar Improvement of the Calmagite Compleximetric Measurement of Magnesium in Plasma, *Clin. Chem.*, 28 (3) (1982) 520-522
- [16] Ratge D., Koshe K. and Wisser H. Measurement of Magnesium in Serum and Urine with a Random Access Analyzer by Use of a Modified Xylydyl blue-1 Procedure, *Clin Chim Acta.*, 159 (1986) 197-203.
- [17] Benamor M. ve Aguerssif N., Simultaneous determination of calcium and magnesium by derivative spectrophotometry in pharmaceutical products, *Spectrochimica Acta Part A*, (69) (2008) 676-681.
- [18] Gürkan R., Ulusoy H. I. and Akçay M. Micellar-Sensitized Spectrophotometric Determination of Magnesium in Drinking Water, *Eurasian J. Anal. Chem.*, (4) (2) (2009) 127-140.
- [19] Bode H., On Sandell's sensitivity, *Fresenius J Anal. Chem.*, 339:898 (1991) 12-15.



An adsorptive stripping voltammetric study based on disposable pencil graphite sensor for the determination of caffeine in local brand ice tea

Burçak ZEREYKAYA¹, Dilek ESKİKÖY BAYRAKTEPE¹, Zehra YAZAN^{1*}

¹Ankara University, Faculty of Science, Department of Chemistry, Ankara/ TURKEY

Abstract

In this study, voltammetric methods were developed for the quantification of caffeine (CAF) analysis based on a practical, economical, sensitive, and eco-friendly pencil graphite electrode (PGE). Initially, the electrochemical behavior of CAF was investigated by cyclic voltammetry (CV), and the results reveal that CAF has an irreversible oxidation signal. The optimum analytical parameters such as, supporting electrolyte, pH, accumulation potential, and accumulation time for the determination of CAF analysis were investigated to develop differential pulse (AdsDPV) and square wave adsorptive stripping voltammetric (AdsSWV) methods. In order to examine the nature of the buffer, Britton Robinson (BR), phosphate buffer (PBS), and 0.1 M H₂SO₄ solutions were tested in the appropriate pH ranges. The best electrolyte and pH were determined as PBS buffer and pH 1.5. The optimum values for accumulation potentials and times were optimized, and under optimized conditions, the oxidation peak current of CAF was proportional to its concentration. The PGE used exhibited wide linear working range for AdsDPV (2.36-1000 µM) and AdsSWV (3.69-1600 µM) methods with the detection limits of 0.71 µM for AdsDPV and 1.107 µM for AdsSWV. The developed methods were applied to the analysis of CAF in an ice tea beverage sample with acceptable recoveries.

Article info

History:

Received: 21.05.2020

Accepted: 14.07.2020

Keywords:

Caffeine, voltammetry, pencil graphite electrode, stripping voltammetry, ice tea

1. Introduction

Caffeine (CAF), called 3,7-dihydro-1,3,7-trimethyl-1H-purine-2,6-dione, also known as mateine or guaranine, is an alkaloid, and it can be found in coffees, teas, guarana, and in cacao [1, 2]. CAF was discovered in 1819 by the German chemist Friedrich Ferdinand Runge [3]. It affects the central nervous system and accelerates the messages to and from the brain [4]. CAF has some physiological effects on human metabolisms, such as increasing blood pressure [5], stimulating the respiratory system [6], and being diuretic [7].

CAF is widely used in pharmaceutical preparations promote diuresis and a positive effect on the cardiovascular system [8]. Also, some drug combinations with CAF have existed for the treatment of migraine [9, 10]. As well as drug formulations, CAF can be found in some commercially available soft drinks such as

energy drinks, ice tea, and some kind of cokes. The U.S. Food and Drugs Administration determined the maximal amount of CAF in soft drinks was approximately lower than 200 mg/L and specified the lethal dose only 10 g of CAF (about 170 mg/kg body weight) per people [11]. Since high concentration levels of CAF are toxic for human beings, it can lead to depression, hyperactivity, nausea and nervousness, heart diseases, kidney failure, asthma, vomiting, trembling, seizures, and DNA modification effects [12-15]. Therefore, developing a fast, sensitive, selective, and reliable method for analyzing CAF is an essential role in human health. Numerous analysis methods have been developed for the analysis of CAF, including spectrophotometry, infrared spectroscopy, chromatography, and voltammetry. These methods, excluding voltammetry, are often time-consuming and require expensive equipment. Also, requiring pretreatment steps, such as extraction and

*Corresponding author. Email address: zdurmus@science.ankara.edu.tr

separation steps are needed in an organic environment. Voltammetric methods are based on the redox reaction of organic agents in a wide range of industrials, pharmaceutical, and cosmetic products. Among them, adsorptive stripping voltammetry-based adsorption phenomena can be preferred for the electrochemical detection of some organic compounds in the term of sensitivity, trace level analysis, and simplicity [16, 17].

In voltammetry, many types of carbon-based working electrodes have been used for years [18, 14, 19]. The working electrodes such as carbon paste, boron-doped diamond, glassy carbon, and screen-printed electrodes required complicated surface cleaning processes since the surfaces of these electrodes are deactivated rapidly. As well as having a problematic cleaning process, the renewability of these surfaces is too hard. Pencil lead graphite electrode (PGE) is cheap, disposable, and easy to use [20-23]. Besides, it has excellent electrochemical reactivity, good mechanical rigidity, low technology, and ease of modification [24-26]. Furthermore, it was described that PGEs offer a renewable surface simpler and faster than polishing procedures [26]. Generally, PGEs consist of graphite, clay, and binder. The chemical and structural properties of the pencil graphite leads were explored in detail by Kariuki [27].

The current study is aimed to develop AdsDPV and AdsSWV voltammetric methods for the determination of CAF at disposable PGE surface in an ice tea beverage. The voltammetric methods developed have a wide linear working range and comparatively low detection limits. To demonstrate the applicability of the proposed methods, CAF analysis was carried out using the standard addition method in real-life samples with satisfactory results. To the best of our literature knowledge, this paper is the first time voltammetric study about the CAF analysis in an ice tea sample using the PGE electrode.

2. Materials and Methods

2.1. Reagents and apparatus

The standard caffeine (CAF) powder was purchased from Sigma Aldrich Company, St. Louis, Missouri, ABD. The 0.01 M CAF stock solution was prepared by dissolving an

appropriate quantity of standard CAF powder in double-distilled water and stored in the fridge at +4 °C. 0.2 M phosphate buffer solution (PBS) was used as the supporting electrolyte, and the pH of the solution was adjusted by 5.0 M NaOH solution. Cyclic voltammetry (CV) and AdsSWV and AdsDPV experiments were performed by using CHI 660C (USA, Texas) and C3 cell stand (Bioanalytical Systems, Inc., USA, BASi) with a solid electrode unit. Ag/AgCl (in 3.0 M NaCl, BAS MF-2052) as reference electrode and platinum wire (BASi MW-1032) as auxiliary electrode were used for electrochemical measurements. Faber Castel brand PG electrode of the dimensions 0.7 × 75 mm (diameter × length) and the active surface area 0.393 (±0.032) cm² [28] was used as a working electrode and supplied from local stationery in Ankara, Turkey, and used as such without any pretreatment procedure. Double distilled water was supplied from the mpMINipure water distillation system (MES, Ankara, Turkey). All pH measurements were carried out using HANNA/HI2211 pH/ORPmeter (LABOR, Istanbul, Turkey). All experiments were performed at room temperature.

2.2 Analytical procedure

The stock solution of CAF (1.0×10^{-2} M) was used in all experiments. In all voltammetric methods, PBS buffer and CAF stock solution were added to the electrochemical cell with a total volume of 10.0 mL. The PGE, reference, and counter electrodes were immersed in the cell. After arranging all the electrode connections, the working solutions were purged with nitrogen gas (99.99% purity) to remove the oxygen, and then the voltammograms were recorded in the potential window of 1.0 V – 1.90 V by using CV, AdsDPV and AdsSWV.

2.3 Real sample preparation

A regional brand of ice tea (Didi) sample content of 80.0 mg/L CAF was regarded to substitute for the stock solution, and in the analytical part of the voltammetric studies, the experiment solution was prepared by mixing the stock solution and the PBS buffer of the desired pH in a 1: 1 ratio and the total volume was completed to 10 mL. Then, the AdsDPV and AdsSWV voltammograms were recorded.

3. Results and Discussion

3.1 Electrochemical behavior of CAF on PGE electrode

The oxidation behaviour of CAF was first studied by CV technique in phosphate buffer pH

1.5 (optimized response) in potential range from 1.0 V to 1.90 V at scan rate 0.1 V/s (Fig. 1). As can be seen, CAF exhibits the oxidation signal at the potential of about 1.5 V. Also, there is no appearance of any reduction peak in the reverse scan, indicating that the electrochemical process is irreversible in nature.

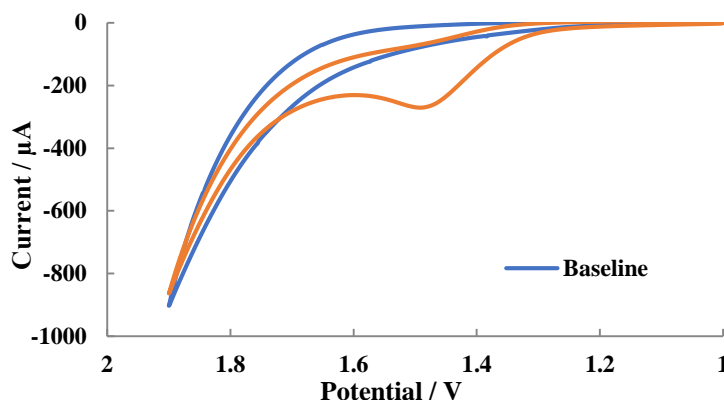


Figure 1. CV voltammograms of baseline (blue line) and 1.0 mM CAF (orange line) in PBS pH 1.5, scan rate: 0.1 Vs⁻¹.

The effect of scan rate on oxidation peak of 1.0 mM CAF on the PGE electrode surface was investigated by CV in phosphate buffer, pH 1.50 at different scan rates within the range 0.1 – 0.6 V/s (Fig. 2). As the scan rate was increased, the oxidation signal of CAF shifted towards more positive potential, confirming the irreversible redox behavior of the electrode reaction of CAF [29]. On the other hand, to monitor the electrochemical process

(adsorption or diffusion-controlled) of CAF, $\log i_p$ - $\log v$, and i_p - v graphs were plotted and given in the inset of Figure 2. The slope value of the $\log i_p$ - $\log v$ graph is about 0.60, indicating that the electrode reaction of CAF was both adsorption and diffusion-controlled process [30-32]. Also, the peak current of CAF depicted linear dependence on the scan rates (inset of Fig. 2) and the regression equation was $i_p = 0.0005v + 0.0001$ ($R^2 = 0.9899$). This result confirms the adsorption-controlled oxidation process of the CAF on the PGE surface [33].

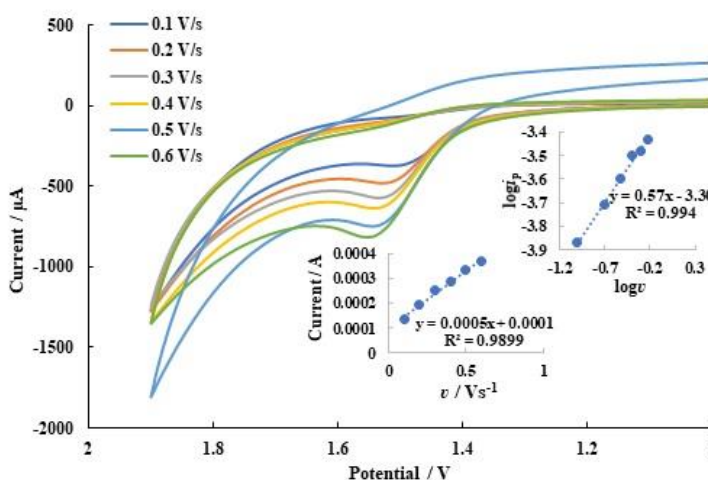


Figure 2. CVs of 1.0 mM CAF with increasing scan rates in PBS buffer solution, pH 1.5. Insets: i_p - v and $\log i_p$ - $\log v$ graphs.

3.2 Effect of supporting electrolyte and pH

The pH value and components of electrolyte solutions are important factors affecting the redox behavior of electroactive species. For this reason, to investigate the effect of supporting electrolyte and pH, PBS (1.5-3.0 with the interval of 0.5), 0.1 M H₂SO₄ (1.0-2.5 with the interval of 0.5) and 0.04 M Britton Robinson (2.0-7.0 with the interval of 1.0) buffer solutions at different pH values for the oxidation of CAF were explored in different pH ranges by using CV technique (Fig. 3). It can be seen that the oxidation peak current of CAF has a maximum value in the PBS buffer solution (pH 1.5) (Fig. 3). This indicated that the best electrolyte for the oxidation of CAF was chosen to be the PBS buffer at the pH of 1.5.

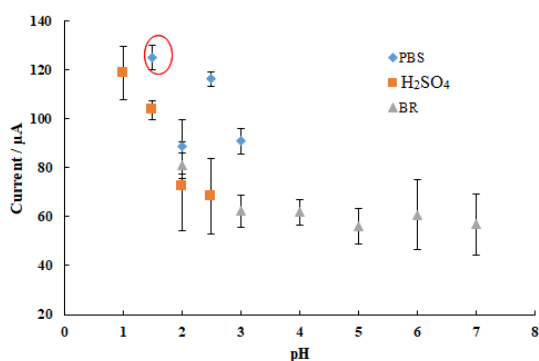


Figure 3. pH-Current results of 1.0 mM CAF obtained by CV in different supporting electrolytes (BR, PBS, and H₂SO₄).

3.3 Optimization of analytical parameters

In adsorptive stripping voltammetric methods, experimental conditions such as accumulation potential and accumulation time are critical parameters that are affected by the electrochemical signal of organic compounds. In this context, to develop AdsDPV and AdsSWV methods for analyzing of CAF, the effect of the accumulation potential and accumulation time on the peak current were investigated for both adsorptive stripping methods. Accumulation potential was changed in the potential ranges, 0.0 - 1.0 V (with 0.1 V

increments) (Fig. 4A and 4B). According to Figure 4A, the peak current value of CAF increases in the potential range, 0.0 to 0.2 V, then decreases in the range 0.3 to 1.0 V. Hence, optimum accumulation potential was selected as 0.2 V for the AdsDPV method. Parallel trials for AdsSWV were done, and the accumulation potential was changed in the range of 0.0 to 1.0 V, and the optimum accumulation potential was selected as 0.3 V. To optimize the accumulation times for AdsDPV and AdsSWV, the accumulation times were changed in the range of 0.0-240 s with 30 s increments. According to the AdsDPV results in Figure 4C, the peak current of CAF increases up to 180.0 s and then decreases, so the best accumulation time for the AdsDPV method was chosen as 180.0 s under these conditions. Similar experiments were also carried out for AdsSWV, and the results were represented in Figure 4D. In the Figure, the peak current of CAF increases with increasing accumulation time up to 120.0 s; then, it decreases slightly. Therefore, the best accumulation time for the AdsSWV method was chosen to be 120.0 s.

3.4 The voltammetric determination of CAF

The practicability of the AdsDPV and AdsSWV methods for the quantitative determination of CAF was studied by measuring the anodic currents of CAF as a function of the increasing concentration levels. Under the optimum conditions, CAF concentration was changed in the range of 0.1 - 1000.0 μM and 0.1 - 1600 μM for AdsDPV and AdsSWV, respectively. The voltammograms in increasing concentrations and the peak current versus concentration of CAF calibration graphs were given in Figure 5A(a) and B(b). The linear regression equations for AdsDPV and AdsSWV were found to be as follows:

$i_p(\text{CAF}) = 0.1978C_{\text{CAF}} + 1.1545$ ($R^2 = 0.9958$) for AdsDPV;

$i_p(\text{CAF}) = 0.1947C_{\text{CAF}} + 5.4664$ ($R^2 = 0.9975$) for AdsSWV.

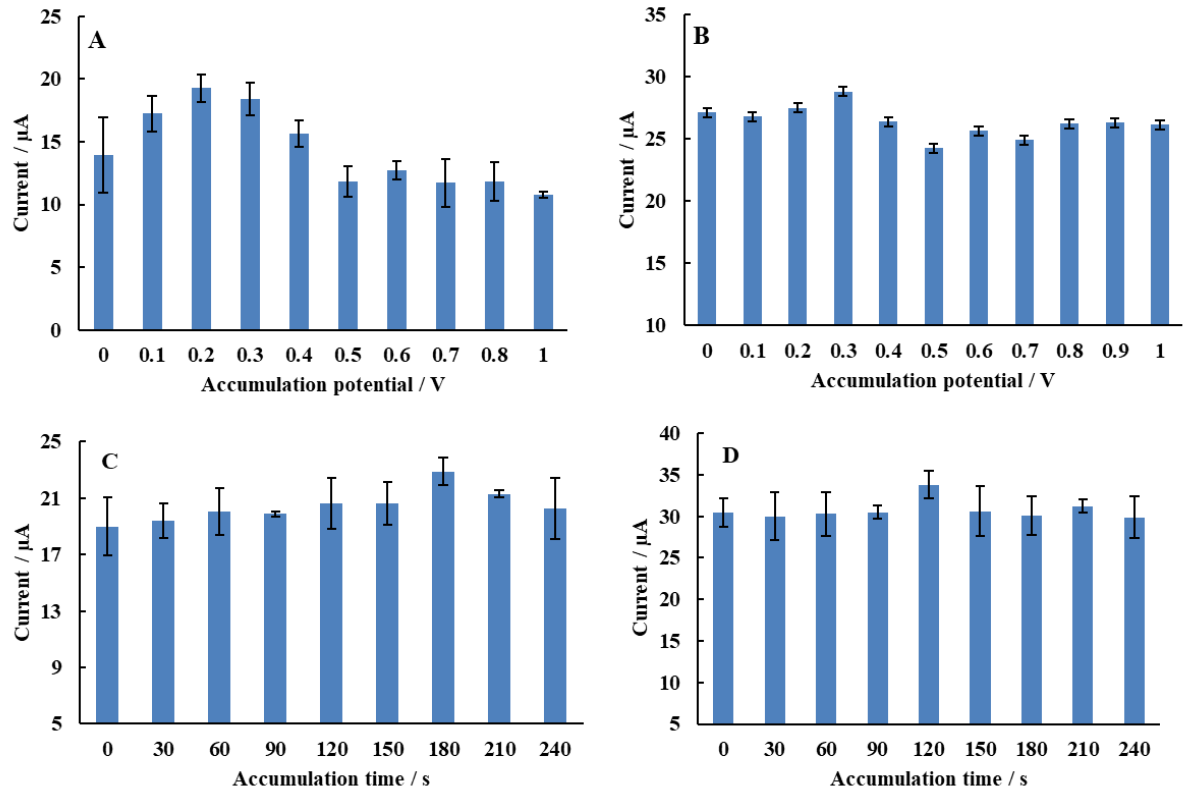


Figure 4. Effect of accumulation potential (A, B) and accumulation time (C, D) on the peak currents of 0.1 mM CAF using AdsDPV (A, C) and AdsSWV (B, D) methods in PBS (pH 1.5).

3.5 The voltammetric determination of CAF

The practicability of the AdsDPV and AdsSWV methods for the quantitative determination of CAF was studied by measuring the anodic currents of CAF as a function of the increasing concentration levels. Under the optimum conditions, CAF concentration was changed in the range of 0.1 - 1000.0 μM and 0.1 - 1600 μM for AdsDPV and AdsSWV, respectively. The voltammograms in increasing concentrations and the peak current versus concentration of CAF calibration graphs were given in Figure 5A(a) and B(b). The linear regression equations for AdsDPV and AdsSWV were found to be as follows:

$$i_p(\text{CAF}) = 0.1978C_{\text{CAF}} + 1.1545 \quad (R^2 = 0.9958) \text{ for AdsDPV;}$$

$$i_p(\text{CAF}) = 0.1947C_{\text{CAF}} + 5.4664 \quad (R^2 = 0.9975) \text{ for AdsSWV.}$$

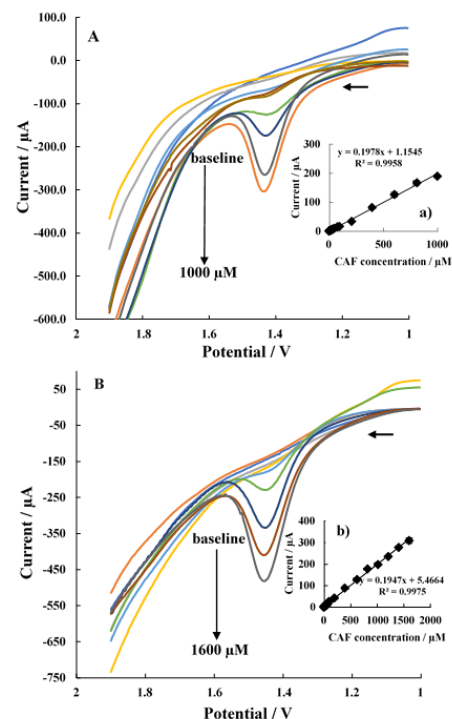


Figure 5. A. AdsDPV and B. AdsSWV voltammograms of CAF at the different concentrations on the PGE surface in the PBS (pH 3.0). Insets a) and b) are the calibration plots for CAF.

The slopes of the calibration curves of CAF obtained by AdsDPV and AdsSWV methods were used to compute the detection (LOD) and the quantification (LOQ) limits with the equations as follows;

$$\text{LOD}=\frac{3s}{m}, \text{ LOQ}=\frac{10s}{m}$$

where s is the standard deviation calculated for the lowest CAF concentration ($0.1 \mu\text{M}$), and m is the slope of the calibration graphs. The LODs were found to be 0.71 and $1.11 \mu\text{M}$ for AdsDPV and AdsSWV, respectively; the LOQs were found to be 2.36 and $3.69 \mu\text{M}$ for AdsDPV and AdsSWV, respectively. Besides, the linear working ranges were found in the range of $2.36 - 1000 \mu\text{M}$ for AdsDPV and $3.69-1600 \mu\text{M}$ for AdsSWV.

The comparison of the analytical performances of the other voltammetric methods for the determination of CAF in different samples was presented in Table 1. As seen in the Table, the detection limits for CAF are in the range of $0.01 - 47.3 \mu\text{M}$ and the LOD value obtained for the AdsDPV method is comparable with the literature reports. Besides, the linear working range of CAF obtained by the AdsSWV method is among the best ones in the literature reports given in Table 1. In addition, the PGE electrode was used directly without any pretreatment and modification processes.

3.6 CAF analysis in commercial ice tea beverage

In order to demonstrate the applicability of the proposed AdsDPV and AdsSWV methods for CAF analysis based on PGE, local commercial ice tea beverage (80 mg/L) was used. The content of CAF in ice tea beverage was determined by the standard addition and recovery tests using proposed methods under optimum experimental conditions. The results obtained are summarized in Table 2, and the recovery values obtained were found in the

range from 99.19% to 115.59% with the RSD % of 6.56 for AdsDPV and AdsSWV $97.62\% - 103.41\%$ with the RSD% of 2.58 . These show the applicability of the method developed in the real sample on the PGE electrode surface without any interference.

3.7 CAF analysis in commercial ice tea beverage

In order to demonstrate the applicability of the proposed AdsDPV and AdsSWV methods for CAF analysis based on PGE, local commercial ice tea beverage (80 mg/L) was used. The content of CAF in ice tea beverage was determined by the standard addition and recovery tests using proposed methods under optimum experimental conditions. The results obtained are summarized in Table 2, and the recovery values obtained were found in the range from 99.19% to 115.59% with the RSD % of 6.56 for AdsDPV and AdsSWV $97.62\% - 103.41\%$ with the RSD% of 2.58 . These show the applicability of the method developed in the real sample on the PGE electrode surface without any interference.

Table 2. Recovery results for CAF from *Didi* ice tea sample using the standard addition method

Method	Claimed, mg/L CAF	Found*, mg/L CAF	Recovery, %	RSD, %
AdsDPV	80.0	83.30; 92.47; 79.35; 83.38	105.79(± 8.63)	6.56
AdsSWV	80.0	79.37; 82.73; 78.77; 78.10	99.68(± 3.19)	2.58

*each value is the average of five experiments, $t=2.78$

for 95% confidence level, t_s/\sqrt{N}

Table 1. The comparison of some voltammetric results for the determination of CAF

Electrode	Analyte	Method	Linear working range, μM	LOD, μM	Application	Literature
PGE	CAF	AdsSWV	0-2574	47.3	Tea samples	[22]
MIP/CP ^a	CAF	DPV	0.06-25	0.015	Cola	[34]
Nafion/MWNTs/GCE ^b	CAF	DPV	0.6-400	0.23	Cola	[35]
MWCNT-Nafion/GCE ^c	CAF	AdsDPV	2.945-377 377-2356	0.513	Drug and Cola	[36]
Nafion-Gr/GCE ^d	CAF	DPV	0.4-40 40-600	0.12	Cola	[37]
Nafion/GO/GCE ^e	CAF	DPV	0.4-80	0.2	Cola, Tea and Energy drink	[38]
SWCNT/CCE ^f	CAF	DPV	0.25-100	0.12	Mineral water	[39]
CF-UME ^g	CAF	FSV [*]	10-200	3.33	Drug	[40]
BDD ^h	CAF	DPV	0.4-25	0.15	Cola, Tea, Coffee and Energy drink	[41]
CPE ⁱ	CAF	SWV	2-1000	0.35	Coffee, Tea, Cola and Drug	[42]
SPE/Nafion/Graphene ^j	CAF	AdsDPV	0.10-0.90 1.0-10	0.021	Cola, Ice tea, Coffee and Energy drink	[43]
GORGCP ^k	CAF	DPV	8-800	0.153	Energy drink and Drug	[44]
PCE/CNFs ^l	CAF	AdsDPV	0.2-1.0	0.056	Energy drink and Cola	[45]
NCOMCP ^m	CAF	DPV	5-600	0.016	Energy drink and Drug	[46]
Fullerene/MWCNT/Naf/GCE ⁿ	CAF	DPV	10-1000	0.072	Drug	[15]
PGE	CAF	AdsDPV	2.36-1000	0.71	Ice tea	<i>This work</i>
		AdsSWV	3.69-1600	1.11		

^aMIP/CP: molecularly imprinted polymer modified carbon paste electrode; ^bNafion/MWNTs/GCE: Nafion/multi-wall carbon nanotubes composite film coated glassy carbon electrode; ^cMulti-Walled Carbon Nanotubes and Nafion modified glassy carbon electrode; ^dNafion-Gr modified glassy carbon electrode; ^eglassy carbon electrode modified with Nafion and graphene oxide; ^fsingle-walled carbon nanotubes on carbon-ceramic electrode; ^gcarbon fiber ultramicroelectrode; ^hBDD: Boron doped diamond electrode; ⁱCarbon paste electrode; ^jNafion and graphene modified screen printed electrode; ^kgraphene oxide-reduced glutathione modified carbon paste; ^lscreen-printed carbon electrode; coated with carbon nanofibers; ^mNano-Cobalt (II, III) oxide modified carbon paste; ⁿfullerene/multiwalled carbon nanotube/Nafion modified glassy carbon electrode; ^{*}FSV: Fast scan voltammetry.

4. Conclusion

This research paper demonstrates the PGE electrode surface without any surface modification was tried as a sensor for CAF determination in ice tea samples. The sensitive detection of CAF was carried out by using adsorptive anodic stripping methods. The effect of scan rate, supporting electrolyte, pH, accumulation time, and accumulation potential values were investigated for the determination of CAF. The linear working ranges, LOD, and

LOQ values obtained by the developed methods were found to be comparable to the methods reported in the literature. The acceptable recovery values for CAF in the *real sample* by using the standard addition method demonstrated that the applicability of the developed methods was satisfactory. The methods proposed may be found as a cheap alternative method for future uses in the beverage industry.

Acknowledgment

Authors highly thankful to the Presidency of Scientific Research Projects of Ankara University for financial supports with the project numbers 20L0430001, 17H0430009 and 13L4240009.

Conflicts of interest

The authors state that did not have conflict of interests.

References

- [1] de Paula Lima J. and Farah A. Caffeine and minor methylxanthines in coffee, in *Coffee, 1st ed. RSC Publishing*, (2019) 543-564.
- [2] Schuster J. and Mitchell E.S., More than just caffeine: Psychopharmacology of methylxanthine interactions with plant-derived phytochemical, *Prog Neuro-Psychoph.* 89 (2019) 263-274.
- [3] Okuroglu E., Tekin T., Kuloglu M., Mercan S., Bavunoglu I., Acikkol M. and Turkmen Z., Investigation of caffeine concentrations in sport supplements and inconsistencies in product labelling, *J. Chem. Metrol.*, 13(1) (2019).
- [4] Farag A.S., Pravcová K., Česlová L., Vytřas K. and Sýs M. Simultaneous determination of caffeine and pyridoxine in energy drinks using differential pulse voltammetry at glassy carbon electrode modified with nafion., *Electroanalysis*, 31(8) (2019) 1494-1499.
- [5] Darakjian L.I. and Kaddoumi A., Physiologically based pharmacokinetic/pharmacodynamic model for caffeine disposition in pregnancy, *Mol. Pharm.*, 16(3) (2019) 1340-1349.
- [6] Mourya S., Bodla R., Taurean R., and Sharma A., Simultaneous estimation of xanthine alkaloids (theophylline, theobromine and caffeine) by high-performance liquid chromatography, *Int. J. Drug Regul. Aff. (IJDRA)*, 7(2) (2019) 35-41.
- [7] Lader M.H., Caffeine withdrawal. Caffeine and Behavior: Current Views & Research Trends: Current Views and Research Trends, London: CRS press, 1999; pp 151.
- [8] Dash S.S. and Gummadi S.N., Catabolic pathways and biotechnological applications of microbial caffeine degradation, *Biotechnol. Lett.*, 28(24) (2006) 1993-2002.
- [9] Diener H., Pfaffenrath V., Pageler L., Peil H. and Aicher B. The fixed combination of acetylsalicylic acid, paracetamol and caffeine is more effective than single substances and dual combination for the treatment of headache: A multicentre, randomized, double-blind, single-dose, placebo-controlled parallel group study, *Cephalalgia*, 25(10) (2005) 776-787.
- [10] Tokola R.A., Kangasniemi P., Neuvonen P.J. and Tokola O. Tolfenamic acid, metoclopramide, caffeine and their combinations in the treatment of migraine attacks. *Cephalalgia*, 4(4) (1984) 253-263.
- [11] Sereshti H. and Samadi S. A rapid and simple determination of caffeine in teas, coffees and eight beverages, *Food Chem.*, 158 (2014) 8-13.
- [12] Greenberg J.A., Dunbar C.C., Schnoll R., Kokolis R., Kokolis S. and Kassotis J. Caffeinated beverage intake and the risk of heart disease mortality in the elderly: A prospective analysis., *Am J Clin Nutr.*, 85(2) (2007) 392-398.
- [13] Lucas M., Mirzaei F., Pan A., Okereke O.I., Willett W.C., O'Reilly É.J., Koenen K. and Ascherio A. Coffee, caffeine, and risk of depression among women., *Arch. Intern. Med.*, 171(17) (2011) 1571-1578.
- [14] Švorc L.u. Determination of caffeine: A comprehensive review on electrochemical methods., *Int. J. Electrochem. Sci.*, 8 (2013) 5755-5773.
- [15] Tajou K.Y., Dongmo L.M. and Tonle I.K. Fullerene/MWCNT/nafion modified glassy carbon electrode for the electrochemical determination of caffeine, *Am. J. Anal. Chem.*, 11(2) (2020) 114-127.
- [16] Kalvoda R. Adsorptive stripping voltammetry in trace analysis, in *Contemporary electroanalytical chemistry*. Berlin: Springer, 1990; pp 403-405.
- [17] Kalvoda R. Review of adsorptive stripping voltammetry—assessment and prospects, *Fresenius J. Anal. Chem.*, 349(8-9) (1994) 565-570.
- [18] Fanjul-Bolado P., Hernández-Santos D., Lamas-Ardisana P.J., Martín-Pernía A. and Costa-García A. Electrochemical characterization of screen-printed and conventional carbon paste electrodes, *Electrochim. Acta.*, 53(10) (2008) 3635-3642.

- [19] Wring S.A. and Hart J.P. Chemically modified, carbon-based electrodes and their application as electrochemical sensors for the analysis of biologically important compounds, A review, *Analyst*, 117(8) (1992) 1215-1229.
- [20] Bayraktepe D.E., Yazan Z. and Önal M. Sensitive and cost effective disposable composite electrode based on graphite, nano-smectite and multiwall carbon nanotubes for the simultaneous trace level detection of ascorbic acid and acetylsalicylic acid in pharmaceuticals, *Talanta*, 203 (2019) 131-139.
- [21] David I.G., Iordache L., Popa D.E., Buleandra M., David V. and Iorgulescu E.-E. Novel voltammetric investigation of dipyrindamole at a disposable pencil graphite electrode, *Turk J Chem.*, 43(4) (2019) 1109-1122.
- [22] Ly S.Y., Jung Y.S., Kim M.H., Kwon Han I., Jung W.W. and Kim H.S. Determination of caffeine using a simple graphite pencil electrode with square-wave anodic stripping voltammetry, *Microchim. Acta.*, 146(3-4) (2004) 207-213.
- [23] Özcan A., Gürbüz M., and Özcan A.A. Preparation of a disposable and low-cost electrochemical sensor for prothion detection based on over-oxidized poly (thiophene) modified pencil graphite electrode, *Talanta*, 187 (2018) 125-132.
- [24] Dagar K. and Pundir C. An improved amperometric l-lactate biosensor based on covalent immobilization of microbial lactate oxidase onto carboxylated multiwalled carbon nanotubes/copper nanoparticles/polyaniline modified pencil graphite electrode, *Enzyme Microb. Technol.*, 96 (2017) 177-186.
- [25] Dede E., Sağlam Ö. and Dilgin Y. Sensitive voltammetric determination of niclosamide at a disposable pencil graphite electrode, *Electrochim. Acta.*, 127 (2014) 20-26.
- [26] Dilgin D.G. and Karakaya S. Differential pulse voltammetric determination of acyclovir in pharmaceutical preparations using a pencil graphite electrode, *Mater. Sci. Eng. C.*, 63 (2016) 570-576.
- [27] Kariuki J.K. An electrochemical and spectroscopic characterization of pencil graphite electrodes, *Electrochem. Soc.*, 159(9) (2012) 747-751.
- [28] Eşiköy Bayraktepe D. and Yazan Z. Application of single-use electrode based on nano-clay and MWCNT for simultaneous determination of acetaminophen, ascorbic acid and acetylsalicylic acid in pharmaceutical dosage, *Electroanalysis*, 32(6) (2020) 1263-1272.
- [29] Wang J., Analytical electrochemistry 3rd ed. Wiley-vch hoboken, NJ. 2006
- [30] Chitravathi S. and Munichandraiah N. Voltammetric determination of paracetamol, tramadol and caffeine using poly (nile blue) modified glassy carbon electrode., *J. Electroanal. Chem.* 764 (2016) 93-103.
- [31] Erden S., Bayraktepe D.E., Yazan Z. and Dinç E. TiO₂ modified carbon paste sensor for voltammetric analysis and chemometric optimization approach of amlodipine in commercial formulation, *Ionics.*, 22(7) (2016) 1231-1240.
- [32] Radi A., El-Ghany N.A. and Wahdan T. Voltammetric behaviour of rabeprazole at a glassy carbon electrode and its determination in tablet dosage form, *Il Farmaco*. 59(7) (2004) 515-518.
- [33] Ali, H. S., Abdullah, A. A., Pinar, P. T., Yardım, Y. and Şentürk, Z. Simultaneous voltammetric determination of vanillin and caffeine in food products using an anodically pretreated boron-doped diamond electrode: its comparison with HPLC-DAD, *Talanta*, 170 (2017) 384-391.
- [34] Alizadeh T., Ganjali M.R., Zare M. and Norouzi P. Development of a voltammetric sensor based on a molecularly imprinted polymer (MIP) for caffeine measurement, *Electrochim. Acta.*, 55(5) (2010) 1568-1574.
- [35] Yang S., Yang R., Li G., Qu L., Li J. and Yu L. Nafion/multi-wall carbon nanotubes composite film coated glassy carbon electrode for sensitive determination of caffeine, *J. Electroanal. Chem.*, 639(1-2) (2010) 77-82.
- [36] Zhang J., Wang L., Guo W., Peng X., Li M. and Yuan Z. Sensitive differential pulse stripping voltammetry of caffeine in medicines and cola using a sensor based on multi-walled carbon nanotubes and nafion, *Int. J. Electrochem. Sci.*, 6(4) (2011) 997-1006.

- [37] Sun J.-Y., Huang K.-J., Wei S.-Y., Wu Z.-W. and Ren F.-P. A graphene-based electrochemical sensor for sensitive determination of caffeine, *Colloids Surf. B*, 84(2) (2011) 421-426.
- [38] Zhao F., Wang F., Zhao W., Zhou J., Liu Y., Zou L. and Ye B., Voltammetric sensor for caffeine based on a glassy carbon electrode modified with nafion and graphene oxide, *Microchim. Acta.*, 174(3-4) (2011) 383-390.
- [39] Habibi B., Abazari M. and Pournaghi-Azar M.H. A carbon nanotube modified electrode for determination of caffeine by differential pulse voltammetry, *Chinese J. Catal.*, 33(11-12) (2012) 1783-1790.
- [40] Nunes R.S. and Cavaleiro É.T. Caffeine determination at a carbon fiber ultramicroelectrodes by fast-scan cyclic voltammetry, *J. Braz. Chem. Soc.*, 23(4) (2012) 670-677.
- [41] Švorc L.u., Tomčík P., Svítková J., Rievaj M. and Bustin D. Voltammetric determination of caffeine in beverage samples on bare boron-doped diamond electrode, *Food chem.*, 135(3) (2012) 1198-1204.
- [42] Mersal G.A. Experimental and computational studies on the electrochemical oxidation of caffeine at pseudo carbon paste electrode and its voltammetric determination in different real samples, *Food Anal. Methods.*, 5(3) (2012) 520-529.
- [43] Lezi N., Economopoulos S., Prodromidis M., Economou A. and Tagmatarchis N. Fabrication of a “green” and low-cost screen-printed graphene sensor and its application to the determination of caffeine by adsorptive stripping voltammetry, *Int. J. Electrochem. Sci.*, 12(2017) 6054-6067.
- [44] Shehata M., Azab S. and Fekry A. May glutathione and graphene oxide enhance the electrochemical detection of caffeine on carbon paste sensor in aqueous and surfactant media for beverages analysis?, *Synth. Met.*, 256 (2019) 116122.
- [45] Tyszczyk-Rotko K., Pietrzak K. and Sasal A. Adsorptive stripping voltammetric method for the determination of caffeine at integrated three-electrode screen-printed sensor with carbon/carbon nanofibers working electrode, *Adsorption*, 25(4) (2019) 913-921.
- [46] Fekry A., Shehata M., Azab S. and Walcarius A. Voltammetric detection of caffeine in pharmacological and beverages samples based on simple nano-co (ii, iii) oxide modified carbon paste electrode in aqueous and micellar media, *Sens. Actuators B Chem.*, 302 (2020) 127172.

pH and thermoresponsive comb-type grafted hydrogels based on polyethylene glycol diglycidyl ether and monoamino/diamino terminated jeffamines: synthesis, characterization and physicochemical properties

Ahmet ERDEM^{1*} 

¹ Kocaeli University, Faculty of Technology, Department of Biomedical Engineering, Umuttepe Yerleşkesi 41001-Kocaeli, Turkey

Abstract

In the present study, the synthesis of thermo- and pH-sensitive comb-type grafted hydrogels based on polyetheramine was performed using polyethylene glycol diglycidyl ether [PEGDGE] as the activator. Monoamino terminated Jeffamine® M2005 was used as the polyether to incorporate the hydrophobic and thermo-sensitive character in the copolymer, while diamino terminated Jeffamine® ED600 was used as the crosslinker to initiate the amine-epoxy ring-opening reaction. These polyethylene glycol [PEG]-polypropylene glycol [PPG] hydrogels present pH responsive properties and thermo-sensitivity due to the presence of cationic functional groups and the Jeffamine moieties, respectively. Fourier-transform infrared (FTIR) spectroscopy and swelling behavior at different pH [2-10] and temperatures [4-50 °C] were applied to examine the physicochemical properties of the hydrogels. The volume-phase transition temperature [VPTT] of the hydrogels was determined based on PPG content and pH of the solution. The physicochemical features of the hydrogels depended on the Jeffamine used and the ratio of Jeffamine units introduced. The maximum swelling capacity of the hydrogels as a function of time was determined at 4 °C and pH 5, while the optimum deswelling capacity was obtained at 40 °C and pH 7.4. Results showed that the dual responsive PEG-PPG based hydrogels may be suitable for potential application as drug delivery system sensors.

Article info

History:

Received: 21.05.2020

Accepted: 15.09.2020

Keywords:

Hydrogels,
Thermo-response,
pH response,
Swelling and
deswelling kinetics,
Polyethylene glycol.

1. Introduction

Stimuli responsive polymeric materials have received great attention over the last years, due to their interesting features with respect to different applications in the field of biomedicine, pharmacy and biotechnology. Generally, these polymeric materials are widely represented by hydrogels composed of either three-dimensional homo or copolymer crosslinked network [1]. These hydrogels' behavior is mainly based on their structural properties as well as environmental conditions. Over the last decades, hydrogels with environmentally responsive properties have been largely applied in smart material research. This class of hydrogels show dramatic volume change in respect to different stimuli such as temperature, pH, ionic activity, magnetic field, electrical, UV or visible light [2, 3]. Thanks to this volume change character, also known as volume phase transition [VPT], various applications such as controlled drug delivery, tissue engineering, catalysts, etc. have been widely

developed. Amongst all, temperature and pH responsive hydrogels have been extensively investigated attributed to their important physicochemical characteristics. In essence, derivatives of poly[N-isopropylacrylamide] [4] and poly[acrylic acid] [5] have proven to be the most used polymers in the preparation of thermo- and pH-sensitive hydrogels, respectively. In addition, some investigated reports on crosslinked polyethylene glycol [PEG]/ polypropylene glycol [PPG] hydrogels have demonstrated to possess temperature responsive properties [6-8]. The interaction between hydrophobic PPG and water molecules tends to show significantly temperature-dependent [9]. On the other hand, PEG, in comparison to other standard polymers, has an exceptional character where is phase separation over a critical point that relies on molar weight with increasing temperature [10].

Different forms of PEG and PPG such as di- and tri-block copolymers also known commercially as pluronic or poloxamers are one of the most widely researched topics, attributed to their thermo-sensitive

*Corresponding author. Email address: ahmet.erdem@kocaeli.edu.tr

<http://dergipark.gov.tr/csj> ©2020 Faculty of Science, Sivas Cumhuriyet University

properties particularly in the field of controlled drug delivery and tissue engineering [11-13], paints, coatings and cosmetic formulations [14, 15]. In general, the synthesis of PEG-PPG crosslinked hydrogels has been mostly achieved using different reactive end groups of methacrylate [16, 17] and acrylate [18, 19] via free radical polymerization. However, this technique being air-sensitive has mostly been performed under controlled conditions in closed small-scale environments [20]. Thus, polycondensation and polyaddition polymerization reactions have proven to be the most widely used alternatives for the preparation of such hydrogels [6, 8], considering these reaction methods are not particularly sensitive to water, oxygen or impurity. Moreover, these polymerization reactions are widely applied in the production of industrial epoxy resin by reacting diepoxides with di- or tri-amines. Recently, amino terminated PEG and PPG polymers under the trade name Jeffamine® series, manufactured by Huntsman have demonstrated to be ideal not only for the production of epoxy resins, but also in the synthesis of epoxy-amine based hydrogel [21]. Krakovsky et al. in a recent study prepared elastic epoxy based hydrogels by reacting Bisphenol A propoxylate diglycidyl ether with α , ω -diamino terminated Jeffamine ED2003 and ED600 [22]. In another study, Ribeles et al. investigated the thermal behavior of prepared Jeffamine ED2003 based hydrogels [23]. Also, Krakovsky et al. reported the synthesis of an epoxy network based on hydrophobic Jeffamine D series and polyethylene glycol bis[glycidyl ether] [PEGDGE] by analyzing their thermal transitional behaviors [20]. Recently, Anghelache et al. investigated the preparation of thermo-responsive hydrogels that were formed via the reaction of diamino terminated PPG and PEGDGE. Results showed that the volume phase transition was mainly dependent on the PEG/PPG ratio [6].

To date, the synthesis of such hydrogels is not limited solely to the use of diamino functional Jeffamine® ED and D series, but monoamino functional Jeffamine [Jeffamine M2005] has also demonstrated efficiency in the synthesis of temperature sensitive hydrogels. Typically, this functional Jeffamine® M2005 composed of monoamino terminated polyoxyethylene-block-polyoxypropylene [POE-POP] has been used in the functionalization of polysaccharides to form comb-type grafted thermo-responsive hydrogels [24, 25]. Normal types of temperature sensitive PEG / PPG based hydrogels with different structure have been extensively prepared. [6, 20, 22, 23]. However, in terms of fast response with respect to the stimuli responsiveness, one of the useful ways to improve response rates is via the adaptation of

the hydrogel's structure at molecular level by grafting on the backbone of the polymers [17, 18]. In our previous studies, we prepared and compared PEG-PPG based normal- and comb-type grafted hydrogels and investigated their fast response rate to pH and temperature. Results depicted comb-type grafted hydrogels with the fastest response rates [26]. In addition, the volume phase transition temperature [VPTT] of the hydrogels depended mostly on the PEG-PPG ratio [6, 8]. In this study, PEG-PPG based thermo- and pH sensitive comb-type grafted cationic hydrogels were successfully prepared via amine-epoxy ring opening reaction by varying PPG ratio. The effects of grafted PPG content, swelling and deswelling capacity as a function time as well as solubility fractions of the hydrogels were analyzed systematically at varying temperatures and pH conditions. In addition, the VPTT changes of hydrogels were investigated following the difference in PPG content and solution pH. Accordingly, it was observed that PPG ratio is vital in achieving efficient thermo-responsive hydrogels with rapid response and low solubility. The proposed novel comb-type cationic hydrogels show great potential for applications in various fields such as drug delivery, actuators, and smart sensors.

2. Experimental

2.1. Materials

In the preparation of the epoxy networks, α , ω -diamino terminated polyoxypropylene-block-polyoxyethylene-block-polyoxypropylene [Jeffamine ED600] and monoamino terminated polyoxyethylene-block-polyoxypropylene [Jeffamine M2005] of average molecular weights 528 and 2090 g/mol, respectively, were supplied by Huntsman [Texas, USA]. Polyethylene glycol bis[glycidyl ether] [PEGDGE] of average molecular weight 500 g/mol was purchased from Sigma-Aldrich [Darmstadt, Germany]. Scheme 1 displays the chemical formulas of PEG and PPG based reactants. Toluene was used as the extracting solvent for non-reacted molecules was supplied by Sigma-Aldrich. AMC-2 catalyst [Aerojet Chemicals, Rancho Cordova, CA], composed of 50% trivalent organic chromium complexes and 50% phthalate esters was used to minimize possible epoxy homopolymerization. All obtained products were dried under vacuum at 40 °C for 48 hours before use.

2.2. Preparation of comb-type grafted PEG-PPG Hydrogels

Five different networks were prepared based on the initial molar concentrations of the reactive groups

$[r = 2[\text{NH}_2]_0/[\text{E}]_0]$, where r is the molar ratio of amine $[\text{NH}_2]$ to epoxy groups.

Catalytic amount of AMC-2 catalyst (1 drop) was added to this composition as a catalytic inhibitor of side reactions. All reactants in the composition mixture were first stirred homogeneously at 100 °C for 15 min and then poured into silicon molds. In these molds, the reactions were performed under nitrogen atmosphere at 120 °C for 48 h. The obtained gels based on hydrophobic Jeffamine® M2005 to PEG diepoxide mole ratio were labeled JM0, JM10, JM20, JM30, and JM40 as shown in Table 1.

At the end of this reaction phase, non-reacted soluble fractions in the hydrogel networks were removed via a

triple extraction step using toluene. The final products were carefully dried first in open air and then at 40 °C under vacuum for about 48 h. The soluble fraction (SF) was calculated using the following equation:

$$\text{SF (\%)} = \frac{W_0 - W}{W_0} \times 100 \quad (1)$$

where, W_0 and W are the weights of the hydrogels before and after purification, respectively.

FTIR spectrum of dried hydrogels was obtained using Shimadzu 8201 FT infrared spectrophotometer at a resolution of 4 cm^{-1} in the range of 4000–400 cm^{-1} .

Table 1. Chemical composition of PEG-PPG based hydrogel with soluble fractions

Hydrogel	Diepoxy		JM2005		JED600		SF
Code	g	mmol	g	mmol	g	mmol	%
JM0	1.00	2.00	0.00	0.00	0.53	1.00	6.29
JM10	1.00	2.00	0.41	0.20	0.47	0.90	12.20
JM20	1.00	2.00	0.84	0.40	0.42	0.80	24.23
JM30	1.00	2.00	1.25	0.60	0.37	0.70	31.99
JM40	1.00	2.00	1.67	0.80	0.32	0.60	39.60

2.3. Swelling analysis

The swelling behavior of the synthesized hydrogels with respect to change in pH and temperature was evaluated by immersing weighted hydrogels into the different pH buffer solution of 2.5, 5.0, 7.4, and 10.0 as well as different temperatures from 4 to 50 °C for 24 h. The ionic strength of all pH buffer solutions was adjusted to 0.1 M beforehand. Once the swollen hydrogels reached equilibrium, they were separated from the buffer solution, blotted with filter paper and then measure accurately in triplicates and the average value recorded. The swelling ratio [SR] was subsequently calculated following the equation below.

$$\text{SR} = \frac{W_s}{W_d} \quad (2)$$

where, W_s and W_d are the weights of the equilibrium swollen and dried gels, respectively.

The dynamic swelling behaviors of the hydrogels were analyzed by calculating the change in SR as a function of time at 4 °C in pH 7.4 buffer solutions. At regular time intervals, the hydrogel samples were removed from the buffer solutions, blotted, and weighed to

calculate the water retention using the following equation:

$$\text{SR}_t = \frac{W_t}{W_d} \quad (3)$$

where, W_d represents the weights of the dried samples and W_t represents the weights of the swollen hydrogels at time t .

2.4. Deswelling capacity

The deswelling rate of the hydrogels was investigated using swollen samples in pH 7.4 buffer solution at 4 °C for 24 h and then transferred to an oven of temperature 40 °C. At this temperature, the weight difference of the hydrogels was gravimetrically determined at varying time intervals as described above. The water retention [WR] percentage was calculated using the equation below.

$$\text{Water retention} = \frac{W_t - W_d}{W_s} \times 100 \quad (4)$$

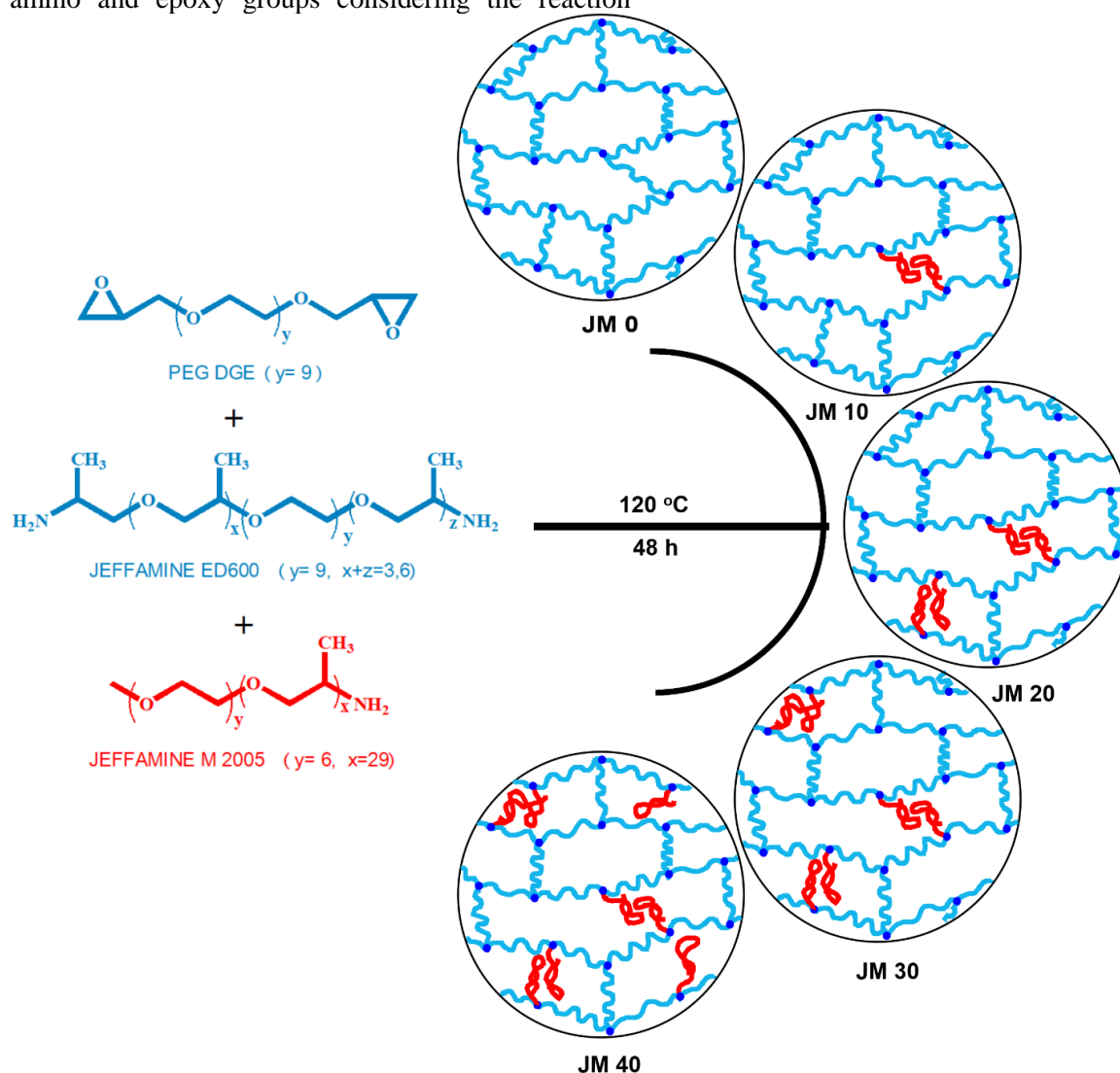
where, W_s represents the weights of equilibrium swollen hydrogels at 40 °C, W_t represents the weights of hydrogels at time t and W_d represents the weights of dried samples.

3. Results and discussion

3.1. Synthesis and characterization of PEG-PPG based comb-type grafted hydrogels

Five different compositions of hydrogels were synthesized via ring-opening reactions by reacting Jeffamine® M2005 and PEGDGE using Jeffamine® ED600 as the crosslinking agent. The schematic reaction processes are depicted in Scheme 1. The various hydrogel networks are formed by increasing the mole ratio of the monoamino-terminated polymer. A constant molar ratio of 1:2 was used between the amino and epoxy groups considering the reaction

capability of one primary amines being able to bind with two epoxy rings. As observed in the reaction mechanism shown in Scheme 2, primary amines react with an epoxy moiety to form secondary amines followed by possible second reaction where another epoxy ring can be opened by secondary amines to form tertiary amine compounds. In addition, hydroxyl groups formed as intermediates during the ring-opening reaction process may participate by reacting with epoxide rings as side reactions. Thus, the use of AMC-2 catalyst was incorporated as an inhibitor to eliminate side reactions generated by hydroxyl groups [27].

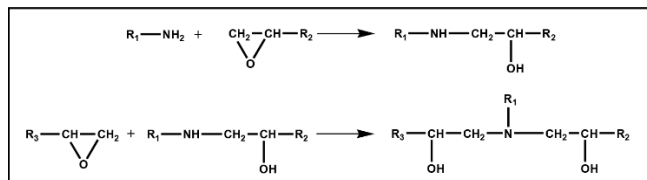


Scheme 1. Illustration of chemical reactions involved in the preparation of comb-type grafted PEG-PPG based hydrogels.

In general, during the preparation of such hydrogel networks, defects often exist described by loops and pendant links. These defects normally known as soluble fractions demonstrates negative effects during the characterization and application of the final product. Therefore after synthesis, it is essential for a

suitable solvent to be used in the extraction of the comb-type grafted network, toluene was used as a suitable solvent to extract unreacted soluble PPG and PEG residues in the hydrogel by washing several times. For these hydrogels, an increase in the amount of Jeffamine M2005 increased the amount of soluble

fractions from 6.3% to 39.6% for JM0 and JM40, respectively. This is attributed to the decreasing amount of crosslinker and the entanglement of high molecular weight Jeffamine M2005 in the hydrogel network [20].



Scheme 2. Schematic reaction mechanism representation of primary amines with epoxy moieties in the formation of epoxy networks.

Fourier transform infrared [FTIR] spectroscopy was used to analyze the functionality of the hydrogels. Figure 1 depicts the FTIR spectra for varying ratio of PPG content for dried comb-type grafted hydrogels. The characteristic peaks at 846, 947, 1100, 1250, 1295, 1347, and 1464 cm^{-1} were attributed to stretching vibrations for the polyether chains. The bands at 756 and 911 cm^{-1} were assigned to the typical stretching and vibrations of epoxy rings which disappeared after the reaction [28]. Increase in the amount of incorporated Jeffamine M2005 was confirmed by the increasing intensity of symmetrically deformed and asymmetrically spread peak of PPG methyl groups at 1373 and 2969 cm^{-1} , respectively [6]. Also, the broad band observed at 3454 cm^{-1} relates to hydroxyl [-OH] groups formed during the ring-opening reaction process.

3.2. Effect of contact time on the swelling capacity of hydrogels

The effect of hydrogel swelling as a function of time was investigated at a constant pH 7.4 and at a temperature of 4 °C. The obtained results are illustrated in Figure 2. Swelling analysis performed at 4 °C was due to the cloud point temperature of Jeffamine® M2005 determined as 18 °C [29]. All synthesized hydrogels demonstrated to reach equilibrium swelling within 24 h. Based on formulated samples, swelling capacity of hydrogels increased with increasing amount of Jeffamine® M2005. Therefore, the equilibrium swelling of the hydrogels were in the magnitude of JM40>JM30>JM20>JM10>JM0. Crosslinking density in hydrogels plays a vital role in their network stability. A gradual increase in the amount of Jeffamine® M2005 decreased the crosslinking density of the hydrogels. However, hydrogel samples with high crosslinking density reached equilibrium swelling faster than lower crosslinked hydrogels due to the hydrophobic nature of

Jeffamine® M2005 that tend to slow water penetration into the hydrogel network.

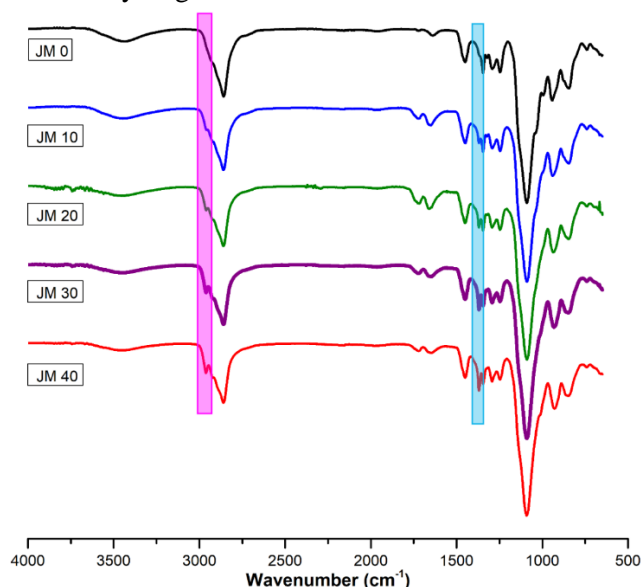


Figure 1. FTIR spectra of the prepared hydrogels.

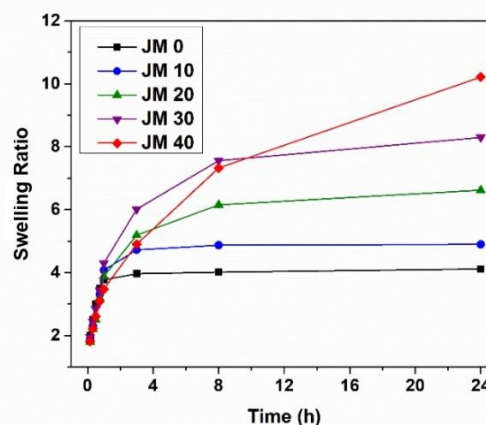


Figure 2. Swelling capacity of PEG-PPG based hydrogels as a function of time at 4 °C and pH 7.4 buffer solution.

3.3. Effect of pH on the swelling capacity of hydrogels

The effect of pH on equilibrium swelling of the hydrogels was evaluated at varying pH of 2.5, 5.0, 7.4 and 10.0 at constant temperature of 4 °C. The deduced results are summarized in Figure 3. The prepared hydrogels are composed of cationic amine components such as tertiary amines or unreacted secondary/primary amines. These functional groups play an important role in the swelling capacities of the hydrogels with respect to medium pH. Maximum swelling capacities were determined at pH 5.0 as 4.69, 6.31, 7.93, 10.73, and 12.22 g/g for JM0, JM10, JM20, JM30, and JM40, respectively. Considering the high acidity of pH 2.5,

the obtained lower swelling capacities as compared to pH 5.0 for all hydrogels was attributed to the excess presence of H^+ ions in solution that in tend reduced the osmotic pressure difference between outside and inside of the hydrogels [30], thus directly decreasing the swelling ability of the hydrogels. By the increasing pH to 7.4, swelling capacity of the hydrogels gradually decreased to 4.11, 4.89, 6.61, 8.29, and 10.21 g/g for JM0, JM10, JM20, JM30, and JM40, respectively. This decrease was related to decreasing charge density on hydrogels as pH increases thereby decreasing electrostatic interaction between hydrogels and water molecules [31]. However, swelling ratios of hydrogels did not decrease as much as before with increasing the pH from 7.4 to 10.0 due to the low electrostatic interaction change.

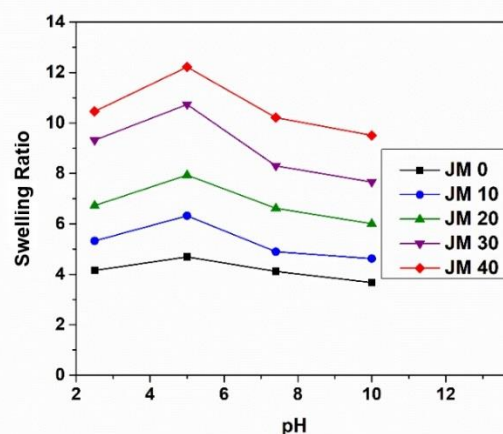


Figure 3. Swelling capacity of PEG-PPG based hydrogels at different pH and constant temperature of 4 °C.

3.4. Temperature response of hydrogels based on swelling analysis

The thermo-responsive properties of the prepared comb-type grafted hydrogels were evaluated by determining swelling capacity at different temperature values ranging from 4 to 50 °C at constant pH 5.0 and 7.4. Based PPG-containing hydrogels, The decrease in swelling capacity of hydrogels with temperature indicates that they are thermo-sensitive [

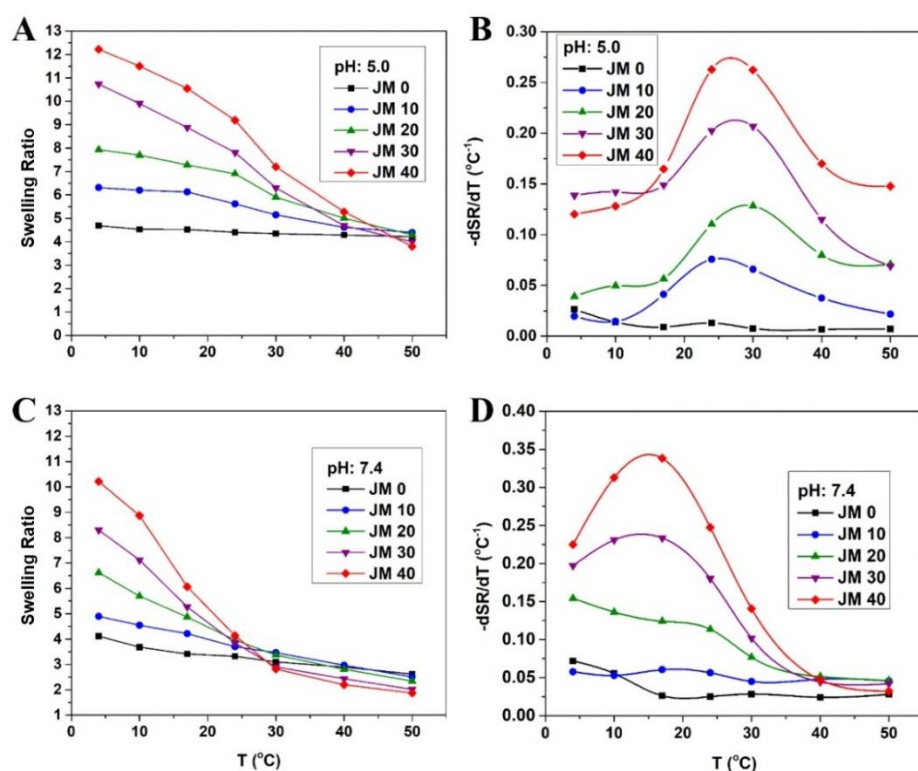


Figure 4. The swelling capacity of PEG-PPG based hydrogels as a function of temperature change A) original curves at pH 5.0, B) derivative curves at pH 5.0, C) original curves at pH 7.4, and D) derivative curves at pH 7.4.

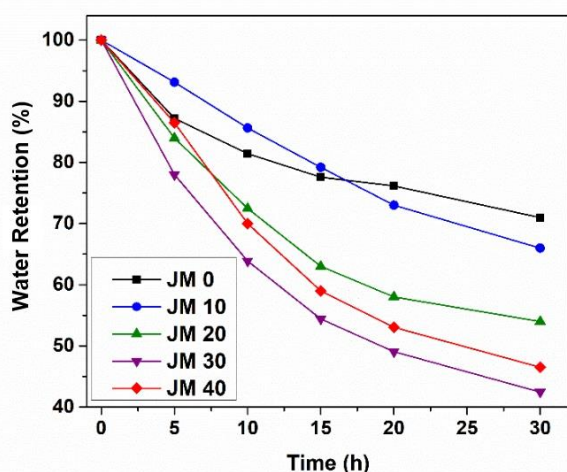


Figure 5. Water retention dependence on the deswelling time of PEG-PPG based hydrogels as the water temperature changes from 4 to 40 °C.

4. Conclusions

Crosslinked PEG-PPG thermo- and pH-sensitive hydrogels based on Jeffamine® M2005, Jeffamine® ED600, and PEGDGE were synthesized and characterized physico-chemically. The thermo- and pH-responsive behavior of hydrogels were evidenced via appropriate swelling measurements. Jeffamine® M2005 induced interesting thermosensitive properties in the hydrogels due to its preponderantly intramolecular or intermolecular interactions and hydrophobic character. At high temperature, the swelling capacity of the hydrogels was mainly controlled by PPG concentration, which indicated an increase in swelling with increasing PPG hydrophobic content. While at lower temperature, the swelling ability was majorly controlled by crosslinking density that demonstrated the hydrogels swelling increased with decreasing crosslinker ratio. Comparatively, deswelling analysis showed that JM30 deswelled faster than JM40 due to its higher crosslinking density and suitable thermo-responsive properties. Thus, depicting JM30 as the most suitable thermo-responsive hydrogel with highest sensitivity and lower soluble fractions than JM40. In addition, VPTT of the PEG-PPG based hydrogels demonstrated to be in close agreements with the phase separation temperature of Jeffamine® M2005 at pH 7.4. In conclusion, the prepared dual sensitive PEG-PPG hydrogels have chance for interesting potential applications in controlled drug delivery like our previous study [26]. Further studies are in development to appreciate their performances in this field.

Conflict of Interests

The authors declare no conflict of interest.

Acknowledgements

A great thanks to the HUSTMAN Corp. for the gift of the jeffamine chemicals.

References

- [1] Ahmed EM., Hydrogel: Preparation, characterization, and applications: A review. *Journal of advanced research*, 6(2) (2015) 105-121.
- [2] Peppas NA, Hilt JZ, Khademhosseini A, Langer R. Hydrogels in biology and medicine: from molecular principles to bionanotechnology, *Advanced Materials*, 18(11) (2006) 1345-1360.
- [3] Ratner BD, Hoffman AS, Schoen FJ, Lemons JE. Biomaterials science: an introduction to materials in medicine: Elsevier; 2004.
- [4] Calik MK, Ozdemir M., Synthesis, characterization and, swelling behavior of semi-IPN nanocomposite hydrogels of alginate with poly (N-isopropylacrylamide) crosslinked by nanoclay, *Journal of Applied Polymer Science*, 133(12) (2016).
- [5] Kocak G, Tuncer C, Bütün V., pH-Responsive polymers, *Polymer Chemistry*, 8(1) (2017) 144-176.
- [6] Anghelache A, Teodorescu M, Stănescu PO, Drăghici C, Vuluga DM. Novel crosslinked thermoresponsive hydrogels with controlled poly (ethylene glycol)—poly (propylene glycol) multiblock copolymer structure, *Colloid and Polymer Science*, 292(4) (2014) 829-638.
- [7] Pahimanolis N, Sorvari A, Luong ND, Seppälä J. Thermoresponsive xylan hydrogels via copper-catalyzed azide-alkyne cycloaddition, *Carbohydrate Polymers*, 102 (2014) 637-644.
- [8] Erdem A, Ngwabebhoh FA, Yildiz U., Synthesis, characterization and swelling investigations of novel

- polyetheramine-based hydrogels, *Polymer Bulletin* 74(3) (2017) 873-893.
- [9] Saito S, Otsuka T., Dissolution of some polymers in aqueous solutions of urea, of its related compounds, and of tetraalkylammonium salts, *Journal of Colloid and Interface Science*, 25(4) (1967) 531-536.
- [10] Brown C., Water soluble polymers, New York: Elsevier, 1974; pp. 424
- [11] Ma W-D, Xu H, Wang C, Nie S-F, Pan W-S., Pluronic F127-g-poly (acrylic acid) copolymers as in situ gelling vehicle for ophthalmic drug delivery system, *International Journal of Pharmaceutics*, 350(1-2) (2008) 247-256.
- [12] Gioffredi E, Boffito M, Calzone S, Giannitelli SM, Rainer A, Trombetta M, et al., Pluronic F127 hydrogel characterization and biofabrication in cellularized constructs for tissue engineering applications, *Procedia Cirp.*, 49 (2016) 125-32.
- [13] Erdem A, Ngwabebhoh FA, Yildiz U., Fabrication and characterization of soft macroporous Jeffamine cryogels as potential materials for tissue applications, *RSC Advances*, 6(113) (2016) 111872-11881.
- [14] Sharma RK, Shah U., Aggregation Behavior of PEO-PPO-PEO Tri-Block Copolymer (Pluronic® L64) in Nonionic Surfactant Additives Environment, *Tenside Surfactants Detergents*, 51(3) (2014) 274-281.
- [15] Singh V, Khullar P, Dave PN, Kaur N. Micelles, mixed micelles, and applications of polyoxypropylene (PPO)-polyoxyethylene (PEO)-polyoxypropylene (PPO) triblock polymers, *International Journal of Industrial Chemistry*. 41(1) (2013) 12-19.
- [16] Sosnik A, Cohn D, Román JS, Abraham GA., Crosslinkable PEO-PPO-PEO-based reverse thermo-responsive gels as potentially injectable materials, *Journal of Biomaterials Science, Polymer Edition* 14(3) (2003) 227-239.
- [17] Niu G, Djaoui AB, Cohn D., Crosslinkable PEO-PPO-PEO triblocks as building blocks of thermo-responsive nanoshells, *Polymer*, 52(12) (2011) 2524-2530.
- [18] Lee S-Y, Tae G., Formulation and in vitro characterization of an in situ gelable, photopolymerizable Pluronic hydrogel suitable for injection, *Journal of Controlled Release*. 119(3) (2007) 313-319.
- [19] Kim MR, Park TG., Temperature-responsive and degradable hyaluronic acid/Pluronic composite hydrogels for controlled release of human growth hormone, *Journal of Controlled Release*, 80(1-3) (2002) 69-77.
- [20] Krakovský I, Cayuela JC, i Serra RS, Salmerón-Sánchez M, Dodda JM. Epoxy networks and thermosensitive hydrogels prepared from α , ω -diamino terminated polyoxypropylene and polyoxyethylene bis (glycidyl ether), *European Polymer Journal*, 55 (2014) 144-152.
- [21] Epoxy formulations using Jeffamine® Polyetheramines, www.huntsman.com.
- [22] Krakovský I, Székely NK., SANS and DSC study of water distribution in epoxy-based hydrogels. *European polymer journal*, 47(12) (2011) 2177-88.
- [23] Ribelles JLG, Sanchez MS, de la Osa LT, Krakovský I. Thermal transitions in α , ω -diamino terminated poly (oxypropylene)-block-poly (oxyethylene)-block-poly (oxypropylene) aqueous solutions and their epoxy networks, *Journal of Non-Crystalline Solids*, 351(14-15) (2005) 1254-1260.
- [24] Mocanu G, Souguir Z, Picton L, Le Cerf D., Multi-responsive carboxymethyl polysaccharide crosslinked hydrogels containing Jeffamine side-chains. *Carbohydrate Polymers*, 89(2) (2012) 578-585.
- [25] Marques NdN, Balaban RdC, Halila S, Borsali R. Synthesis and characterization of carboxymethylcellulose grafted with thermoresponsive side chains of high LCST: The high temperature and high salinity self-assembly dependence, *Carbohydrate Polymers*, 184 (2018) 108-117.
- [26] Erdem A., Preparation and characterization of rapid temperature responsive cationic comb-type grafted POE-POP based hydrogel as prospective excellent actuators/sensors, *Colloids and Surfaces A: Physicochemical and Engineering Aspects* (2020) 125523-125529.
- [27] Esen H, Küsefoğlu S, Wool R., Photolytic and free-radical polymerization of monomethyl maleate esters of epoxidized plant oil triglycerides, *Journal of Applied Polymer Science*, 103(1) (2007) 626-633.
- [28] Teodorescu M, Cursaru B, Stanescu P, Draghici C, Stanciu ND, Vuluga DM., Novel hydrogels from diepoxy-terminated poly (ethylene glycol) s and aliphatic primary diamines: synthesis and equilibrium swelling studies, *Polymers for Advanced Technologies*, 20(12) (2009) 907-915.
- [29] Wilfert S, Iturmendi A, Henke H, Brüggemann O, Teasdale I, Thermoresponsive Polyphosphazene-Based Molecular Brushes by Living Cationic Polymerization, *Macromolecular Symposia*, Wiley Online Library, (2014): 9-18
- [30] Gunasekaran S, Wang T, Chai C., Swelling of pH-sensitive chitosan-poly (vinyl alcohol) hydrogels, *Journal of Applied Polymer Science*. 102(5) (2006) 4665-4671.
- [31] Deen GR, Mah CH., Influence of external stimuli on the network properties of cationic poly (N-acryloyl-N'-propyl piperazine) hydrogels, *Polymer*, 89 (2016) 55-68.
- [32] Gehrke SH., Synthesis, equilibrium swelling, kinetics, permeability and applications of

- environmentally responsive gels, *Responsive gels: volume transitions II*: Springer, (1993); p. 81-144.
- [33] Turan E, Demirci S, Caykara T., Thermo-and pH-induced phase transitions and network parameters of poly (N-isopropylacrylamide-co-2-acrylamido-2-methyl-propanosulfonic acid) hydrogels, *Journal of Polymer Science Part B: Polymer Physics*, 46(16) (2008) 1713-24.
- [34] Liu Y-Y, Fan X-D., Synthesis and characterization of pH-and temperature-sensitive hydrogel of N-isopropylacrylamide/cyclodextrin based copolymer, *Polymer*, 43(18) (2002) 4997-5003.
- [35] Van Durme K, Van Mele B, Loos W, Du Prez FE., Introduction of silica into thermo-responsive poly (N-isopropyl acrylamide) hydrogels: A novel approach to improve response rates, *Polymer*, 46(23) (2005) 9851-9862.
- [36] Cates RS., Influence of crosslink density on swelling and conformation of surface-constrained Poly (N-isopropylacrylamide) hydrogels, *Graduate thesis*, 15 (2010) 15-18.



Pressure and temperature effects on magnetoelectric band energies in GaAs / In_xGa_{1-x}As cylindrical quantum wires

Pınar BAŞER ¹✉

¹ Sivas Cumhuriyet University, Department of Physics, 58140, Sivas-TURKEY

Abstract

Low-dimensional systems, consisting of GaAs / InGaAs heterostructures, have attracted considerable attention due to their many applications in optoelectronic and microelectronic devices. In the present work, the electron and the heavy-hole ground state energy in an InGaAs/GaAs cylindrical quantum well wires (CQWWs) is investigated with the consideration of geometrical confinement. The ground state energy was calculated as a function of hydrostatic pressure and temperature. Under the constant pressure and at a certain magnetic field value, while the ground state energy of the electron and the hole decreases depending on the temperature, it is observed that the energy increases as the hydrostatic pressure increases under the constant temperature. These calculations are interpreted with graphics.

Article info

History:

Received: 02.06.2020

Accepted: 05.08.2020

Keywords:

Ground State Energy, GaAs/ In_xGa_{1-x}As Quantum Wire, Hydrostatic Pressure, Temperature

1. Introduction

Heterostructures are semiconductor devices obtained by the development of crystal growth techniques. It is used in the construction of high performance, fast and high frequency optical devices with heterostructures. Particle movements can be controlled in these structures, thus providing a high advantage in device designs. Low-dimensional structures include quantum wells (QWs), quantum well wires (QWWs) and quantum dots (QDs)[1-3].

As the III-V group semiconductors InAs is active in the infrared region, it has found wide application in optoelectronic systems. For some applications there is a need of good quality InAs layers. The electron mobility of the InAs semiconductor compound is equal to 30000 cm²/Vs and is approximately three times greater than the mobility value of the GaAs semiconductor material. The mobility is proportional to the carrier conductivity. As mobility increases, so does the current-carrying capacity of transistors. A higher mobility shortens the response time of photodetectors. A larger mobility reduces series resistance, and this improves device efficiency and reduces noise and power consumption. The band gap value of the InAs semiconductor compound is

0.35 eV and is four times smaller than that for GaAs. This makes InAs / InGaAs compound based devices exhibit good electronic performance [4-6].

Alloys such as In_xGa_{1-x}As are used in detector structures, especially in semiconductor technology. In gallium indium arsenic (InGaAs), there is contact of indium semiconductor compound to gallium arsenic. Generally, it can be used in high power, high frequency electronics and it is superior to other known semiconductors such as silicon and gallium arsenic (GaAs) due to the high speed movement of the electron in this material group and the femtosecond life span of the carriers. The band spacing of indium gallium arsenic (InGaAs) has made this material indispensable for the construction of the detector, especially for fiber optic communications around 1300 and 1500 nm [7- 8]. InGaAs was first obtained in 1978 by T. P. Pearsall by growing it on indium phosphate (InP) [9]. Pearsall found the bandwidth of this material, the effective mass of electrons and holeholes, their mobility and the properties of In_xGa_{1-x}As.

High Electron Moblity Transistor (HEMT) devices made using In_xGa_{1-x}As are one of the fastest transistor types, and this material is a

*Corresponding author. Email address: pbaser@cumhuriyet.edu.tr

very popular material for infrared detectors. $\text{In}_x\text{Ga}_{1-x}\text{As}$ has become more preferable (replaced by Germanium) due to the high stability current of germanium used in these materials. It is generally used in short wavelength infrared cameras. It can also be used to produce $\text{In}_x\text{Ga}_{1-x}\text{As}$ laser. Lasers of 905nm, 980nm, 1060nm and 1300nm were produced [10-12].

Hydrostatic pressure and temperature is a preventive external parameter that changes the electronic and optical properties of devices made of semiconductor materials. Therefore, the dependence of the optical and electrical properties of the GaAs / GaAlAs and GaAs/InGaAs systems under pressure, temperature, electric and magnetic fields has attracted considerable attention [13-15].

In this study, the variation of electron and hole ground state energy levels in the cylindrical quantum well wire (CQWW) with GaAs / $\text{In}_x\text{Ga}_{1-x}\text{As}$ was calculated with temperature and pressure. Numerical results showed that the particle ground state energy in QWs is highly dependent on external parameters.

2. Theory

Using the Hamiltonian new effective mass approach of the electrons and heavy-hole particles in GaAs/ $\text{In}_x\text{Ga}_{1-x}\text{As}$ CQWWs, the temperature can be written as below, under hydrostatic pressure, and outside magnetic field [16].

$$H = \frac{1}{2m_e^*(P,T)} \left(\vec{P}_e + \frac{e}{c} \vec{A}_e \right)^2 + \frac{1}{2m_h^*(P,T)} \left(\vec{P}_h - \frac{e}{c} \vec{A}_h \right)^2 + V_e(\rho_e, P, T) + V_h(\rho_h, P, T) \quad (1)$$

where $\vec{P}_{e(h)}$ is the momentum operator, $\vec{A}_{e(h)}$ is the vector potential of the magnetic field, which is written as $\vec{A}(\vec{r}) = \frac{1}{2}(\vec{B} \times \vec{r})$, with $\vec{B} = B\hat{z}$. In cylindrical coordinates, the components of the vector potential are chosen as $A_\rho = A_z = 0$ and $A_\phi = \frac{B\rho_{e(h)}}{2}$. The subscripts e and h stand for electron and hole, respectively. $m_{e(h)}^*(P, T)$, $\varepsilon(P, T)$ and $V_{e(h)}(\rho_{e(h)}, P, T)$ are hydrostatic pressure and temperature dependent effective masses, dielectric constants and spatial confinement potentials. Since the effective

masses of GaAs and $\text{In}_x\text{Ga}_{1-x}\text{As}$ are close together, the effective mass of GaAs is used in calculations [17]. Dependence of the electron active mass on the hydrostatic pressure and temperature is given by Eq. 2 [23].

$$m_e^*(P, T) = \left[1 + E_P^\Gamma \left(\frac{2}{E_g^\Gamma(P, T)} + \frac{1}{E_g^\Gamma(P, T) + 0.341} \right) \right]^{-1} m_0 \quad (2)$$

For heavy hole the temperature dependency is ignored and hydrostatic pressure dependency is given by

$$m_h^*(P) = [0.134 + (a_2 P + a_3 P^2)] m_0 \quad (3)$$

where $a_2 = -0.1 \times 10^{-2} \text{ GPa}^{-1}$ and $a_3 = 5.5 \times 10^{-4} \text{ GPa}^{-2}$. The isotropic hole mass is defined in Eq 3. In calculation, the values of the physical parameters pertaining to the material GaAs in Ref [23] is used the heavy hole isotropic hole mass is calculated from

$$(m_h^*)^{-1} = \left(\frac{2}{3} \right) (m_h^*(x, y))^{-1} + \left(\frac{1}{3} \right) (m_h^*(z))^{-1} \quad (4)$$

It was used as in $\varepsilon(P, T)$ is the pressure and temperature dependent static dielectric constant and given by [18-20].

$$\varepsilon(P, T) = \begin{cases} 12.74 e^{-1.67 \times 10^{-2} P} e^{9.4 \times 10^{-5} (T - 75.6)}, & T \leq 200K \\ 13.18 e^{-1.73 \times 10^{-2} P} e^{20.4 \times 10^{-5} (T - 300)}, & T > 200K \end{cases} \quad (5)$$

Similarly, $E_g^\Gamma(P, T)$ is the band gap defined for GaAs and InGaAs semiconductors.

$$E_g^\Gamma(P, T) = E_g^0 + \alpha P - \beta T^2 (T + c)^{-1} \quad (6)$$

For the parameter values in this equation, Ref. [17] can be seen. The confinement potential $V_{e(h)}(\rho_{e(h)}, P, T)$ is given by

$$V_{e(h)}(\rho_{e(h)}, P, T) = \begin{cases} V_{0e(h)}(P, T) & \rho_{e(h)} \geq R(P) \\ 0, & \rho_{e(h)} < R(P) \end{cases} \quad [22] \quad (7)$$

$\rho_{e(h)}$ is the spatial confinement variable in cylindrical coordinates for electron and hole. Where $V_{0e}(P, T)$ and $V_{0h}(P, T)$ are the

confinement potentials of the electron and hole, respectively and the values of $V_{0e}(P, T)$ and $V_{0h}(P, T)$ can be defined as in Eq. 8 [21].

$$\begin{aligned} V_{0e}(P, T) &= G_c \left(E_g^{GaAs}(P, T) - E_g^{GaInAs}(P, T) \right) \\ V_{0h}(P, T) &= G_v \left(E_g^{GaAs}(P, T) - E_g^{GaInAs}(P, T) \right) \end{aligned} \quad (8)$$

where G_c and G_v are conductivity band offset and valence band offsets respectively, in this study the values are taken as 0.7 and 0.3. $R(P)$ is defined as the pressure radius of the well as in Eq. 9,

$$R(P) = R(0)[1 - 3P(S_{11} + 2S_{12})P]^{1/2} \quad (9)$$

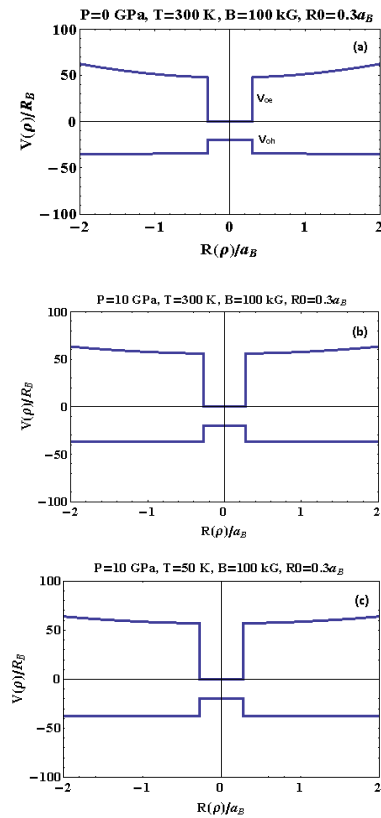


Figure 1: Spatial and parabolic confinement for $B = 100$ kG **a)** $P=0$ kG, $T=300$ K **b)** $P=10$ kG, $T=300$ K, **c)** $P=10$ kG, $T=50$ K.

Where $R(0)$ is the wire radius without hydrostatic pressure and S_{11} and S_{12} are the compliance constants of GaAs [22, 23]. In Figure 1, the potential profile consisting of the sum of the parabolic siege and the spatial siege

originating from the magnetic field is given with the press and temperature.

The ground state wave function in CQWWs under magnetic field, hydrostatic pressure and temperature [24]. The wave functions for the electron and hole ground state are given by Eq. 10.

In Eq. 10 the variable N is the normalization constant, ${}_1F_1(-a_{01}, 1, \xi)$ and $U(-a'_{01}, 1, \xi)$ are confluent hypergeometric functions which are corresponding solutions of inside and outside of the CQWWs respectively, in the presence of a uniform magnetic field parallel to the wire axis. We defined the variable $\xi_{e(h)} =$

$\frac{\rho_{e(h)}^2}{2\alpha_{c[e(h)]}^2}$ in terms of cyclotron radius $\alpha_{c[e(h)]} = \sqrt{\frac{\hbar}{m_{e(h)}^* \omega_{c[e(h)]}}}$ where $\omega_{c[e(h)]} = \frac{eB}{m_{e(h)}^*}$ is the cyclotron frequency. The Eq. 10 satisfies the boundary condition $\frac{\partial \psi_{int}}{\partial \rho_{e(h)}} = \frac{\partial \psi_{ext}}{\partial \rho_{e(h)}}$ at, $\rho_{e(h)} = R(P)$, the normalization constant (N), $a_{01e(h)}$ and $a'_{01e(h)}$ are the eigenvalues for the ground state of the problem inside and outside the wire for an electron and hole, respectively. E_{e1} and E_{hh1} are magnetoelectric band energies for the lowest energy electron and highest energy heavy hole in the conductivity band and valence band. Ref. [24] terminology is calculated and the ground state of the system, electron (E_{e1}) and hole energy (E_{hh1}), respectively are found as follows.

$$\begin{aligned} E_{e1} &= \hbar \omega_{c(e)} \left(a_{01(e)} + \frac{1}{2} \right) \\ E_{hh1} &= \hbar \omega_{c(h)} \left(a_{01(h)} + \frac{1}{2} \right) \end{aligned} \quad (11)$$

$$\psi(\vec{\rho}_e, \vec{\rho}_h) = \begin{cases} N \exp\left(-\frac{\xi_e}{2}\right) {}_1F_1\left(-a_{o1(e)}, 1, \xi_e\right), & \rho_e \leq R(P) \\ N \frac{{}_1F_1\left(-a_{o1(e)}, 1, \xi_{R(e)}\right)}{U\left(-a'_{o1(e)}, 1, \xi_{R(e)}\right)} \exp\left(-\frac{\xi_e}{2}\right) U\left(-a'_{o1(e)}, 1, \xi_e\right), & \rho_e > R(P) \\ N \exp\left(-\frac{\xi_h}{2}\right) {}_1F_1\left(-a_{o1(h)}, 1, \xi_h\right), & \rho_h \leq R(P) \\ N \frac{{}_1F_1\left(-a_{o1(h)}, 1, \xi_{R(h)}\right)}{U\left(-a'_{o1(h)}, 1, \xi_{R(h)}\right)} \exp\left(-\frac{\xi_h}{2}\right) U\left(-a'_{o1(h)}, 1, \xi_h\right), & \rho_h > R(P) \end{cases} \quad (10)$$

3. Results and Discussion

We chose semiconductor parameters to avoid complications. For example, the compound $\text{In}_{0.53}\text{Ga}_{0.47}\text{As}$ is known to transform when the Ga alloy concentration goes beyond $x = 0.6$ [gamma-L transition] and $x = 0.8$ [gamma-x transition]. Therefore, the In concentration was chosen as $x = 0.47$ [25]. Also in calculations, effective mass values of GaAs were taken as $m_e^* = 0.067m_o$ and $m_h^* = 0.135m_o$. For InGaAs / GaAs semiconductor compound, Rydberg Constant $R_B = m_e^* e^4 / 2\hbar^2 \epsilon^2 \sim 5.80 \text{ meV}$ and Bohr Radius $a_B = \hbar^2 \epsilon / m_e^* e^2 \sim (94.53 \text{ \AA})$ are equal to, where $\epsilon = 13.13$ is the dielectric constant for GaAs.

Fig. 2 shows the change of electron and hole ground state energy with hydrostatic pressure. In these calculations, wire radius $R = 0.3 a_B$, $T = 300 \text{ K}$ and $B = 100 \text{ kG}$ were used.

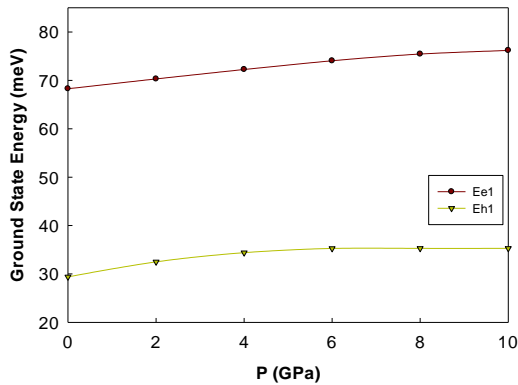


Figure 2: Ground state electron and heavy-hole ($E_{e(hh1)}$) energy as a function of hydrostatic pressure for $R = 0.3 a_B$, $T = 300 \text{ K}$ and $B = 100 \text{ kG}$.

Fig. 3 shows the variation of electron and heavy hole ground state energy with temperature (T) for In concentration $x = 0.47$ at $P = 0 \text{ GPa}$ and $B = 100 \text{ kG}$.

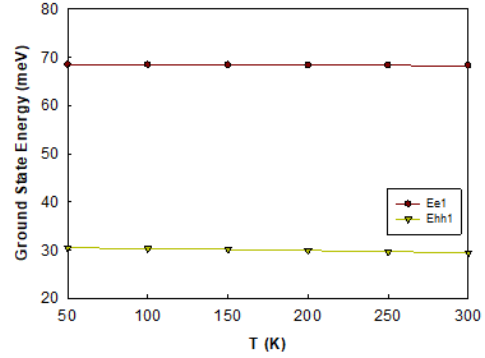


Figure 3. Ground state electron and hole energy ($E_{e(hh1)}$) as a function of temperature for $R = 0.3 a_B$, $T = 300 \text{ K}$ and $B = 100 \text{ kG}$

When Table 2 is examined, when the temperature is changed between 0-300 K, it is seen that the biggest change in the parameters in the table occurs in the value of the dielectric constant, and even this change is about 2%. Changes in other parameters are much smaller than this value. For example, when the temperature for the electron is 50 K, $E_{e1} = 68.52 \text{ meV}$. When the temperature was increased to 300 K, it was calculated as $E_{e1} = 68.28 \text{ meV}$. The amount of change between these values is less than 0.3%.

It is clear from Table 2 that the dependence of the ground state energy in the GaAs/ InGaAs system on temperature is negligible, that is, the system is very stable under temperature changes. On the other hand, hydrostatic pressure appears to be very effective when the parameter changes in Table 1 are examined on the system. The potential height and the effective mass increase with increasing pressure, thereby increasing the energy.

Table 1. The variation of dielectric constant, effective masses, potential heights and wire radius, with hydrostatic pressures for $T = 300$ K and $B=100$ kG.

$P(\text{GPa})$	$\epsilon(P, T)$	m_e/m_0	m_h/m_0	$V_{0e}(\text{meV})$	$V_{0h}(\text{meV})$	R/a_B
0	13.18	0.063	0.146	476.2	204.2	1.00
2	12.73	0.072	0.148	508.8	217.7	0.98
4	12.29	0.080	0.151	531.8	227.9	0.97
6	11.88	0.087	0.16	547.9	234.8	0.95
8	11.47	0.092	0.173	556.3	238.4	0.94
10	11.08	0.096	0.191	556.97	238.7	0.92

Table 2. The variation of dielectric constant, effective masses, potential heights and wire radius, with temperatures for $P=0$ GPa and $B=100$ kG.

$T(\text{K})$	$\epsilon(P, T)$	m_b/m_0	m_w/m_0	$V_{0e}(\text{meV})$	$V_{0h}(\text{meV})$
0	13.52	0.066	0.0416	487.5	208.9
50	12.70	0.066	0.0415	486.7	208.5
100	13.58	0.066	0.0411	485.1	207.9
150	13.61	0.065	0.0407	481.1	206.1
200	13.66	0.064	0.0402	481.0	206.0
250	13.73	0.064	0.0396	478.7	205.2
300	13.80	0.063	0.0389	476.5	204.2

4. Conclusion

We calculated the magneto electric band energies for electron and heavy hole particles under $R = 3a_B$ and $B = 100$ kG magnetic field as a function of hydrostatic pressure and temperature using the effective mass approach in a one-dimensional GaAs / InGaAs cylindrical quantum well wires. The graphs show that as the hydrostatic pressure increases in both particles, the ground state energy increases. This increase in pressure and energy can be explained by looking at the value of the parameters. As pressure increases, wire radius and dielectric constant decrease while the confinement potential and effective mass value increase. In this case, particle energies increase as the quantum confinement effects on the electron and hole increase.

The effective mass and potential height decrease as the dielectric constant increases with temperature. We can say that the temperature change almost does not affect the electronic energy and the hole energy because when the Table 2 is examined, it is seen that the amount of change of the parameters is less than 2%. As it is clearly seen in Fig. 1 b) and c), at $P = 10$ GPa, at $T = 50$ K and $T = 300$ K, a small amount of decrease is observed as the temperature rises. However, increasing dielectric constant and decreasing potential height reduces the confinement effects of the particle and contributes to the reduction of electronic energy as the reduction in effective mass increases the mobility of the particle. Furthermore, we have also shown that, the binding energy is very stable for a large (0-300K) of temperature variation.

Conflicts of interest

The author state that did not have conflict of interests.

References

- [1] Frensley, W. R. , VLSI Electronics Microstructure Science, *Chapter Heterostructure and Quantum Well Physics*, 24 (1994) 1-24.
- [2] Lim, H., Yoon, S. I., Kim, G., Jang A.R., Shin, H. S., Stacking of two –dimensional materials in lateral and vertical directions, *Chem. Mater.*, 26 (2014) 4891-4903.
- [3] Withers, F., et al., Light-emitting diodes by band-structure engineering in van der Walls hetetostructures, *Nat. Mater.*, 14 (2015) 301-306.
- [4] S. Paul, J. B. Roy, and P. K. Basu, Empirical expressions for the alloy composition and temperature dependence of the band gap and intrinsic carrier density in $GaxIn1-xAs$, *J. Appl. Phys.*, 69 (1991) 827-829.
- [5] Pearsall, T. P. and Hirtz, J. P., The carrier mobilities in $Ga_{0.47}In_{0.53}As$ grown by organo-mettalic CVD and liquid-phase epitaxy, *J. Cryst. Growth*, 54 (1981) 127-131.
- [6] Pearsall, T. , IEEE Xplore - $Ga_{0.47}In_{0.53}As$: A ternary semiconductor for photodetector applications, *IEEE Journal of Quantum Electronics*, 16 (1980) 709-720.
- [7] Razeghi, M., Hirtz, J. P., Ziemelis, D., Delalande, C., Etienne, B. and Voos, M., Growth of $Ga_{0.47}In_{0.53}As-InP$ quantum wells by low pressure metalorganic chemical vapor deposition, *Appl. Phys. Lett.*, 43 (1983) 585-587.
- [8] M. Razeghi, J. Nagle and C. Weisbuch, Gallium Arsenide and Related Compounds, 1985 (Inst. Phys. ConJ Ser. 74) 319.
- [9] Pearsall, T.P., Bisaro, R., Ansel, R. and Merenda, P., The growth of $GaxIn1-xAs$ on (100) InP by liquid-phase epitaxy, *Appl. Phys. Lett.*, 32 (1978) 497-499.
- [10] Pearsall P. and Papuchon, M., The $Ga_{0.47}In_{0.53}As$ homojunction photodiode A new avalanche photodetector in the near infrared between 1.0 and 1.6 μm , *Appl. Phys. Lett.*, 33 (1978) 640-642.
- [11] Goldberg, Y. A. and Shmidt, N. M. Gallium Indium Arsenide, in Handbook Series on Semiconductor Parameters, M. Levinshtein, S. Rumyantsev, and M. S. Shur, (Eds.) 2, 62, World Scientific, Singapore (1999).
- [12] A. V., Thathachary, N., Agrawal, L. Liu, S. Datta, Electron Transport in Multigate $InxGa1-x As$ Nanowire FETs: From Diffusive to Ballistic Regimes at Room Temperature” , *Nano Lett.*, 14 (2) (2014) 626-633.
- [13] Peter, A. J. , Gnanasekar, K. , Navaneethakrishnan, K. , Binding energy of impurity states in a parabolic quantum dot in a strong magnetic field, *Phys. Stat. Sol. (b)*, 242 (2005) 2480-2488.
- [14] Kasapoğlu, E. The hydrostatic pressure and temperature effects on donor impurities in $GaAs/Ga1-xAlxAs$ double quantum well under the external fields, *Phys. Lett., A* 373 (2008) 140-143.
- [15] Ozturk, O. , Ozturk E. , Elagoz S. , Electronic properties of double $GaAlAs/GaAs$ and $GaInAs/GaAs$ quantum wells as dependent on well width, *Cumhuriyet Sci.J.*, 40 (2019) 471-476.
- [16] Elagoz, S., Karki, H.D., Baser, P., Sokmen I. , The magnetoexciton binding energy dependency on aluminium concentration in cylindrical quantum wires, *Superlatt. and Microstruct.*, 45 (2009) 506-513.
- [17] P Başer, I Altuntas, S Elagoz, The hydrostatic pressure and temperature effects on hydrogenic impurity binding energies in $GaAs/InxGa1-xAs/GaAs$ square quantum well, *Superlattice Microst.*, 92 (2016) 210-216.
- [18] Villamil, P., Beltran, C., Montenegro N. P., Magnetoexciton binding energies in a quantum wire, *J. Phys.: Condens. Matter.*, 13 (2001) 4143-4153.
- [19] Gang, L. Spiros, V. B., Bajaj, K. K., Exciton binding energy in a quantum wire in the presence of a magnetic field, *J. Appl. Phys.*, 77 (1995) 1097-1105.
- [20] Baghranyan, H. M., Barseghyan, M. G., Kirakosyan, A. A., Effects of hydrostatic pressure and temperature on interband optical transitions in $InAs/GaAs$ vertically coupled double quantum dots, *J. Phys. Conf. Ser.*, 350 (2012) 012017 1-6.

- [21] Bastard, G. Hydrogenic impurity states in a quantum well: A simple model”, *Phys. Rev. B.*, 24 (1981) 4714-4722.
- [22] Balandin, A. and Bandyopadhyay, S., Excitons in a quantum wire subjected to a magnetic field, *Phys. Rev. B*, 52 (1995) 8312-8316.
- [23] Baser, P., Karki, H. D., Demir, I., Elagoz, S., The hydrostatic pressure and temperature effects on the binding energy of magnetoexcitons in cylindrical quantum well wires, *Superlatt. Microstruct.*, 63 (2013) 100-109.
- [24] Elagoz, S., Uslu, O., Baser, P., Çift Parabolik Kuşatma Altında Kuantum Sistemi Elektronik Enerji Düzeyleri, *Marmara University Journal of Science and Technology*, 20 (2008) 1-12 .
- [25] Başer P., Elagoz, S., The hydrostatic pressure and temperature effects on hydrogenic impurity binding energies in lattice matched InP/ In_{0.53}Ga_{0.47}As / InP square quantum well, *Superlattice Microst.*, 102 (2017) 173-179.

Antiproliferative effects of cetuximab on triple negative breast cancer cell line MDA-MB-231

İdil ÇETİN^{1*} 

¹ University of Istanbul, Faculty of Science, Department of Biology, Istanbul, TURKEY

Abstract

In this study, antiproliferative effects of the anti-EGFR monoclonal antibody Cetuximab were evaluated using MDA-MB-231 cell line originated from triple negative breast cancer. As cell kinetic parameters, we evaluated Cell index, mitotic index, labeling index and apoptotic index. For this purpose, 20 μ M, 45 μ M and 60 μ M Cetuximab concentrations were applied to the cells using the real-time cell analysis system (xCelligence DP) and IC50 values were determined. IC50 concentrations were used for all other parameters. According to experimental results, Cetuximab administration inhibited cell kinetics of MDA-MB-231 cells. xCelligence DP instrument detected IC50 concentrations of Cetuximab for cell line. These values were 45 μ M for MDA-MB-231 cells. When these IC50 value applied to cells, significant decrease was detected in mitotic index, labelling index and significant increase was detected in apoptotic index for experimental groups. Student's t tests for paired samples were used to assign statistical significance. $p < 0.05$ level of significance was accepted. According to the results obtained, Cetuximab has the potential to slow down the prognosis of the triple negative breast cancer subtype.

Article info

History:

Received: 12.06.2020

Accepted: 01.09.2020

Keywords:

TNBC,
Breast Cancer,
Cetuximab,
MDA-MB-231.

1. Introduction

Although cancer seems to be a single disease, it can be described as a disease group formed by the combination of many diseases. Breast cancer, which is the second species of this disease group that causes death in women, has an important place among cancer diseases. Triple-negative breast cancer (TNBC) known as an aggressive cancer type is characterized by its appearance at younger ages, higher average tumor size, high-grade tumors, and sometimes higher rate of node positivity [1]. In addition, this group is known for the occurrence of metastases in the internal organs such as lung and brain, although early peak of relapse and less in bone between the first and third years after diagnosis [2].

One of the member of the class I superfamily of receptor tyrosine kinases (RTKs) is the epidermal growth factor receptor (EGFR). These RTKs include different signaling proteins. All members consist of three regions: 1- Ligand binding site, 2- single membrane-spanning site, 3- site containing a cytoplasmic intracellular tyrosine-kinase. Receptors of this superfamily are expressed in various tissues such

as neuronal, epithelial and mesenchymal tissues under normal conditions [3].

EGFR is a tyrosine kinase receptor and is overexpressed in different types of cancer. For instance, breast, ovary, colorectal and head and neck cancer. It plays an important role in the work of mechanisms necessary for tumor formation and progression [4]. EGFR is associated with advanced disease, poor prognosis, and resistance to therapy and therefore EGFR is an ideal candidate for various types of cancer [5].

A monoclonal antibody Cetuximab binds to the extracellular domain of EGFR. In many human cancers, including head and neck and colorectal cancers, EGFR is overexpressed. Binding of EGFR with its endogenous ligand is prevented by this process and this blocks the receptor-dependent transduction pathway, and provides many antitumor agents [6, 7].

In this study, it was aimed to evaluate the effects of the anti-EGFR monoclonal antibody Cetuximab on MDA-MB-231 cell line originated from triple negative breast cancer at the cellular level by using different cell kinetics parameters.

*Corresponding author. Email address: idil.cetin@istanbul.edu.tr

2. Materials and Methods

2.1. Cell culture

The MDA-MB-231 cells used in the experiments were purchased by our research laboratory from American Type Culture Collection (ATTC Manassas, VA, USA). Cells were cultured in DMEM (Invitrogen, Carlsbad, CA, USA) supplemented with 10% (v/v) fetal bovine serum (FBS; Invitrogen, Carlsbad, CA, USA), 100-unit ml^{-1} penicillin and 100 $\mu\text{g ml}^{-1}$ streptomycin. Cells were maintained at 37 °C in a atmosphere containing 95% humidity and 5% CO_2 .

2.2. Preparation of drug concentration

Application doses of 20 μM , 45 μM and 60 μM concentrations were prepared by diluting a total of 1 mM Cetuximab (Sigma) stock solution.

2.3. Cell index (CI)

For cell index analysis, xCELLigence DP system was used. In experimental process for the impedance background measurement 100 μL of appropriate medium was added to each well. Then 5000 cell/well were seeded for MDA-MB-231 cell line. The final volume was 200 μL . 16 well E-Plates were incubated at 37°C with 95% humidity and 5% CO_2 and monitored on the RTCA system at 15-minute time intervals for up to 24 hours without treatment and following 72 hours with treatment. The DP unit is wired to an external laptop running the xCELLigence software (version 1.2.1).

2.4. Mitotic index (MI)

For evaluation of MI, cells were planted in 24-well plates. Each well contained 3×10^4 cells for both cell lines. Cells were incubated 24 hrs after cell seeding. Cells were treated with optimum Cetuximab concentration 0-72 hrs. At the end of these experimental period, for fixation, Carnoy fixative was used and the cells were made clear with the Feulgen method and stained with Giemsa. For analysing MI, approximately 3000 cells were counted.

2.5. Apoptotic index (AI)

DAPI (6-diamidino-2-phenylindole) was used to determine the apoptotic nucleus. It is a blue fluorescent dye. Cells were cultured in 6-well culture dishes and fixed with methanol: FTS mixture after the experimental process until staining was performed.

Washing was carried out to remove the dye. For washing, PBS was used. A fluorescent microscope was used to identify apoptotic cells.

2.6. Statistical analysis

All parameters of cell kinetics (CI, MI, LI, AI) were evaluated according to the controls and each other. Therefore, in order to analyze the results one-way Anova test, Dunnett's test and Student's t-test were used. These statistical analyses were performed using SPSS statistics software (V22.0 IBM, Armonk, NY, USA). In the tests $p < 0.05$ level of significance was accepted.

3. Results

3.1. Cell index

Cell index values obtained by applying Cetuximab to MDA-MB-231 cells at 20 μM , 45 μM and 60 μM concentrations were compared with the standard curves; while no significant antiproliferative effect can be seen at a concentration of 20 μM , it is believed that DNA damage occurs at concentrations of 45 μM and 60 μM (Figure 1). In addition, after 24 h Cetuximab applying, the IC_{50} value of MDA-MB-231 cells was determined as 45 μM with the xCelligence DP device's own system.

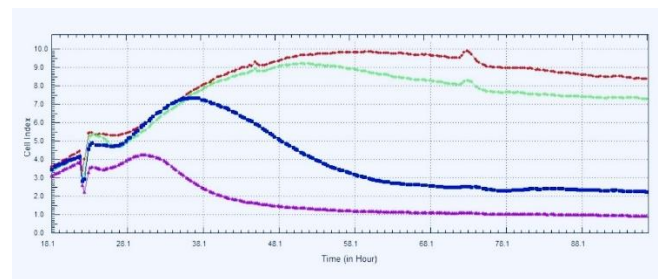


Figure 1: Graph of cell index of MDA-MB-231 cells treated with Cetuximab at concentrations of 20 μM , 45 μM and 60 μM (--- Control, --- 20 μM , --- 45 μM , --- 60 μM).

3.2. Mitotic Index

In order to assess the change in mitotic index values by applying Cetuximab on MDA-MB-231 cells; cultured cells were treated at a concentration of 45 μM for 24 h, 48 h and 72 hours. The results showed that this concentration decreased the mitotic index from 4,24 % to 2,76 % at 24 h; from 5,56 % to 1,98 % at 48 h and 6,18 % to 0,93 % at 72 h (Figure 2).

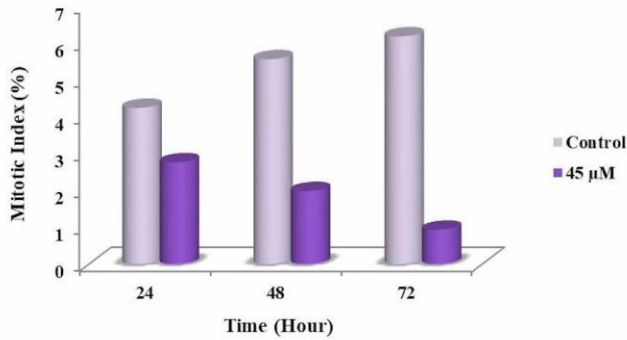


Figure 2: Mitotic index values of MDA-MB-231 cells treated with 45 µM Cetuximab for 24-72 hours ($p < 0.05$).

3.3. Labelling index

Labelling index values belonging to MDA-MB-231 cell line after administration of 45 µM concentration Cetuximab was shown in Figure 3. Labelling index values decreased from 7,81 to 3,57 at 24 h; from 8,18 to 2,26 at 48 h and from 8,32 to 1,19 at 72 h for MDA-MB-231 cell line. Labelling index values of MDA-MB-231 cells decreased significantly with time as a result of Cetuximab administration. This decrease was statistically significant ($p < 0.05$).

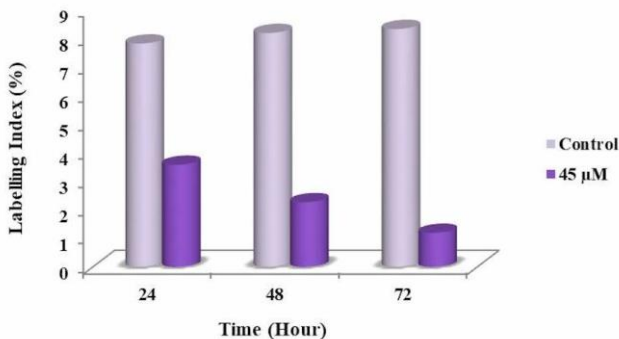


Figure 3: Labelling index values of MDA-MB-231 cells treated with 45 µM Cetuximab for 0-72 hours ($p < 0.05$).

3.4. Apoptotic Index

Administration of 45 µM concentration of Cetuximab to MDA-MB-231 cells caused apoptotic cell death. Apoptotic index values increased from 7,23 to 15,26 at 24 h; from 10,62 to 21,22 at 48 h and from 11,22 to 29,43 at 72 h for MDA-MB-231 (Figure 4). Apoptotic index values of MDA-MB-231 cells increased significantly with time as a result of Cetuximab administration. This decrease was statistically significant ($p < 0.05$).

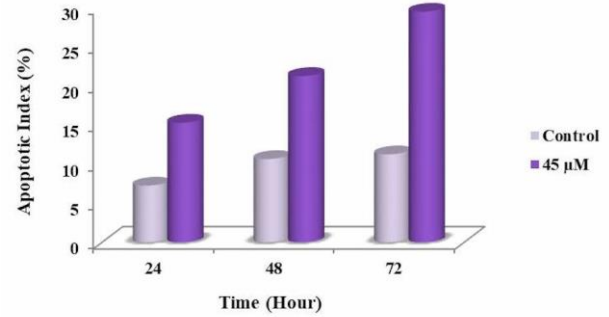


Figure 4: Apoptotic index values of MDA-MB-231 cells treated with 45 µM Cetuximab for 0-72 hours ($p < 0.05$).

4. Discussion

Because of the toxic side effects of traditional drugs used in cancer treatment and the emergence of resistant cells after treatment, cancer treatment is not fully successful and the disease-free survival is reduced [8]. Many studies have shown that triple negative breast cancer has a worse prognosis than hormone receptor positive breast cancers [9- 14]. Current treatment options are limited especially for TNBC among the different types of breast cancers. Therefore discovery and development of novel molecules is very important in terms of treatment options. Among breast cancers, TNBC subtype metastatic progression is characterized by poor prognosis and also. Metastatic progression is one of the poor prognosis indicators of TNBC. In addition, the absence of biomolecules that can be targets for targeted therapies is the main feature of TNBC [15]. Therefore, there are currently no FDA-approved targeted therapies for breast cancer subtypes. At first triple negative breast cancer is very sensitive to chemotherapy, but a lot of triple negative breast cancer patients develop resistance to chemotherapy rapidly, at which point metastatic disease can be quite fatal [16].

In many human malignancies, EGFR is abnormally activated by many mechanisms, such as receptor overexpression, overexpression of receptor ligands, gene amplification [17]. 72% of patients diagnosed with TNBC have overexpression of EGFR [18-22]. Studies have shown that EGFR mRNA levels are higher in TNBC than luminal A type breast cancer, which is positive for the hormone receptor [23, 24]. Cetuximab activates cellular immunity and antitumor mechanisms while inhibiting the downstream signal of EGFR [25]. In our study the effects of EGFR inhibitor Cetuximab were evaluated MDA-MB-231 cell line which expressed EGFR more.

Experimental findings have led to the several clinical studies' initiation to evaluate the effect of EGFR

inhibition (EGFRi) on triple negative breast cancer with metastatic potential. In the Phase II study, patients who had advanced breast cancer and who were not previously selected for chemotherapy evaluated EGFR kinase inhibitors [26]. Clinical studies also required the evaluation of the combination of DNA alkylating agent carboplatin with ligand blocking monoclonal antibody Cetuximab in addition to kinase inhibitors [27].

A study by Wang et al using MTT showed that Cetuximab is effective in many cell lines and increases the chemotherapeutic efficacy of other drugs on the cells [28]. In the study with MDA-MB-231 and SUM159 cell lines to evaluate breast cancer stem cells, fluorescence-activated cell sequencer analysis (Aldefluor + or CD44 + and CD24- / low) and mammosphere formation efficacy were measured. In this study, *in vitro* conditions, cells were treated alone with the combination of Cetuximab or Ixabepilone and Cetuximab. This study using Cetuximab alone or in combination showed that Cetuximab, applied *in vitro* conditions in breast cancer cells, decreases mammosphere formation efficiency and cancer stem cell population [29].

Brand et al. have demonstrated that after the EGFR expression is deactivated, it remains dependent on EGFR for proliferation of triple negative breast cancer cell types [30]. Liao et al. investigated the efficacy of paclitaxel and cetuximab and conjugated Nanodiamond on the MDA-MB-231 cell line. They found that this combination increased the anticancer effects in this cell line [31]. The study by Oliveras-Ferreros et al. showed that the use of Cetuximab alone inhibits cell viability in MCF10A and MDA-MB-468 cell lines where EGFR is over-expressed compared to other cell lines which EGFR is under-expressed in [32]. In the current study, the use of Cetuximab alone caused an increase in apoptotic index values in triple negative breast cancer cell line MDA-MB-231 which overexpress EGFR.

As a result, in our study; when antiproliferative effects of Cetuximab on MDA-MB-231 cells originated from triple negative breast cancer was evaluated, Cetuximab decreased cell proliferation at an optimum concentration of 45 µM concentration for MDA-MB-231 cells. It caused a significant decrease in cell index, mitosis phase and cell percentages in synthesis and also caused an increase in apoptotic index.

Acknowledgements

This work was supported by Scientific Research Project Coordination Unit of Istanbul University. Project No: FBA-2017-24288.

Conflicts of interest

The authors state that they did not have conflict of interests


References

- [1] Dent R, Trudeau M, Pritchard KI, Hanna WM, Kahn HK, Sawka CA et al. Triple-negative breast cancer: clinical features and patterns of recurrence, *Clin Cancer Res*, 13 (2007), 4429-34.
- [2] Criscitiello C, Azim HA, Schouten PC, Linn SC, Sotiriou C. Understanding the biology of triple-negative breast cancer, *Annals of Oncology*, 23 (2012), vi13-vi18.
- [3] Buettner R, Mora LB, Jove R. Activated STAT signaling in human tumors provides novel molecular targets for therapeutic intervention., *Clin Cancer Res*, 8 (2002), 945-54.
- [4] Hamid O. Emerging treatments in oncology: focus on tyrosine kinase (erbB) receptor inhibitors., *J Am Pharm Assoc*, 44 (2004), 52-8.
- [5] Galizia G, Lieto E, De Vita F, Orditura M, Castellano P, Troiani T et al. Cetuximab, a chimeric human mouse anti-epidermal growth factor receptor monoclonal antibody, in the treatment of human colorectal cancer., *Oncogene*, 26 (2007), 3654-60.
- [6] Martinelli E, De Palma R, Orditura M, De Vita F, Ciardiello F. Anti-epidermal growth factor receptor monoclonal antibodies in cancer therapy, *Clin Exp Immunol*, 158 (2009), 1-9.
- [7] Koukourakis MI, Tsoutsou PG, Karpouzis A, Tsiarkatsi M, Karapantzios I, Daniilidis V et al. Radiochemotherapy with cetuximab, cisplatin, and amifostine for locally advanced head and neck cancer: a feasibility study, *Int J Radiat Oncol Biol Phys*, 77 (2010), 9-15.
- [8] Muthu M, Cheriyan VT, Rishi AK. CARP-1 / CCAR1: A biphasic regulator of cancer cell growth and apoptosis, *Oncotarget*, 6 (2015), 6499-6510.
- [9] Van de Rijn M, Perou CM, Tibshirani R, Haas P, Kallioniemi O, Kononen J et al. Expression of cytokeratins 17 and 5 identifies a group of breast carcinomas with poor clinical outcome, *Am J Pathol*, 161 (2002), 1991-1996.

- [10] Shin BK, Lee Y, Lee JB, Kim HK, Lee JB, Cho SJ et al. Breast carcinomas expressing basal markers have poor clinical outcome regardless of estrogen receptor status, *Oncol Rep*, 19 (2008), 617-625.
- [11] Sørlie T, Perou CM, Tibshirani R, Aas T, Geisler S, Johnsen H et al. Gene expression patterns of breast carcinomas distinguish tumor subclasses with clinical implications, *Proc Natl Acad Sci USA*, 98 (2001) 10869-10874.
- [12] Sorlie T, Tibshirani R, Parker J, Hastie T, Marron JS, Nobel A et al. Repeated observation of breast tumor subtypes in independent gene expression data sets, *Proc Natl Acad Sci USA*, 100 (2003), 8418-8423.
- [13] Sotiriou C, Neo SY, McShane LM, Korn EL, Long PM, Jazaeri A et al. Breast cancer classification and prognosis based on gene expression profiles from a population-based study, *Proc Natl Acad Sci USA*, 100 (2003), 10393-10398.
- [14] Banerjee S, Reis-Filho JS, Ashley S, Steele D, Ashworth A, Lakhani SR et al. Basal-like breast carcinomas: clinical outcome and response to chemotherapy, *J Clin Pathol*, 59 (2006), 729-735.
- [15] Lehmann BD, Pietenpol JA, Tan AR. Triple-negative breast cancer: molecular subtypes and new targets for therapy, *Am. Soc. Clin. Oncol. Educ. Book*, 35 (2015) e31-e39.
- [16] Uhm JE, Park YH, Yi SY, Cho EY, Choi YL, Lee SJ et al. Treatment outcomes and clinicopathologic characteristics of triple-negative breast cancer patients who received platinum-containing chemotherapy, *Int J Cancer*, 124 (2009), 1457-1462.
- [17] Baselga J, Arteaga CL. Critical update and emerging trends in epidermal growth factor receptor targeting in cancer, *J Clin Oncol*, 23 (2005) 2445-59.
- [18] Viale G, Rotmensz N, Maisonneuve P, Bottiglieri L, Montagna E, Luini A et al. Invasive ductal carcinoma of the breast with the "triple-negative" phenotype: prognostic implications of EGFR immunoreactivity, *Breast Cancer Res Treat*, 116 (2009), 317-328.
- [19] Nielsen TO, Hsu FD, Jensen K, Cheang M, Karaca G, Hu Z et al. Immunohistochemical and clinical characterization of the basal-like subtype of invasive breast carcinoma, *Clin Cancer Res*, 10 (2004), 5367-5374.
- [20] Kim MJ, Ro JY, Ahn SH, Kim HH, Kim SB, Gong G. Clinicopathologic significance of the basal-like subtype of breast cancer: a comparison with hormone receptor and Her2/neu-overexpressing phenotypes, *Hum Pathol*, 37 (2006), 1217-1226.
- [21] Liu H, Fan Q, Zhang Z, Yu H, Meng F. Basal-HER2 phenotype shows poorer survival than basal-like phenotype in hormone receptor-negative invasive breast cancers, *Hum Pathol*, 39 (2008) 167-174.
- [22] Shien T, Tashiro T, Omatsu M, Masuda T, Furuta K, Sato N et al. Frequent overexpression of epidermal growth factor receptor (EGFR) in mammary high grade ductal carcinomas with myoepithelial differentiation, *J Clin Pathol*, 58 (2005) 1299-1304.
- [23] El Guerrab A, Bamdad M, Kwiatkowski F, Bignon YJ, Penault-Llorca F, Aubeil C. Anti-EGFR monoclonal antibodies and EGFR tyrosine kinase inhibitors as combination therapy for triple-negative breast cancer, *Oncotarget*, 7 (2016) 73618- 73637.
- [24] Darbeheshti F, Izadi P, Razavi ANE, Kamali F, Yekaninejad MS, Bazzaz JT. Significance of EGFR mRNA expression in luminal and triple negative breast tumors, *International Journal of Cancer Management*, 11 (2018), e9763.
- [25] Trivedi S, Srivastava RM, Concha-Benavente F, Ferrone S, Garcia-Bates TM, Li J et al. Anti-EGFR targeted monoclonal antibody isotype influences antitumor cellular immunity in head and neck cancer patients. *Clin Cancer Res*, 22 (2016), 5229-37.
- [26] Dickler MN, Cobleigh MA, Miller KD, Klein PM, Winer EP. Efficacy and safety of erlotinib in patients with locally advanced or metastatic breast cancer, *Breast Cancer Res Treat*, 115 (2009) 115-121.
- [27] Carey LA, Rugo HS, Marcom PK, Mayer EL, Esteva FJ, Ma CX et al. TBCRC 001: randomized phase II study of cetuximab in combination with carboplatin in stage IV triple-negative breast cancer, *J Clin Oncol*, 30 (2012) 2615-2623.
- [28] Wang F, Chen Y, Huang L, Liu T, Huang Y, Zhao J et al. Cetuximab enhanced the efficacy of chemotherapeutic agent in ABCB1/P-glycoprotein-overexpressing cancer cells, *Oncotarget*, 6 (2015), 40850-40865.
- [29] Tanei T, Choi DS, Rodriguez AA, Liang DH, Dobrolecki L, Ghosh M et al. Antitumor activity of Cetuximab in combination with Ixabepilone on triple negative breast cancer stem cells, *Breast Cancer Research*, 18 (2016) 6.
- [30] Brand TM, Iida M, EF Dunn, Luthar N, Kostopoulos KT, Corrigan KL et al. Nuclear Epidermal Growth Factor Receptor Is a Functional Molecular Target in Triple-Negative

- Breast Cancer, *Mol Cancer Ther*, 13 (2014) 1356-68.
- [31] Liao WS, Ho Y, Yu-Wei Lin YW, Raj EN, Liu KK, Chen C. Targeting EGFR of triple-negative breast cancer enhances the therapeutic efficacy of paclitaxel- and cetuximab-conjugated nanodiamond nanocomposite, *Acta Biomaterialia*, 86 (2019) 395-405.
- [32] Oliveras-Ferraro C, Vazquez-Martin A, López-Bonet E, Martín-Castillo B, Del Barco S, Brunet J et al. Growth and molecular interactions of the anti-EGFR antibody Cetuximab and the DNA cross-linking agent cisplatin in gefitinib-resistant MDA-MB-468 cells: New prospects in the treatment of triple-negative/basal-like breast cancer, *International Journal of Oncology*, 33 (2008) 1165-1176.

Antioxidant and prooxidant activity of new 1,2-diols and thiadiazoles derivatives in *Saccharomyces cerevisiae* yeast cells

Arzu KARATEPE ^{1*} , Ahmet ÇETİN ¹

¹ Bingöl University, Department of Chemistry, Bingöl/ TURKEY

Abstract

The present research was undertaken to determine the effect of substituted 2,2'-[(2R,3R)-2,3-dihydroxy-1,4-dioxobutane-1,4-diyl]bis(N-R-hydrazine-1-carbothioamide and (1R,2R)-1,2-bis[5-(R-amino)-1,3,4-thiadiazole-2-yl]ethane-1,2-diols on the antioxidant status of the yeast *Saccharomyces cerevisiae* cells. This cell serves a good eukaryotic model system for the study of molecular mechanisms of oxidative stress. The *Saccharomyces cerevisiae* yeast cells were treated a series of 1,2-diols and thiadiazoles compounds and the malondialdehyde (MDA) and antioxidant vitamins (A, E, C) levels in the medium were measured by HPLC-UV. In the comparison done among groups, the MDA which is an indicator of lipid peroxidation and Vitamin E concentrations were showed statistically changed in the samples. Exposure of yeast cells to L9 showed an increase in MDA and decrease in vitamin E levels but L2 and L8 showed decrease in MDA and increase in vitamin E levels. The results showed that compounds L9 caused a considerable oxidative stress and L2 and L8 have antioxidant activity.

Article info

History:

Received: 06.07.2020

Accepted: 25.08.2020

Keywords:

1,2-diols, thiadiazoles, MDA, vitamin, *saccharomyces cerevisiae*, antioxidant.

1. Introduction

The natural or chemical materials such as pharmaceuticals, dyes, organic materials and biologically active compounds are containing the nitrogen atom containing heterocycles [1]. The 1,3,4-thiadiazole nucleus is well-known heterocyclic nuclei, which is a functional group of a variety of medicinal agents and natural products. Because of their diverse biological activity, the 1,3,4-thiadiazole groups have become great interest by the researchers as important class of heterocycles. These biological activities are including antimicrobial [2], antituberculosis [3], antioxidant [4], antiinflammatory [5], anticonvulsants [6], antidepressant and anxiolytic [7], antihypertensive [8], anticancer [9] and antifungal activity [10].

The diverse biological activities of the 1,3,4-thiadiazole rings are associated with incorporating a toxophoric -N=C-S linkage of which has been showed in many pesticides [11-14] and therefore 1,3,4-thiadiazoles and their Schiff bases have recently received significant importance [15]. Some natural products include enantiomerically pure 1,2-diols and this molecule is valuable intermediates in the organic synthesis of biologically active compounds [16]. They are readily transformed into chiral epoxides [17] aziridines, and amino alcohols [18]. Moreover, the 1,2-diol functionality is found in a number of synthetic and pharmaceutical intermediates [19].

The production of pharmaceuticals, chemical catalysts, and agrochemicals are need optically pure 1,2-diols [20]. Although the only commercial 1, 2, 4-thiadiazole drug is the antibiotic cefozopram, many drugs such as acetazolamide, methazolamide, megalol are containing 1,3,4-thiadiazole nucleus which are available in the market [2, 21].

As a result of these studies, it is suggested that 1,3,4-thiadiazole derivatives have wide biological effects.

However, the nitrogen containing heterocyclic compounds becomes an important goal in modern organic synthesis for efficient antioxidant activity, nowadays.

The hydrogen peroxide, superoxide anions and hydroxyl radicals, which are known reactive oxygen species (ROS), are generated by aerobic life style and living cells are exposed to these molecules. Free radicals are highly reactive ions or molecules that have unpaired electron [22, 23]. In some special cases, if the amount of reactive oxygen species increases and the antioxidant capacity exceeds, oxidative stress occurs [1]. The extracellular xenobiotics and substances can be generating this stress condition by which cause the loss of cellular integrity [2]. The several lethal diseases such as cancer and neurodegenerative disorders as well as aging related with oxidative stress has been in great focus due to its correlation with a normal and inevitable eukaryotic process [3]. Reactive oxygen species (ROS) which are destroy to DNA via oxidative

*Corresponding author. Email address: akaratepe23a@gmail.com

<http://dergipark.gov.tr/csj> ©2020 Faculty of Science, Sivas Cumhuriyet University

damage, have been associated many health problems such as coronary heart diseases and carcinogenesis [24,25].

The complex physiological response contains both enzymes (e.g., catalase, superoxide dismutase) and protective molecules for resistance to oxidative stress [22, 23] and the non-enzymatic low molecular weight molecules such as ascorbate, tocopherols, flavonoids and glutathione are important in scavenging ROS [23].

The *Saccharomyces cerevisiae* yeast cells that possibility of using genetic approaches are made a common experimental model for studies of stress response at the molecular level. Mammalian and yeast cells activate a wide response involving several defense mechanisms which named adaptive response, to adapt sensitive cells for environmental change such as temperature shifts and increased ROS levels [26].

The aim of this work was to find antioxidant ability new chemical structures 1,2-diols and thiadiazoles by using *Saccharomyces cerevisiae* yeast cells.

2. Materials and Methods

2.1. Materials and chemicals

The vitamin A (all trans-retinol), MDA (1,1,3,3-tetraethoxypropane for standart) were obtained from Sigma (St. Louis, MO, USA). Vitamin C (ascorbic acid), vitamin E (α -tocopherol), HClO_4 , methanol, H_3PO_4 and KH_2PO_4 were purchased from Merck (Darmstadt, Germany). Stock solutions of compounds were prepared as 5000 μM solutions in DMSO (dimethylsulfoxid).

2.2. Applied cells

Saccharomyces cerevisiae yeast cells were used to determine antioxidant activity. *Saccharomyces cerevisiae*, a member of the fungi kingdom, is a single-celled microorganism. *Saccharomyces cerevisiae* is ascomycetic yeast. The yeasts are contain high vitamin level, therefore increases its value as a nutrient. These cells are often used as a model for molecular responses to oxidative stress metabolism [26].

The dry yeast sample containing the Microorganism *Saccharomyces cerevisiae* was stored at $+4^\circ\text{C}$ during the study. Preparation, cultivation of microorganism culture and the addition and incubation of chemicals to investigate the effect on microorganism were done in the Microbiology Laboratory. For *Saccharomyces cerevisiae* development and reproduction to be used in the experiment, Malt Extract Broth (Difco) was inoculated into and incubated for 48 h. at $25 \pm 1^\circ\text{C}$. The prepared yeast, broth culture is inoculated into YEDP (1 g yeast extract for 100 ml, 2 g bactopectone, 2 g glucose, 2 g agar) into the medium at a rate of 1% (10^4 yeast / ml) at $25 \pm 0.1^\circ\text{C}$ for 48 h. has been incubated.

2.2. Chemical compounds used

The whole of the work will be carried out in the chemistry department of Firat University biochemistry and microbiology cell culture laboratory. The structure of the compounds 2,2'-[(2R,3R)-2,3-dihydroxy-1,4-dioxobutane-1,4-diyl]bis(N-R-hydrazine-1-carbothioamide and (1R,2R)-1,2-bis[5-(R-amino)-1,3,4-thiadiazole-2-yl]ethane-1,2-diol to be used in the studies is given below [27].

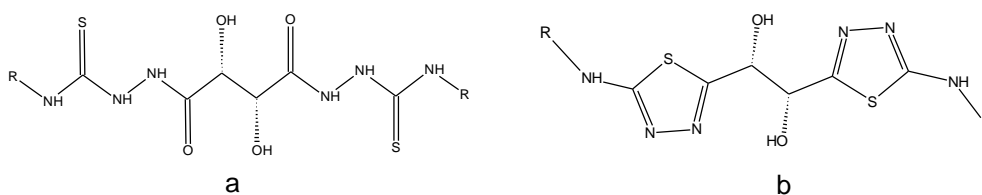


Figure 1. Structure of compounds a) 1,2-diols and b) thiadiazoles **R**: L1,L6 phenyl, L2,L7 p-tolyl, L3,L8 p-methoxyphenyl, L4,L9 allyl and L5,L10 ethyl.

2.3. Test compounds treatment *Saccharomyces cerevisiae* yeast cells for antioxidant prooxidant activity

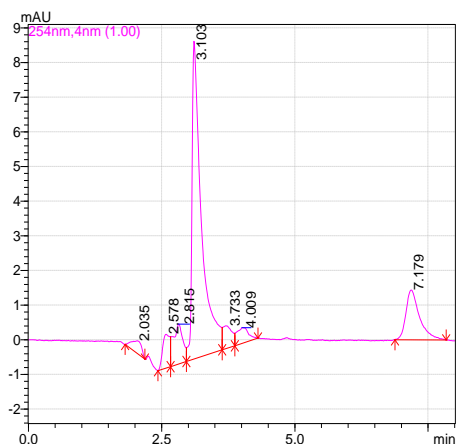
Saccharomyces cerevisiae yeast cells were added in test tubes at a density of about $1 \times 10^6 \text{ ml}^{-1}$ cell, and incubated for 1 day before the experiment. The test

compounds were prepared at specific concentration by dissolving in DMSO. The final concentrations of test compounds in cells were 50 μM and incubated and stirred 24h.

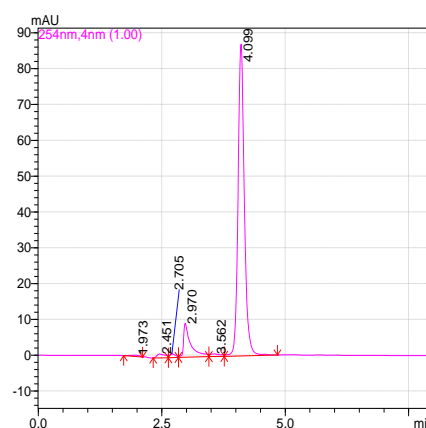
2.4. Determination of MDA and vitamin C

MDA and vitamin C levels were assayed according to the method of Karatepe, small modifications [28]. Briefly, the cells were collected and were gently rinsed twice with 2 ml of ice-cold Krebs–Ringer–Hepes buffer at the end of the incubation period (128 mM NaCl, 20 mM Hepes, 1.4 mM MgSO₄, 1.4 mM CaCl₂, 1 mM

NaH₂PO₄ and 5.2 mM KCl, pH 7.4). Then the mediums were treated with 0.1 ml of 0.5 M perchloric acid and 0.1 ml water. The cells were scraped from the tubes and the lysates were centrifuged 5 min at ambient temperature. The supernatant were taken and separated 17.5 % methanol (v/v) in 30 M monobasic potassium phosphate buffer (pH 3.6) mobile phase.



a



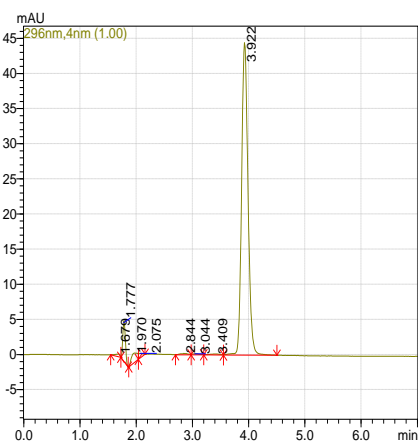
b

Figure 2. HPLC chromatograms a) MDA (retention time 7.179) b) vitamin C (retention time 4.099).

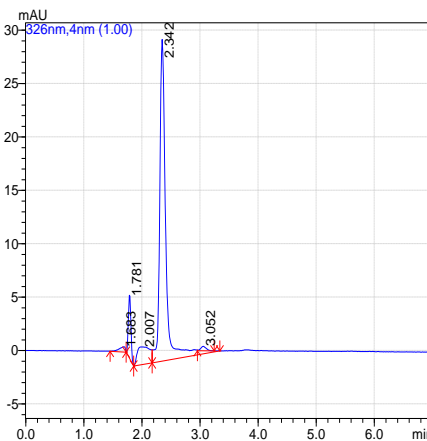
2.5. HPLC quantification of vitamin E and vitamin A

Lipid soluble vitamins in cells were assayed according to the method of Catignani [29]. After incubation with the compounds in 100 µl of the cells suspensions, 200 µL of Ethanol: Sulfuric acid (99: 1) and 100 µL of water was added for precipitation of proteins. After thorough mixing with vortex, it was centrifuged at 4500 rpm for 5 minutes. Then 100 µL of n-hexane (0.05% butylated hydroxytoluene) was added on the centrifuged samples. With the addition of hexane, the

lipid-soluble vitamins in the medium were extracted into the hexane phase. The tubes were mixed on vortex and centrifuged again. At the end of the centrifuge, the hexane phase was carefully separated and taken into the glass tube. 100 µL of n-hexane was added onto the sample again, mixed and centrifuged, and the n-hexane phase was combined with the hexane phase in the glass tube. The extracted hexane phase was carefully evaporated by using nitrogen gas. The residue from the hexane was dissolved in 100 µl of mobile phase (methanol/acetonitrile/chloroform, 47:42:11, v/v). 20 µL of this solution was taken and injected into HPLC.



a



b

Figure 3. HPLC chromatograms a) vitamin E (retention time 3.922) b) vitamin A (retention time 2.342).

2.6. Apparatus

Liquid chromatographic system consisted of LC-20AD pumps, DGU-20A5 degasser, SIL 20A autosampler, CTO-10AS VP column oven, SPD-M20A DAD system. These apparatus were connected via a communication module (Model CBM-20A), and controlled by a Shimadzu LC Solution Workstation (Shimadzu, Kyoto, Japan). A Shimadzu Shim-pack vp-ODS column (150 L×4.6) was used.

2.7. Statistical analysis

SPSS 22.0 for Windows software (SPSS Inc., New York, IBM, USA) were used for statistical analyses. The statistical significance was set at $P < 0.05$ and results are expressed as mean±S.D. Comparison between mean values for antioxidant parameters were made by independent sample t-test.

3. Results and Discussion

3.1. Selection of working type

Only *in vitro* method cannot be sufficient to determine antioxidant activity, and therefore *in vivo* methods are required to assess antioxidant activity. Due to this fact, antioxidant activities of the new compounds have been tested by using *Saccharomyces cerevisiae* yeast cells as *in vivo* model [30].

3.2. Induction of lipid peroxidation by test compounds

The mean MDA levels of the groups are given in Table 1 and Figure 2a. Significant differences were found in MDA levels. After 24 h incubation of the *Saccharomyces cerevisiae* yeast cells with test compounds, the levels of MDA in L2, L3 and L8 groups statistically decreased and compound L9 induced lipid peroxidation from compared to the controls.

3.3. Effects of the compounds on the vitamins A and E levels of cells

Vitamins E levels are increased by the L2 and L8 and decreased by the L9 compounds treatment (Table 1 and Figure 2b). Vitamin A and C levels were not changed all compounds statistically. The stopping chain reactions, metal ion binding activity, radical capture activity and reducing force factors explain of a possible antioxidant substance which it posses antioxidant activity [31].

This work was carried out in order to verify and to clarify the contribution of the biological side effects and relation of new compounds with reactive oxygen species (ROS). Reactive oxygen species (ROS) are formed and degraded by all aerobic organisms, leading to either physiological concentrations required for normal cell function or excessive quantities, the state called oxidative stress [32]. The malondialdehyde (MDA) [33] and isoprostanes [34], well known lipid peroxidation products, are produced ROS-mediated oxidation of membrane lipids.

Table 1. The mean values of the vitamin A, E, C and MDA of *Saccharomyces cerevisiae* yeast cells treated with the compounds

Groups	C vitamin, ppm	MDA, ppm	Vitamin A, ppm	Vitamin E, ppm
Control	0.79±0.04	22.24±0.57	0.07±0.009	0.87±0.08
L1	0.72±0.05	21.47±1.15	0.07±0.011	0.74±0.05
L2	0.84±0.04	17.34±0.88**	0.08±0.003	0.94±0.05*
L3	0.69±0.06	19.33±1.26*	0.08±0.007	0.74±0.04
L4	0.74±0.07	21.26±2.15	0.07±0.005	0.86±0.04
L5	0.74±0.06	20.84±1.32	0.07±0.004	0.74±0.04
L6	0.75±0.08	20.76±1.23	0.07±0.006	0.75±0.03
L7	0.75±0.07	21.59±1.15	0.07±0.007	0.76±0.03
L8	0.85±0.07	17.66±0.81**	0.08±0.004	0.96±0.05*
L9	0.64±1.00	26.40±0.94*	0.07±0.004	0.72±0.03*
L10	0.74±0.08	21.84±0.53	0.06±0.008	0.79±0.04

* $p < 0.05$; ** $p < 0.01$;

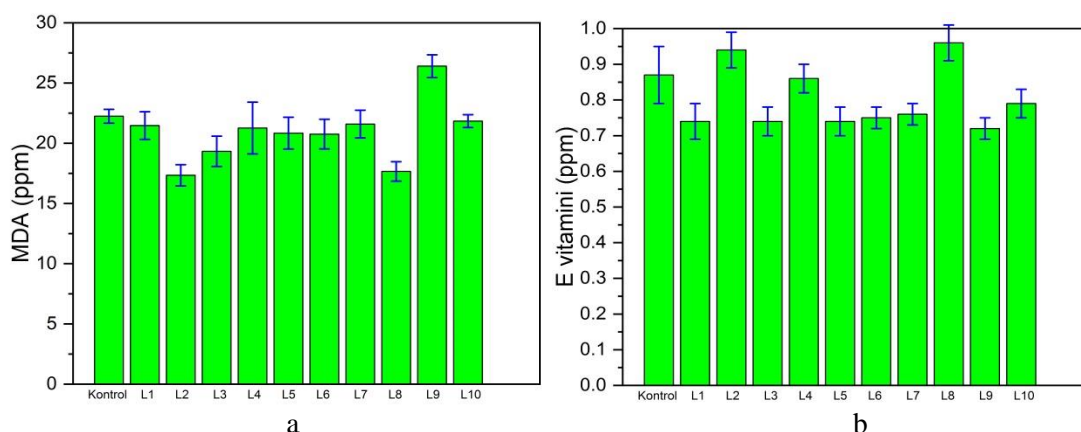


Figure 4. Comparison of the mean concentration of the a) MDA and b) vitamin E compound treated cells, (* $p \leq 0.05$, ** $p \leq 0.01$).

ROS are continuously produced in actively metabolizing cells. However, *Saccharomyces cerevisiae*, like all organisms, contains effective antioxidant defense mechanisms, which detoxify ROS as they are generated and maintain the intracellular redox environment in a reduced state. An oxidative stress is said to occur when ROS overwhelm these defenses, resulting in genetic degeneration and physiological dysfunction, leading eventually to cell death.

The cellular antioxidant systems have two major groups, enzymatic and nonenzymatic [32]. The vitamin C, vitamin E and carotenoids are non enzymatic low molecular weight antioxidant compounds and they are consumed by the metabolism and may fall below normal ranges. For the evaluation of oxidative stress in biological systems, the analyses of levels of antioxidants and MDA are very important. *Saccharomyces cerevisiae*, as a typical eukaryotic model microorganism has some advantages in comparison to humans and animals, such as its simple structure that known genetic background and easy manipulation. Moreover, *Saccharomyces cerevisiae* genome possesses a strikingly high-level of functional conservation within the human genome and other higher eukaryotes. In consideration of these advantages, *Saccharomyces cerevisiae* has become a prominent model for evaluating some cell damages to quickly provide functional clues [30].

In order to eliminate the harmful effects of oxidative stress, many researches are carried out to illuminate the oxidation antioxidant mechanisms and produce solutions. These mechanisms are very important in various living systems, especially human beings. Yeast cells and mammalian cells largely are similar. For this reason, aging, apoptosis and various diseases caused by oxidative stress are important in lighting studies.

Cytotoxicity of xenobiotics could be explained by the impairment of either cellular regulation system, intracellular synthesis of macromolecules or cellular transduction signalling. For the determination of antioxidant and prooxidant activity of test compounds, we choose and consider MDA and antioxidant vitamins [35]. The cell death occurs as a result of membranes that change structure and lose function with lipid peroxidation and increased production of MDA [36]. MDA can be measured by many methods and it is one of the most important indicators of lipid peroxidation [37, 38]. The results show that in the *Saccharomyces cerevisiae* yeast cells, L9 compound induced oxidative damage by generating lipid peroxidation which it increased MDA formation and decreased antioxidant vitamin E levels. The presence of high MDA levels in sample points to the induction of peroxidation following L9 administration.

As seen from the table and figures, L1, L3, L4, L5, L6, L7 and L10 did not affect vitamins A, E, C and MDA levels but L2 and L8 caused significant increase vitamin E and the decrease MDA concentrations statistically which has not been previously described. This indicates that the L2 and L8 supplements were able to spare the vitamin E concentrations with decreasing the lipid peroxidation in the cells.

The Vitamin E antioxidant capacity is very large and high because its antioxidant duty performs by using all mechanisms such as radical destruction, breaking the chain, suppression, repairing broken structures [31, 32].

The more literatures showed that the thiadiazole nuclei have anticonvulsant, anti-leishmanial, antimicrobial, antidepressant, antioxidant, radio protective, anticancer and anti-inflammatory activities.

Kus et al [39] synthesized some novel 5-[(2-(substituted phenyl)-1H-benzimidazole-1-yl)methyl]-methyl-1,3,4- thiadiazole-2-amines and tested for

antioxidant properties by using various *in vitro* systems. They have stated that some compounds prevented lipid peroxidation slightly at 10^{-3} M concentration.

The 6-[3-(4-fluorophenyl)-1H-pyrazol-4-yl]-3-[(2-naphthylthio)methyl]-[1,2,4] triazolo [3,4-b]-[1,3,4] thiadiazole (FPNT) and 6-[3-(4-chlorophenyl)-1H-pyrazol-4-yl]-3-[(phenylthio)methyl]-[1,2,4] triazolo [3,4-b]-[1,3,4] thiadiazole (CPPT) *in vitro* antioxidant activity had investigated by DPPH and ABTS radical scavenging methods as well as by lipid peroxide assay [40]. The results of these assays proved FPNT to be an excellent antioxidant.

The antioxidant activity studies of 1,3,4-thiadiazoles demonstrated that the thiol, thiosulfonic acid and phosphorothioate derivatives of thiadiazoles exhibit evident antioxidant activity. This activity can explain direct link between biological function and thiol containing aromatic ring [41].

The thiol and aminothiols derivative thiadiazoles were synthesized by the Prouillac et al [42] and examined them for their antioxidant ability. The new compounds demonstrated the most scavenging activity for DPPH• and ABTS•+ free radicals.

Conclusion

The increase in free radical formation causes an increase in MDA level and GSH-Px enzyme activity and a decrease in vitamin E level.

As a result of our experimental studies, the groups that the chemical substances used have affected their activities significantly.

In conclusion, we investigated the antioxidant and prooxidant effects of test compounds on *Saccharomyces cerevisiae* yeast cells and the results of this work demonstrate that L9 compound caused oxidative stress and L2 and L8 have antioxidant activity.

The antioxidant activity evaluation results have demonstrated that only aromatic groups exhibit evident antioxidant activity. It seems that our findings are compatible with the literature.

Acknowledgment

We thanks to Dr. Sevda KIRBAĞ for giving and helping for cell studies.

References

- [1] Yang D., An B., Wei W., Tian L., Huang B., Wang H. Coppercatalyzed domino synthesis of nitrogen heterocycle-fused benzoimidazole and 1,2,4-benzothiadiazine 1,1-dioxide derivatives, *A C S Comb Sci.*, 17 (2015) 113–119.
- [2] Iizawa, Y., et al. Therapeutic effect of cefozopran (SCE-2787), a new parenteral cephalosporin, against experimental infections in mice, *Antimicrobial Agents and Chemotherapy* 37 (1993) 100-105.
- [3] Oruc, E.E., et al. 1,3,4-thiadiazole derivatives. Synthesis, structure elucidation, and structure-antituberculosis activity relationship investigation, *Journal of Medicinal Chemistry*. 47 (2004) 6760-6767.
- [4] Foroumadi, A., et al. Antituberculosis agents VIII. Synthesis and in vitro antimycobacterial activity of alkyl α -[5-(5-nitro-2-thienyl)-1,3,4-thiadiazole-2-ylthio]acetates, *Farmaco*, 58 (2003) 1073-1076.
- [5] Kamal M.D., et al. Synthesis, anticonvulsant, and anti-inflammatory evaluation of some new benzotriazole and benzofuran-based heterocycles, *Bioorganic and Medicinal Chemistry*, 14 (2006) 3672–3680.
- [6] Mullick P., et al. Thiadiazole derivatives as potential anticonvulsant agents, *Bulletin of the Korean Chemical Society*, 32 (2011) 1011-1016.
- [7] Clerici, F., et al. Synthesis of 2-amino-5-sulfanyl-1,3,4-thiadiazole derivatives and evaluation of their antidepressant and anxiolytic activity, *Journal of Medicinal Chemistry* 44 (2001) 931-936.
- [8] Hasui, T., et al. Identification of benzoxazin-3-one derivatives as novel, potent, and selective nonsteroidal mineralocorticoid receptor antagonists, *Journal of Medicinal Chemistry*, 54 (2011) 8616-8631.
- [9] Zheng, K. B., et al. Synthesis and antitumor activity of N1-acetylamino-(5-alkyl/aryl-1,3,4-thiadiazole-2-yl)-5-fluorouracil derivatives, *Chinese Chemical Letters*, 19 (2008) 1281-1284.
- [10] Chen, C.J., et al. Synthesis and antifungal activities of 5-(3,4,5-trimethoxyphenyl)-2-sulfonyl-1,3,4-thiadiazole and 5-(3,4,5-trimethoxyphenyl)-2-sulfonyl-1,3,4-oxadiazole derivatives, *Bioorganic & Medicinal Chemistry*, 15 (2007) 3981-3989.
- [11] Suzuki, F., Kawakami, I., Yamamoto, S., Kosai, Y. Japan Kokai, 7776432 1977; *Chem. Abstr.*, 88 (1978) 100351
- [12] Abdel-Ramhan A. E., Mahmoud A. M., El-Sherief H.A., Gahatta A.G., *Chem. Abstr.*, 98 (1983) 72012b.
- [13] Foerster H., Mues V., Baasner B., Hagemann H., Eue I., Schmidt R. European Patent, 60426 1981; *Chem. Abstr.*, (1983) 72107m.
- [14] Tiwari N., Chaturvedi B., Nizamuddin A. synthesis and fungicidal activities of some 2-aryloxymethyl-1,3,4-thiadiazolo[2,3-b]-quinazolin-4-one and 2-aryloxymethyl-5-substituted-1,3,4-thiadiazolo[3,2-a]-1,3,5-triazine-7-thiones, *Indian*

- J. Chem.*, 28 (1989) 200-202.
- [15] Singh H., Yadav L.D.S., *Agri. Biol. Chem.*, 40 (1976) 759-764; (b) Chaaban I., Oji O.O.J. *Indian Chem Soc.*, 61 (1984) 523-525; (c) Mohsen A., Omer M.E., Aboulwafa O.M.J. *Heterocycl. Chem.*, 21 (1984) 1415-1418; (d) Hiremath S.P., Birador J.S., Kudari S.M.J., *Indian Chem. Soc.*, 61 (1984) 74-76.
- [16] Rao A. V. R., Bose D.S., Gurjar M.K., Ravindranatran T. *Tetrahedron*, 45 (1989) 70317040; (b) Seydenpenn J. *Chiral Auxiliaries and Ligands in Asymmetric Synthesis*, John Wiley: New York, (1995); (c) Wright A.E., Schafer M., Midland S., Munnecke D.E., Sims J.J., *Tetrahedron Lett.*, 30 (1989) 5699-5702.
- [17] Kolb H.C., Sharpless K.B., A simplified procedure for the stereospecific transformation of 1,2-diols into epoxides, *Tetrahedron*, 48 (1992) 10515-10530.
- [18] Lohray B.B., Ahuja J.R., *J. Chem. Soc.* (1991) 95-97; (b) Nicolaou K.C., Huang X., Snyder S.A., Rao P.B., Bela M., Reddy M.V., *Angew., Chem. Int.*, 41 (2002) 834.
- [19] Parida S., Dordick J.S.J. *Am. Chem. Soc.*, 113 (1991) 2253-2259; (b) Nelson W.L., Wennerstrom J.E., Sankar S.R.J. *Org. Chem.*, 42 (1977) 1006-1012; (c) Bian chi D., Bosetti A., Cesti P., Golini, P. *Tetrahedron Lett.*, 33 (1992) 3231-3234.
- [20] Kurina-Sanz M., Bisogno F.R., Lavandera I., Orden A.A., Gotor V., Promiscuous substrate binding explains the enzymatic stereo- and regiocontrolled synthesis of enantiopure hydroxy ketones and diols, *Adv. Synth. Catal.*, 351 (2009) 1842– 1848.
- [21] Supuran C.T., Scozzafava A., Carbonic anhydrase inhibitors, *Curr Med Chem Immunol Endocrinol Metab Agents*, 1 (2001) 61–97.
- [22] Singh, N., Rajini, P. S., Free radical scavenging activity of an aqueous extract of potato peel, *Food Chem*, 85 (2004) 611.
- [23] Prior, R. L., Wu, X., Schaich, K., Standardized Methods for the Determination of Antioxidant Capacity and Phenolics in Foods and Dietary Supplements, *J. Agric. Food Chem.*, 53 (2005) 4290.
- [24] Uchida, K., Role of Reactive Aldehyde in Cardiovascular Diseases, *Free Radical Biol. Med.*, 28 (2000) 1685.
- [25] Cadenas, E., Davies, K. J. A., Mitochondrial Free Radical Generation, Oxidative Stress, and Aging, *Free Radical Biol. Med.*, 29 (2000) 222.
- [26] Offeing, B.M., Martelli, S., Steochemistry and Antitumour Activity of Platinum Metal Complexes of 2- Acetypyridine Thiosemicarbazones, *Transition Metal Chemistry.*, 22 (1997) 263-269.
- [27] Karatepe A., (1r, 2r)-etan-1,2 diol tiyadiyazol türevlerinin sentezi, karakterizasyonu ve biyolojik özellikleri. Doktora tezi, Bingöl, 2020.
- [28] Karatepe, M., Simultaneous Determination of Ascorbic Acid and Free Malondialdehyde in Human Serum by HPLC/UV. LC-GC, *North America.*, 22 (2004) 362-5.
- [29] Catignani, G.L., Simultaneous Determination of Retinol and α -Tocopherol in Serum of Plazma by Liquid Chromatography, *Clin. Chem*, 2914 (1983) 708-712.
- [30] Almeida, G.M., Thomazellab, D.P.T., Pereira, G.A.G., Monteiro G., Heterologous expression of an alternative oxidase from *Moniliophthora perniciosa* in *Saccharomyces cerevisiae*: Antioxidant function and in vivo platform for the study of new drugs against witches' broom disease, *Fungal Genetics and Biology*, 126 (2019) 50–55.
- [31] Yildirim A., Mavi A., Kara A.A., Determination of antioxidant and antimicrobial activities of *Rumex crispus* L. extracts, *J. Agri. Food. Chem.*, 49 (2001) 4083.
- [32] Nordberg, J., Arner, E.S.J., , Reactive Oxygen Species, Antioxidants and The Mammalian Thioredoxin System, *Free Rad. Biol. and Med.*, 31(11) (2001) 1287-1317.
- [33] Maccarrone, M (Maccarrone, M); Catani, MV (Catani, MV); Iraci, S (Iraci, S); Melino, G (Melino, G); Agro, AF (Agro, AF) A survey of reactive oxygen species and their role in dermatology, *J. of the Eu. Academy of Der. and Ven.*, 8 (1997) 185-202.
- [34] Morrow J.D., The isoprostanes: their quantification as an index of oxidant stress status in vivo, *Drug Metab Rev.*, 32 (2000) 377-85.
- [35] Vaca, C.E., Wilhelm J., Ringdahl M. H., Interaction of lipid peroxidation products with DNA. A review, *Mutation Res.*, 195 (1988) 137-149.
- [36] Ennamanya J.P., Lavergneb J.P., Reboudb G., Mode of action of bolesatine, a cytotoxic glycoprotein from *Boletus satanas* Lenz., *Mechanistic approaches Toxicolog*, 100 (1995) 51-55.
- [37] Bird, R.P., Draper, H.H., Comperative Studies on Different Methods of Malondialdehyde Determination, *Methods in Enzymology.*, 105 (1984) 299-305.
- [38] Tomita M., Okuyama T., Kawai S.J., Determination of malonaldehyde in oxidized biological materials by high-performance liquid chromatography, *Chromatogr*, 31 (1990) 391-7.
- [39] Kus C., Kilcigil G.A., Ozbey S., Kaynak F.B., Kaya M., Coban T., Eke B., C., Synthesis and Antioxidant Properties of Novel N-Methyl-1,3,4-Thiadiazol-2-Amine and 4-Methyl-2H-1,2,4-Triazole-3(4H)-Thione Derivatives of Benzimidazole Class Bioorg, *Med. Chem.*, 16 (2008) 4294-4303.

- [40] Dhanya S., Arun M.I., Prakash S., et al. 6-[3-(4-Fluorophenyl)-1H-pyrazol-4-yl]-3-[(2-naphthyloxy)methyl][1,2,4]triazolo[3,4-b][1,3,4]thiadiazole as a potent antioxidant and an anticancer agent induces growth inhibition followed by apoptosis in HepG2 cells, *Arabian Journal of Chemistry*, 3 (2010) 211-217.
- [41] Cressier D., Prouillac C., Hernandez P., et al., Synthesis, Antioxidant Properties and Radioprotective Effects of New Benzothiazoles and Thiadiazoles, *Bioorg. Med. Chem.*, 17 (2009) 5275-5284.
- [42] Prouillac C., Vicendo P., Garrigues J.C., Poteau R., Rima G., Evaluation of new thiadiazoles and benzothiazoles as potential radioprotectors: free radical scavenging activity in vitro and theoretical studies (QSAR, DFT), *Free Rad Biol Med.*, 46 (2009) 1139-1148



Summarising big data: public GitHub dataset for software engineering challenges

Abdulkadir ŞEKER^{1,*}, Banu DİRİ², Halil ARSLAN¹, Mehmet Fatih AMASYALI²

¹Sivas Cumhuriyet University, Department of Computer Engineering, Sivas/ TURKEY

²Yıldız Technical University, Department of Computer Engineering, İstanbul/ TURKEY

Abstract

In open-source software development environments; textual, numerical, and relationship-based data generated are of interest to researchers. Various data sets are available for this data, which is frequently used in areas such as software engineering and natural language processing. However, since these data sets contain all the data in the environment, the problem arises in the terabytes of data processing. For this reason, almost all of the studies using GitHub data use filtered data according to certain criteria. In this context, using a different data set in each study makes a comparison of the accuracy of the studies quite difficult. In order to solve this problem, a common dataset was created and shared with the researchers, which would allow to work on many software engineering problems.

Article info

History:

Received:29.04.2020

Accepted:12.06.2020

Keywords:

GitHub,
Ghtorrent,
Big data,
MongoDB.

1. Introduction

One of the most common among cloud-based open-source versioning systems is GitHub. GitHub has become the world's largest code server that hosted more than 100 million developers and more than 40 million repos (<https://en.wikipedia.org/wiki/GitHub>). Repo is abbreviation for repository of projects, it can be thought of as a folder where we store projects. On GitHub-like platforms, development processes are distributed. Developers can make different contributions to projects from any location, via commenting, coding, opening issues, or fixing some bugs. By the results of these activities, large amounts of data are generated for researchers working on natural language processing and software engineering. In addition to these text data, from the social relationships of users with each other and with repos also extract different features. Thanks to these features, GitHub data is of great importance and interest for academic and commercial studies.

In studies with GitHub data, researchers obtain data via the GitHub API or use some datasets. The most widely used of these datasets is known as GHTorrent [1–3]. The GHTorrent dataset was developed in the software engineering department of the TU Delft University [4]. The dataset presents all the data on the platform as downloadable dumps. The sizes of the GitHub datasets

reach very high levels as they contain information from the entire platform. Working with data in such sizes is a problem in itself. When studies using GitHub data are examined, it is seen that almost all of them have created specific sub-datasets. Researchers have used the data in their studies by filtering the data according to their problems and possibilities. It is not possible to compare the successes of even the studies on similar subjects since each researcher works on the dataset that he/she has created.

To address this problem in the literature, the copy of the GHTorrent dataset containing GitHub data up to 2015 was localized and filtered with certain parameters, duplicate data was extracted, new fields to link the data were added, and a MongoDB dataset was created. In this way, a data set, which is much smaller than the GitHub environment, has been produced and shared, which will offer the opportunity to work on the challenges of software engineering in many areas such as task, user, project, and software development. It is possible to use this dataset easily during the algorithm or model development phase. The dataset was shared as a MongoDB archive for the developed codes to be applied to big data without being changed.

2. Definition of Problem

In studies using GitHub data, filtered datasets are used. Even if the problems studied are the same, since the

*Corresponding author. Email address: aseker@cumhuriyet.edu.tr

<http://dergipark.gov.tr/csj> ©2020 Faculty of Science, Sivas Cumhuriyet University

datasets are specific to each study, the accuracy of the claimed success rates has become controversial. For example, the works are given in Table 1 are all about *pull request* (PR). However, as can be seen, they have used different types of content and filtered data of different types. In order to provide a solution to this situation and to be able to conduct rapid experiments at the beginning of the studies, a small dataset was designed and produced to represent the big data.

Table 1. The Filtered Dataset from some studies

Study	Number of repos	Type of filter
Zhang-2014 [5]	3587	Has more than 100 PR
Veen-2015 [6]	475	-
Yu-2015 [7]	40	Has more than 100 PR and non-forked
Junior-2018 [8]	32	Has more than 100 PR and at least 5 developers
Zhao-2019 [9]	74	Develop with Java

GHTorrent consists of a lot of information about projects, definitions and contents of a problem (issue), comments, information about pull requests, code commit activities, repos that users follow, ... (Table 2).

Table 2. The Information of GHTorrent Dataset

Domain	Collections
User	Users, Followers, Watchers, RepoCollaborators
Project	Projects, Forks
Development	Commits, CommitComments
Contribution	Issues, IssueComments, PullRequests, PullRequestComments

This dataset offers GitHub data in different formats as SQL tables and MongoDB collections. In this study, a public subset of data was created with the version covering data up to 2015. With the MongoDB queries, some errors detected in the GHTorrent dataset have been corrected, free from repetitive data, link features that are noticed to be missing from the collections have been added, convert to a simple and easy-to-operate size and content. While creating the dataset, all the data (approximately 750 GB) stored as MongoDB collections were downloaded to the local environment and put through the processes mentioned above. These processes have been developed in MongoDB in order to suitable for big data. The queries used for all transactions are shared on GitHub;

<https://github.com/kadirseker00/GitDataSCP>.

Users is selected as the restrictive collection when filtering the dataset. A dataset has been created with all the information associated with the 100 selected users. All collections have been shared as CSV format, which is the most suitable in terms of size.

3. Pre-Processes

3.1. Filtering

The 100 most active users on GitHub from the *Users* collection were selected; According to list below url;
<https://gist.github.com/paulmillr/2657075>

Based on these users, all data that has any relationship with them was filtered from other collections. The steps for filtering are shown in detail in Figure 1.

3.2. Solving mistaken or missed data

In order to obtain the dataset free from errors, it must be put through some process. In this section, the related MongoDB queries are given below each problem. Since the data selected in the dataset is planned in the user base, it is needed to determine the primary keys for collections. In this context, as a primary key (or distinctive feature); "user id" will be used on the data related to users, similarly "repo id" is used on the data associated with repos. Therefore, the existing problems with these fields must be eliminated.

Firstly, the documents that has null value of these key features have been removed (Figure 1).

```
db.Pull_requests.deleteMany({user_id: null})
```

Figure 1 Remove null data

It has been noticed that the dataset contains duplicate documents that are thought created by users or retrieve mistakenly. Documents containing repeated data in key fields such as *user id*, *repo id* or *full name* were also removed.

```
db.Issues.aggregate([
  {$match: {"issue_id": {$nin: [null]}},
  {$group: {"_id": "$issue_id",
    "doc": {"$first": "$$ROOT"}}},
  {$replaceRoot: {"newRoot": "$doc"}},
  {$out: "Issues"}], {allowDiskUse: true}
]);
```

Figure 2 Remove duplicate data

It has been noticed that the dataset contains duplicate documents that are thought created by users or retrieve mistakenly. Documents containing repeated data in

key fields such as *user id*, *repo id* or *full name* were also removed (Figure 2).

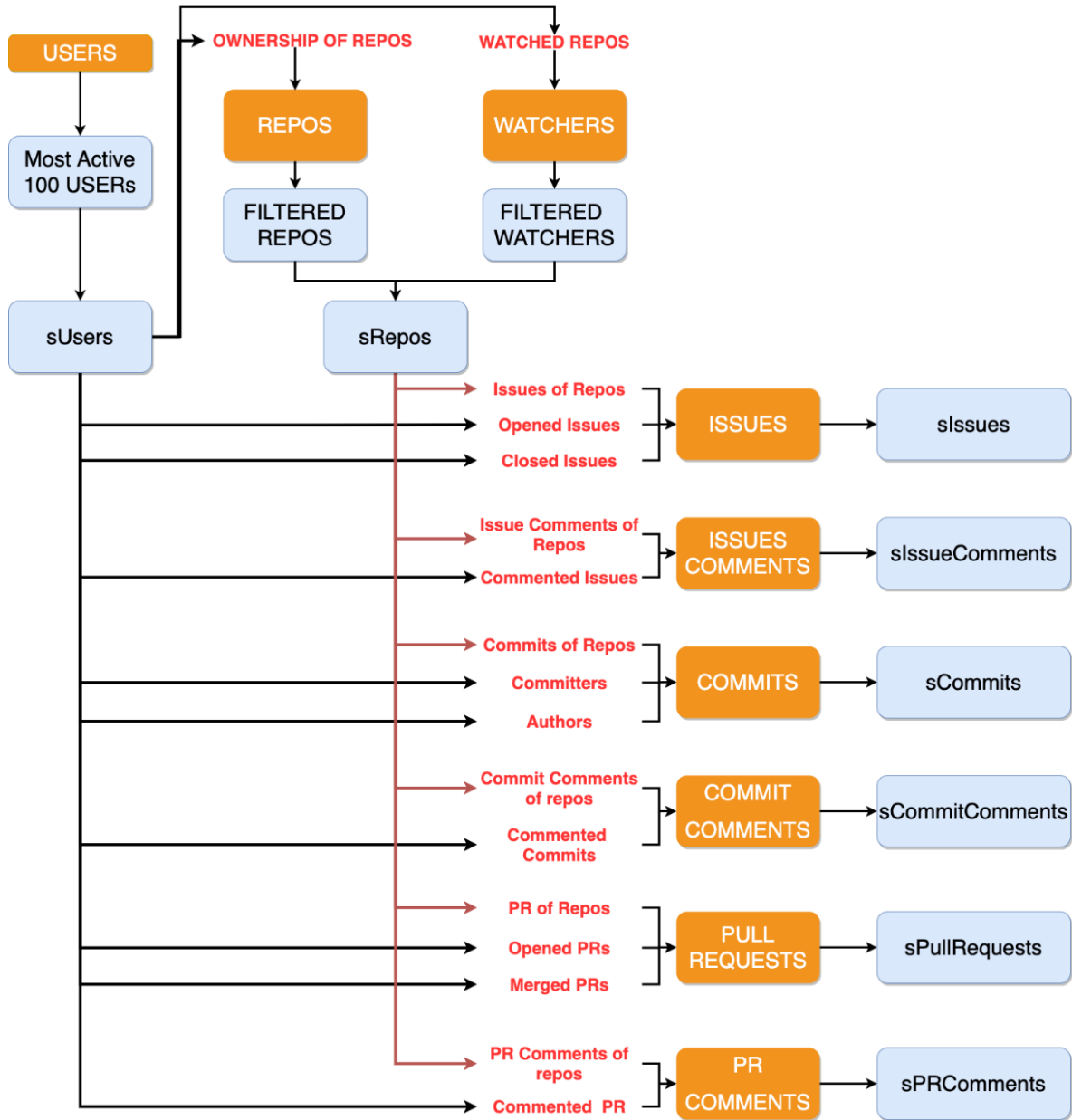


Figure 3 The filtering process with the most active 100 users

In some collections, it has been observed that the key fields do not exist or that their substitutes aren't sufficient.

- a. Issues, Watchers collections have the *owner* and *name* fields of the repo. The *full_name* field is created by combining two fields directly (Figure 4).

```
db.Watchers.aggregate([{$addFields:
  {full_name: {$concat:
    ["$owner", "/", "$repo"]}},
  {$out:"Watchers"}
]);
```

Figure 4 Create "full_name" field

- b. In the CommentCommits collection, there is no *owner* and *name* fields. To obtain them firstly has been parsed the *repo url* field and extracted these fields. Then *full_name* has been created as combining them (Figure 5). A sample repo url; <https://github.com/johndue/projectX>)

```
db.CommentCommits.aggregate([
  {$addFields:
    {full_name: {$concat: [
      {$arrayElemAt: [{$split: ["$url", "/" ]}, 4]},
      "/" ,
      {$arrayElemAt: [{$split: ["$url", "/" ]}, 5]}
    ]}
    }
  },
  {$out: "CommentCommits"}
]);
```

Figure 5 Extract "full_name" from url field

- c. After the process a or b, the field of *repo_id* has added to related collections as aggregate (join) with Repos collection on *full_name*. The query below means; find the documents from both collections which have the same *full_name*, then get the *repo_id* of this document from a collection and add it to a related document in the other collection (Figure 6).
- d. Similarly, since there is no field of *user_id* in the *Followers* collection, this field was added by join with *Users* collection on *login* field. (*login* is the name of user in GitHub database.)

After handling these adding key or link fields process, the sub dataset has been created. The comparison of size between the GHTorrent and proposed filtered data set are given in Table 3. As can be seen from Table 3, working with huge data causes serious time losses, especially during the algorithm or model development phase. In this context, it is thought that the proposed filtered data set will provide researchers with a common data pool but will also save time in their studies. Dataset is published on page below;

<https://github.com/kadirseker00/GitDataSCP>

```
db.CommitComments.aggregate([
  {$lookup:
    {from: "repos", let: {item: "$full_name"},
    pipeline: [
      {$match: {$expr: {$eq: ["$full_name", "$$item"]}}},
      {$project: {"repo_id": 1}}
    ],
    as: "fromComments"}
  },
  {$replaceRoot: {newRoot:
    {$mergeObjects: [
      {$arrayElemAt: ["$fromComments", 0]}, {"$ROOT"}]}
    }
  },
  {$project: {'fromComments': 0}},
  {$out: "FilteredCommitComments"}
]);
```

Figure 6 Join with repos and other collection on "full_name"

Table 3. The comparison of GHTorrent and proposed dataset

Name of Collection	~ Disk Size		~ Number of documents	
	GHTorrent	Proposed	GHTorrent	Proposed
Users	1 GB	0.8 MB	5,000,000	100
Repos	30 GB	45 MB	20,000,000	40,000
Commits	298 GB	4 GB	41,000,000	500,000
Commit Comments	1 GB	90 MB	2,000,000	250,000
Issues	11 GB	3 GB	17,000,000	3,000,000
Issue Comments	15 GB	4 GB	31,000,000	9,000,000
Pull Requests	23 GB	5 GB	8,000,000	1,500,000
Pull Requests Comments	6 GB	1 GB	5,000,000	1,200,000
Followers	1 GB	20 MB	7,000,000	130,000
Forks	8 GB	5 MB	11,000,000	7,000
Watchers	7 GB	8 MB	38,000,000	50,000
RepoCollaborators	1 GB	2 MB	5,000,000	4,000

4. Results and Discussion

In this study, a common dataset was proposed to the researchers working for the solution of software engineering challenges as a result of filtering with the GHTorrent dataset that contains an up-to-date copy of GitHub data. All filtering operations were performed in accordance with the big data in MongoDB environment so that the current versions of the data set can be extracted, and extensions/enhancements can be made.

In the proposed dataset, the fields that will link between the collections have been added, the missing or repeated data noticed in the dataset have been removed.

As a result, a clear and easy-to-operate GitHub dataset has been generated. The GitHub link given in the study can be used for downloading the dataset. It is planned to studies on the software engineering challenges with this proposed dataset.

References

- [1] V. Cosentino, J. Luis, and J. Cabot. Findings from GitHub: methods, datasets and limitations. *Proceedings of the 13th Int. Workshop on Mining Softw. Repositories*, (2016), 137–141.
- [2] V. Cosentino, J. L. Canovas Izquierdo, and J. Cabot. A Systematic Mapping Study of Software Development With GitHub, *IEEE Access*, 5 (2017) 7173–7192.
- [3] Z. Kotti and D. Spinellis. Standing on shoulders or feet?: the usage of the MSR data papers, *Proceedings of the 16th Int. Conference on Mining Software Repositories*, (2019) 565–576.
- [4] G. Gousios. The GHTorrent dataset and tool suite, *Proceedings of the 10th Working Conf. on Mining Soft. Repositories*, (2013) 233–236.
- [5] Y. Zhang, G. Yin, Y. Yu, and H. Wang. Investigating social media in GitHub's pull-requests: a case study on Ruby on Rails, *Proceedings of the 1st International Workshop on Crowd-based Soft. Development Methods and Technologies - CrowdSoft 2014* (2014) 37–41.
- [6] E. van der Veen, G. Gousios, and A. Zaidman. Automatically Prioritizing Pull Requests, *2015 IEEE/ACM 12th Working Conference on Mining Soft. Repositories*. (2015) 357–361.
- [7] Y. Yu, H. Wang, V. Filkov, P. Devanbu, and B. Vasilescu. Wait for It: Determinants of Pull Request Evaluation Latency on GitHub. *2015 IEEE/ACM 12th Working Conference on Mining Software Repositories*, (2015) 367–371.
- [8] M. L. de L. Júnior, D. M. Soares, A. Plastino, and L. Murta. Automatic assignment of integrators to pull requests: The importance of selecting appropriate attributes, *J. Syst. Softw.*, 144 (2018) 181–196.
- [9] G. Zhao, D. A. da Costa, and Y. Zou. Improving the Pull Requests Review Process Using Learning-to-rank Algorithms, *Empir. Softw. Eng.*, (2019) 1–31.

Investigation of 58S bioactive glass tablets

Lale CİVAN^{1,2} , Macid NURBAS^{3*} 

¹ Department of Biotechnology and Biosafety, Eskişehir Osmangazi University, 26480, Eskişehir, Turkey

² Department of Materials Science and Engineering, Eskişehir Technical University, 26555, Eskişehir, Turkey

³ Eskişehir Osmangazi University, Department of Chemical Engineering, 26480, Eskişehir, Turkey

Abstract

In this study, bioactive glass powders were successfully synthesized by using the sol-gel process and bioactive glass powders were tableted by direct dry pressing method. The morphology and surface properties of bioactive glass tablets were examined via field emission scanning electron microscope (FE-SEM) devices. X-ray diffraction (XRD) was utilized to evaluate the phases formed in the sol-gel bioactive glass tablets. Surface characterization of the tablets immersed in simulated body fluid (SBF) was carried out with XRD, FE-SEM, and Fourier transform infrared (FTIR). XRD, FTIR, and EDS analysis proved that the sample contained hydroxyapatite. Also, the in vitro mineralization assay demonstrated that bioactive glass tablets are capable of inducing the creation of hydroxyapatite after dipped in SBF. All analyze results showed that bioactive glass tablets have good apatite-forming activity.

Article info

History:

Received: 30.05.2020

Accepted: 14.09.2020

Keywords:

Bioactive glass tablet,
Biocompatibility,
Biomaterials,
Surface
characterization,
Sol-gel preparation.

1. Introduction

Bioactive glasses are osteo-productive materials that give the ability to repair damaged bone. These properties are due to the developing dissolution in the physiological environment where the release of calcium, sodium, and phosphate ions begins to form and the apatite layer will form a vigorous bond with the surrounding bone tissues [1]. Bioactive glasses are one of the most promising bone regeneration materials because they can connect easily bone and assistance bone growth [2]. In addition, these glasses are capable of forming chemical bonds to the surface layer of the scaffold to promote new bone growth. In the 90s, 58S bioactive glasses were produced with a sol-gel method, which showed similar properties with 45S5 and showed higher dissolution rates for apatite formation [3].

The sol-gel process is a chemical-based synthesis road in which the solution having the precursor for the composition is subjected to polymer-type reactions at room temperature to form the gel [4]. Sol-gel is an important method that makes it probable to manufacture glasses containing compositions that cannot be achieved by conventional melting methods [5]. It also allows the chemical composition of bioactive glasses to be significantly expanded

compared to the conventional melting process [6]. The sol-gel method has determined to be an ideal technique for preparing bioactive glasses. It is a process that allows the synthesis of glassy materials at low temperatures [7]. The sol-gels are made utilizing low-temperature hydrolysis and condensation process. Solution chemistry provides an easy mixing and good homogenization of chemicals. Low reaction temperatures avoid crystallization and phase separation, thus let the formation of glass that cannot normally be prepared [2]. The sol-gel process allows the formation of a silica network around the polymer chains via introducing the polymer into the sol. TEOS has been added to control the degree of covalent bonding between inorganic and organic components and as a silica precursor [8].

Since dry press molding does not require a complex experimental process, it can be commonly used in some specific fields. Dry press molding is a method of forming the tablet form by mixing powder and additive which does not destroy the structure of the bioactive particles. The tableting of bioactive powder particles is the only physical reaction that the bioactive properties of the material are maintained. This demonstrates that bioactive glass tablets have excellent bioactivity as bone healing materials and can be used in biomedical applications [9]. The aim of this study is to form high bioactivity glass particles by the sol-gel method and to

*Corresponding author. Email address: mnurbas@gmail.com

tablet these bioactive glass particles and finally characterize this material. In the mineralization study, the hydroxyapatite formation process was systematically investigated. The phases, microstructures, and structural analysis of the tablets were identified by XRD, FE-SEM, FTIR before and after immersion in SBF.

2. EXPERIMENTAL STUDIES

2.1. 58S bioactive glass powders and tablets

Triethyl phosphate, Tetraethoxysilane Merck, Calcium nitrate tetrahydrate Acros organics, Hydrochloric acid was obtained from Isolab chemicals company. The bioactive glass powder content was determined in moles, 36% CaO, 60% SiO₂, 4% P₂O₅, and Triethyl phosphate (Ca(NO₃)₂·4H₂O), Tetraethoxysilane, hydrochloric acid, and deionized water were used in this formulation. This study was carried out in four stages according to the method used by Chen et al [9]. First, 2.32 g triethyl phosphate, 20.48 g tetraethoxysilane, and 14.04 g Ca(NO₃)₂·4H₂O were added to a mixture of 2.60 g hydrochloric acid (2 M) and 15.64 g water, respectively. The mixture was stirred in a continuous magnetic stirrer until homogeneous. Then the zeta potential value of the sample was determined as -0.0245 mV. Second, the sol was aged at room temperature for 48 hours to fully react hydrolysis of the polycondensation. During this period of aging, the sol solidified as a transparent gel. Transparent solidification is indicative of monomerization.

In the third step, the gel was kept in the oven at 60 °C and 120 °C, respectively, for 24 hours to remove excess water and ethanol. The sample exposed to this temperature changes from transparent to white color and this event indicated that the polymerization is complete. Finally, the dried gel was applied to thermal processing in an oven at 650 °C for 3 hours to remove unreacted organic material. Thus, there was a burning reaction in the sample. After grinding for 3 hours at 650 °C, the sample was ground in a mortar and 0.5 grams for each tablet was weighed. To prepare tablets of good mechanical strength, it is necessary to reduce the grain size of the large bioactive glass samples to reduce the stress concentration effect of the bioactive glass tablets. The milled 58S bioactive glass particles were then made into tablet form by applying 22000 pounds (10 metric tons) pressure on a Carver hand press using. Sol and solid bioactive glass tablets that solidify into a transparent gel are shown in Fig. 1.

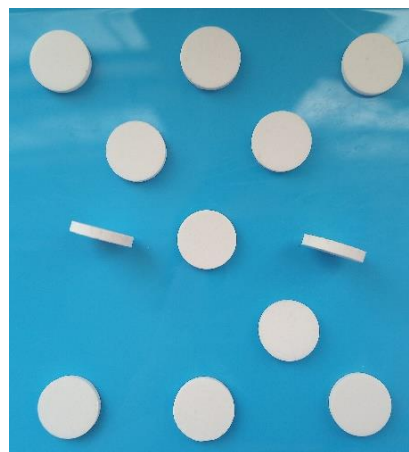


Figure 1. Bioactive glass tablets created by dry pressing method

2.2. In vitro bioactivity of bioactive glass tablets

The talent to form hydroxyapatite in vitro on the surface of the material was assessed by a simulated body fluid dipping test as described by Kokubo et al.[10]. The pH of the simulated body fluid solution was arranged to 7.40 with TRIS and HCl (1 M). The mineralization test with simulated body fluid was carried out at 37 °C for different periods of 7, 14, 21 and 30 days. Acetone was utilized to finish the mineralization process of tablets while removing from simulated body fluid. The tablets were then washed sequentially with ethanol and deionized water and finally left in a 60 °C oven for 1 hour to dry. Subsequently, the morphology of the newly formed hydroxyapatite on the tablet surface was investigated by field emission scanning electron microscopy. Mineral composition and crystal structure of hydroxyapatite were described with X-Ray Diffraction and FTIR spectroscopy analysis.

3. RESULTS AND DISCUSSION

3.1. Simultaneous thermal analysis (STA)

In order to determine the thermal processing temperature, simultaneous thermal analysis (STA) was done by examining the mass change of the organic-containing sample depending on the increasing temperature (Fig. 2). The mass reduction of the coating formed as a function of time or temperature was determined by Perkin Elmer STA 8000 brand device. Tg/DTA analysis was performed on the heat-processed sample at 650 °C for 3 hours. There were three stages of weight loss and a fragmentation reaction became in

Tg analysis. Because the analysis was carried out under a nitrogen atmosphere.

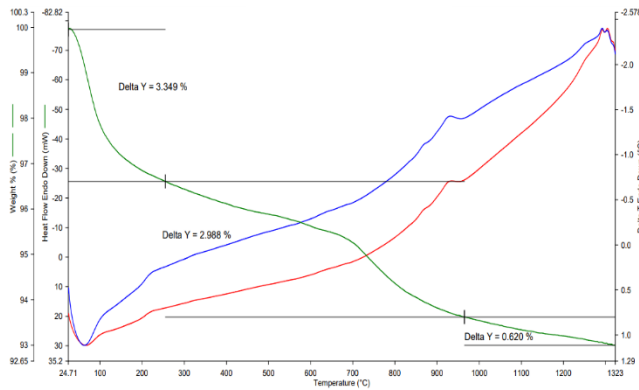


Figure 2. Tg / DTA Analysis

3.2. XRD analysis

The phases of the tablets obtained were characterized by the Panalytical Empyrean brand X-Ray diffraction (XRD) device. The XRD measurement was made in the range of $5-80^\circ$ and the formed phases were calcite and hydroxyapatite before and after 7 days immersion in the SBF (Fig. 3). Fracture peaks observed at $2\theta = 25.8^\circ, 31.7^\circ, 39.8^\circ, 46.7^\circ, 48.6^\circ, 60.4^\circ, 65^\circ, 66.4^\circ$ of hydroxyapatite crystals. It corresponded to the reflections of (002), (211), (310), (222), (320), (331), (511), (422) before immersion in the SBF. The prolongation of the hydroxyapatite peak length of the tablet immersed in simulated body fluid for 7 days is evidence of bioactivity. XRD results indicated that bioactive glass tablets have well bioactivity in vitro and mineralization products are hydroxyapatite.

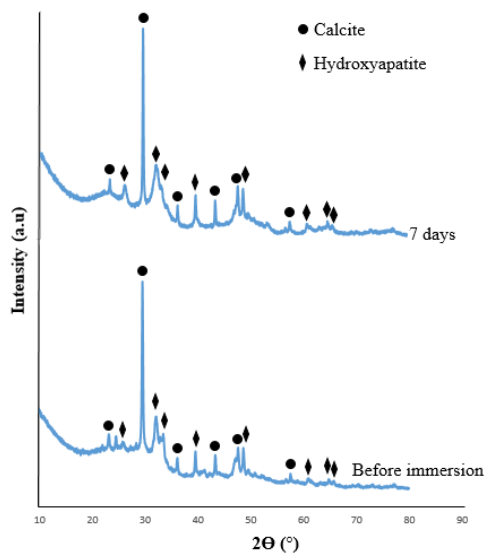


Figure 3. XRD analysis of the sample which was kept in SBF for 7 days and was not kept

3.3. FTIR analysis

Chemical characterization of the samples was performed using Perkin Elmer Spectrum Two brand Fourier Transform Infrared Spectroscopy in the range of $400-4000\text{ cm}^{-1}$. Fig. 3 FTIR spectra of bioactive glass tablets before and after dipped in SBF may reflect the surface composition and structure of hydroxyapatite. Two peaks appearing at 603 cm^{-1} and 565 cm^{-1} before being dipped in SBF P-O is connected to bending vibration. The reason for the occurrence of a two-part peak is that the molecules in the crystal lattice are regulated in a regular manner due to the reinforced intermolecular interaction and eventually lead to band division. After being dipped in SBF for 7 days, these peaks length in the split phosphate band grew. When the mineralization time was increased to 7 days, the hydroxyapatite crystallization process was accelerated and the intensity of the peaks increased as the mineralization time increased. At the same time, these peaks approaching each other were seen in 571 cm^{-1} and 569 cm^{-1} . Furthermore, the peak corresponding to the P-O tensile vibration before submerged in the SBF appeared at 941 cm^{-1} and is clearly visible. Peaks at 875 cm^{-1} and 1644 cm^{-1} correspond to C-O tensile vibration. This indicates that the mineralization goods contain a carbon element. As a result, the mineralization product of bioactive glass tablets was hydroxyapatite after immersion in the SBF solution.

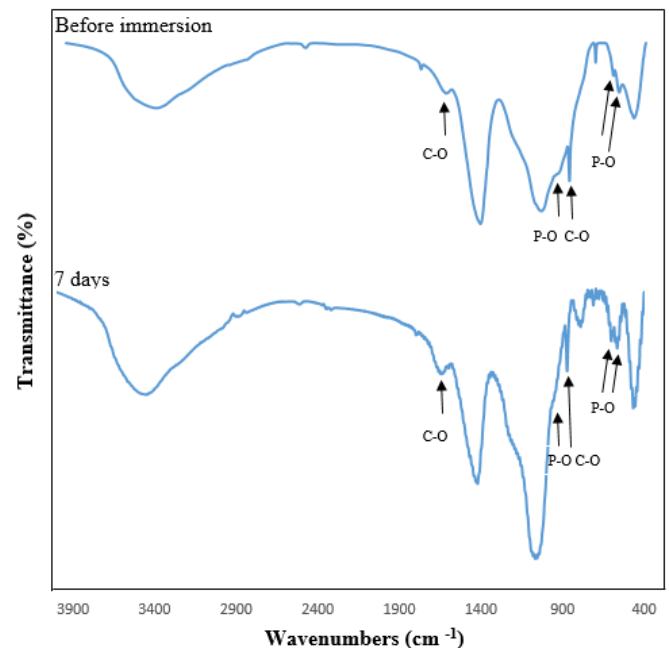


Figure 4. FTIR analysis of the sample which was kept in simulated body fluid for 7 days and not kept

3.4. FE-SEM analysis

The microstructure of the 58S bioactive glass tablet was examined using a Hitachi Regulus 8230 FE-SEM device. The FE-SEM Fig. 5 proved that the bioactive glass tablet has heterogeneous and irregular morphology. Vapor-liquid interfaces between bioactive glass powders occur with the drying process. Due to the impact of the interfacial stress, the curvature of the liquid surface has emerged between the particles. This was created a strong tensile force that caused the gel skeleton to precipitate. In the end, the particles were in close contact. This caused the soft and tough particles to come together. Therefore, the formed bioactive glass particles required to be pulverized before dry pressing molding.

FE-SEM analysis revealed a large number of inhomogeneous nanoparticles on the bioactive glass tablets (Fig. 5). Initially, cracks were not observed in the microstructure. Nuclei formed on the surface of the

sample dipped in SBF for 30 days grew. The surface was completely covered with formed hydroxyapatite clumps. However, large bioactive glass particles began to disintegrate in the sample immersed in SBF for 30 days. Because the particles forming the tablets are not homogeneous, many micro-cracks have appeared on the surface of bioactive glass tablets (Fig. 7). After being dipped in SBF the tablets produced stress concentration and swollen. Cracks have been formed between the bioactive glass tablets and the SBF solution under the influence of water abrasion and ion exchange, as a result of physical and chemical reactions. While the Ca/P ratio was 10.30 before immersion in SBF (Fig. 5), this ratio was determined as 18.18 and 7.42 in the sample dipped for 7 days (Fig. 6). Calcite was formed from the excess of calcium on the surface of the tablets. The Ca/P ratio of the sample immersed for 30 days decreased to 3.58, 2.88, and 3.07 (Fig. 7).

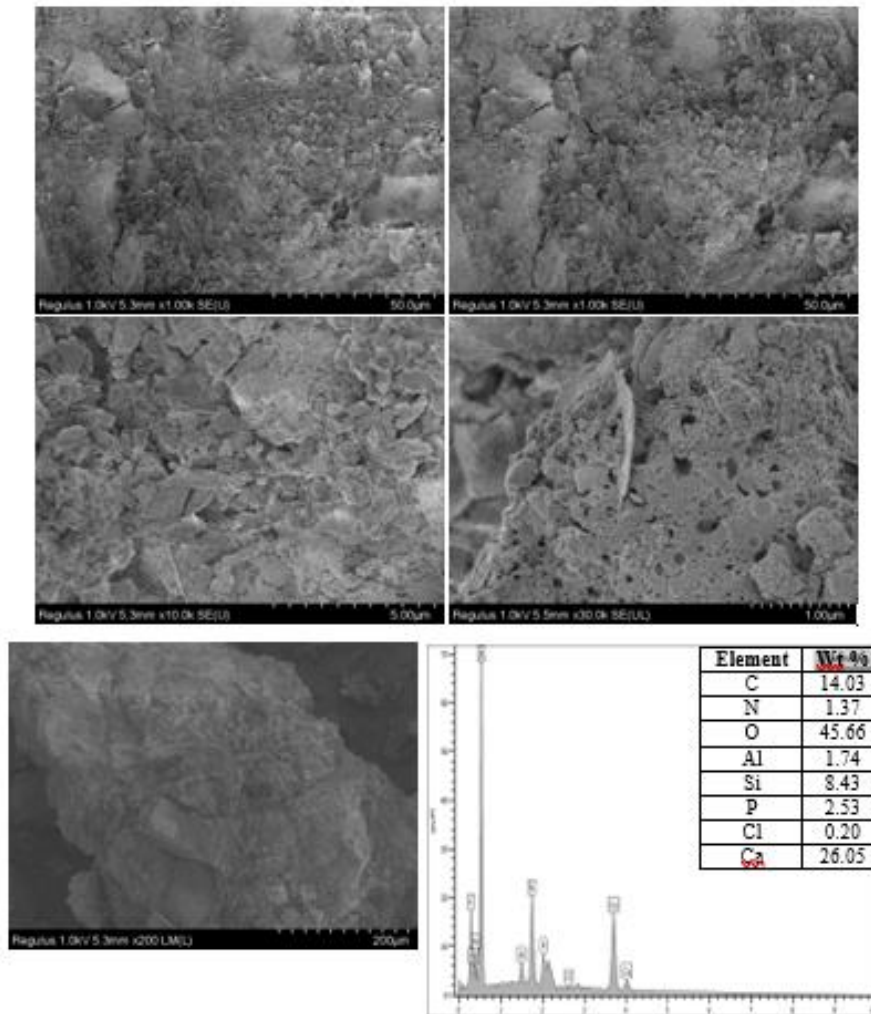


Figure 5. FE-SEM and EDS analysis of a heat-treated sample at 650 °C for 3 hours

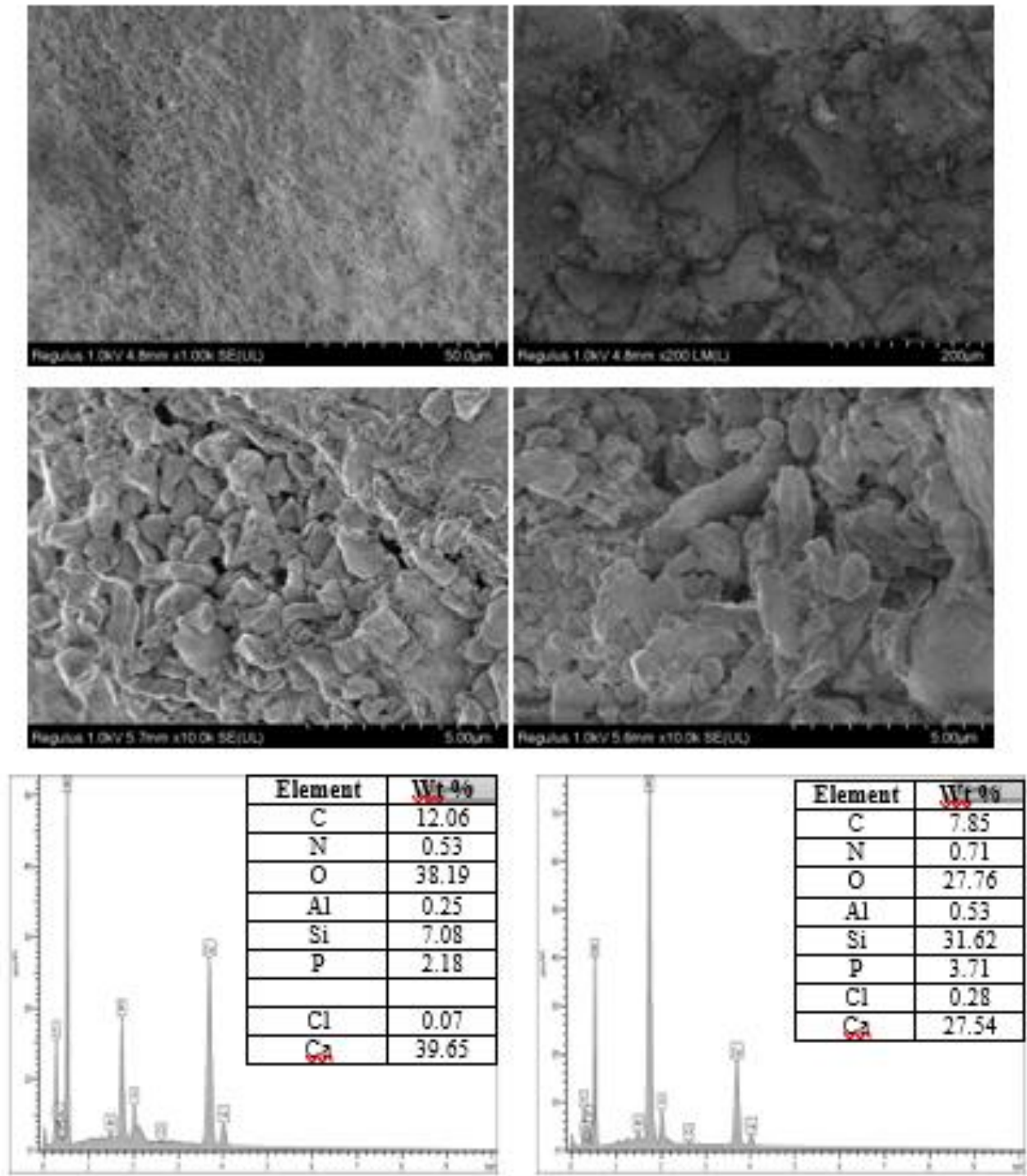


Figure 6. FE-SEM and EDS analysis of the sample held in simulated body fluid for 7 days

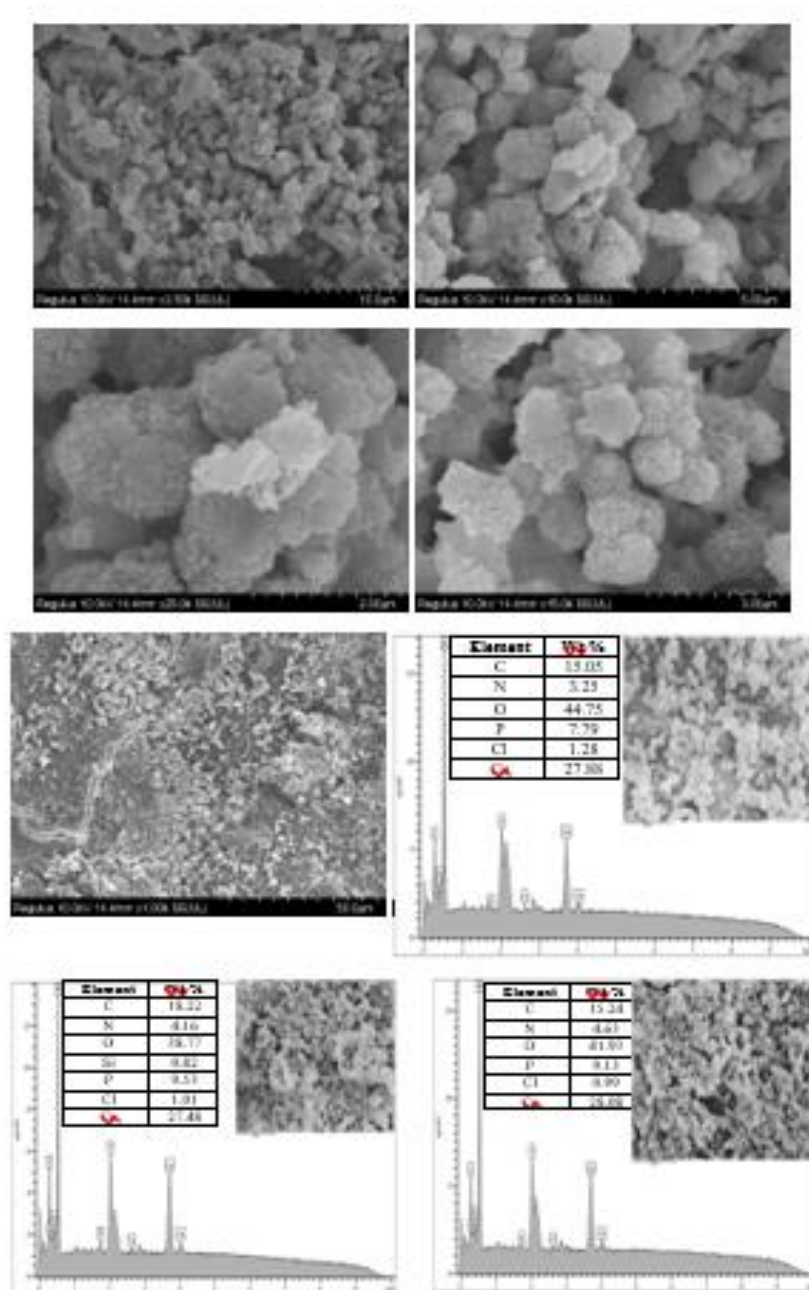


Figure 7. FE-SEM and EDS analysis of the sample held in simulated body fluid for 30 days

4. Conclusions

In this study, bioactive glass powders were successfully created via the sol-gel method. Powders were brought to the tablet form. It can be seen that the bioactive glass tablets made by dry pressing technology are pill-like and homogeneously structured, and the surface was slightly rough. In this

study, 58S bioactive glass tablets were prepared and characterization studies were performed. Bioactivity of the formed tablets was appraised in vitro. The XRD, FTIR, and EDS analysis demonstrated that a dense layer of hydroxyapatite was formed on the surface of bioactive glass tablets after immersion in SBF and that the tablets had perfect bioactivity. The results show that the tablets created have the potential to use as a biological scaffold in tissue engineering. As a

consequence of the FTIR analysis, the formation of P-O bonds in the structures of the samples was determined. The peaks became sharp with an increase in the waiting time in the SBF. In other words, it has been determined that the formation of hydroxyapatite increases.

Acknowledgements

This study was financially supported by Eskisehir Osmangazi University Scientific Research Project (Project Number: 2018 /15A207).

Conflicts of Interest

The authors declare no conflict of interest.

REFERENCES

- [1] Faure J., Drevet R., Lemelle A., Jaber N.B., Tara A., El Btaouri H., Benhayoune H., A new sol-gel synthesis of 45S5 bioactive glass using an organic acid as catalyst, *Materials Science and Engineering C*, 47 (2015) 407-412.
- [2] Martin R.A., Yue S., Hanna J.V., Lee P., Newport R.J., Smith M.E., Jones J.R., Characterizing the hierarchical structures of bioactive sol-gel silicate glass and hybrid scaffolds for bone regeneration, *Philosophical Transactions of the Royal Society A: Mathematical, Physical and Engineering Sciences*, 370 (2012) 1422-1443.
- [3] Mesquita-Guimarães J., Leite M., Souza J., Henriques B., Silva F., Hotza D., Boccaccini A., Fredel M., Processing and strengthening of 58S bioactive glass-infiltrated titania scaffolds, *Journal of Biomedical Materials Research Part A*, 105 (2017) 590-600.
- [4] Hench L.L., West J.K., The sol-gel process, *Chemical Reviews*, 90 (1990) 33-72.
- [5] Almeida R., Gama A., Vueva Y., Bioactive sol-gel scaffolds with dual porosity for tissue engineering, *Journal of Sol-gel Science and Technology*, 57 (2011) 336-342.
- [6] Zhong J., Greenspan D.C., Processing and properties of sol-gel bioactive glasses, *Journal of Biomedical Materials Research: An Official Journal of The Society for Biomaterials, The Japanese Society for Biomaterials, and The Australian Society for Biomaterials and the Korean Society for Biomaterials*, 53 (2000) 694-701.
- [7] Catauro M., Bollino F., Renella R., Papale F., Sol-gel synthesis of SiO₂-CaO-P₂O₅ glasses: influence of the heat treatment on their bioactivity and biocompatibility, *Ceramics International*, 41 (2015) 12578-12588.
- [8] Valliant E.M., Romer F., Wang D., McPhail D.S., Smith M.E., Hanna J.V., Jones J.R., Bioactivity in silica/poly (γ -glutamic acid) sol-gel hybrids through calcium chelation, *Acta Biomaterialia*, 9 (2013) 7662-7671.
- [9] Chen J., Zeng L., Chen X., Liao T., Zheng J., Preparation and characterization of bioactive glass tablets and evaluation of bioactivity and cytotoxicity in vitro, *Bioactive Materials*, 3 (2018) 315-321.
- [10] Kokubo T., Takadama H., How useful is SBF in predicting in vivo bone bioactivity?, *Biomaterials*, 27 (2006) 2907-2915.

Numerical investigation of heat transfer from heat sources placed in a horizontal rectangular channel

Ayla DOĞAN¹, Mecit SIVRIOĞLU², Senol BASKAYA²

¹Akdeniz University, Faculty of Engineering, Department of Mechanical Engineering, Antalya, TURKEY

²Gazi University, Faculty of Engineering, Department of Mechanical Engineering, Ankara, TURKEY

Abstract

In this study, three dimensional mixed convection heat transfer from discrete heat sources placed in a horizontal rectangular channel has been investigated numerically. 8x4 flush-mounted discrete heat sources were mounted on the lower and upper surfaces of the channel. Air is used as working fluid ($Pr \approx 0.7$). The heaters at the bottom and at the top wall were kept at a constant heat flux. Side walls, upper and lower walls are insulated and considered adiabatic. Nusselt number distributions and the effect of the Grashof number ($5.8 \times 10^6 \leq Gr^* \leq 2.3 \times 10^7$) and Reynolds number ($150 \leq Re \leq 971$) on the buoyancy-driven secondary flow have been investigated. Distributions of velocity vectors and temperature contours have been determined by the numerical method, and the results have been presented in detail. Governing equations were solved by the control volume method using suitable boundary conditions. The numerical parametric study was made for aspect ratio of $AR=8$, at various Reynolds and Grashof numbers.

Article info

History:

Received: 02.06.2020

Accepted: 02.09.2020

Keywords:

Electronic cooling, mixed convection, numerical study, heat sources.

1. Introduction

Mixed convection heat transfer in horizontal channels has received a considerable attention and has been applied in a wide range of engineering applications, such as heat exchangers, cooling of electronic equipment solar collectors, chemical processes and similar industrial applications. The most common methods applied for the cooling of electronic equipment comprise mixed convection using air or a liquid as the coolant fluid.

An earlier investigation on electronic cooling was conducted by Kennedy and Zebib [1]. They investigated heat transfer from discrete heat sources between horizontal parallel planes under mixed convection conditions. Four different local heat source configurations were studied numerically and experimentally. Incropera et al. [2] who had another earlier study investigated heat transfer from a single and an array of flush mounted heat sources for water and FC-77 in a rectangular channel. Numerical mixed convection in an inclined channel with discrete heat sources subjected to uniform heat flux was studied by Choi and Ortega [3].

Three-dimensional mixed convection heat transfer from an array of discrete heat sources in a horizontal

rectangular duct was studied numerically by Mahaney et al. [4]. The obtained results showed that the variation of the row-average Nusselt number with Reynolds number exhibits a minimum, suggesting that heat transfer may be enhanced due to buoyancy-induced secondary flow, by reducing the flow rate and hence the pumping requirements.

Dogan et al. [5] investigated experimentally mixed convection heat transfer in a top and bottom heated rectangular channel with discrete heat sources for air. The lower and upper surfaces of the channel were equipped with 8x4 flush-mounted heat sources subjected to uniform heat flux. Whole sides of the channel are insulated. The experimental study was made for an aspect ratio of (AR) 6, Reynolds numbers $955 \leq Re_{Dh} \leq 2220$ and modified Grashof numbers $Gr^* = 1.7 \leq 10^7$ to $6.7 \leq 10^7$.

Ozsunar et al. [6] investigated numerically mixed convection heat transfer in a rectangular channel under various operating conditions. They analyzed the effects of Grashof number, Reynolds number and inclination on mixed convection heat transfer. Air is used as the working fluid. A uniform heat flux was subjected to the lower surface of the channel, sidewalls are insulated and the upper surface is

*Corresponding author. Email address: ayladogan@akdeniz.edu.tr

<http://dergipark.gov.tr/csj> ©2020 Faculty of Science, Sivas Cumhuriyet University

exposed to the surrounding air. The numerical study was made for inclination angles $0^\circ \leq \theta \leq 90^\circ$, Reynolds numbers $50 \leq Re \leq 1000$, and modified Grashof numbers $Gr = 7.0 \times 10^5$ to 4.0×10^6 .

Numerical investigation of three-dimensional laminar mixed convection heat transfer in a vertical channel with an array of heated blocks, simulating electronic components, have been investigated by Amirouche and Bessaih [7]. The governing equations used in the problem were solved by the finite-volume method. Heated elements were kept at constant temperature. Calculations were performed for a wide range of Grashof numbers and Reynolds numbers. None heated block cases were also considered. The obtained results were compared with experimental data obtained for similar parameters.

Alami et al. [8] investigated numerically free convection heat transfer from electronic components in a horizontal channel with slots. The governing equations were solved using a control volume method, and the SIMPLER algorithm was used for treatment of the pressure-velocity coupling. The results were obtained for Rayleigh numbers ($10^4 \leq Ra \leq 8 \times 10^5$), Prandtl number ($Pr=0.72$), opening width ($C=0.15$), block gap ($0.15 \leq RD \leq 1.0$), and block height ($B=0.5$).

In their experimental study, Dogan and Öney [9] investigated convective heat transfer in a horizontal channel with expanded heat sources with aluminum foam heat sinks. In order to investigate the effects on electronic element performance, they determined their effects on heat transfer by placing aluminum foam heat sinks on copper heaters in discrete form. The heat transfer results obtained for the empty surface and the foamed surface were compared and it is seen that with the use of aluminum foam heat sinks increases the heat transfer rate between approximately 36% and 70%.

Doğan and Ozbalcı [10] have experimentally investigated the natural convection heat transfer from porous materials mounted in an inclined rectangular duct. The experiments were made for different Rayleigh Number range from 2.03×10^7 to 1.33×10^8 and the channel inclination angles were varied from 0° to 90° . They determined that duct inclination angles and the use of porous materials have important effects on heat transfer.

In the literature reviews, it was seen that there are very few articles that modeling electronic elements

both separately and numerically. The present numerical study reports the initial results of a numerical investigation of mixed convection heat transfer in a horizontal channel, which is discretely heated at the upper and lower and the remaining channel surfaces are insulated. The numerical results have been compared with the experimental results in a previous detailed study by Dogan [11].

2. Numerical Model

The system under consideration is a three-dimensional channel model. The geometry and coordinate system of the horizontal channel with rectangular cross section used in the present study are depicted in Figure 1. Each of the lower and upper surfaces of the channel are equipped with 8×4 flush mounted heat sources, subjected to a uniform heat flux. The remaining sides of the channel are assumed to be completely insulated.

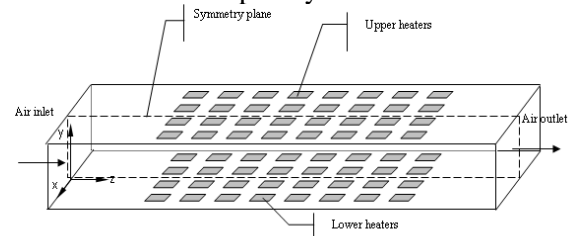


Figure 1. Schematic illustration of the computational domain

In this study, basic conservation equations defining the problem were solved with PHOENICS (Parabolic Hyperbolic or Elliptic Numerical Integrated Code Series) code working with the finite volume method. PHOENICS is a program that simulates heat and mass transfer, fluid mechanics, chemical reactions and similar events (Rosten and Spalding [12]). This CFD code provides iterative numerical approaches for solving nonlinear partial differential equation sets. Numerical solution procedure commonly used SIMPLE is an advanced form of the algorithm (Spalding [13]). Hybrid method was used for convection-diffusion transport. Equation sets are solved by TDMA (Tridiagonal-Matrix-Algorithm) algorithm.

Reliability criteria must be met in studies using the CFD method. In general, in CFD applications, for the solution results to give real values, the solution must be independent of the cell structure, and basic conservation equations must be satisfied. In this study, a $21 \times 20 \times 99$ cell structure was determined to be appropriate.

3. Mathematical Formulation

Some approaches are used to facilitate the solution of governing equations. One of them is the Boussinesq approach. In this approach, all other fluid transport properties are considered constant, except for the change in density. The equations written according to this approach are given below.

In steady state conditions, for three-dimensional laminar incompressible flow, continuity, momentum and energy equations in Cartesian coordinates can be written as follows.

Continuity equation;

$$\frac{\partial u}{\partial x} + \frac{\partial v}{\partial y} + \frac{\partial w}{\partial z} = 0 \quad (1)$$

x-momentum equation;

$$u \frac{\partial u}{\partial x} + v \frac{\partial u}{\partial y} + w \frac{\partial u}{\partial z} = -\frac{1}{\rho} \frac{\partial p}{\partial x} + \nu \left(\frac{\partial^2 u}{\partial x^2} + \frac{\partial^2 u}{\partial y^2} + \frac{\partial^2 u}{\partial z^2} \right) \quad (2)$$

y-momentum equation;

$$u \frac{\partial v}{\partial x} + v \frac{\partial v}{\partial y} + w \frac{\partial v}{\partial z} = -\frac{1}{\rho} \frac{\partial p}{\partial y} + \nu \left(\frac{\partial^2 v}{\partial x^2} + \frac{\partial^2 v}{\partial y^2} + \frac{\partial^2 v}{\partial z^2} \right) + \beta g (T - T_0) \quad (3)$$

z-momentum equation;

$$u \frac{\partial w}{\partial x} + v \frac{\partial w}{\partial y} + w \frac{\partial w}{\partial z} = -\frac{1}{\rho} \frac{\partial p}{\partial z} + \nu \left(\frac{\partial^2 w}{\partial x^2} + \frac{\partial^2 w}{\partial y^2} + \frac{\partial^2 w}{\partial z^2} \right) \quad (4)$$

In these equations, p represents pressure, ν kinematic viscosity and ρ density.

Energy equation;

$$u \frac{\partial T}{\partial x} + v \frac{\partial T}{\partial y} + w \frac{\partial T}{\partial z} = \alpha \left(\frac{\partial^2 T}{\partial x^2} + \frac{\partial^2 T}{\partial y^2} + \frac{\partial^2 T}{\partial z^2} \right) \quad (5)$$

Here; $\alpha = k / \rho c_p$ is the thermal diffusion coefficient and viscous dissipation is neglected. Transport properties of the fluid have been accepted as constant. These assumptions necessarily bring some errors. However, the fact that the temperature changes are not excessive prevents these errors to be large.

The expression $\beta g (T - T_0)$ in the equation (3) above is defined as the term related to the buoyancy force,

and indicates the acceleration of the fluid due to natural convection. T_0 indicates the inlet temperature

3.1. Boundary conditions

Inlet boundary conditions;

$$u_{z=0} = 0, \quad v_{z=0} = 0, \quad w_{z=0} = w_0, \quad T_{z=0} = T_0, \quad p_{z=0} = p_0 \quad (6)$$

Outlet boundary conditions;

Assuming that the length of the channel is long enough, it can be written that the changes of the dependent variables in the direction of the channel axis at the output are zero.

$$\left. \frac{\partial T}{\partial z} \right|_{z=L} = 0, \quad \left. \frac{\partial u}{\partial z} \right|_{z=L} = 0, \quad \left. \frac{\partial v}{\partial z} \right|_{z=L} = 0, \quad \left. \frac{\partial w}{\partial z} \right|_{z=L} = 0 \quad (7)$$

Symmetry plane;

$$u_{x=0} = 0, \quad \left. \frac{\partial v}{\partial x} \right|_{x=0} = 0, \quad \left. \frac{\partial w}{\partial x} \right|_{x=0} = 0, \quad \left. \frac{\partial T}{\partial x} \right|_{x=0} = 0 \quad (8)$$

Side wall;

$$\left. \frac{\partial T}{\partial x} \right|_{x=W/2} = 0 \text{ (adiabatic)} \quad (9)$$

Assuming that there is no slippage on the upper, lower and side walls, conditions on these surfaces are written as given below;

$$u_{y=0} = 0, \quad u_{y=H} = 0, \quad u_{x=W/2} = 0 \quad (10)$$

$$v_{y=0} = 0, \quad v_{y=H} = 0, \quad v_{x=W/2} = 0 \quad (11)$$

$$w_{y=0} = 0, \quad w_{y=H} = 0, \quad w_{x=W/2} = 0 \quad (12)$$

Channel top surface;

$$-k \left. \frac{\partial T}{\partial y} \right|_{y=H} = \begin{cases} 0 & \text{adiabatic (for unheated surfaces)} \\ q''_{conv} & \text{constant heat flux (for heated surfaces)} \end{cases} \quad (13)$$

Channel bottom surface;

$$-k \frac{\partial T}{\partial y} \Big|_{y=0} = \begin{cases} 0 & \text{adiabatic (for unheated surfaces)} \\ \dot{q}_{conv}'' & \text{constant heat flux (for heated surfaces)} \end{cases} \quad (14)$$

The non-dimensional numbers resulting from the above formulations are defined as
Hydraulic diameter;

$$Dh = \frac{4A}{P} \quad (15)$$

A: Channel cross-area (m²)

P: Channel perimeter (m)

Reynolds number;

$$Re = \frac{w_0 Dh}{\nu} \quad (16)$$

w₀: inlet velocity (m/s)

Grashof number;

$$Gr = \frac{g\beta(T_s - T_b)D_h^3}{\nu^2} \quad (17)$$

Modified Grashof number;

$$Gr^* = \frac{g\beta\dot{q}_{conv}''D_h^4}{k\nu^2} \quad (18)$$

g: Gravitational acceleration (m s⁻²)

β: Thermal expansion coefficient (K⁻¹)

q''_{conv}: Average convection heat flux (W/m²)

ν: Kinematic viscosity (m² s⁻¹)

Nusselt number can be calculated as shown below;

$$Nu_{D_{h, upper j}} = \frac{\dot{Q}_{conv, upper j} D_h}{A_{h, upper j} (\bar{T}_{s, upper j} - T_{bj}) k} \quad (19)$$

Nu: Nusselt number

Q̇_{Conv}: Convection heat transfer (W)

D_h: Hydraulic diameter (m)

A_h: Surface area (m²)

T_s: Surface temperature (°C)

T_b: Local bulk temperature (°C)

k: Thermal conductivity of air (W/m K)

In a study conducted with the CFD method, the most important criterion is that the results are in agreement with an experimental study. In Figure 2, the results obtained from the experimental setup for mixed convection heat transfer from discrete heat sources placed in a three-dimensional rectangular channel were compared with the present numerical results, and the results were seen to be in agreement.

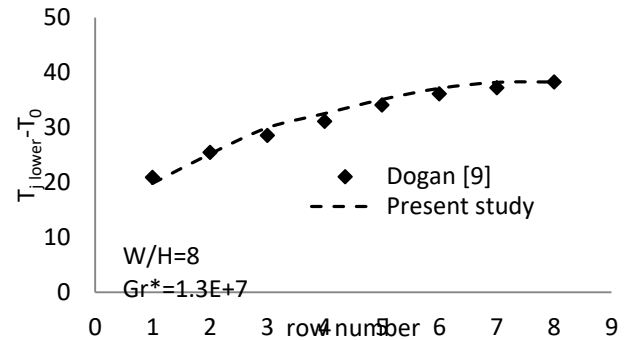


Figure 2. Comparison of numerical and experimental results for the lower heater temperatures for W/H = 8, Re = 971 and Gr* = 1.3x10⁷.

In Figure 3 (a) and (b), the change of Nusselt number according to the Grashof number is given for the value of W/H = 8 and Reynolds number 971 for upper and lower heaters, respectively.

As can be seen from the Figure 3 (a), the row averaged Nusselt number increased with the increase of Grashof number. In the inlet section of the channel the Nusselt number distributions show forced convection thermal entry region properties. The region where the buoyancy induced flow becomes dominant is described as the mixed convection region. For each Grashof number, Nusselt number decreases in the first four rows, and from the 5th row onwards, the Nusselt number increases along the channel, with the effect of the secondary flow. At the lower Grashof number of 5.8x10⁶ the secondary flow effects decreases, and the variation of the Nusselt number is more close to that for forced convection flow. When Nusselt number distributions in the upper part of the heaters are examined (Figure 3 (b)), forced convection behavior manifests itself, and there is a slight fluctuation in the last three rows. This is due to the fact that the fluid moving upward from the bottom affects the upper heaters.

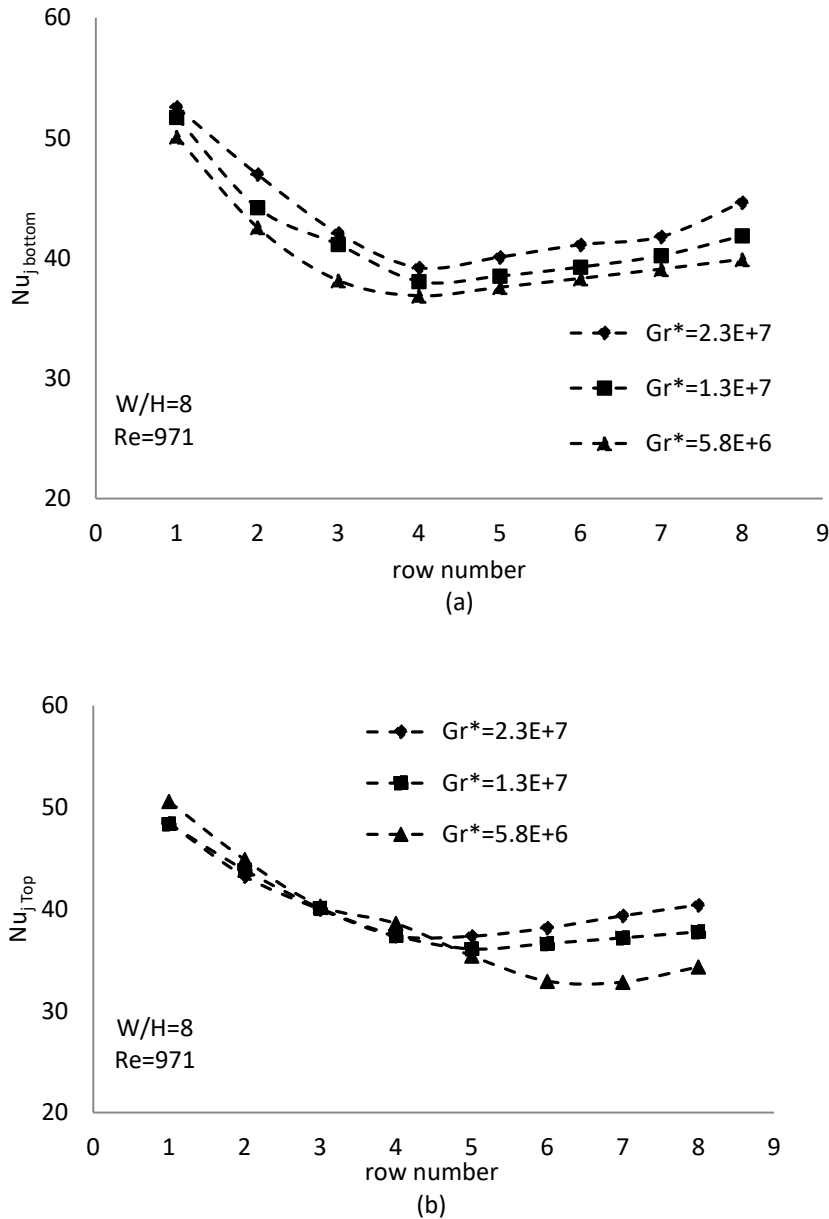


Figure 3. Nusselt number distributions for various modified Grashof numbers

Figure 4 (a) and (b) shows row averaged Nusselt number distributions for both upper and lower heaters for

different Reynolds numbers. As can be seen in Figure 4 (a), for all Reynolds numbers, the row averaged Nusselt numbers take a maximum value at the first rows, and from the 5th row, the buoyancy driven secondary flow has positive effects on the heat transfer, and as a result, Nusselt number increases. At 971, which is the maximum value of the Reynolds number, there is a decrease in the Nusselt number from the first row, but from the 5th row there is not much change on the Nusselt number along the channel. The higher the Reynolds number

the smaller are the fluctuations in the Nusselt number. Therefore, it can be said that the forced convection effects of Reynolds number at the maximum value of 971 are higher. Looking at the distribution of the Nusselt numbers in the upper part of the channel in Figure 4 (b), it can be said that the forced convection effects dominate under all Reynolds numbers. For minimum Reynolds number ($Re=150$), it was observed that there was not much change in the Nusselt numbers along the channel.

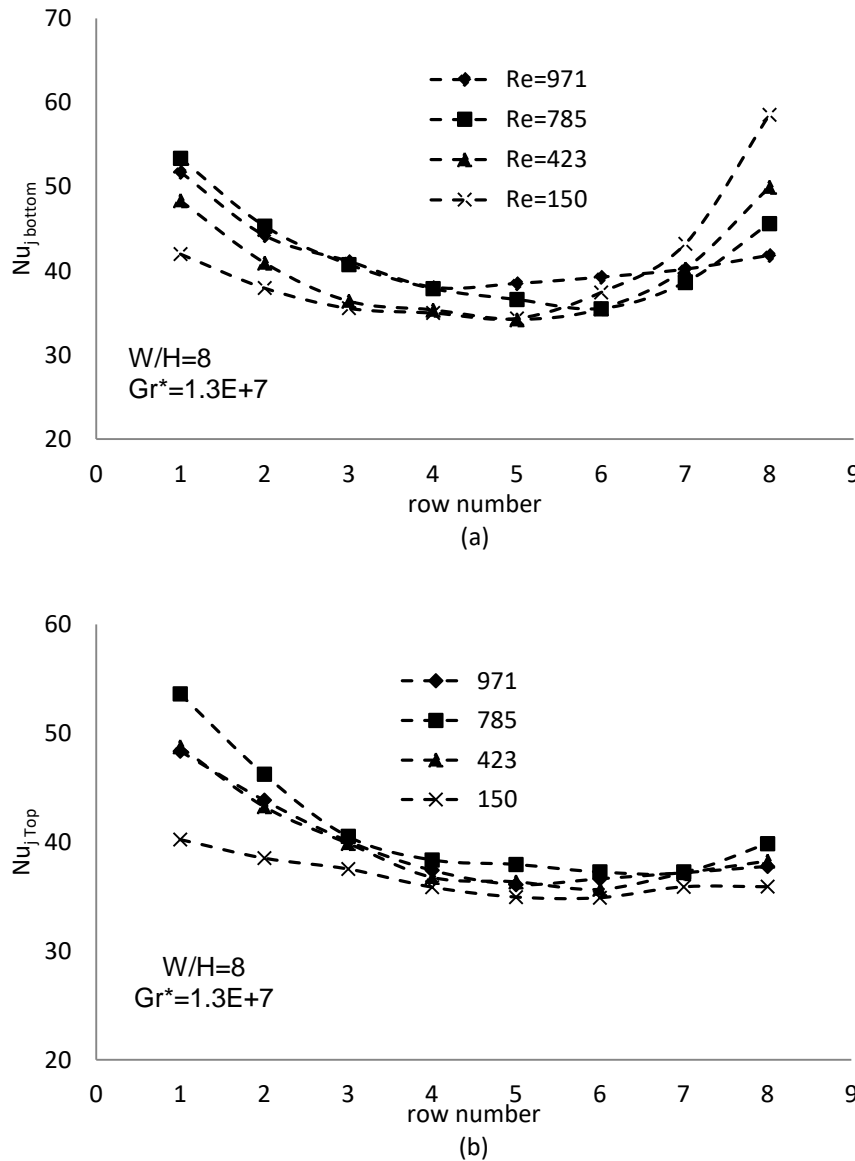
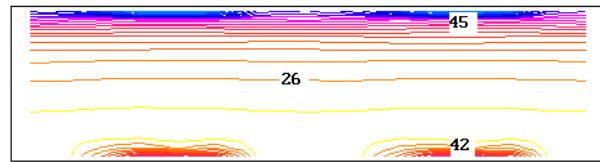


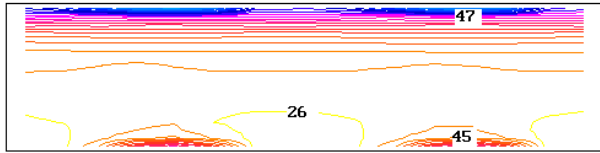
Figure 4. Nusselt number distributions for various Reynolds numbers

In Figure 5, temperature contour graphics are given for $W/H=8$ and $Gr=1.3 \times 10^7$. As can be seen in the figure, the upper heaters temperatures increase along the channel, but are higher than that of the lower heaters temperatures. When looking at the temperature contours, it is seen that the air rises and reaches maximum values at the upper part of the channel. It is seen that the fluid temperature is low in the middle part, since the middle part of the channel is under the influence of the main flow stream. The fluid temperature also increases along the channel depending on the surface temperatures.

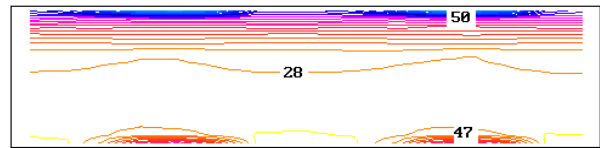
When looking at the vector velocity distributions in Figure 6, the vortex cycle is not very evident during the first heaters. It is observed that the velocity profiles did not deteriorate too much during the first heater and their vorticity was almost absent. It seems that instability begins at the second row and the flow is now completely disrupted throughout the channel. It was observed that the velocity profiles in the upper part did not change much. The local velocities are very small at the top of the channel at low speeds, causing the heaters to overheat.



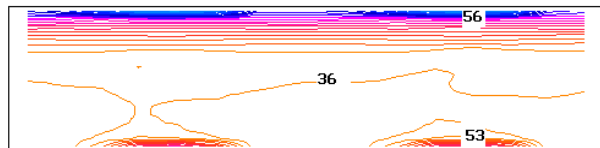
1st row



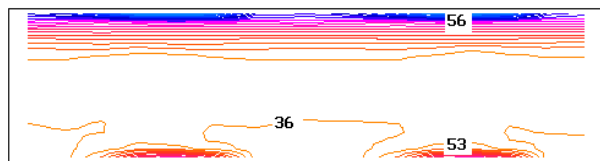
2nd row



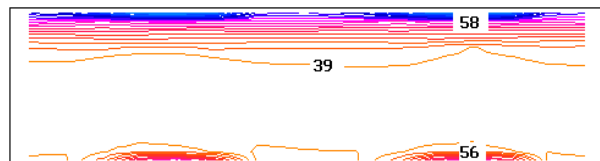
3rd row



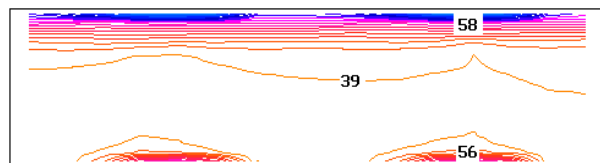
4th row



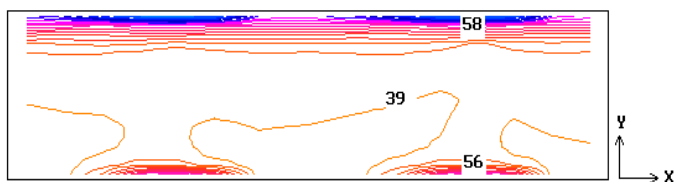
5th row



6th row

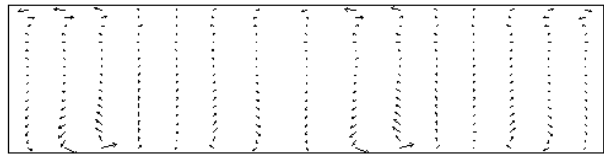


7th row



8th row

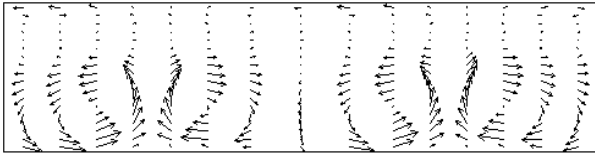
Figure 5. Temperature contour plots in the x-y plane for $Re_{Dh}=1459$, $W/H=8$, $Gr_{Dh}^*=1.3 \times 10^7$



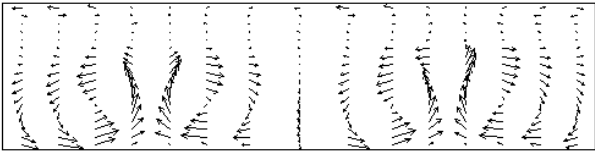
1st row



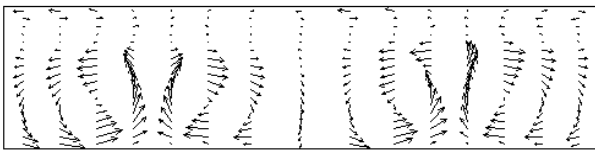
2nd row



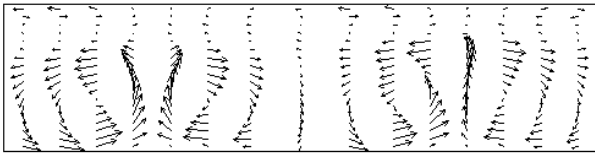
3rd row



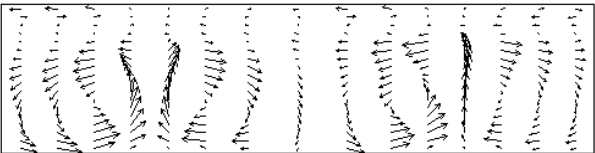
4th row



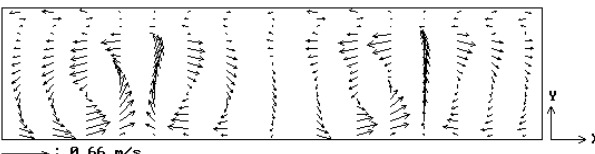
5th row



6th row



7th row



8th row

Figure 6. Vector velocity profiles in the x-y plane for $Re_{Dh}=1459$, $W/H=8$, $Gr_{Dh}^*=1.3 \times 10^7$

4. Conclusions

In this study, heat transfer under laminar mixed convection conditions in a horizontal channel with rectangular cross-section, discrete heaters with uniform heat flux on the upper and lower surfaces, was investigated numerically. For the heaters located in the lower part, the flow from the first row of the heaters has shown forced convection behavior, and an increase in the Nusselt numbers has been observed due to the effect of the secondary flow effective towards the middle rows (5, 6, 7, 8). For higher Grashof numbers, the buoyancy driven secondary flow was more effective. For higher Reynolds numbers, the Nusselt number has taken the maximum value, and forced convection effects have become more prominent. At the lower value of the Reynolds number, the difference between the Nusselt numbers for each row has decreased, and the secondary flow effect has become more dominant. The upper heaters, on the other hand, are mostly under the influence of the main stream, the forced convection feature outweighs and the Nusselt number is constantly decreasing throughout the number of rows. Only a slight increase was observed in the last row ($j = 8$). The reason for this increase is that the flow that moves upward from the bottom causes an intense air movement towards the heaters at the outlet. This situation caused an increase in the Nusselt number. For higher Grashof and lower Reynolds numbers, the elements at the upper channel were seen to be much warmer. This is undesirable. Especially in the design of electronic systems, placing the elements that emit low heat on the upper part is an important issue in terms of system security and efficiency.

References

- [1] Kennedy K. J., Zebib A., Combined free and forced convection between horizontal parallel planes: some case studies, *Int. J. Heat Mass Transfer.*, 26 (1983) 471–474.
- [2] Incropera F. P., Kerby J. S., Moffatt D. F., Ramadhyani S., Convection heat transfer from discrete heat sources in a rectangular channel. *Int. J. Heat Mass Transfer.*, 29 (1986) 1051–1058.
- [3] Choi C. Y., Ortega A., Mixed convection in an inclined channel with a discrete heat source, *Int. J. Heat Mass Transfer.*, 36 (1993) 3119–3134.
- [4] Mahaney H. V., Ramadhyani S., Incropera F. P., Numerical simulation of three-dimensional mixed convection heat transfer from an array of discrete heat sources in a horizontal rectangular duct., *Numer. Heat Transfer.*, 16 (1989) 267–286.
- [5] Dogan A., Sivrioğlu M., Baskaya S., Experimental investigation of mixed convection heat transfer in a rectangular channel with discrete heat sources at the top and at the bottom, *Int. Commun. Heat Mass Transfer.*, 32 (2005) 1244–1252.
- [6] Özsunar A., Başkaya Ş., Sivrioğlu M., Numerical analysis of Grashof number, Reynolds number inclination effects on mixed convection heat transfer in rectangular channels, *Int. J. of Comm. Heat Mass Transfer.*, 28 (2001) 985–994.
- [7] Amirouche Y., Bessaïh R., Numerical simulation of laminar mixed convection air-cooling from an array of heated electronic components mounted in a vertical channel, *International Renewable Energy Congress* November 5-7, – Sousse, Tunisia., (2010) 268–275.
- [8] El Alami M., Najam M., Semma E., Oubarra A., Penot F., Electronic components cooling by natural convection in horizontal channel with slots, *Energy Conversion and Management.*, 46 (2005) 2762–2772.
- [9] Doğan A., Oney B., Experimental investigation of convection heat transfer from aluminum foam heat sinks, *Journal of the Faculty of Engineering and Architecture of Gazi University*, 29 (2014) 71–78.
- [10] Doğan A., Özbalcı O., Experimental Investigation of Free Convection from Foam Heat Sinks in an Inclined Rectangular Channel, *Cumhuriyet Sci. J.*, 39 (2018) 756–765.
- [11] Dogan A., Investigation of mixed convection heat transfer from a rectangular cross-section channel with discrete heat sources at the top and at the bottom, Ph.D. Thesis, Gazi University, Ankara, Turkey, (2003).
- [12] Rosten H., Spalding D. B., The PHOENICS Beginners Guide, London: CHAM I. Ltd, 1987.
- [13] Spalding D.B., The PHOENICS Encyclopedia, London: CHAM Ltd, 1994.

Estimation of the future fracture epidemiology in the patients applying to the emergency department with long short time memory method

Özhan PAZARCI¹ , Yunis TORUN² , Serkan AKKOYUN^{3,*} 

¹ Department of Orthopedics and Traumatology, Sivas Cumhuriyet University, Sivas/Turkey

² Department of Electrical and Electronics Eng., Sivas Cumhuriyet University, Sivas/Turkey

³ Department of Physics, Faculty of Science, Sivas Cumhuriyet University, Sivas/Turkey

Abstract

Operation rooms, human resources and equipment planning are essential for increasing the effectiveness of diagnostic and treatment methods in line with the needs of emergency cases. In this study, 151822 patients admitted to the emergency department (ED) within 3 years were examined in three categories including gender, fracture sites and causes of fracture. However, fracture cases were treated as time series and Long Short Time Memory (LSTM) method was used to estimate the number of future fracture cases. In the learning phase, the number of monthly cases in the next 6 months was estimated using 30-month case numbers. The Root Mean Square Error (RMSE), Mean Absolute Error (MAE) and Mean relative Error (MRE) values of the error rate between the estimated and actual number of cases were given.

Article info

History:

Received:01.05.2020

Accepted:12.06.2020

Keywords:

Emergency,
Fractured,
Long Short Time
Memory

1. Introduction

With the changing living conditions, trauma and fracture patterns also change [1]. Epidemiological studies are used to identify them and to plan health services. The ability to act based on knowledge is important in today's world. In the field of health, patient information creates an intense accumulation of data. There are several methods for proper evaluation and analysis of this data. In recent years, machine learning was introduced in the medical applications and showed its remarkable efficiency in clinical diagnosis and decision support [2]. Presently, the recurrent neural network (RNN) was well employed in solving time series prediction problems and achieved prominent results in many fields. Several variants of RNN have been developed, and among them, long short-term memory (LSTM) network is one of the most popular variants. LSTM learns long-term dependencies by incorporating a memory cell that can preserve state over time [3].

The answer to the question "What will happen in the future?" is important in providing health services. The artificial neural network method is also emphasized in

the literature in predicting future patients [4]. Artificial neural networks have also started to be used in the field of orthopedics [5]. Our study stands out with the use of this method to predict future fracture patients. Current orthopedic literature in this area is generally in the direction of fracture diagnosis from patient images [6]. There are also studies suggesting the diagnosis of a fracture in automated systems with deep learning methods [7]. The general challenge in healthcare today is that physicians have access to a large amount of data about patients, but they have little time and tools to analyze them. The intelligent clinical decision supports in this direction are important for health service delivery planning, cost calculation and personnel distribution planning. These methods are used in future patient estimates [8]. There are few studies using the LSTM (Long Short Time Memory) model to predict patients who have had a heart attack [9, 10]. LSTM has been using for a long time in solving forecasting problems and analyzing big data [11]. However, no studies on the future prediction of orthopedic cases admitted to the emergency departments have been found in the recent literature.

With the presented study, using the LSTM method,

*Corresponding author. Email address: sakkoyun@cumhuriyet.edu.tr

<http://dergipark.gov.tr/csj> ©2020 Faculty of Science, Sivas Cumhuriyet University

complex and heterogenic patient information and future patient prediction were made. According to this study, patients with limb fractures were examined epidemiologically from 151.822 patients who have applied to the emergency department in the last 3 years. In the study, it was aimed to present the fractures epidemiologically according to age, gender groups, distribution throughout the year, fracture region - shape and causes of the accident. Besides, it was tried to predict future case projections using LSTM method. The availability of LSTM in this area has been studied.

2. Materials and Methods

2.1. Data collecting

Among 151.822 patients who applied to the emergency department of the Sivas Cumhuriyet University Medical Faculty in 2011-2013, 2.105 patients who applied for the extremity fracture were included in the study. The data were obtained by scanning backward from the registry. Age, gender, diagnosis and causes of accidents were noted. The patients were divided into four groups according to their ages as 18-40, 40-65, 65-80 and greater than 80 old. The distribution of fractures according to gender was examined. Open and closed fracture rates were noted. The broken regions are listed as shown in Table 1. The data analysis was done in SPSS (Ver.23) program. Data were examined by considering percentage distribution, frequency and arithmetic means.

2.2. Long short time memory (LSTM)

Although Neural Network (NN) has achieved success in many applications, it does not achieve the desired accuracy in time series prediction. Recurrent Neural network (RNN) architecture, which enables the addition of the effect of past data to the next output in the time series prediction, reaches higher accuracy than NN in this series. However, if past inputs are connected to a longer sequence, performance rates decrease due to the short memory of RNNs. Long Short-Term Memory, LSTM architecture, which has been developed as a different version of RNN, allows the creation of longer past input-output relations [12]. In this study, Vanilla LSTM architecture by Gers and Schmidhuber was used in LTSM method that has many versions [13]. The LTSM block consists of three gates named input gate, output gate, gate candidate and forget gate and a sub-block. The main idea of LSTM is that the current input of each block, x_t and h_{t-1} , which represents the short-term output of the previous

block and the long-term output from the previous blocks, takes c_{t-1} into account for obtaining the block output. An LTSM block generates the short term h_t and long term c_t belonging to that block.

The output of the forget gate is a nonlinear function of the current input with the state from the previous block, expressed by the sigmoid activation function;

$$f_t = \sigma_g(W_f x_t + U_f h_{t-1} + b_f) \quad (1)$$

where f_t is the output of forget gate, b_f is the bias for forget gate, σ_g denotes gate sigmoid activation function. W_f and U_f corresponds forget gate coefficients. This output is between 0 and 1, and generates information on whether to be processed in the previous state in the current block or not. The input gate generates an output to calculate c_t with a sigmoid activation function of x_t and h_{t-1} inputs.

$$i_t = \sigma_g(W_i x_t + U_i h_{t-1} + b_i) \quad (2)$$

where i_t is the output of the input gate, b_i is the bias for forget gate, σ_g denotes gate sigmoid activation function. W_i and U_i corresponds to input gate coefficients. The output gate generates information about whether the information in the previous door will be moved to the next block or not.

$$o_t = \sigma_g(W_o x_t + U_o h_{t-1} + b_o) \quad (3)$$

where o_t is the output of the input gate, b_o is the bias for forget gate, σ_g denotes gate sigmoid activation function. W_o and U_o correspond to input gate coefficients. The output gate generates information about whether the information in the previous door will be moved to the next block or not. If the long term memory information of the current block is c_t the cell candidate block output is generated with z_t .

$$z_t = \tanh(W_z x_t + U_z h_{t-1} + b_z) \quad (4)$$

$$c_t = f_t \times c_{t-1} + i_t \times z_t \quad (5)$$

$$h_t = o_t \times \tanh(c_t) \quad (6)$$

3. Results and Discussion

The recent Covid-19 epidemic also showed us that the estimation of the volume of patients is very important for planning for health service. Although

some operations could be postponed to reduce the effect of the outbreak by reducing the hospital burden with lower patient acceptance, fractured patients treatment could not be postponed because of the urgency of treatment. Our study shows that the method we use can be used in other diagnostic fields as well.

The extraction of future projections of the cases with LSTM was carried out by coding deep learning codes in the Matlab programming language. The total of 36-month case data is divided into two parts: 30 months for the training and last 6 months cases for the estimation. The error between the LSTM estimation and the number of cases for each month in 6 months and the actual number of cases was used to measure the performance of the future estimator presented.

3.1. Performance indexes

To assess prediction performance of LSTM based case prediction, three performance indexes were used. Mean absolute error (MAE) was calculated as

$$MAE = \frac{1}{n} \sum_{i=1}^n |f_i - \hat{f}_i| \quad (7)$$

Mean relative error (MRE) is calculated as

$$MRE = \frac{1}{n} \sum_{i=1}^n \frac{|f_i - \hat{f}_i|}{f_i} \quad (8)$$

Root mean square error (RMSE) is calculated as

$$RMSE = \left[\frac{1}{n} \sum_{i=1}^n |f_i - \hat{f}_i|^2 \right]^{\frac{1}{2}} \quad (9)$$

where f_i is the actual value, \hat{f}_i is the predicted value for n instants.

3.2. Simulation environment and result

The prediction model was set up with the Matlab Neural Network Toolbox Results (Matlab R2018a). More than one scenario has been established for the estimation of the cases. These scenarios are as follows.

Scenario 1: Estimation of the number of cases by gender for the next 6 months.

Scenario 2: Estimation of the number of cases for the next 6 months according to the occurrence of the case.

Scenario 3: Estimation of cases by fracture site classes for the next 6 months according to the fracture sites occurring in cases.

Open fractures constituted 8.8% (186 of all cases) of all fractures that applied to the emergency department. These fractures are; Fractures were 46.2%, tibia shaft 11.8%, ankle 7.5%, and tibia distal 6.5% fractures. The leading cause of open fractures was a direct impact to bone 73.7%. In our study, the spine, pelvis, talus, calcaneus and femur shaft open fractures were not observed.

According to the first scenario, 6-month estimation of the number of cases of men and women was made with LSTM, and their performance is shown in figure 1 and 2, respectively. In the estimation made for women, it is seen that there are approximately 20 cases between the number of cases realized in the first two months and the number of cases estimated, but the difference between the number of cases estimated for each month and the number of cases realized is less than 10. In the prediction of cases with male gender, a better estimation performance was obtained compared to women. Within the six-month forecast period, each case number error was estimated with ± 10 errors, and the RMSE value was found to be 9.8.

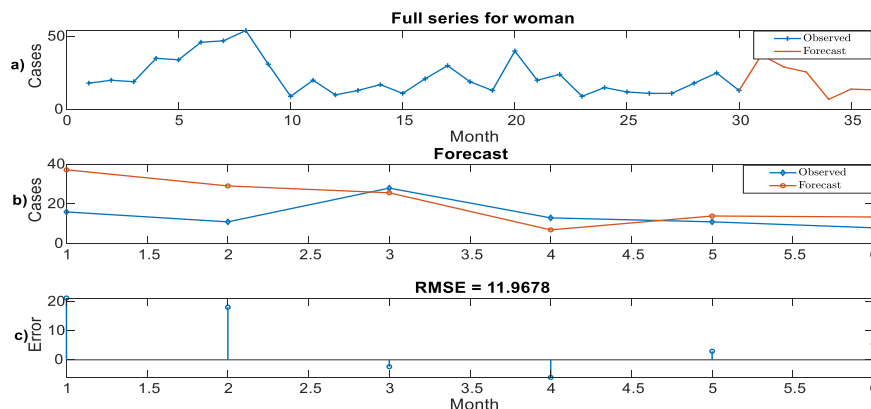


Figure 1. a) Full series of the case for woman (a), Predicted and actual case numbers (b), Prediction error for each month (c)

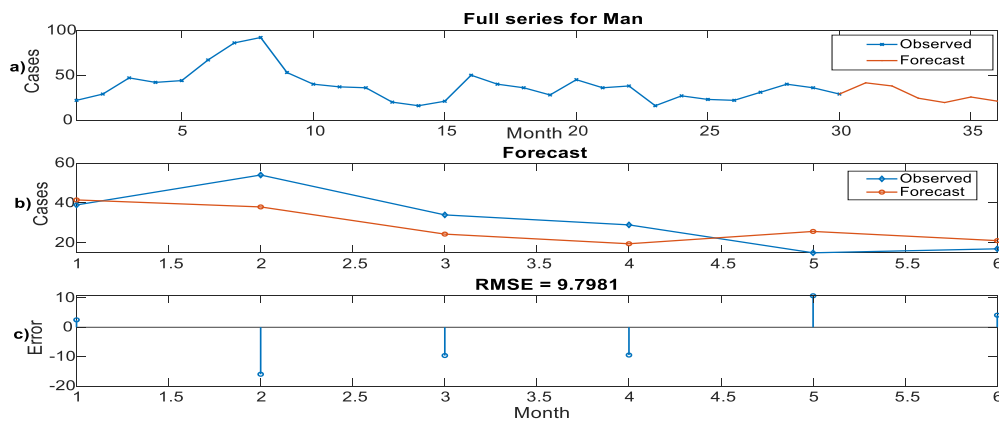


Figure 2. Full series of the case for man (a), Predicted and actual case numbers (b), Prediction error for each month (c)

In scenario 2, a classification was made according to the reason for the occurrence of the cases and an attempt was made to estimate the number of 6-month cases according to these classes. According to the reason of the broken cases, the cases were defined in eight classes which are a) normal falling, b) falling from the ladder, c) falling from a high place, d) the impact took as a result of the fight, e) sports injury, f)

traffic accident, g) stress and h) others not in another class. The number of cases for 30 months and the number of estimates and actual cases for the next 6 months are shown in Figure 3. The graph with the blue line shows the number of cases that occurred, while the red line shows the number of cases that were estimated.

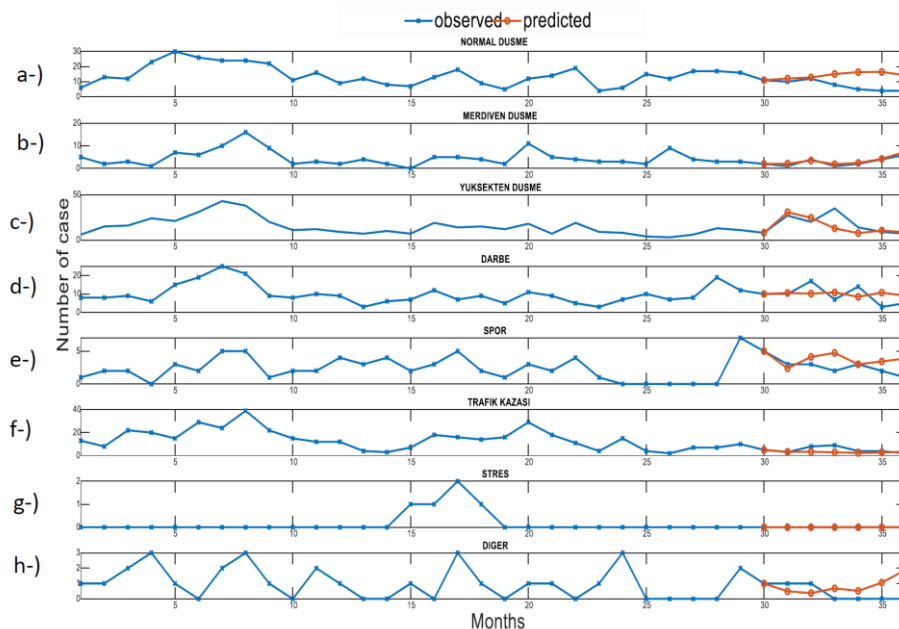


Figure 3. Observed and predicted case according to the cause formation

In scenario 3, cases are divided into two main classes as Upper limb and Lower limb according to fracture areas. Upper limb identifies cases to separate fracture sites and these fractures are Clavicula, Scapula, Humerus, Forearm, Hand-phalanx, Scaphoid, Spine, and Pelvis fractures.

Lower Limb fractures are classified according to 9 lower fracture regions and they are Femur, Patella, Tibia, Tarsal bones, Talus, Calcaneus, Foot phalanx, Ankle, Metatars fractures. In Table1, estimation performances of the number of cases according to the 6-month fracture region

are given. RMSE, MAE and MREs of the prediction errors of each major fracture region and the specific region where the fracture occurs are indicated in the table. Average RMSE, MAE

and MRE values of each class were calculated as 1.053, 0.839 and 0.358, respectively.

Table 1. Performance indices of 6-month forecasts by broken region

Broken region		RMSE	MAE	MRE
UPPER LIMB				
Clavícula		5,441	4,576	1,052
Scapula		1,463	1,266	0,476
Humerus	Proximal	1,290	1,045	0,135
	Shaft	1,460	1,147	0,806
	Distal	3,869	2,719	0,572
Forearm	Proximal	1,311	1,085	0,274
	Shaft	1,742	1,090	0,402
	Distal	2,119	1,841	0,137
Hand-phalanks		7,700	7,031	1,231
Schaphoid		1,856	1,538	0,000
Spine		0,545	0,351	0,934
Pelvis		3,118	2,738	0,188
LOWER LIMB				
Femur	Proximal	4,143	3,298	0,420
	Shaft	2,403	1,746	0,836
	Distal	1,041	0,810	0,963
Patella		0,806	0,702	0,361
Tibia	Proximal	1,489	1,178	0,933
	Shaft	1,221	1,176	0,028
	Distal	1,617	1,497	0,555
Tarsal bones		0,582	0,454	0,996
Talus		0,451	0,304	0,415
Calcaneus		0,730	0,373	0,000
Foot phalanks		0,378	0,285	0,083
Ankle		1,118	0,935	0,041
Metatars		1,695	1,322	0,769
<i>Mean</i>		<i>1,053</i>	<i>0,839</i>	<i>0,358</i>

4. Conclusions

Knowing the epidemiological distribution and rates of fractures is important for preventive medicine as well as health service delivery and planning. According to our study, fall-related fractures in childhood are more common, while osteoporotic fractures caused by minor trauma are observed in the foreground in elderly patients. Hand fractures that occur as a result of the direct impact on bone are more common in adults who form an active workforce. In long bone open fractures, which are difficult and costly to treat, tibial fractures are in the first place. Despite all preventive activities, motor vehicle accidents are the leading cause of fractures. Epidemiological studies

should be carried out at certain intervals according to changing living conditions and human activities. Removing future projections of fracture cases is very important for the programming of emergency and orthopedic clinical human resources, medical equipment and patient services. In this study, for the first time, a 6-month case number estimation from 30-month case numbers was made by using LSTM, which is one of the deep learning methods. Since the shape of the fracture affects the planning of the health service provided, the causes of the fracture again, satisfactory results were obtained in 3 different scenarios, according to the gender, the occurrence of the case and the fracture regions formed in the cases,

according to the fracture class classes for the next 6 months.

Conflicts of interest

The authors state that did not have conflict of interests

References

- [1] Kosuge D, Barry M. Changing trends in the management of; children's fractures. *Bone and Joint Journal*, 97(4) (2015) 442-448.
- [2] Court-Brown CM, Caesar B. Epidemiology of adult fractures: A review. *Injury*, 37(8) (2006) 691-697.
- [3] Xia J, Pan S, Zhu M, Cai G, Yan M, Su Q, et al. A Long Short-Term Memory Ensemble Approach for Improving the Outcome Prediction in Intensive Care Unit. *Computational and Mathematical Methods in Medicine*, 2019 (2019) 1–10.
- [4] Pham T, Tran T, Phung D, Venkatesh S. Predicting healthcare trajectories from medical records: A deep learning approach. *Journal of Biomedical Informatics*, 69(2) (2017) 18–29.
- [5] Olczak J, Fahlberg N, Maki A, Razavian AS, Jilert A, Stark A, et al. Artificial intelligence for analyzing orthopedic trauma radiographs: Deep learning algorithms—are they on par with humans for diagnosing fractures? *Acta Orthopaedica*, 88 (2017) 581–586.
- [6] Lindsey R, Daluiski A, Chopra S, Lachapelle A, Mozer M, Sicular S, et al. Deep neural network improves fracture detection by clinicians. *Proceedings of the National Academy of Sciences of the United States of America*, 115(45) (2018) 11591-11596.
- [7] Cheng CT, Ho TY, Lee TY, Chang CC, Chou CC, Chen CC, et al. Application of a deep learning algorithm for detection and visualization of hip fractures on plain pelvic radiographs. *European Radiology*, 29 (2019) 5469-5477.
- [8] Choi E, Bahadori MT, Schuetz A, Stewart WF, Sun J. Doctor AI: Predicting Clinical Events via Recurrent Neural Networks. *JMLR Workshop and Conference Proceedings* 2015.
- [9] Maragatham G, Devi S. LSTM Model for Prediction of Heart Failure in Big Data. *Journal of Medical Systems*, 43 (2019) 111.
- [10] Golas SB, Shibahara T, Agboola S, Otaki H, Sato J, Nakae T, et al. A machine learning model to predict the risk of 30-day readmissions in patients with heart failure: a retrospective analysis of electronic medical records data. *BMC Medical Informatics and Decision Making*, 18 (2018) 44.
- [11] James AP. Deep Learning Classifiers with Memristive Networks. vol. 14. Cham: Springer International Publishing; 2020.
- [12] Hochreiter S, Schmidhuber J. Long Short-Term Memory. *Neural Computation* 1997.
- [13] Gers FA, Schmidhuber J. Recurrent nets that time and count. Proceedings of the IEEE-INNS-ENNS International Joint Conference on Neural Networks. IJCNN 2000. Neural Computing: New Challenges and Perspectives for the New Millennium, *IEEE*, 3 (2000) 189–94.

AUTHOR GUIDELINES

Thank you for choosing to submit your paper to Cumhuriyet Science Journal. The following instructions will ensure we have everything required so your paper can move through pre-evaluating, peer review, production and publication smoothly. Please take the time to read and follow them as closely as possible, as doing so will ensure your paper matches the journal's requirements.

Submission

Cumhuriyet Science Journal is an international, peer-reviewed, free of charge journal covering the full scope of both natural and engineering sciences. Manuscripts should be submitted by one of the authors of the manuscript as online submission after registration to the Cumhuriyet Sciences Journal. Microsoft Word (.doc, .docx, .rtf), files can be submitted. There is no page limit. If there is a problem while uploading the files of manuscript, please try to reduce their file size, especially manuscripts including embedded figures. Submissions by anyone other than one of the authors will not be accepted. The submitting author takes responsibility for the paper during submission and peer review. If for some technical reason submission through the online submission system is not possible, the author can contact csj@cumhuriyet.edu.tr for support.

Submission or processing charges

Cumhuriyet Science Journal does not charge any article submission, processing charges, and printing charge from the authors.

Terms of Submission

Papers must be submitted on the understanding that they have not been published elsewhere (except in the form of an abstract or as part of a published lecture, review, or thesis) and are not currently under consideration by another journal. The submitting author is responsible for ensuring that the article's publication has been approved by all the other coauthors. It is also the authors' responsibility to ensure that the articles emanating from a particular institution are submitted with the approval of the necessary institution. Only an acknowledgment from the editorial office officially establishes the date of receipt. Further correspondence and proofs will be sent to the author(s) before publication unless otherwise indicated. It is a condition of submission of a paper that the corresponding author permit editing of the paper for readability. All enquiries concerning the publication of accepted papers should be addressed to csj@cumhuriyet.edu.tr. Please note that Cumhuriyet Science Journal uses iThenticate software to screen papers for unoriginal material. By submitting your paper to Cumhuriyet Science Journal are agreeing to any necessary originality checks your paper may have to undergo during the peer review and production processes. Upon receiving a new manuscript, the Editorial office conducts initial pre-refereeing checks to ensure the article is legible, complete, correctly formatted, original, within the scope of the journal in question, in the style of a scientific article and written in clear English. Any article that has problems with any of the journal criteria may be rejected at this stage.

Peer Review

This journal operates a single blind review process. All contributions will be initially assessed by the editor for suitability for the journal. Papers deemed suitable are then typically sent to a minimum of two independent expert reviewer to assess the scientific quality of the paper. The author is required to upload the revised article to the system within 15 days by making the corrections suggested by the referee. The article will be rejected if there are no fixes in it. The Editor is responsible for the final decision regarding acceptance or rejection of articles. The Editor's decision is final.

Title and Authorship Information

The following information should be included

Paper title

Full author names

Full institutional mailing addresses

Corresponding address

Email address

Abstract

The manuscript should contain an abstract. The researchers who are native speakers of Turkish have to add Turkish title and abstract as well. The abstract should be self-contained and citation-free and should be 250-300 words.

Keywords

Keywords of the scientific articles should be selected from the web address of www.bilimadresleri.com

Introduction

This section should be succinct, with no subheadings.

Materials and Methods

This part should contain sufficient detail so that all procedures can be repeated. It can be divided into subsections if required.

Conflicts of interest

Sample sentence if there is no conflict of interest: The authors stated that did not have conflict of interests.

Acknowledgements

Sample sentences for acknowledgements: The work was supported by grants from CUBAP (T-11111). We would like to acknowledge Prof. Mehmet Sözer, MD, for his precious technical and editorial assistance. We would like to thank

References

References to cited literature should be identified by number in the text in square brackets and grouped at the end of the paper in numerical order of appearance. Each reference must be cited in the text. Always give inclusive page numbers for references to journal articles and a page range or chapter number for books. References should be styled and punctuated according to the following examples

[1] Keskin B. and Ozkan A.S., Inverse Spectral Problems for Dirac Operator with Eigenvalue Dependent Boundary and Jump Conditions, *Acta Math. Hungar.*, 130-4 (2011) 309– 320.

[2] National Cancer Institute, Surveillance Epidemiology and End Results. Cancer of the Corpus and Uterus, NOS. Available at: http://seer.cancer.gov/statfacts/html/corp.html?statfacts_page=corp. Retrieved March 2, 2008. (Sample reference of website)

[3] Isaacson K.B., Endometrial ablation. In: UpToDate, Basow, DS (Ed), UpToDate, Waltham, M.A., 2008. (Sample reference of Uptodate topics)

[4] Speroff L., Fritz M.A., Anovulation and The Polycystic Ovary. In. Speroff L., Fritz M.A., (Eds). *Clinical Gynecologic Endocrinology and Infertility*. 7th ed. Philadelphia, Pa: Lippincott Williams and Wilkins; 2005: chap 12. (Sample reference of online book chapters found in websites).

[5] Mazur M.T., Kurman R.J., Dysfunctional Uterine Bleeding. In: Mazur M.T., Kurman R.J., (Eds). *Diagnosis of endometrial biopsies and curettings. A practical approach*. 2nd ed. Berlin: Springer, 2005; pp 100-120. (Sample reference of printed book chapters)

Preparation of Figures

Each figure can be integrated in the paper body or separately uploaded and should be cited in a consecutive order. Figure widths can be 4-6 inch as 300 dpi. The labels of the figures should be clear and informative. The name and the subtitles of the figures must be 9-point font.

Preparation of Tables

Tables should be cited consecutively in the text. Every table must have a descriptive title and if numerical measurements are given, the units should be included in the column heading. Tables should be simple with simple borders and text written as left text. The name and the subtitle of the tables must be 9-point font

Proofs

Corrected proofs must be returned to the publisher within 2 weeks of receipt. The publisher will do everything possible to ensure prompt publication. It will therefore be appreciated if the manuscripts and figures conform from the outset to the style of the journal.

Copyright

Open Access authors retain the copyrights of their papers, and all open access articles are distributed under the terms of the Creative Commons Attribution license, which permits unrestricted use, distribution and reproduction in any medium, provided that the original work is properly cited.

The use of general descriptive names, trade names, trademarks, and so forth in this publication, even if not specifically identified, does not imply that these names are not protected by the relevant laws and regulations.

While the advice and information in this journal are believed to be true and accurate on the date of its going to press, neither the authors, the editors, nor the publisher can accept any legal responsibility for any errors or omissions that may be made. The publisher makes no warranty, express or implied, with respect to the material contained herein.

Ethical Guidelines

New methods and ethically relevant aspects must be described in detail, bearing in mind the following:

Human Experiments. All work must be conducted in accordance with the Declaration of Helsinki (1964). Papers describing experimental work on human subjects who carry a risk of harm must include:

A statement that the experiment was conducted with the understanding and the consent of the human subject.

A statement that the responsible Ethical Committee has approved the experiments.

Animal Experiments. Papers describing experiments on living animals should provide:

A full description of any anaesthetic and surgical procedure used.

Evidence that all possible steps were taken to avoid animal suffering at each stage of the experiment. Papers describing experiments on isolated tissues must indicate precisely how the donor tissues were obtained.

Submission Preparation Checklist

As part of the submission process, authors are required to check off their submission's compliance with all of the following items, and submissions may be rejected that do not adhere to these guidelines.

The submission has not been previously published, nor is it before another journal for consideration (or an explanation has been provided in Comments to the Editor).

The submission file is in Microsoft Word document file (Times New Roman) format.

Where available, URLs for the references have been provided.

The text is single-spaced; uses a 11-point font; employs italics, rather than underlining (except with URL addresses); and all illustrations, figures, and tables are placed within the text at the appropriate points, rather than at the end.

The text adheres to the stylistic and bibliographic requirements outlined in the Author Guidelines, which is found in About the Journal.

If submitting to a peer-reviewed section of the journal, the instructions in Ensuring a Double-Blind Review have been followed.